THEORETICAL, EXPERIMENTAL AND NUMERICAL ANALYSIS OF MECHANICAL AND CONTACT BEHAVIOURS OF A THERMOPLASTIC POLYURETHANE ELASTOMER USED AS COVER ROPE IN LIFT INDUSTRY

LUIS ÁNGEL BARTOLOMÉ MARQUÉS

Supervisor:
Dr. Wilson Tato Vega

A thesis submitted for the award of the degree of
Doctor por Mondragon Unibertsitatea

Mechanical and Manufacturing Department
Engineering Faculty
Mondragon Unibertsitatea

October 2012

A mi ama

"It was the best of times, it was the worst of times,

it was the age of wisdom, it was the age of foolishness,

it was the epoch of belief, it was the epoch of incredulity,

it was the season of Light, it was the season of Darkness,

it was the spring of hope, it was the winter of despair,

we had everything before us, we had nothing before us,

we were all going direct to heaven,

we were all going direct the other way..."

"A tale of two cities", Charles Dickens

STATEMENT OF ORIGINALITY

I hereby declare that the work carried out and presented in this thesis is original and my own. To the best of my knowledge and belief, no part of this dissertation has previously been submitted for any similar qualification or degree and any literature or figures not emerged from this original piece of work are referenced as such.

Luis Bartolomé
(October 2012)

ACKNOWLEDGEMENTS

"You only live once, but if you do it right, once is enough"

Mae West

Después de todo este tiempo, que recordaré siempre como uno de los mejores de mi vida, uno se da cuenta que el trabajo realizado en esta tesis se ha llevado a cabo gracias a la ayuda y el apoyo de diversas personas e instituciones. Por ello mediante estas líneas quisiera darles las gracias a todos ellos y disculparme si es que me olvido de alguien.

En primer lugar me gustaría agradecer sinceramente a mi director Dr. Wilson Tato por su dedicación, paciencia, rigor, apoyo…, en el fondo quiero darle las gracias por su excelente dirección de esta tesis.

Al departamento de Mecánica y Producción Industrial en general, y a los miembros de la línea de Superficies en particular, por brindarme la oportunidad de poder realizar esta tesis. A Jon por sus colaboraciones y aportaciones, y por soportarme algunas veces. A Xabo, Marisun, Andrea… por sus pequeñas pero valiosas ayudas. A los técnicos del taller, especialmente a Gotzon, por sus rápidas soluciones y mostrarme cómo funcionan las máquinas. A Larraitz por su ayuda en el trabajo de laboratorio. A Beñat y Jon por sus colaboraciones y sobrellevar mis correcciones. Y en especial me gustaría agradecerles a Exabier y Ainhara por acompañarme a comer tantas veces y aguantarme durante ese tiempo.

A Orona S. Coop., en especial a Orona-EIC, por ofrecerme la oportunidad de poder realizar esta tesis y financiarla. A todas las personas que durante este tiempo han trabajado en los diversos proyectos que se han llevado a cabo en el grupo de Tribología. A Mikel Urchegui por su visión global y sus consejos. Y en especial me gustaría agradecerles a Hodei y Mikel Ezkurra por prestarme atención durante "unos cinco minutos", ya sabéis el tiempo es relativo y nosotros viajamos muy rápido.

Al Centre Català del Plàstic por la más que valiosa colaboración prestada y a las personas (Angelica, Silvia, Tobias, Vera…) que trabajan allí por su excelente trato y recibimiento durante mis cortas estancias con ellos. A la Dra. Ma. Lluisa Maspoch por recibirme y tratarme tan atentamente. Al Dr. Marcelo de Sousa por su magnífica ayuda en la extrusión del TPU. Al Dr. José Gámez por su tiempo y trabajo. Y en este punto me gustaría agradecer de todo corazón al Dr. Antoni Martínez por abrirme las puertas del centro desinteresadamente, por dedicarme su tiempo y sobre todo por su inestimable ayuda, sin la cual gran parte de esta tesis no hubiera sido posible.

A los doctorandos de MPI (a los de arriba, a los de abajo, a los de al lado) por hacer que el día a día fuera tan ameno: Pablo, Trini, Jon Ander, Arkaitz, Nagore, Alaitz, Ione, Nuria (a ti gracias por dejarme algunas veces okupar tu casa), Iñigo, Josu… (no os puedo poner a todos). A los compañeros que me recibieron en la 6009 tan amablemente (Mikel, Lauren, Imanol, Jon y Zurbi) y a los que llegaron después: Aitor, gracias por coger siempre el teléfono, Haritz, gracias por ser tan encantador con los auxiliares de vuelo, y Christian, gracias por Divertirnos Saliendo por Centroeuropa (DSC). Y de forma muy especial me gustaría agradecerles a dos personas todo este tiempo trabajando juntos. A Joseba por su ayuda en los detalles y en lo que no son detalles, por tus explicaciones y por estar a "mi lado" haciendo tan grato el trabajo diario, *thanks man*. Y a Asier, que aunque lo primero que hice fue quitarte el sitio, durante este tiempo hemos llegado a ser amigos, ha sido un verdadero placer coincidir contigo.

A mis amigos Trepi, Cubas, Iñako y Espino, gracias por no tener ni idea de lo que hago en el trabajo y muchas más gracias por no quererlo saber cuando estamos juntos.

También quisiera dar las gracias a mi familia y a los que han llegado a ella en este tiempo (Andere y Oian), a mis hermanos Jesus (allá donde estés viéndonos), Juanjo, Mar, Patxi, Rober, Rosa y Pedro por estar siempre ahí y apoyarme siempre. Y en especial a mi Ama por su amor incondicional y porque con su constancia, trabajo duro, tesón y sacrificio me has enseñado a no rendirme nunca.

Y para finalizar, le quiero dar las gracias a Román por tanto, que realmente no sé por dónde empezar. Gracias por estar y vivir conmigo durante este tiempo sin recriminarme nada, por entender que mis días en el trabajo han estado sólo bien, por creer y confiar más en mí que yo mismo y por tu amino y cariño cuando los he necesitado. Gracias porque sin ti nada de todo esto hubiera sido posible.

ABSTRACT

Thermoplastic polyurethane elastomers (TPU) are a class of elastomer that can be processed by heat without being destroyed. In addition to the unique mechanical performance properties of elastomers (soft, high deformation elastically, the ability to dissipate energy…), TPUs exhibit high abrasion and bending fatigue resistances. Therefore, they are used as cover rope in the lift industry. These elastomeric cover ropes allow downsizing sheaves and homogenizing contact pressures over sheaves. Therefore, in order to understand the behaviour of TPU coatings when they pass over sheaves, the contact behaviour must be analyzed.

In the present work, the contact between an ether-based TPU processed by extrusion and a hard material (gray iron) has been investigated using theoretical, experimental and numerical analysis. The contact behaviour has been studied dividing into normal and tangential contacts. Therefore it has been necessary to obtain a model of the TPU mechanical behaviour at moderate strains (under 100%) and a friction model between the TPU and the gray iron.

As result of this work, an analytic visco-hyperelastic model with the deformation history, which has been implemented into numeric calculus using an iterative FEA based technique, has been proposed. Moreover an analytic friction model, which has been locally implemented into numeric calculus using finite element method, has been also proposed. Finally, these both models have been validated using simulations of normal contact (indentation) between the TPU and the gray iron as well as tangential (sliding) contact.

RESUMEN

Los elastómeros termoplásticos de poliuretano (TPU) son materiales elastoméricos que se pueden procesar calentándolos sin destruirlos. Además del comportamiento mecánico típico de los elastómeros (baja dureza, muy deformables elásticamente, alta tenacidad…), estos elastómeros presentan alta resistencia a la abrasión y a fatiga por flexión. Por ello, resultan ser convenientes como recubrimiento de los cables de hilos metálicos empleados en la industria de elevación. Este tipo de recubrimientos permiten reducir el tamaño de las poleas y homogeneizar las presiones sobre ellas. Por tanto, para lograr entender el comportamiento de los recubrimientos de TPU sobre las poleas, se debe estudiar su comportamiento en contacto.

En esta tesis se ha llevado a cabo el estudio teórico, experimental y numérico del comportamiento de un TPU de tipo éter procesado por extrusión en contacto con un material mucho más rígido (fundición gris laminar). Para ello el comportamiento en contacto se ha dividido en dos partes: contacto normal y tangencial. De esta forma ha sido necesario la obtención de un modelo de comportamiento mecánico del TPU a bajas deformaciones (<100%) y de un modelo de rozamiento entre el TPU y la fundición.

De esta forma se ha obtenido un modelo visco-hiperelástico analítico para el TPU que considera la historia de las deformaciones sufridas y que ha sido implementado en el cálculo numérico mediante una técnica iterativa basada en los elementos finitos. También se ha propuesto un modelo de rozamiento analítico en función de la velocidad de deslizamiento y la presión de contacto que ha sido implementado localmente en el cálculo numérico mediante elementos finitos. Finalmente ambos modelos han sido validados en simulaciones entre el TPU y la fundición tanto en contacto normal (indentación) como en contacto tangencial (deslizamiento).

LABURPENA

Poliuretanozko termoplastiko elastomeroak (TPU) beroarekin suntsitu gabe prozesa daitezkeen materiala elastomeroak dira. TPU material hauek elastomeroen ohiko konportamentu mekanikoez gain (elastikoki deformazio handiak onartzea, zailtasun handia, bigun izatea, eta abar) urradura eta flexio bidezko nekearekiko erresistentzia handia aurrezten dute. Hori dela eta igogailuen industrian erabilitako kable metalikoen estaldura gisa komenigarriak dira. Mota honetako estaldurek poleen tamaina murriztu eta haienganako presioak homogeneizatzea ahalbidetzen dute. Horregatik TPU estaldurek poleekiko duten portaera mekanikoa ulertu ahal izateko, beren kontaktu portaera ikertu behar da.

Lan honetan estrusio bidez prozesatutako eter motako TPU-aren jarrera askoz gogorragoa den material batekin kontaktuan dagoenean (galdaketa grisa) ikertu da analisi teoriko, esperimentala eta zenbakizko erabiliz. Horretarako ikerketa lana deformazio txikiko TPU-aren portaera mekanikoa eta TPU eta galdaketaren arteko marruskaduraren modelo baten garapenean oinarritu egin da. Hauekin bi zatian normala eta tangentziala banatu izan den kontaktuzko portaeraren ikerketa da.

Modu honetan TPU-ak jasandako deformazio historia kontuan hartzen duen modelo bisco-hiperelastiko analitiko bat garatu egin da. Material modelo hori zenbakizko kalkuluan inplementatua izan da elementu finituetan oinarritutako teknika iteratibo baten bitartez. Horrez gain kontaktu bidezko presio eta irristatze abiaduran oinarritutako marruskadura modelo analitikoa bat proposatu da, zein elementu finituen bitartez zenbakizko kalkuluan inplementatua izan da. Azkenik bi modelo hauek TPU eta galdaketaren arteko kontaktu normal (indentazio) eta tangentzialen simulazioen bitartez balioztatuak izan dira.

TABLE OF CONTENTS

LIST OF FIGURES

LIST OF TABLES

ABBREVIATIONS

BDO	1,4-butandiol
CE	Chain extender diol
DI	Di-isocyanate
DIC	Digital correlation image
DMT	Adhesion model of Derjaguin, Muller and Toporov
EPM	Ethylene propylene rubber
EDM	Electric discharge machining
FEA	Finite element analysis
IR	Polyisoprene or synthetic natural rubber
JKR	Adhesion model of Johnson, Kendall and Roberts
MDL	Macrodiol
MD	Melt flow direction
MDI	4,4'-methylene bis(phenyl di-isocianate)
M-D	Adhesion model of Maguis and Dugdale
NR	Natural rubber
NBR	Nitrile-butadiene rubber
PA6	Polyamide 6
PA12	Polyamide 12
PTMEG	Polytretamethylene ether glycol
SAXS	Small-angle X-ray scattering
SBR	Styrene-butadiene rubber
SBS	Styrene- butadiene -styrene based thermoplastic elastomer
SEBS	Styrene-ethylene-butylene-styrene based thermoplastic elastomer
SEDF	Strain energy density function
TD	Transverse melt flow direction
TPA	Thermoplastic polyamide elastomer
TPC	Thermoplastic polyester elastomer
TPE	Thermoplastic elastomer
TPO	Olefin-based thermoplastic elastomer
TPS	Styrene-based thermoplastic elastomer

TPU	Thermoplastic polyurethane elastomer
TPV	Dynamically crosslinked (or dynamic vulcanizates) thermoplastic
UV	Ultraviolet
bpp	Bits per pixel
dpi	Dots per inch

SYMBOLS

A_c	[m^2]	Contact area
A_r	[m^2]	Real contact area
A_0	[m^2]	Apparent or nominal contact area
a	[m]	Radius of Hertzian contact area
a_c	[m]	Radius of contact area
a_δ	[m]	Radius of contact area with a sheet of thickness δ
C_{ij}	[-]	Elastic constant of strain energy density function
c	[Nsm^{-1}]	Viscous damping coefficient
D	[-]	Surface fractal dimension
E	[Pa]	Young's or tensile modulus
E''	[Pa]	Elastic loss modulus
e	[-]	Engineering strain
e_{fit}	[-]	Scalar strain parameter
e_{vm}	[-]	Scalar strain parameter
e_1, e_2, e_3	[-]	Principal engineering strain
F	[N]	Force
$F_{adhesion}$	[N]	Adhesion contribution to elastomer friction
$F_{cohesion}$	[N]	Wear contribution to elastomer friction
$F_{hysteresis}$	[N]	Deformation contribution to elastomer friction
F_N	[N]	Normal force
F_N^{Hz}	[N]	Normal force using Hertz theory
F_r	[N]	Friction force
$F_{viscous}$	[N]	Lubrication contribution to elastomer friction
G	[Pa]	Shear modulus
g	[ms^{-2}]	Gravity constant
H	[Nm^{-2}]	Hardness
I_1, I_2, I_3	[-]	Strain invariants
I_m	[-]	Maximum value for I_1 (Gent's SEDF)
K	[Pa]	Bulk modulus
k	[Nm^{-1}]	Stiffness of Hooke's law

k	[J/K]	Boltzmann constant
l_m	[m]	Length of joint links
N	[-]	Number of chains in network
n	[-]	Freely jointed links of a chain
p	[Pa]	Pressure
p_0	[Pa]	Maximum pressure
R	[m]	Radius of sphere
r	[m]	Polar coordinate
r_{ch}	[m]	Distance between crosslinks in network chain
s	[Pa]	True stress
s_1, s_2, s_3	[Pa]	Principal true stresses
s_τ	[Pa]	Shear true stress
T	[K]	Temperature
t	[s]	Time
v	$[\mathrm{ms}^{-1}]$	Velocity
W	$[\mathrm{Jm}^{-3}]$	Elastically stored energy per unit volume
w	$[\mathrm{JK}^{-1}]$	Entropy of network
x	[m]	Displacement
z_0	[m]	Equilibrium distance between atoms
δ	[m]	Thickness
δ_t	[m]	Thickness of the excitation elastomer layer
γ	$[\mathrm{Jm}^{-2}]$	Surface energy
ζ	[-]	Magnification or characteristic length scale
η_c	$[\mathrm{Nsm}^{-2}]$	Viscous damping coefficient in tension
λ	[-]	Extension ratio
$\lambda_1, \lambda_2, \lambda_3$	[-]	Principal extension ratios
λ_e	[-]	Elastic parameter
λ_l	[m]	Horizontal length scale
μ	[-]	Friction coefficient
μ_k	[-]	Coefficient of dynamic friction
μ_s	[-]	Coefficient of static friction
ν	[-]	Poisson's ratio
$\xi_\parallel$	[m]	Parallel cut-off length
$\xi_\perp$	[m]	Perpendicular cut-off length
ρ	$[\mathrm{Kgm}^{-3}]$	Density
σ	[Pa]	Engineering stress
σ^*	[Pa]	Reduced engineering stress

σ_τ	[Pa]	Shear engineering stress
τ	[s]	Relaxation time
ω	[s^{-1}]	Frequency

1 INTRODUCTION

"If we knew what it was we were doing,

it would not be called research, would it?"

Albert Einstein

Thermoplastic elastomers (TPEs) are a class of elastomers that can be processed as thermoplastic materials, i.e. by heat without being destroyed. Thermoplastic elastomers play an important role for a broad range of engineering applications in different industrial areas. In the automotive industry elastomers are utilized in different components, as door seals, suspension system, windscreen wiper, etc. In other industrial fields, thermoplastic elastomers are used in vibration isolation bearings, hoses, impact absorbers, toys, household products, gaskets and footwear. The reason for the widespread applications is that they offer the unique mechanical performance properties exhibited by elastomers in being soft, highly extensible and their ability to dissipate energy, in addition to better recyclability than thermoset elastomers or rubbers. Thermoplastic polyurethane elastomers TPUs, which belong to TPEs, exhibit the typical high elasticity of elastomers in addition to high abrasion resistance. Therefore, they are used to coat steel wire ropes in the lift industry. In this chapter, the reasons for using such coatings are briefly reviewed to introduce the motivation of this study (Section 1.1). Moreover, the scope (Section 1.2) and the outline (Section 1.3) of the thesis are presented.

1.1 Background and motivation

In the lift industry, the most widespread drive system (Janovský 1999) basically consist of an electric motor which drives a sheave and transmits the movement to the car by ropes which rolled up the sheave and a counterweight hangs on the opposite end of the rope (Figure 1.1). Therefore, the movement is obtained by means of traction, defined as the transmission of motion by friction and adhesion between two contacting bodies.

In recent years, the builders, to increase profits, are demanding a reduction in the space for lift facilities of the buildings. In this regard, a great breakthrough occurred when the machine room was no longer needed due to use direct drive gearless motors, i.e. smaller motors. The machine room less (MRL) lifts were launched.

The use of direct drive gearless motors leads to the downsizing of drive sheave due to this type of motor produces less torque. Therefore, the surface of contact to obtain traction is also reduced and the steel wire ropes are subjected to more bending. To solve the problem of traction, elastomeric coatings have been begun to use. Using elastomeric coatings, the friction between the drive sheave and rope is increased, the available contact surface of coated wire ropes is greater than uncoated ones and the contact pressures are homogenized over contact area. The TPUs are used to coat steel wire ropes due to high elasticity and high abrasion resistance. Moreover, the TPUs can be easily processed by extrusion along the steel wire ropes due to their thermoplastic properties.

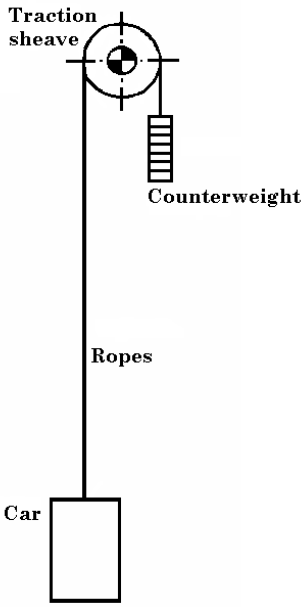

Figure 1.1: Schematic figure of the drive system (traction drive) in a lift (Janovský 1999).

Nevertheless, the contact behaviour between the drive sheave and coated wire ropes is not well understood, mainly because of the contact behaviour of TPUs is not widely studied. Therefore, this thesis aims to investigate the contact behaviour between an extruded TPU and a hard solid (gray iron) and to examine the reliability of finite element techniques to predict accurately this contact behaviour.

1.2 Scope of the thesis

Contact behaviour between thermoplastic polyurethane elastomer and hard solids is determined primarily by the mechanical behaviour of elastomer and friction behaviour between them.

Elastomers have a unique property in that they are highly extensible. This means that they can be subjected to large strains and after unloading they recover almost to their original dimensions. The mechanical behaviour of elastomers is nonlinear and characterized by incompressibility (or near-incompressibility). Elastomers also exhibit a time-dependent behaviour, i.e. viscoelasticity, which can be demonstrated by relaxation and creep tests. In addition, when an elastomer is subjected to cyclic loading-unloading, inelastic effects, as stress softening (Mullins effect), hysteresis loss and residual strains, are shown. In this work it is investigated experimentally the mechanical behaviour of an extruded TPU and how strain history influences when the TPU is preconditioned. Besides, it is discussed the reliability of material models using computational modelling to predict the contact behaviour of TPU.

Elastomer friction, which is a restraint of relative motion between contacting bodies, represents a particularly interesting field of research, as it depends upon many parameters, such load, sliding velocity or temperature. According to Amontons' friction law, the arising tangential force at a sliding interface is proportional to the normal load induced on the contact area and their ratio may be expressed as the coefficient of friction. Despite the debate on the applicability of this law to elastomer friction, the sliding contact between elastomers and hard body exhibits higher coefficient of friction than between rigid materials. This high derivation in exhibited friction compared to other materials is mainly due to the ability of elastomer to deform to large strains, which results in viscoelastic energy dissipation, as well as surface adhesion effects. However, the origins and significance of the different parameters affecting elastomer friction are still a subject of discussion and not fully understood (Baumberger and Caroli 2006). Many models exist trying to describe the complex expected behaviour of elastomer friction using great amount of parameters or variables (Persson 1998, Klüppel and Heinrich 2000) however, the determination of several descriptors is elaborate and might be of little benefit to everyday friction testing. Complicating matters further, these parameters or variables are correlated to each other, i.e. the increase of only one parameter or variable does alter the influence of others significantly and, therefore, general description of the coefficient of friction is very difficult. The friction behaviour between an extruded TPU and a gray iron is investigated experimentally in this work. And it is examined how the sliding contact can be predicted using computational techniques of finite element analysis.

1.3 Outline of the thesis

Chapter 2 reviews the different approaches available to characterise the behaviour of elastomers and it also gives an overview on contact behaviour and friction of elastomers.

The aims and objectives of the thesis, which are laid down of the critical review of literature survey, are summed up in **Chapter 3**.

In **Chapter 4** the extruded thermoplastic polyurethane elastomer that was chosen is characterized to derive its mechanical properties under moderate strains (<100%). The hyperelastic and inelastic behaviours are obtained from cyclic loading-unloading experimental tests in two homogeneous deformation states (uniaxial tension and pure shear) and the viscoelastic behaviour from relaxation tests.

In **Chapter 5** the hyperelastic and viscoelastic models of the extruded thermoplastic polyurethane are evaluated. In addition, an original method using a FEA-based technique to predict the hyperelastic behaviour depending on maximum strain history is proposed and its predictions are compared to experimental tests.

Chapter 6 investigates the behaviour of the thermoplastic polyurethane elastomer on normal contact or indentation. Force, contact area and contact pressures are studied using cyclic loading-unloading experimental indentations. In addition, these experimental indentations are simulated using the hyperelastic model to a given maximum strain and the FEA-based technique to compare the accuracy between them.

In **Chapter 7** the behaviour on tangential (or sliding) contact between a gray iron chosen and the thermoplastic polyurethane elastomer is investigated. A friction model is proposed using tribological tests with different speeds and contact pressures. The proposed friction model is implemented into the finite element calculus of the FEA-based technique to validate the simulations of experimental sliding contacts.

The significant conclusions in this work are summarised in **Chapter 8** along with suggestions for future works.

2 LITERATURE SURVEY

"Quote me as saying I was mis-quoted"

Groucho Marx

This chapter introduces the theoretical background and the fundamental concepts of elastomer research given in literature, which are used to examine the mechanical and contact behaviours of an extruded thermoplastic polyurethane elastomer (TPU). In the first sections (2.1 to 2.4), a general introduction to elastomers and their mechanical properties are given, highlighting the specific characteristics of thermoplastic polyurethane elastomers. The next two sections (2.5 and 2.6) review the literature of contact behaviour and friction of elastomers. Finally, the last section (2.7) gives an overview of how elastomer behaviour and friction are modelled in finite element analysis (FEA).

2.1 Introduction on elastomers

2.1.1 Brief history of elastomers

Although latex was used since ancient, natural rubber (NR) was first introduced to the Occident in the 18th century. Then, two significant milestones occurred during 19th century (White and De 2001). The first, when Charles Goodyear (1800-1860) discovered the process of vulcanisation in 1839, led to the industrial utilisation of rubbers. The second, when John Dunlop (1840-1921) patented the pneumatic tyre in 1888, increased significantly demand for rubbers. In the 20th century the demand for synthetically produced rubbers increased specially during the first and second world wars. The first synthetic natural rubber or polyisoprene (IR) was synthesized by Fritz Hofmann (1866-1956) in 1909, later the styrene-butadiene (SBR) and the nitrile-butadiene rubbers (NBR) were developed by I.G. Farbenindustrie in the 1930s.

The development of thermoplastic elastomers started with the discovery of the diisocyanate reaction polyaddition, which was first applied to produce polyurethane fibres, by I.G. Farbenindustrie in 1937. Therefore, thermoplastic polyurethane elastomers (TPUs) were the first homogeneous elastomers that could be processed by methods commonly used for thermoplastic materials. The first patents covering elastomeric properties of polyurethanes were issued to DuPont and Imperial Chemical Industries in the 1940s. Additional development work led to products that had considerably improved properties through the 1950s and 1960s. Commercial thermoplastic polyurethane elastomers were introduced in the 1960s by B. F. Goodrich and Mobay in the United States, and by Bayer A. G. and Elastogran in Europe (Drobny 2007). Styrene-based thermoplastic elastomers (TPSs) were first developed by Shell and they were introduced commercially in 1966. The thermoplastic polyester elastomers (TPCs) and olefin-based thermoplastic elastomers (TPOs) were developed throughout the 1960s. TPCs were commercialized by DuPont in 1972. Dynamically crosslinked thermoplastic elastomers (TPVs) are based on the extensive research done by Monsanto during the 1970s and 1980s and the first commercial product was introduced in 1981. Thermoplastic polyamide elastomers (TPAs) were introduced in 1982 by ATO Chemie. During the last two decades, many new developments have taken place and new products and applications have been developed by chemical industry.

2.1.2 General introduction on elastomers

An elastomer is a macromolecular material; being extremely highly deformable under the action of comparatively small stress but exhibit almost complete recovery when the stress is released (Ward and Sweeney 2004). The elastomers show large strains with nonlinear stress-strain relationship, viscoelasticity and inelastic effects, which are affected by dynamic and thermal effects (Treloar 1975). A force versus extension curve for elastomer, which is typically nonlinear in shape, is shown in Figure 2.1. Furthermore, the elastomers are considered virtually incompressible with a bulk modulus some thousand times greater than shear or tensile modulus (Brown 2006).

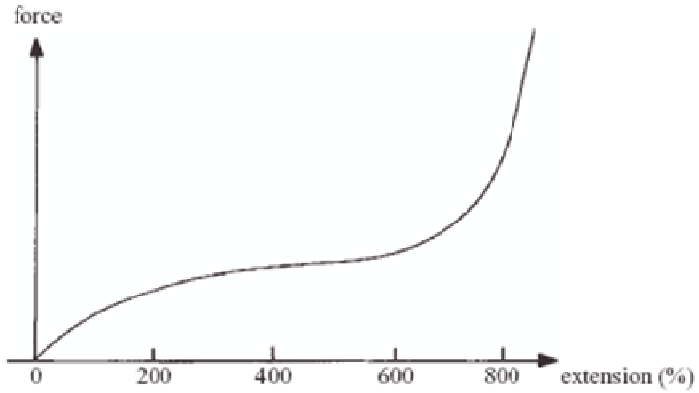

Figure 2.1: Nonlinear force vs. extension curve in uniaxial tension for a typical elastomer (Ward and Sweeney 2004).

The elastomers are diversified into two classes, thermosets and thermoplastics. The main difference is that thermosets, also named rubbers, cannot be reprocessed by heat without being destroyed, while thermoplastics can be. Furthermore, cohesion of their molecules is different, the former are chemically bonded and the latter are physically aggregated. Finally, the thermoplastics can be dissolved in contact with a suitable solvent, however the thermosets swell but do not dissolve. Industrially, the advantages of thermoplastics elastomers (TPEs) are various. First, a more homogeneous processing than thermosets due to TPEs do not require curing agents. Second, the processing also is easy (see Figure 2.2) and therefore low cost. Third, there is wide variety of properties available. Finally, TPEs can be recycled and reused. The disadvantages of TPEs relative to thermosets are the relatively high cost of raw materials, the general inability to load TPEs with low cost fillers (such as carbon black) and poor chemical and temperature resistance. Considering these pros and cons, the rubbers and other types of materials are being replaced by TPEs (Grady and Cooper 2005). The replacements are significant due to the growth of so-called "soft-touch" surfaces and specially due to environmental benefits in car industry, except for vehicle tyres where the replacement by TPEs are not suitable because of they cannot provide the necessary traction without a reduced wear rate (PTS 2007). In lift industry, where the wear rates are not as high as in car industry, the TPEs are used in guides, belts, rope, etc., indeed the thermoplastic polyurethane elastomers are used to coat steel wire ropes. Therefore, this literature review is focused on TPEs, particularly on TPUs. The term rubber is used from now on exclusively to describe thermoset elastomers in this thesis.

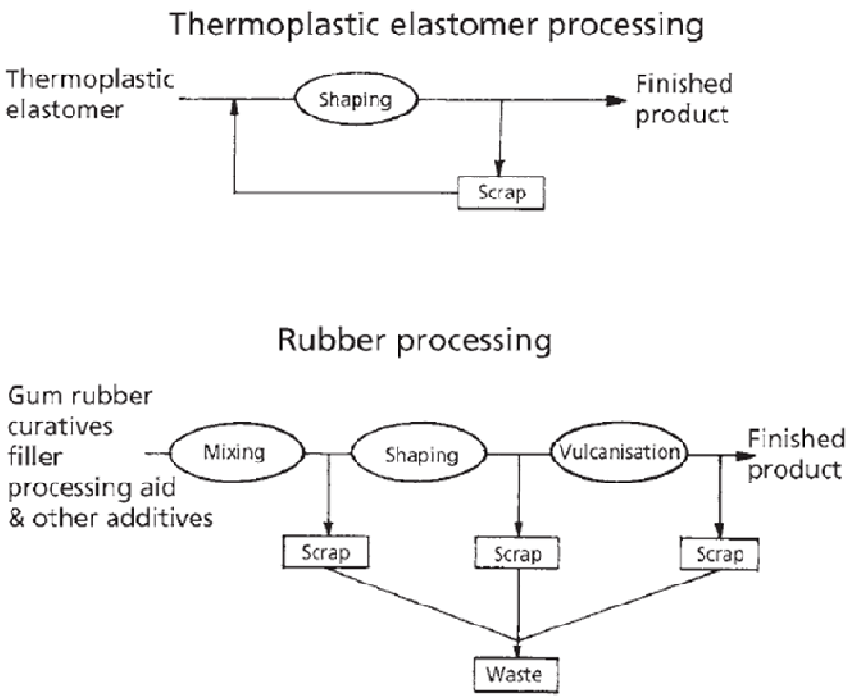

Figure 2.2: Thermoplastic elastomer processing versus rubber processing (White and De 2001).

The general properties of thermoplastic elastomers are toughness, ductility, tear strength, low-temperature flexibility, absence of significant creep and a high coefficient of friction. However, the abrasion resistance (Table 2.1) and hardness (Figure 2.3) are very varied among TPEs.

Table 2.1: Abrasion resistance of some common elastomers (Mardel et al. 1995).

Abrasion resistance	**Elastomer**
Very best	TPU, TPC
Excellent	NR, SBS, SBR, Ethylene-propylene rubber (EPM)
Moderate	NBR, Polybutadiene, Butyl rubber
Poor	Polysulphide
Very poor	Polysiloxane

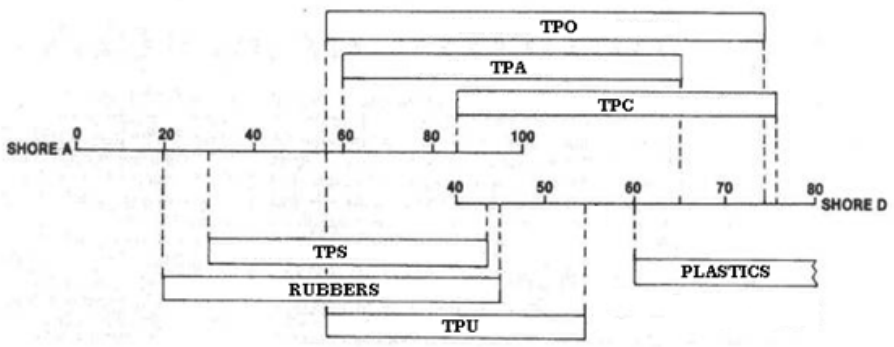

Figure 2.3: Hardness ranges of thermoplastic elastomers (JOBST 2008).

The TPEs are mainly diversified into six classes in accordance with ISO 18064 (ISO, 2003):

- **TPS**: Styrene-based thermoplastic elastomers are the most widespread TPEs as well as being a very large family, including styrene-butadiene-styrene (SBS) and styrene-ethylene-butylene-styrene (SEBS).
- **TPC**: Thermoplastic polyester elastomers are characterized by good thermal melt stability and heat resistance in the end applications. They are used particularly for applications involving exposure to dynamic loads due to their low mechanical loss factor. Moreover, they exhibit good tear strength and fatigue resistance.
- **TPA**: Thermoplastic polyamide elastomers are characterized by high strength and good resilience under flexural load. At the present time, only TPAs of polyamides 12 (PA12) and 6 (PA6) are of any practical significance.
- **TPO**: Olefin-based thermoplastic elastomers are characterized by excellent low-temperature impact strength and moderate elastic behaviour. Actually, they should be classified more as flexible plastics with high toughness rather than elastomers, due to the rubber component is not crosslinked or only very slightly crosslinked.
- **TPV**: Dynamically crosslinked (or dynamic vulcanizates) thermoplastic elastomers are characterized by low to moderate elongation at break and strength, good elastic behaviour and better chemical resistance than TPS. Actually, they are polymer blends of a thermoplastic material and a conventional rubber, which is crosslinked in the extruder during production (dynamic crosslinking) and finely dispersed in the thermoplastic.

- **TPU**: Thermoplastic polyurethane elastomers are a very diverse and versatile family, which are explained below.

Thermoplastic polyurethane elastomers

Thermoplastic polyurethane elastomers (TPUs) are randomly segmented copolymers (Grady and Cooper 2005) with alternating hard and soft segments that repeat multiple times in a single polymer chain. The hard segment is formed by the addition of chain extender (in most cases linear low-molecular weight diols) to the isocyanate, the most widely used is 4,4'-methylene bis(phenyl di-isocianate) (MDI). The soft segment consists of the flexible polyether or polyester chains that connect two hard segments (Figure 2.4). Therefore, TPUs are diversified into two groups depending on the macrodiol used, i.e. ester-based or ether-based. To sum up, TPUs are formed by three chemical components: a di-isocyanate (DI), a macrodiol (MDL) and a chain extender (CE) diol.

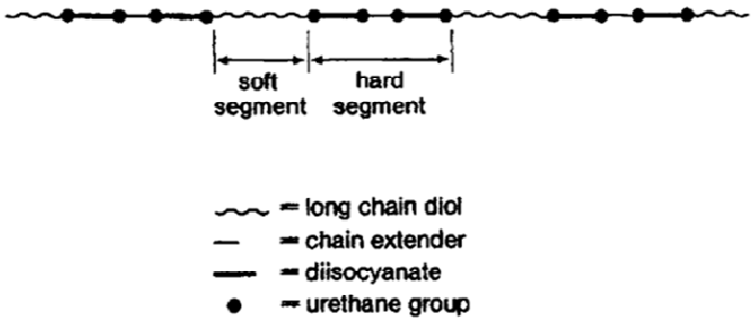

Figure 2.4: Schematic representation of TPU (Drobny, 2007).

The two segments are incompatible at room temperature, which results in microphase separation. Therefore, TPUs have a two-phase micro-structure and the two phases have different properties (Drobny 2007). The relative amount of the two phases controls the physical properties of the TPU by determining which phase is isolated or continuous Figure 2.5). The soft phase contains the soft domains, which have their glass transition below room temperature. The hard phase contains the hard domains, which are below their glass transition at room temperature.

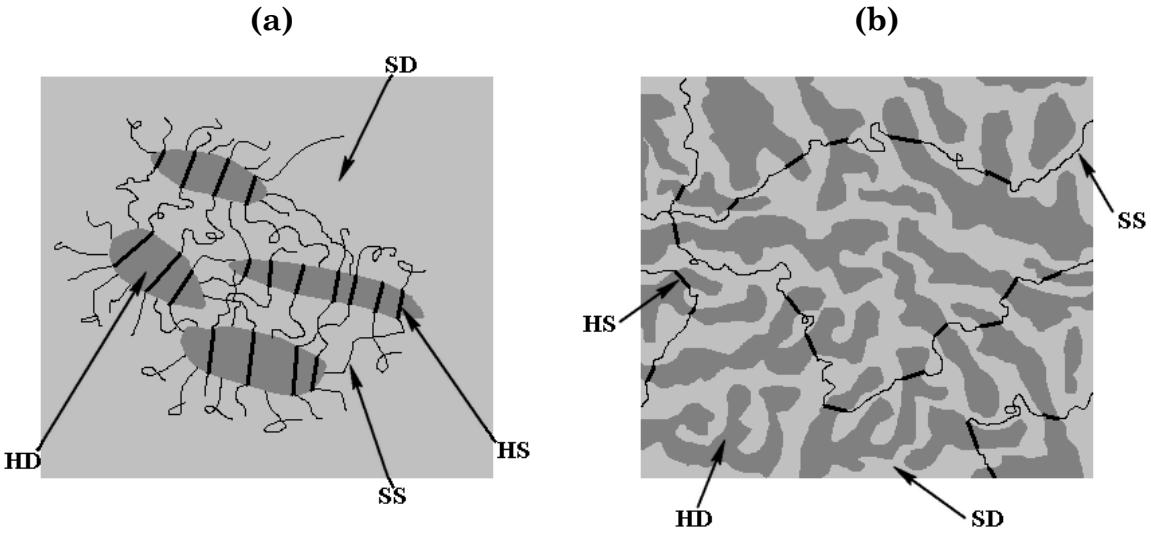

Figure 2.5: Schematic representation of the TPU's micro-structure consists of hard (HS) and soft (SS) segment associations into hard (HD) and soft (SD) domains: (a) at low hard segment content and (b) at a higher hard segment content.

Depending on the ratio of hard to soft segments, TPUs can be formulated in different grades which range from soft flexible elastomeric materials to brittle and high modulus plastics (Petrovic and Ferguson 1991). Therefore, the tensile strength of TPUs varies from 25 to 75 MPa depending on their chemical structures and hardness (Drobny 2007). One of the main advantages of TPUs is their high abrasion resistance. In addition, TPUs have a much higher load bearing capacity than other conventional rubbers at equivalent hardness and good tear strength and bending fatigue. However, they have limited resistance to UV light and hydrolysis. Ester-based TPU shows better abrasion and cut resistance, tensile and tear strength than ether-based. Ether-based are well suited for situations where high resistance against hydrolysis or microbial deterioration and/or improved low-temperature flexibility is required (PTS 2007).

TPUs are also very resistant to oils, motor fuels, hydraulic fluids and many other non-polar solvents. However, chlorinated hydrocarbons or aromatic solvents cause a severe swelling of TPUs. Polar solvents are capable of partially or completely dissolving TPU (White and De 2001). TPUs are recommended for different medical applications, due to their good compatibility with human skin, blood and tissues.

The ease of processing is one of the significant advantages of TPUs. They can be processed by the usual melt-processing methods, such injection moulding, extrusion and calendaring. All the grades cannot be processed universally, each method requires specific grades with suitable morphology and melt viscosity.

2.2 Elasticity

A solid consists of atoms, molecules, long chains of molecules (polymers) and crystallites (metals) if they are observed at microscopic scale. However, at macroscopic scale, these structures cannot be distinguished and they are replaced by a continuous medium. This branch of mechanics is called continuum mechanics. In this section, the essential aspects of continuum mechanics and basic kinematic relations for the description of small and large (finite) strain analyses are introduced. The elastic behaviour of elastomers, also named hyperelastic behaviour, is described under the assumption of full reversibility of stress and strain and no energy dissipation.

2.2.1 Elastomer elasticity at small strains

The stress-strain behaviour of elastomers is non-linear, thus Hooke's law does not apply. But, in a narrow region at small strains (<10%), this behaviour is considered to be approximately linear (Gent 1996).

Two fundamental elastic constants can be used to describe the behaviour of isotropic elastic materials. The bulk modulus K deals with the resistance to compression in volume under hydrostatic pressure and it is defined as the ratio of applied pressure to the volumetric strain. The shear modulus G deals with the resistance to simple shearing stress and it is defined as the ratio of the applied shear stress to shear strain produced. They can be expressed at small strains as follow:

$$K = \frac{E}{3(1-2\nu)} , \tag{2.1}$$

$$G = \frac{E}{2(1+\nu)} , \tag{2.2}$$

where ν is the Poisson's ratio and E is the Young's or tensile modulus measured at small strains. The elastomers are frequently regarded as being incompressible (deformation occurs essentially at constant volume) for many engineering applications when they are not subjected to high hydrostatic loadings (Ward and Sweeney 2004). Therefore the value of Poisson's ratio is close to 0.5 which gives a tensile modulus E of approximately $3G$ at small strains.

2.2.2 Elastomer elasticity at finite strains

The mechanical derivation of constitutive equations is based on the existence of a strain (also referred to stored) energy density function (SEDF) or elastic potential for the stress *W*, corresponding to the change in the Helmholtz free energy of the elastomer upon deformation (Belytschko et al. 2000).

Two approaches are generally available for the mechanical behaviour characterization of the elastomers. Firstly, the approach based on statistical thermodynamics considerations (named statistical or kinetic theory) and secondly, the phenomenological approach which does not take into account the microstructure of the elastomer, i.e. it treats the elastomer as a continuum. Both approaches lead to constitutive equations derived through identifying a strain energy density function, which is a measure of energy stored elastically in a unit volume of elastomer subjected to a specific state of strain assuming an isotropic and homogeneous elastomer (Ward and Sweeney 2004).

Statistical theory of elastomer elasticity

Structural models are based on physical considerations which relate the macroscopic elastomer behaviour to deformation in its structural elastomer network (Treloar 1975). The elastomer network is considered to consist of *N* chains per unit volume. A chain is defined as a molecular segment between successive cross-links and it is idealised to contain *n* freely jointed links each of length l_m.

The probability density $P(r_{ch})$ of finding the end of a molecular chain within a spherical distance r_{ch} of its origin is calculated using Gaussian distribution model:

$$P(r_{ch}) = \left(\frac{b^3}{\Pi^{3/2}}\right)\exp\left(-b^2 r_{ch}^2\right), \tag{2.3}$$

where *b* is considered to be characteristic of a particular molecule. The root mean square of the length is proportional to the square root of the number of links *n* of length l_m in the chain

$$\left(\overline{r_{ch}^2}\right)^{1/2} = n^{1/2} l_m, \tag{2.4}$$

then

$$b^2 = \frac{3}{2nl_m^2}. \tag{2.5}$$

It is implicit that Equation (2.5) is only approximate as its derivation assumes that the distance r_{ch} between the chain crosslinks is much less than the fully extended length of the chain nl_m.

If an elastomer is subject to tensile deformation, the molecular conformations that are possible in a network decrease. This results in an increase in the configurational entropy w of the system, while the internal energy is assumed to remain constant throughout the deformation. The configurational entropy of a single chain is given by the Boltzmann relation,

$$w = -\mathrm{k}T \ln P = \mathrm{k}Tb^2 r_{ch}^2, \tag{2.6}$$

where k is the Boltzmann constant and T the absolute temperature. The force F required to move a single chain end from a distance r_{ch} to a distance $r_{ch} + \mathrm{d}r_{ch}$ is,

$$F = \frac{\partial w}{\partial r_{ch}} = \frac{3\mathrm{k}Tr_{ch}}{nl_m^2}. \tag{2.7}$$

In this statistical model (Treloar 1944), a single elastomer molecule of the chain can be regarded as a spring with the stiffness being both proportional to the absolute temperature and inversely proportional to the number of links in the molecule. The statistical treatment of a network of elastomer molecules can be considered to be similar in principle to a single chain molecule so that the entropy of the whole network of chains can be calculated as a function of the macroscopic deformation state. By the derivation of the free energy or the work of deformation, the stress for a given strain or deformation state can be calculated. The elastically stored energy per unit volume W of the elastomer is derived as a strain energy density function

$$W = \frac{N\mathrm{k}T}{2}\left(\lambda_1^2 + \lambda_2^2 + \lambda_3^2 - 3\right), \tag{2.8}$$

where $\lambda_1, \lambda_2, \lambda_3$ are the principal extension ratios (the ratio of stretched to the unstretched length). It is convenient to assume that the term $N\mathrm{k}T$ can be expressed in terms of the shear modulus G, then Equation (2.8) reduces to the so-called neo-Hookean SEDF

$$W = \frac{G}{2}\left(\lambda_1^2 + \lambda_2^2 + \lambda_3^2 - 3\right). \tag{2.9}$$

The name neo-Hookean is due to Rivlin (1948) showed that the statistical theory was the natural extension of Hooke's law to large deformations. Thus, the above SEDF involves only one physical parameter G, the shear modulus, which may be determined from the degree of crosslinking in the rubber. By assuming a constant volume ($\lambda_1\lambda_2\lambda_3 = 1$), Equation (2.9) can be rewritten as

$$W = \frac{G}{2}\left(\lambda_1^2 + \lambda_2^2 + [\lambda_1\lambda_2]^{-2} - 3\right). \quad \textbf{(2.10)}$$

where W is a function of two independent variables for an incompressible elastomer. The neo-Hookean fits experimental data reasonably well at small deformations ($\lambda \leq 1.3$) and it is not applicable to filled elastomers (Boyce and Arruda 2000). Therefore, other configurations have been developed to improve the curve fitting of experimental observations. One of first structural SEDF for the configurational entropy of a single chain was proposed by James and Guth (1943) and it is called "three-chain model". Treloar (1946) simplified the elastomer network by a "four-chain model", in which four chains are attached to the vertices of a tetrahedron. Later on, a more successful structural SEDF is proposed by Arruda and Boyce (1993), in which eight orientations of chains in space give rise to the known "eight-chain model". This model can capture the nonlinear elastic behaviour of elastomers rather well in uniaxial tension but it cannot successfully do it in equibiaxial tension, due to the difficulty of the model in describing the behaviour for the region of low strains (Boyce and Arruda 2000). More recently the model called "non-affine micro-sphere model" has been suggested by Miehe et al. (2004) also in cases of large strains.

Phenomenological theory of elastomer elasticity

Phenomenological models are based on empirical results and mathematical developments to derive an appropriate function to fit the experimentally observed stress-strain behaviour of elastomer. This approach is considered that the isothermal elastic properties of the elastomer may be described in terms of a strain energy density function W. Under the assumption of an isotropic and elastic behaviour, the function W should be symmetrical with respect to the three principal extension ratios ($\lambda_1, \lambda_2, \lambda_3$).

The phenomenological strain energy density function (SEDF) can be diversified into two types, a first type is developed by means of the invariants of the right Cauchy-Green tensor (I_1, I_2, I_3) and a second type is developed using directly the principal extension ratios ($\lambda_1, \lambda_2, \lambda_3$). The two types of SEDFs are related by

$$I_1 = \lambda_1^2 + \lambda_2^2 + \lambda_3^2, \quad \textbf{(2.11)}$$

$$I_2 = (\lambda_1\lambda_2)^2 + (\lambda_2\lambda_3)^2 + (\lambda_3\lambda_1)^2, \quad \textbf{(2.12)}$$

$$I_3 = \lambda_1^2\lambda_2^2\lambda_3^2. \quad \textbf{(2.13)}$$

The first type of phenomenological SEDFs are given using the invariants (I_1, I_2, I_3), but whether incompressibility is assumed ($I_3 = 1$) then the SEDF is given using only two invariants (Belytschko et al. 2000), thus $W = W(I_1, I_2)$. Therefore, Mooney (1940) proposed a phenomenological SEDF,

$$W = \mathrm{C}_1(I_1 - 3) + \mathrm{C}_2(I_2 - 3), \tag{2.14}$$

with two parameters based on the assumption of a linear relation between the load and deformation during simple shear deformation mode. The Mooney SEDF performs well for moderately large deformation in uniaxial tension and in simple shear. But it is often found to be inadequate for predicting the behaviour for inhomogeneous deformation states, mainly at high strain levels. Rivlin and Saunders (1951) suggested that C_1 should be dependent on I_2. The Money SEDF can be simplified to the neo-Hookean SEDF, Equation (2.8), when $\mathrm{C}_1 = G/2$ and $\mathrm{C}_2 = 0$. It is expressed in terms of invariants as

$$W = \frac{G}{2}(I_1 - 3). \tag{2.15}$$

Using mathematical reasoning alone, Rivlin (1956) proposed a more general SEDF,

$$W = \sum_{i+j=1}^{\infty} \mathrm{C}_{ij}(I_1 - 3)^i (I_2 - 3)^j, \tag{2.16}$$

for incompressible materials using a power series, known as polynomial form. The C_{ij} are material constants. The power series, Equation (2.16), is usually truncated to the first few terms. The number of terms depends on the degree of deformation of the material. At large deformations, a greater number of terms of the polynomial form are taken into account. However, an excessive number of terms can lead to unstable strain energy functions (Belytschko et al. 2000). Different coefficients are considered in the Equation (2.16) to derive specific SEDFs by different authors. An overview of these specific SEDFs is given in Table 2.2.

But the very general nature of Equation (2.16) leads to the difficulty of experimentally determining a suitable strain energy density function, particularly at small strains. Therefore, Gregory (1979) proposed the assumption that SEDF may be considered to be a function of I_1 only, especially for filled elastomers and if the strains are not too large. This assumption leads to the known as reduced polynomial SEDF,

$$W = \sum_{i=1}^{\infty} \mathrm{C}_{i0}(I_1 - 3)^i. \tag{2.17}$$

Yeoh (1993) adopted this approach and proposed (with $i = 3$) a strain energy density function,

$$W = \mathrm{C}_{10}(I_1 - 3) + \mathrm{C}_{20}(I_1 - 3)^2 + \mathrm{C}_{30}(I_1 - 3)^3, \tag{2.18}$$

for filled elastomers. The Yeoh SEDF works well in capturing different deformation states from moderate to large deformations.

Table 2.2: The coefficients of different SEDFs based on the SEDF expressed as an infinite power series in terms of I_1 and I_2.

SEDF reference	Coefficients
Neo-Hookean (Treloar 1944)	C_{10}
Mooney (Mooney 1940)	C_{10} C_{01}
Tschoegl (Tschoegl 1971)	C_{10} C_{01} C_{11}
Isihara (Isihara et al. 1951)	C_{10} C_{01} C_{20}
James (James et al. 1975)	C_{10} C_{01} C_{11} C_{20} C_{02}
Tschoegl2 (Tschoegl 1971)	C_{10} C_{01} C_{22}
Biderman (Treloar 1975)	C_{10} C_{01} C_{20} C_{30}
James-Green-Simpson (James et al. 1975)	C_{10} C_{01} C_{11} C_{20} C_{30}
Haupt-Sedlan (Haupt and Sedlan 2001)	C_{10} C_{01} C_{11} C_{02} C_{30}
Lion (Lion 1997)	C_{10} C_{01} C_{50}

Gent (1996) proposed an alternative high order of the first invariant SEDF

$$W = \frac{E}{6}\ln\left(1 - \frac{I_1 - 3}{I_m - 3}\right), \tag{2.19}$$

which takes the form of a natural logarithm and where E is the tensile modulus at small strains and the I_m is the maximum value for I_1. Boyce and Arruda (2000) suggested that the natural logarithm term in the Gent SEDF may be expanded to yield

$$W = \frac{E}{6}\left[(I_1 - 3) + \frac{1}{2(I_m - 3)}(I_1 - 3)^2 + \frac{1}{3(I_m - 3)^2}(I_1 - 3)^3 + \ldots + \frac{1}{(n+1)(I_m - 3)^n}(I_1 - 3)^{n+1}\right], \tag{2.20}$$

which is a form of the reduced polynomial form, Equation (2.17), with all coefficients C_{ij} related to E and I_m.

The second type of phenomenological SEDFs describes the elastomers using the principal extension ratios or principal stretches ($\lambda_1,\lambda_2,\lambda_3$). Varga (1966) proposed the first SEDF,

$$W = \mu_v\left(\lambda_1 + \lambda_2 + \lambda_3 - 3\right), \tag{2.21}$$

as the sum of the principal extension ratios, where μ_v is an elastomer parameter. The range of validity of this SEDF is comparable with the neo-Hookean SEDF, Equation (2.8). Ogden (1972) proposed the widest SEDF

$$W = \sum_{i=1}^{n} \frac{2\mu_i}{\alpha_i^2}\left(\lambda_1^{\alpha_i} + \lambda_2^{\alpha_i} + \lambda_3^{\alpha_i} - 3\right), \tag{2.22}$$

in terms of the principal extension ratios for an incompressible material, where μ_i and α_i are arbitrary material parameters. The Ogden SEDF may basically fit any set of experimental data. Nevertheless, the parameter identification is complicated due to two aspects: it may require a large number of parameters to capture the elastomer behaviour and the nonlinear way in which the parameters appear in the expression.

2.2.3 Elasticity in homogeneous deformation states

In principle, stress-strain data at six homogeneous deformation states (uniaxial, planar and equibiaxial tensions and uniaxial, planar and equibiaxial compressions) are needed to predict accurately the behaviour of elastomers. Assuming incompressibility, the number of required deformation states is reduced, since hydrostatic pressure can be superimposed on other stress states without altering the deformation state (Figure 2.6). Therefore, experimentally only three deformation states are used to characterize an elastomer. Usually uniaxial, equibiaxial and planar tensions are chosen to due to friction troubles between the elastomer and the grips in the case of compression tests (Brown 2006).

For a homogeneous deformation states, Rivlin (1956) showed that a set of relationships,

$$\begin{aligned}
\frac{s_1 - s_2}{\lambda_1^2 - \lambda_2^2} &= 2\left(\frac{\partial W}{\partial I_1} + \lambda_3^2 \frac{\partial W}{\partial I_2}\right),\\
\frac{s_1 - s_3}{\lambda_1^2 - \lambda_3^2} &= 2\left(\frac{\partial W}{\partial I_1} + \lambda_2^2 \frac{\partial W}{\partial I_2}\right),\\
\frac{s_2 - s_3}{\lambda_2^2 - \lambda_3^2} &= 2\left(\frac{\partial W}{\partial I_1} + \lambda_1^2 \frac{\partial W}{\partial I_2}\right),
\end{aligned} \tag{2.23}$$

exist between the principal extension ratios ($\lambda_1,\lambda_2,\lambda_3$), the true principal stresses (s_1,s_2,s_3), relating to the deformed state, and the partial derivates of W with respect to the two invariants I_1 and I_2. The left hand side of Equation (2.23) is defined as the reduced stress.

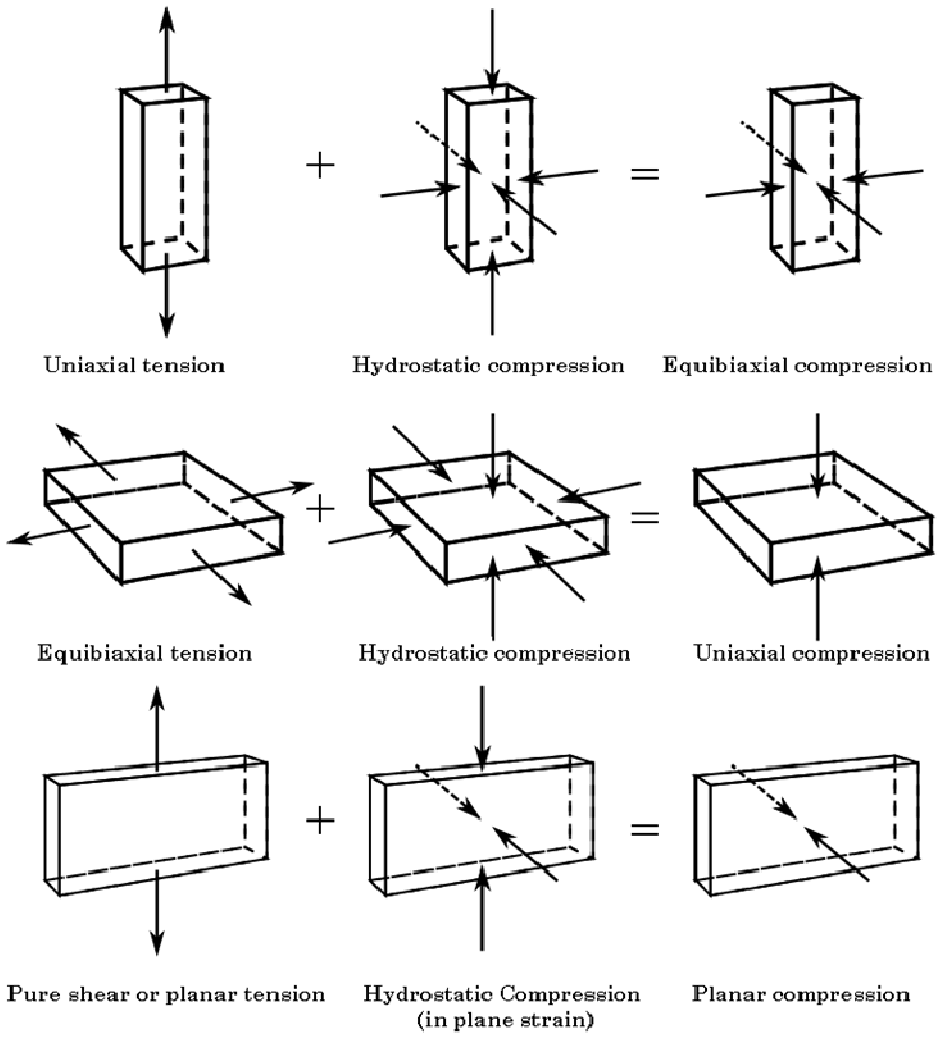

Figure 2.6: Equivalence between the different homogeneous deformation states for an incompressible elastomer.

The engineering stress σ, which relates to the undeformed state, is related to the true stress s by

$$\sigma_i = \frac{s_i}{\lambda_i}. \tag{2.24}$$

Using these relationships, the reduced stress σ_{red} for the different homogeneous deformation states (Figure 2.6) are defined below. In uniaxial tension, $\lambda_1 = \lambda;\ \lambda_2 = \lambda_3 = \lambda^{-1/2}$ and $\sigma_1 = \sigma;\ \sigma_2 = \sigma_3 = 0$, the reduced stress is given by

$$\sigma_{red} \equiv \frac{\sigma}{\left(\lambda - \lambda^{-2}\right)} = 2\left[\left(\frac{\partial W}{\partial I_1}\right) + \frac{1}{\lambda}\left(\frac{\partial W}{\partial I_2}\right)\right]. \quad \textbf{(2.25)}$$

In planar tension or pure shear, $\lambda_1 = \lambda;\ \lambda_2 = 1;\ \lambda_3 = \lambda^{-1}$ and $\sigma_1 = \sigma;\ \sigma_2 \neq 0;\ \sigma_3 = 0$, the reduced stress is expressed as

$$\sigma_{red} \equiv \frac{\sigma}{\left(\lambda - \lambda^{-3}\right)} = 2\left[\left(\frac{\partial W}{\partial I_1}\right) + \left(\frac{\partial W}{\partial I_2}\right)\right]. \quad \textbf{(2.26)}$$

Finally, in equibiaxial tension, $\lambda_1 = \lambda;\ \lambda_2 = \lambda;\ \lambda_3 = \lambda^{-2}$ and $\sigma_1 = \sigma_2 = \sigma;\ \sigma_3 = 0$, the expression of the reduced stress term is

$$\sigma_{red} \equiv \frac{\sigma}{\left(\lambda - \lambda^{-5}\right)} = 2\left[\left(\frac{\partial W}{\partial I_1}\right) + \lambda^2\left(\frac{\partial W}{\partial I_2}\right)\right]. \quad \textbf{(2.27)}$$

Gregory (1979), with the measurements of the stress-strain behaviour of carbon filled natural rubbers, observed a simple relationship between different deformation states (simple shear, uniaxial tension and compression), i.e. plots of the reduced stress terms σ_{red} versus the invariant $(I_3 - 1)$ all lie on the same curve independent of the deformation state. Davies et al. (1994) confirmed this observation, with carbon black filled elastomers (Figure 2.7).

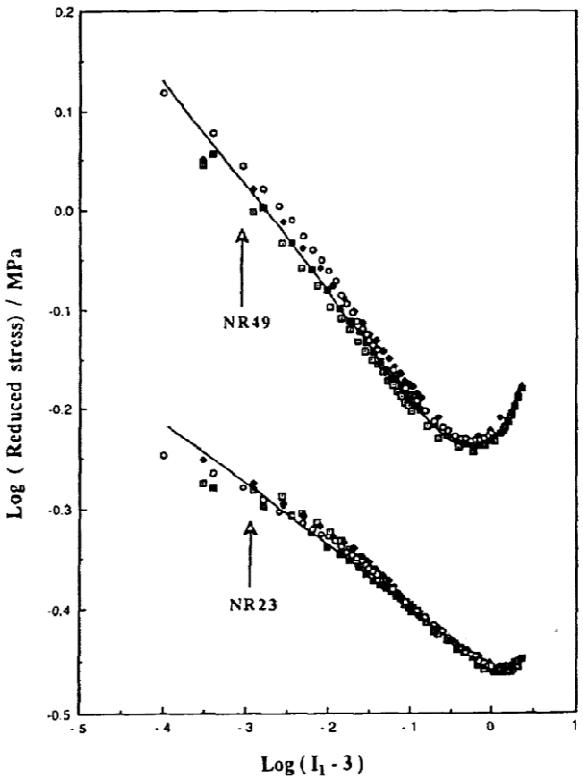

Figure 2.7: Stress-strain data on two different formulations for uniaxial tension and compression, pure shear and simple shear, measurements plotted as reduced stress vs. $(I_1 - 3)$ in double logarithmic form (Davies et al. 1994).

2.3 Viscoelasticity

In the previous Section 2.2 only is described the elastic or hyperelastic behaviour of elastomers. But the elastomers subjected to a specific stress exhibit a mechanical response which is combination of both characteristics, elastic solid and viscous fluid (Ferry 1980). The mechanical behaviour of viscoelastic materials involves, as first mathematical approximation, some combination of Hooke's law of elasticity, which lays that stress is proportional to strain, and Newton's law of viscosity, which lays that stress is proportional to the rate of change in strain with time. Mathematically the elastic component is represented as an ideal spring with a force

$$F = kx, \tag{2.28}$$

where k is the stiffness of the spring and x is the displacement. Fluids obeying Newton's law of viscosity may be idealised as a dashpot and it is described as

$$F = c\left(\frac{\partial x}{\partial t}\right), \tag{2.29}$$

where c is a viscous damping coefficient. In terms of the tensile engineering stress σ, Young's modulus E, engineering strain e and viscous coefficient in tension η_c, Equations (2.28) and (2.29) may be expressed as

$$\sigma = Ee, \tag{2.30}$$

$$\sigma = \eta_c\left(\frac{\partial e}{\partial t}\right). \tag{2.31}$$

The viscoelastic behaviour of elastomers are often described as an array (generalized models) of springs and dashpots, either in series or in parallel, known as Maxwell or Voigt elements, shown in Figure 2.8.

Maxwell and Voigt models can be characterised by a relaxation time

$$\tau = \frac{\eta_c}{E}. \tag{2.32}$$

The strain can be calculated using a Maxwell model as

$$e = e_0 + \frac{\sigma t}{\eta_c}, \tag{2.33}$$

and for Voigt model as

$$e = \frac{\sigma_0}{E}\left[1 - \exp\left(\frac{-t}{t_0}\right)\right]. \tag{2.34}$$

When an elastomer is held at a fixed displacement, the amount of stress decreases with time (stress relaxation) and if it is subjected to a fixed load, the length increases over time (creep). Then, it is more convenient to describe stress relaxation experiments by a generalized Maxwell model and creep experiments by a generalized Voigt model. The behaviour is further complicated when a elastomer is periodically deformed at a fixed amplitude, as stress softening, hysteresis and residual strains (these inelastic effects are discussed in Section 2.4) occurs, due to the breaking of weak chains, crosslinks or filler-elastomer network. It is worth emphasising that the mechanical models only give a mathematical representation of the measured behaviour and they are not use when trying to describe the viscoelastic properties at molecular level

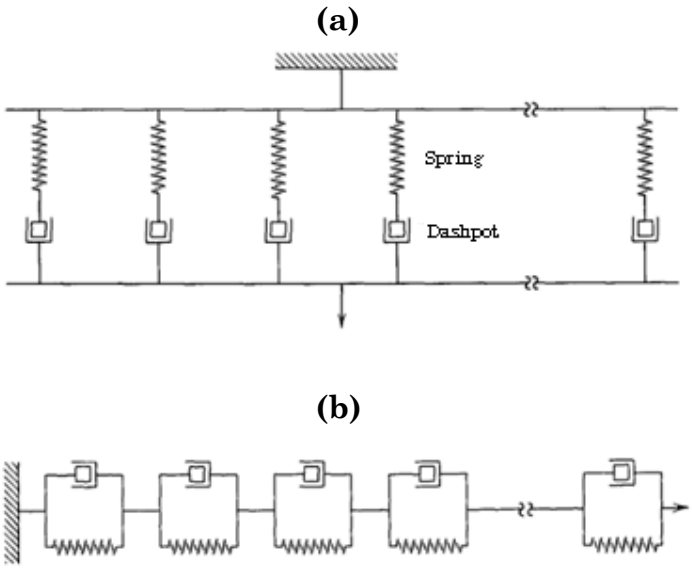

Figure 2.8: (a) Generalized Maxwell model, as array of springs and dashpots in series, (b) generalized Voigt model, as array of springs and dashpots in parallel (Ferry 1980) .

2.4 Inelasticity

The theories discussed earlier assume that the material is a perfectly elastic elastomer. However, there are cases where a significant departure from perfect elasticity takes place. The principal inelastic effects which vary from elasticity under cyclic loading-unloading conditions are stress-softening, hysteresis loss and residual strain. These inelastic effects are mainly exhibited by rubbers, but they are significant with filled rubbers. However the

inelastic effects are clearly significant with filled as well as unfilled TPUs, due to their segmented structure (Wang and Cooper 1983).

The inelastic effects have been the subject of several experimental and theoretical studies, meanly to study the mechanisms by which the chemical and physical micro-structures determine such effects. Some observations of studies are discussed below, but bearing in mind that there are not unanimous explanations of the physical origins of the inelastic effects.

On the first loading, a breakage of the original hard domains into smaller units was observed by means of in-situ small-angle X-ray scattering (SAXS) (Desper et al. 1985). Moreover, once breakage of original two-phase structure starts, a significant increase in internal energy was shown by calorimetric measurements of heat flux combined with work input (Godovsky et al. 1986). This increase is associated with the less efficient molecular packing of hard segments, which suggests a reduction in hydrogen bonding during deformation. However, the density of hydrogen bonds appears to be independent of strain (Seymour et al. 1970). Thus, new hydrogen bonds must be formed rapidly on the time-scale of straining to balance the breakage of hydrogen bonds during the deformation. Otherwise, a progress of orientation of the various bonds was observed by infrared spectroscopy during deformation (Yeh et al. 2003). Initially, the chains of hard segments were oriented perpendicular to direction of extension and the chains of soft segments were aligned parallel to direction of extension. But beyond $e \approx$ 1-2, the chains of hard segments rotated along direction of chains of soft segments, parallel to direction of extension.

On subsequent cycling, within the envelope of previous strains, a different behaviour has been observed. Reversible movements of hard segment and soft segment portions of chains were showed by in-situ SAXS (Blundell et al. 2002) and by infrared spectroscopy (Yeh et al. 2003) simultaneous with cyclic deformations. Buckley et al. (2010) showed a remarkable degree of uniformity in their relative hysteresis on subsequent loadings to the same maximum strain. Therefore, the first loading causes significant damage in the initial structure, such that subsequent loadings deform a new structure, which is not subjected to additional damage structural. Moreover, calorimetric measurements showed that there was no increase in internal energy (Godovsky et al. 1989), consistent with no further structural breakage.

2.4.1 Stress softening

The stress-strain response in an elastomer typically depends strongly on the maximum loading previously encountered. On the initial loading, virgin elastomers exhibit a relatively stiff response. When the elastomer is subsequently unloaded, then reloaded, the stress-strain response shows a progressive softening on each loading cycle (Brown 2006). Therefore, a lower stress at maximum strain in current cycle than in previous cycle is exhibited by elastomers subjected to cyclic loading-unloading conditions (Figure 2.9a). After a few cycles, the number depending on the amount of filler and the maximum strain, the stress-strain response stabilizes, i.e. difference between successive cycles becomes negligible. The stress-softening effect was firstly observed in a thorough experimental work of carbon-black filled vulcanized rubbers under uniaxial tension by Mullins (1947), thus it is widely known as the Mullins effect.

2.4.2 Hysteresis loss

The energy within a perfectly elastic material is completely recovered when the force is removed. However, elastomers dissipate energy due to internal molecular friction when they are deformed (Harwood and Payne 1968). This lost energy is dissipated in the form of heat in the elastomer and it is one of the sources of elastomer friction.

If a typical loading and unloading curve for an elastomer (Figure 2.9b) is plotted, then the area under the loading curve and x-axis is proportional to the energy input and the area under the unloading curve relates to the recovered energy. The area between both curves is the dissipated energy or hysteresis loss. The hysteresis loss is important during the first cycle and it becomes a steady value after several cycles (Lion 1996).

2.4.3 Residual strain

In general, the elastomers do not return to their initial state when they are entirely unloaded. This inelastic behaviour leads to a residual strain (Figure 2.9a). Under cyclic loading conditions, the residual strain is especially significant during the first cycle and its increase becomes negligible after several subsequent cycles (Qi and Boyce 2005).

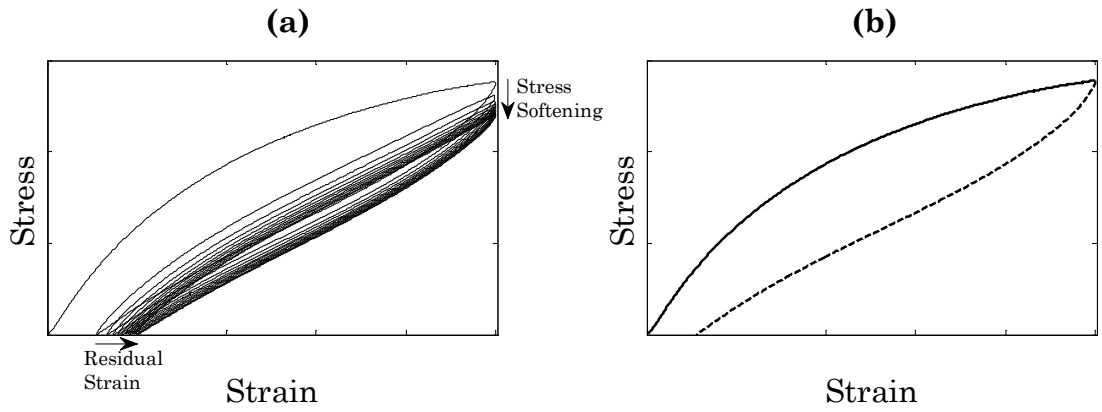

Figure 2.9: (a) Loading-unloading cycles for a TPU dumbbell specimen, stress softening and residual strains are pointed out. (b) The area between the loading curve (thick line) and the unloading curve (dashed line) is a measure of hysteresis loss. (The specimen was stretched up to 50% at 10 mm/s rate of transverse).

2.5 Elastomer contact

Contact mechanics studies mainly the area of contact (shape and size) and the distribution of contact pressures using the profiles of bodies close to contact and the force applied. In contact mechanics it is often distinguished between the apparent contact area and the real contact area. When two bodies with nominally smooth surfaces on a macroscopic scale are brought in contact, real contact will only occur in small randomly distributed areas due to the bodies have surfaces with roughness on many different length scales. Then, the area of real contact is usually an extremely small fraction of the apparent contact area. The contact regions are small areas where asperities from one body are squeezed against asperities of the other body, depending on the conditions the asperities can deform elastically or plastically. Therefore, the real contact area is dependent on the length scale of interest, the magnification ζ give a value for it. At low magnification ($\zeta = 1$), a complete contact appears to occur between the bodies at many macro asperity contact regions. When the magnification is increased, it can be observed (Figure 2.10) that only partial contact occurs at the asperities. In many cases the local pressure in the contact regions at the asperities can became so high, and then the material yields plastically before reaching the atomic scale. In these cases the size of the real contact area will be established mainly by the yield stress of the body (Persson et al. 2005).

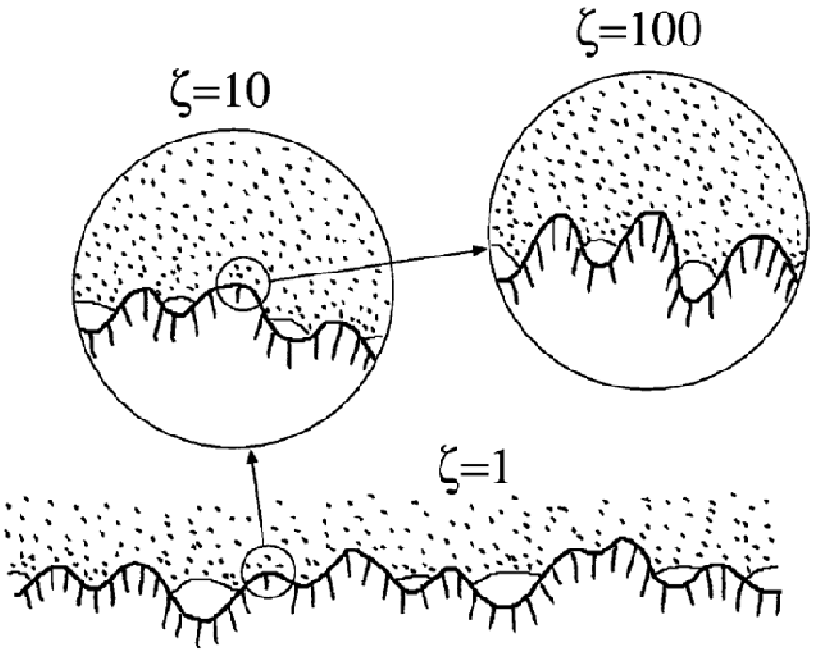

Figure 2.10: Contact between two bodies, a rubber block (dotted area) and hard rough substrate (dashed area), at increasing magnification ζ (Persson et al. 2005).

Contact mechanics has a long history and different contact theories have been developed. The first theory was presented by Hertz (1882), which gave the solution for the frictionless normal contact of two elastic bodies of quadratic profile when the dimensions of the contact area being small compared to the dimensions of each body. This theory lays down that the real contact area A_r varies nonlinearly with the load F_N : $A_r \propto F_N^{2/3}$.

In the case of the elastic contact between two smooth spheres (Figure 2.11), the radius of contact area a can be calculated using the elastic Hertzian theory as

$$a = \sqrt[3]{\frac{3F_N}{8}\frac{\left(1-\nu_1^2\right)/E_1 + \left(1-\nu_2^2\right)/E_2}{1/2R_1 + 1/2R_2}}, \tag{2.35}$$

where ν_i are the two Poisson's ratios and E_i the two Young's modulus for each sphere, R_i gives the radius of each sphere (Johnson 1985).

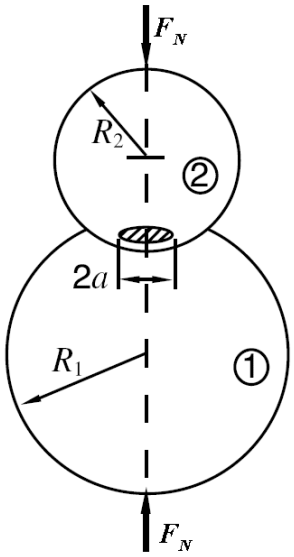

Figure 2.11: Two spheres in elastic contact, the contact area for both spheres with radius R_1 and R_2 has a width of 2a when a normal load F_N is applied (Bhushan 2001).

The pressure p in each sphere has a semi-elliptical distribution

$$p(r) = \frac{3}{2}\frac{F_N}{\pi a^2}\left(1 - \frac{r^2}{a^2}\right)^{1/2}, \tag{2.36}$$

with the maximum

$$p_0 = \frac{3}{2}\frac{F_N}{\pi a^2}, \tag{2.37}$$

at the centre of the contact area (Figure 2.12), i.e. when $r = 0$.

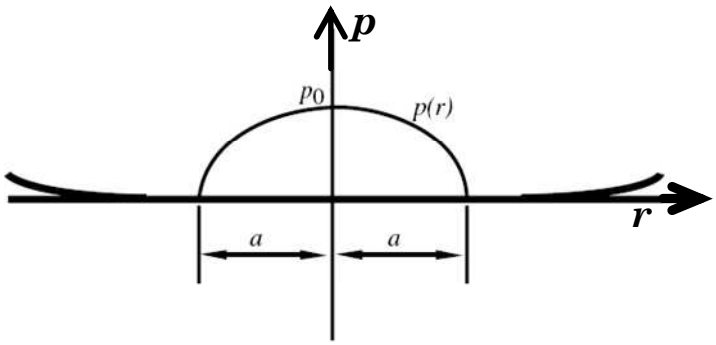

Figure 2.12: Semi-elliptical pressure distribution resulting from elastic contact between two spheres (Bhushan 2001).

For the case of a rigid sphere contacting a flat surface, e.g. steel sphere contacting a elastomer sheet, where the deformation of the stiffer sphere becomes negligible due to

$E_1 \gg E_2$ and where the radius of flat surface may be assumed to be infinite ($R_2 \simeq \infty$), thus Equation (2.35) can be simplified as

$$a = \sqrt[3]{\frac{3RF_N\left(1-\nu^2\right)}{4E}}, \tag{2.38}$$

where E and ν are the Young's modulus and Poisson's ratio, respectively, of material of the flat surface and R is the radius of sphere (Johnson 1985). More configurations of elastic contact can be found in many contact mechanics textbook, e.g. Johnson (1985) and Bhushan (2001).

However, Johnson et al. (1971) found for small loads that the contact area between two smooth elastic bodies is significantly larger than predicted by the Hertzian theory (Figure 2.13). Then, they (Johnson, Kendal and Roberts) proposed the JKR model, which includes an adhesion contribution that was ignored by Hertz theory. Therefore, the radius of contact area a between a sphere and a flat surface is now given by

$$a^3 = \frac{3R\left(1-\nu^2\right)}{4E}\left[F_N + 3\pi\gamma R + \sqrt{\left(6\pi\gamma RF_N + \left(3\pi\gamma R\right)^2\right)}\right], \tag{2.39}$$

where γ is the energy of adhesion of both surfaces or Dupré energy of adhesion. It is worth pointing out that when if $\gamma = 1$ then it is obtained Equation (2.38), i.e. Hertz solution. Moreover, if no load is applied, the contact area is not zero as was suggested by Hertz, but Equation (2.39) reduces to

$$a^3 = \frac{3R\left(1-\nu^2\right)\left(6\pi\gamma R\right)}{4E}, \tag{2.40}$$

so that a force

$$F = -\frac{3}{2}\pi R\gamma, \tag{2.41}$$

has to be applied to break the contact between the bodies.

By the other hand, Derjaguin et al. (1975) gave a completely different model of adhesion between elastic bodies, named DMT model by Derjaguin, Muller and Toporov, in which the adhesion forces act in an annular zone around the contact but do not deform the profile. The separation occurs when the contact is reduced to a point under an adherence force

$$F = -2\pi R\gamma. \tag{2.42}$$

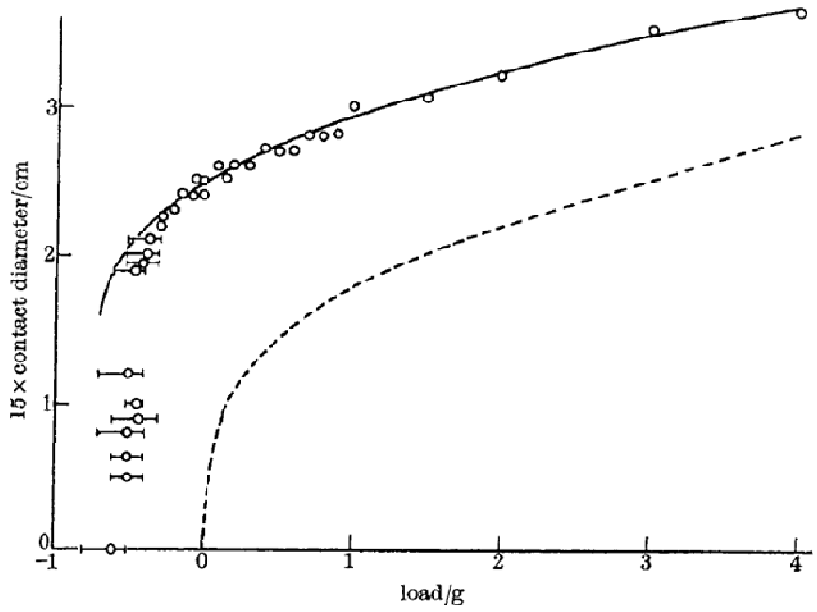

Figure 2.13: Experimental results of the contact diameter of a rubber sphere contacting a rubber flat under small loads compared to the prediction by the JKR model (thick line) and the Hertz theory (dashed line) (Johnson et al. 1971).

At first these models were thought to be competitive, but Tabor (1976) emphasized that the main defect of DMT model was to neglect the deformations due to adhesion force outside of the contact area, whereas the defect of the JKR model was to neglect these adhesion forces. Therefore, he proposed a continuous transition from the DMT model to the JKR model in function of an elasticity parameter

$$\lambda_e = 1.16\left(\frac{R\gamma^2}{E^2 z_0^3}\right)^{1/3}, \tag{2.43}$$

where z_0 is the equilibrium distance between atoms. The DMT model applies when $\lambda_e \ll 1$ (hard solids, small radii, weak adhesion) and the JKR model is applied when $\lambda_e \gg 1$ (soft solids, large radii, strong adhesion) (Buehler 2006). Later, Maugis (1992) proposed an adhesion model (M-D) using a Dugdale approximation to recover the JKR-DMT transition. The Figure 2.14 shows an adhesion map where is pointed out the appropriate model depending on λ_e. In the Hertz zone the adhesion forces are negligible. The Bradley zone is the case of rigid bodies at low loads (Bradley 1932).

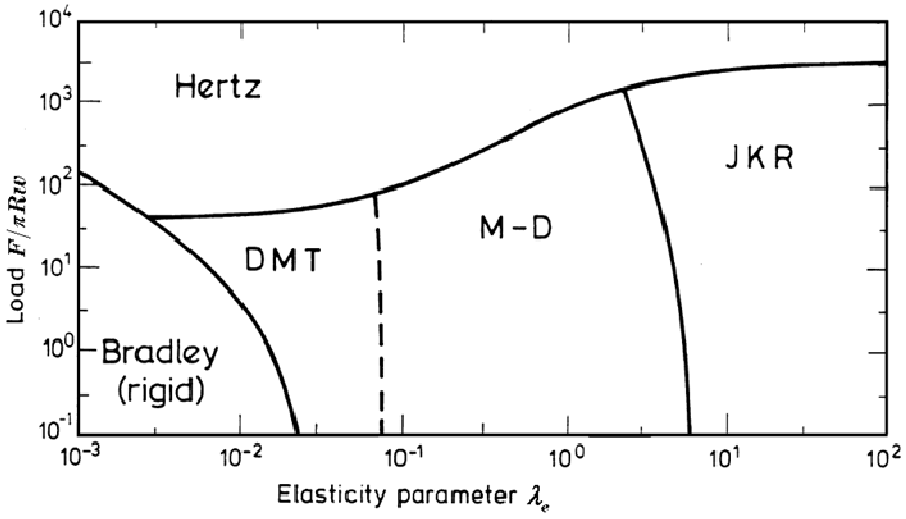

Figure 2.14: Adhesion map for elastic contact (Johnson 1998).

Archard (1957) applied the Hertz theory to the contact between rough surfaces and showed that for a model of small spherical asperities where distributed on top of larger spherical asperities and so on, the real contact area varies nearly linearly with the squeezing force F_N . A similar conclusion was reached by Greenwood and Williamson (1966). Their model (GW model) assumed that the surface asperities all have the same radii in their summits with a Gaussian distribution in heights (Figure 2.15a). Bush et al. (1975) developed a more general contact model, in which they approximated the summits by paraboloids and applied the Hertzian theory for the deformation. The height distribution was described by a random process, and they found that the real contact area increases linearly with F_N at low load. Persson (2001) extended this model to include surface roughness at any length scale (Figure 2.15b). Using this model, the real contact area is exactly proportional to the squeezing force F_N .

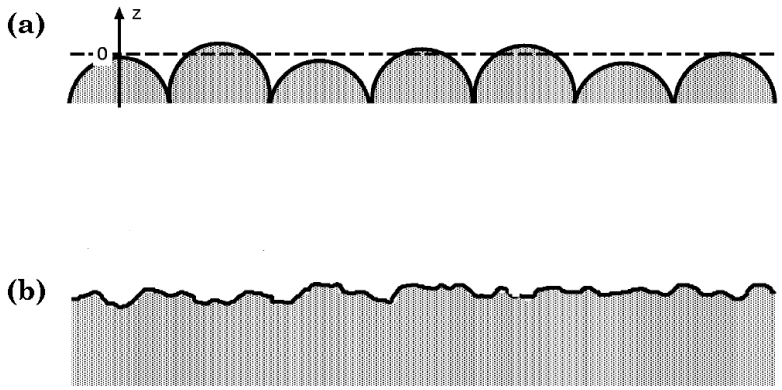

Figure 2.15: Two models of surfaces: (a) the asperities have a random height distribution and (b) randomly rough surface (Persson et al. 2005).

When an elastomer block slides over a rigid and rough substrate, it is excited periodically by the deformation process of rough asperities, which lead to energy dissipation due to internal damping in the elastomer. Therefore, adhesional influences are thought to be negligible in a rigid-body/elastomer contact, so that the resulting frictional force is often assumed to be almost entirely characterized by internal losses in the elastomer (Persson 1998). If the relative sliding velocity increases, the excitation of the elastomer by surface asperities occurs at a higher frequency, so that the time available for the elastomer to relax after the deformation decreases, and the elastic modulus increases. Therefore, it is likely that both the indentation depth as well as the real contact area decrease (Figure 2.16).

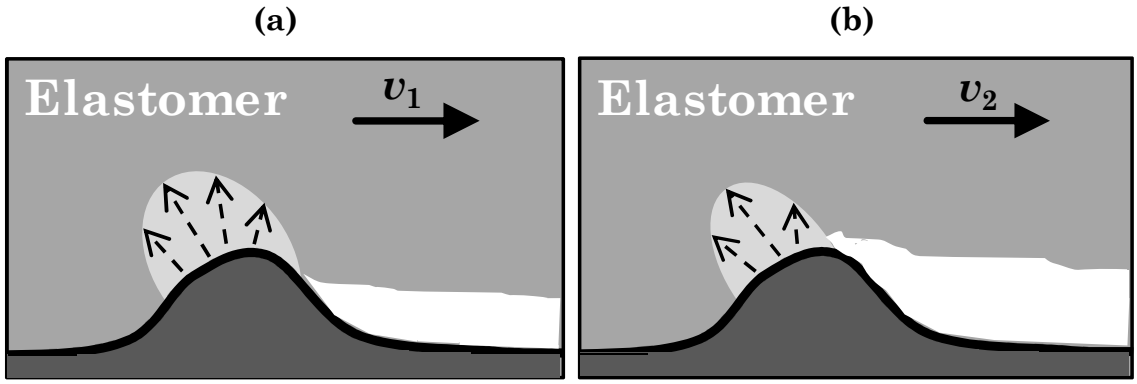

Figure 2.16: Schematic figure of an elastomer (top) sliding over a surface asperity. The main dissipation occurs in the enclosed volume highlighted in grey, while sliding velocity v_1 in (a) is lower than v_2 in (b).

2.6 Elastomer friction

Friction is a restraint of relative motion of one body over or along another. The friction, whether desired or not, is present in most engineering applications. High friction is desirable between tyres and roads, between mechanical parts that are bolted together, in braking system and in countless other examples. Low friction is desirable between sliding parts in computer hard disk systems, in roller bearings, in engines and in many other mechanical devices. There are two regimes of friction: static and dynamic. Static friction occurs between contacting bodies before relative sliding, i.e. there is a static situation due to the friction force prevents the relative motion between contacting bodies. When the force in the direction of potential movement is higher than friction force, then a relative motion begins between the bodies. Therefore, the contacting bodies are in dynamic or kinetic friction. Sum up, the static friction force may be defined as the force required putting a body into motion, whereas the

dynamic or kinetic friction force is required to maintain a body in motion. In this section, an overview on general friction and a state of the art of elastomer friction is given.

2.6.1 History of friction

Friction has been considered since ancient times due to involvements in different practical applications, as moving large stones, building weapons, etc. Leonardo da Vinci (1452-1519) is thought to be the first person to describe the phenomenon of friction by experiments on objects being moved over a surface. Actually, the scientific study of friction began in the late 17th century. Classically, there are two schools about scientific interpretation of friction: French or Continental School and English School (ASM 1992)

French or Continental School

Based on the performed studies by Leonardo da Vinci in the 15th century, Amontons (1699) proposed the first two laws of friction, actually, of dynamic friction:

1. Friction force is directly proportional to applied load.

2. Friction force is independent of apparent contact area.

Later Euler (1748a and 1748b) studied and analyzed static friction between contacting bodies using inclined planes. Moreover, the analytical study of Amontons' laws was proposed by Euler and he was the first to distinguish between the coefficients of static friction μ_s and dynamic friction μ_k. Euler also suggested that friction was due to the flashing contacts along rough surfaces.

Finally, Coulomb (1785) confirmed experimentally the laws proposed by Amontons and he proposed a third law, which is added to the former two laws:

3. Friction force is independent of sliding velocity.

These three laws were considered valid until the 20th century. Coulomb developed an equation to calculate friction force

$$F_r = \mu F_N, \tag{2.44}$$

where F_N is the load or normal force (acting perpendicular to the contact surface) and μ is the friction coefficient, which is a dimensionless variable. Coulomb suggested that friction is due to the interlocking of surface asperities. Nowadays, friction behaviour with constant friction coefficient is known as "Coulomb friction".

Therefore, the French or Continental School of friction is based on mechanical interaction of roughness and interlocking of surface asperities. The main finding of French School was that contact occurs only in a certain number of points. But it established that friction depends only on geometry of roughness and it did not take into account the shape change of asperities by deformation or plasticity.

English School

Unlike before, English School focused on adhesion force between materials to describe friction. Desaguliers (1734), who was French but grew up in England, introduced the concept of cohesive force (now adhesion force) and he found that friction force could be attributed to adhesion force of asperities when they come into contact.

Tomlinson (1929) proposed a similar interpretation at microscopic scale, i.e. the short-range molecular forces are responsible for adhesion force. Bowden and Tabor (1964) focused on adhesion as the main cause of friction, but also found that material surface involves in friction. Therefore, they took into account plastic deformation of surface asperities and showed that mechanical properties of material surface are significant. They proposed that surface asperities are deformed until their plasticization and contact pressure was equal to hardness H of material, so real contact area could be given as:

$$A_r = \frac{F_N}{p} = \frac{F_N}{H}. \tag{2.45}$$

If the friction force is due to shear breakage of the asperities on contact, the coefficient of friction may be given by

$$\mu = \frac{F_f}{F_N} = \frac{A_r \sigma_\tau}{A_r H} = \frac{\sigma_\tau}{H}, \tag{2.46}$$

where σ_τ is shear stress.

A correct interpretation of friction has characteristics of both Schools, nowadays friction is considered as a mechanism at atomic scale, i.e. friction force comes from interlock between atomic asperities and adhesion force of atomic range (Van der Waals force, hydrogen bond, etc.).

2.6.2 Friction of elastomers

Due to mechanical properties of elastomers, Equation (2.44) is not directly applicable to them. The very low elastic modulus and the high internal friction, due to viscoelastic nature,

are both reasons for the difficulties encountered in the use of Amonton-Coulomb's laws in elastomer friction (Persson 1998). Therefore, elastomer friction force is commonly described as a contribution of different factors (Kummer 1966)

$$F_f = F_{adhesion} + F_{hysteresis} + F_{viscous} + F_{cohesion}. \quad \textbf{(2.47)}$$

The adhesion or surface contribution ($F_{adhesion}$) results from the intermolecular interaction between two surfaces and strongly depends on the type of elastomer, the contact partner and filler particles. The hysteresis or deformation contribution ($F_{hysteresis}$) is a viscoelastic effect resulting from the irreversible viscoelastic energy dissipation through the bulk deformation of a certain volume of elastomer (Grosch 1963). The dissipated energy shows a characteristic maximum with respect to the relative sliding velocity. The lubricated contribution ($F_{viscous}$) reduces the friction force due to the viscous shear of a fluid at the interface. The friction force is given by shear viscosity of the fluid alone when the elastomer loses completely contact with the surface of other body. The cohesive or wear contribution ($F_{cohesion}$) is due to the additional energy lost from crack initiation and wear in case of abrasion (Fukahori and Yamakazi 1995). Complicating matters further, the four contributions are not independent of each other, e.g. Schallamach waves (Schallamach 1971) are a mechanism that relates the adhesion and hysteresis contributions due to the detachment is formed by surface adhesion and results in deformation of elastomer (Figure 2.17).

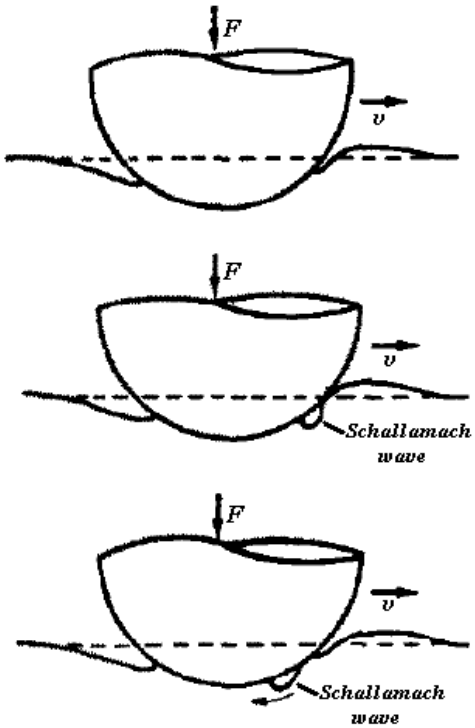

Figure 2.17: Schematic diagrams showing the formation of a detachment fold or Schallamach wave (redrawn from Barquins 1993).

Assuming a dry, smooth contact with reasonably low shear forces, the friction force during sliding at an elastomer/rigid interface is considered to arise from the combination of adhesion and hysteresis contributions

$$F_f = F_{adhesion} + F_{hysteresis}, \tag{2.48}$$

hence the lubrication and wear contributions are negligible (Tabor 1960). Moreover, Gabriel et al. (2010) proposed an additional geometric contribution, which may increase the friction force significantly above that expected from a consideration of the interfacial coefficient of friction alone when elastomer is wrapped around a rigid spherical slider (Figure 2.18a). This contribution increases with the depth of penetration of the rigid surface into the elastomer (Figure 2.18b). The ratio between both contributions may change depending on the conditions of contact, surface roughness, etc. Persson (2001) stated that adhesion contribution diminishes for rough interfaces (as in tyre/road contact), so that the friction force arises from the hysteresis contribution alone. In contrast, the adhesion contribution is the main influence on elastomer friction for very smooth contacts and the influence of hysteresis contribution can be negligible. A suitable modification can reduce the contributions, but the influence of each contribution is not simple to determine. For this reason, just a single term can not describe the complexity of elastomer friction.

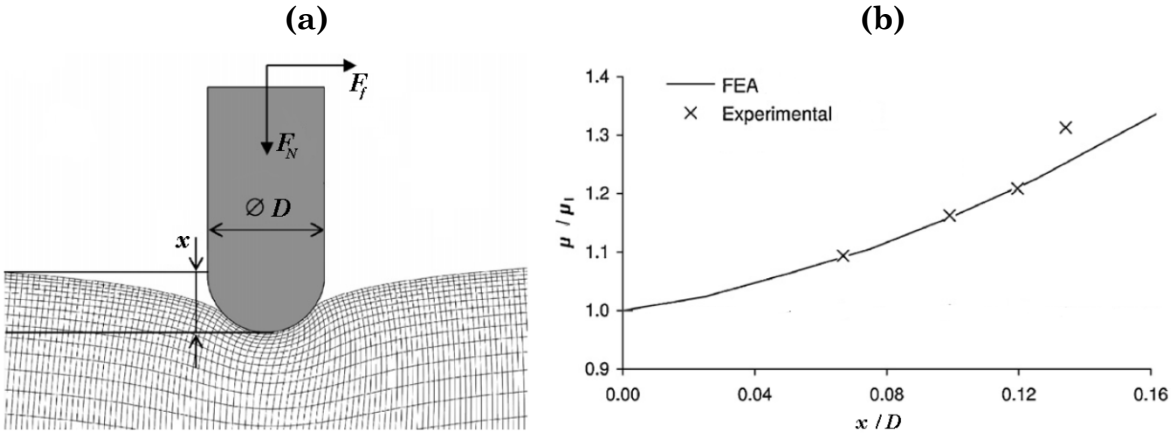

Figure 2.18: (a) Model of a rigid spherical slider indenting into an elastomer sheet. (b) Increase of the geometric contribution with the depth of penetration *x*. (Gabriel et al. 2010).

There are different parameters or variables influencing the frictional behaviour of elastomers (Table 2.3), depending on arguments or approaches that are used to characterize this behaviour. Using geometric arguments (surface roughness and asperity interlocking), mechanical properties-based arguments (shear properties of solids), chemical compatibility

arguments, work conditions-based (velocity of sliding, load, temperature) arguments, fluid dynamics approaches, etc., the frictional behaviour is commonly characterized and predicted. Therefore, the number of possible variables for use in predictive friction models of elastomers becomes quite large. A summary of several friction models is given in the following section.

Table 2.3: Factors influencing the friction behaviour of elastomers (Blau 2001).

Category	Factor
Contact geometry	Conformity of the bodies (mating of macro-scale shapes) Real and nominal (or apparent) contact area between sliding bodies
Surface geometry	Surface roughness and waviness (asperity shapes, size distribution…) Surface lay (directionality) with respect to relative motion
Relative motion	Unidirectional or reciprocating motion Constancy of motion (accelerations, pauses, start-stop) Magnitude of relative surface velocity
Material properties	Stiffness, elasticity and mechanical properties Dynamic properties Ageing properties
Applied forces	Magnitude of normal forces or loads (contact pressure) Constancy of applied forces Adhesion forces
Temperature	Thermal effects on elastomer properties (thermoelastic instabilities) Friction induced temperature rise between sliding bodies
Lubrication	Formation of friction-altering films (film thickness) Viscosity of lubricant (temperature and pressure dependence) Oxidation and acidification of lubricant
Wear	Formation of wear patterns Creation of debris (third-bodies)
Stiffness-vibrations	Contact compliance (stick-slip) Damping of frictional or external vibrations Feedback between frictional stimulus and structural response

2.6.3 Friction models of elastomers

As stated previously, in contrast to other solids, elastomer does not obey Amontons-Coulomb's laws, and hence neither Equation (2.44). Instead, the coefficient of friction usually decreases as normal stress increases. Describing this characteristic, Thirion (1946) proposed firstly an empirical friction model

$$\frac{1}{\mu} = \mathrm{m_a} + \mathrm{m_b}\left(\frac{o}{E}\right), \tag{2.49}$$

where $\mathrm{m_a}$ and $\mathrm{m_b}$ are constants, derived from an extrapolation of the reciprocal of the coefficient of friction against pressure. The former is calculated from the ordinate at the origin, while the latter is derived from the slope.

On the other hand, Schamallach (1952) studied the dependence of friction force in respect to the real contact area. The experimental results pointed out the dependence of contact radius a on the normal load F_N, expressed as:

$$2a \propto F_N^{1/3}, \tag{2.50}$$

which is similar to the contact theory of Hertz, given in Equation (2.38). If the contact area is proportional to the friction force (Bowden and Tabor 1964), see Equation (2.46), then

$$\mu \propto \frac{a^2}{F_N}. \tag{2.51}$$

Substituting Equation (2.50) into Equation (2.51), the friction coefficient is described as:

$$\mu = C_v F_N^{-1/3}, \tag{2.52}$$

where C_v is an experimental parameter, which has to be measured for each velocity. It is worth noting that this empirical friction model, given by Equation (2.52), does not describe the frictional behaviour for all load cases, especially at very low and high pressures. Furthermore, these first empirical friction models of elastomers do not incorporate the viscoelastic behaviour and also assume the apparent contact to be equal to the real contact area.

In the last decade great efforts have been undertaken to propose different friction models of elastomers taking into account different parameters, as relative sliding velocity, normal pressure, temperature, surface roughness, viscoelastic behaviour, lubrication and wear. The vast complexity of parameters makes difficult the overall description of friction models of elastomers, but the friction models may be divided in different categories to point out a brief review. Therefore, it is possible to use mathematical models, multi-scale approach or experiments to determine the frictional behaviour of elastomers.

Mathematical models of elastomer friction

The mathematical or numerical models need assumptions about the frictional behaviour of the contact bodies. Assuming isothermal (T = cte) behaviour, Savkoor (1966) proposed a rubber friction model

$$\mu_k = \mu_s + (\mu_{\mathrm{m}} - \mu_s)\mathrm{e}^{\frac{h_v^2}{2}\ln^2\left(\frac{|v|}{v_{\max}}\right)}, \tag{2.53}$$

depending on sliding velocity v. Where, h_v is a dimensionless parameter reflecting the width of the speed range in which friction varies significantly and μ_{m} is the maximal coefficient for maximum sliding velocity $v_{\max}$.

Persson (1998) assumed that viscoelastic behaviour of elastomers is the main contribution to the sliding friction. He proposed a friction model

$$\mu \approx -C_r \frac{E''(\omega_0)}{|E(\omega_0)|}, \tag{2.54}$$

where E'' is the elastic loss modulus (imaginary part of elastic complex modulus), C_r is a parameter depending on surface roughness and $\omega_0 \sim v/d_a$, where v is the sliding velocity and d_a is length related to real contact area.

Klüpple and Heinrich (2000) developed a friction model for contact between a road and a tyre (rubber), assuming the total friction to be mainly influenced by adhesion and hysteresis, see Equation (2.48). They suggested the hysteresis contribution as an integral over the interval of mechanical excitation frequencies

$$\mu_{hysteresis} = \frac{F_{hysteresis}}{F_N} = \frac{1}{2(2\Pi)^2}\frac{\delta_t}{pv}\int_{\omega_{\min}}^{\omega_{\max}} \omega d\omega E''(\omega) S_z(\omega), \tag{2.55}$$

where δ_t is the thickness of the excitation elastomer layer, p is the normal pressure, v is the sliding velocity, E'' is the elastic loss modulus (imaginary part of elastic complex modulus) and S_z is a complex parameter to describe the surface topography. To characterize rough surface (road), they used the height-difference correlation function

$$C_z(\lambda_l) = \xi_{\perp}^2 \left(\frac{\lambda_l}{\xi_{\parallel}}\right)^{6-2D} \qquad \text{for} \quad \lambda_l < \xi_{\parallel}, \tag{2.56}$$

where λ_l is the horizontal length scale, D is the surface fractal dimension ($2 < D < 3$) and the ξ are the cut-off lengths perpendicular ($\perp$) and parallel ($\parallel$) to the profile. Thus, the Fourier transform of C_z is the spectral power density S_z. For the description of the adhesion contribution they suggested

$$\mu_{adhesion} = \frac{F_{adhesion}}{F_N} = \frac{s_\tau}{p}\frac{A_r}{A_0}, \tag{2.57}$$

where s_τ is the true shear stress in the real contact area A_r and A_0 is the apparent contact area. It is further noticed, that Equations (2.55) and (2.57) are based on the relationship suggested by Amontons, Equation (2.44). The model work under well-defined laboratory conditions, however, it may not be applicable to practical purposes where surfaces are not well defined. Moreover, in order to use this friction model, at least 19 parameters are necessary to obtain a prediction of the coefficient of friction. Therefore, multi-scale or reduced models are used to overcome the high numerical effort of mathematical models when finite element method is used.

Multi-scale or reduced models of elastomer friction

The multi-scale or reduced models consider only the main effects, leading to friction models which yield a frictional coefficient depending on the sliding velocity, temperature and normal pressure. Rieger (1968) proposed a velocity- and temperature-dependent rubber friction model

$$\mu = \mu_0 + c_1 T\left[\ln v - \ln(c_2 T)\right], \tag{2.58}$$

where μ_0, c_1 and c_2 are three parameters which have to determined by experiments. Nackenhorst (2000) found that the temperature can be neglected when only small sliding velocities (from 10^{-3} to 10 m/s) occur, then the model of Rieger (1968) may be written as

$$\mu = \mu_1\left(\frac{N}{P_0}\right)^{\delta} + c_1 \ln\frac{v}{v_1} - c_2 \ln\frac{v}{v_2}, \tag{2.59}$$

where μ_1, P_0, δ, c_1, c_2, v_1 and v_2 are seven parameters deduced from experiments.

A friction model for elastomer sliding on a smooth surface was proposed by Tabaddor (1989),

$$\mu = \left(\frac{g}{E}\right)\left(\frac{E}{p}\right)^{1/3}, \tag{2.60}$$

where g is the gravity constant and E is the Young's modulus of elastomer. Other friction models of elastomers were proposed by Gutzeit et al. (2004), Wriggers and Reinelt (2009) and Moldenhauer and Kröger (2010).

Experimental models of elastomer friction

The experimental approach is a very pragmatic and often useful due to all physical effects are measured with their interactions. However, experiments are time and cost consuming and are only valid for the tested configurations. There are several experimental approaches, e.g. Le Gal and Kluppel (2006) and Gäbel et al. (2008), but they are mainly developed for rubbers of tyres.

3 AIM AND OBJECTIVES

"Science may be described as the art

of systematic oversimplification"

Karl R. Popper

The purpose of this chapter is to describe how it has been determined and it has been approached the work carried out in this thesis. Firstly, the critical review (Section 3.1) of the literature survey is presented. Secondly, from this critical review, the aims and objectives (Section 3.2) of the thesis are established. Finally, the methodology to accomplish these objectives is described.

3.1 Critical review of literature survey

The work reviewed is concerned with the mechanical and contact behaviours of elastomeric materials, but the studies were mainly focused on rubbers. Therefore, limited research work has been carried out on the mechanical and contact behaviours of thermoplastic elastomers, specifically of thermoplastic polyurethane elastomers.

TPUs, as rubbers, usually exhibit elastomeric behaviour, i.e. large strains with nonlinear stress-strain relationship (hyperelasticity), viscoelasticity and inelastic effects. Although the TPUs present an elastomeric behaviour, their micro-structure, which is composed of hard and soft segments forming a two-phase micro-structure, differs from the rubbers. Moreover, the mechanical properties of TPUs are strongly determined by presence of hard segments, which act as physical crosslinks, imparting the elastomeric behaviour and playing a role similar to chemical crosslinks in vulcanized rubbers (Qi and Boyce 2005). Therefore, the strain energy of density functions (Equations 2.15-2.23), which are mainly developed for rubbers, can be used to characterized hyperelastic behaviour of TPUs, as it was performed by Kanyanta and Ivankovic (2010) with a TPU for biomedical applications using

the Yeoh SEDF, Equation (2.18). But Lambert-Diani and Rey (1999) developed different SEDFs for rubbers and for thermoplastic elastomers using experimental data of elastomers reported in the literature. Moreover, the SEDFs for TPUs found in the literature are based on the experimental stress-strain behaviour, thus can be used only to predict the mechanical behaviour of a particular TPU under certain conditions, e.g. a SEDF for a representative TPU was developed taking into account rate-dependent hysteresis and softening by Qi and Boyce (2005). On the other hand, the inelastic effects of TPUs are studied focusing on the sensitivity to chemical structure (Buckley et al. 2010) but not to manufacturing process, deformation state and experimental conditions.

As mechanical behaviour of elastomers, the research work of elastomer friction is also focused on rubbers and their compounds, mainly to study contact behaviour of tyre. But some friction studies are focus on thermoplastic elastomers, as TPV (Karger-Kocsis et al. 2008) and TPU (Verheyde et al. 2009 and Karger-Kocsis 2006), under low loads (~ 1 N) and at specific sliding velocities ($\sim 10^{-1}$ m/s). Thus, there is a lack in the literature of friction studies and models for TPU under different loads at a large range of sliding velocities.

Finally, some analytic solutions of contact problems with elastomers (Johnson 1985) have been found but these solutions only take into account the viscoelastic behaviour with a constant Young's modulus. Therefore, numeric methods are used to predict accurately the contact behaviour of elastomers (Bhushan 2001), commonly finite element method (Belytschko et al. 2000 and Wriggers 2006). The FEM is used due to the non-linearities (large deformations, material, contact and friction) submitted in contact problems of elastomers may be easily introduced in finite element calculus. The algorithms of large deformations and to contact usually are provided by finite element package, but the material and friction constitutive models should be implemented by users.

3.2 Approach of objectives

The primary aim of this work is to investigate the contact behaviour between a extruded TPU and gray iron (hard solid) at moderate deformations (under 100%) using experimental techniques as well as computational modelling to predict such behaviour.

In order to accomplish this aim, different objectives have been established:

- To characterize mechanical behaviour of the extruded TPU experimentally in order to obtain a material model.
- To study friction behaviour between the TPU and gray iron experimentally in order to develop a friction model.
- To implement these analytical models of material and of friction into finite element code in order to discuss the contact behaviour.
- To carry out computational experiments using the finite element method in order to validate the implemented models and the simulation method.

Figure 3.1 shows the strategy used to study the contact behaviour between TPU and gray iron based on material and friction models using finite element analysis.

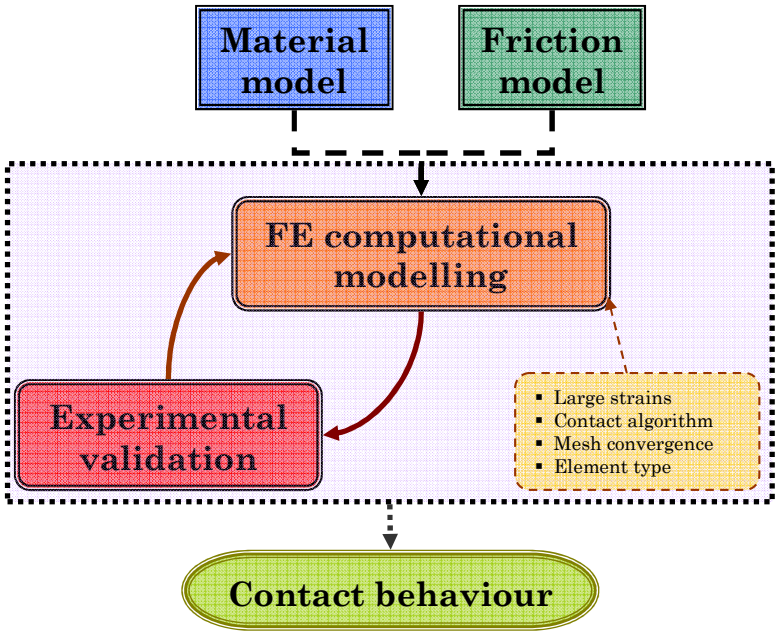

Figure 3.1: Scheme of strategy to study the contact behaviour.

3.3 Working methodology

Although this initial strategy outlines the approach to discuss the contact behaviour, actually its development was carried out using a working methodology which exactly does not follow the steps of the initial strategy. The working methodology is briefed in Figure 3.2 together with the structure of this thesis.

The mechanical behaviour of extruded TPU is characterized experimentally using cyclic loading-unloading tests for two homogeneous deformation states (uniaxial tension and pure shear) and relaxation tests. Furthermore, the inelastic effects are also studied from the data of cyclic tests. Thus, in Chapter 4, it is investigated about whether the elastomeric behaviour of extruded TPU is subject to dependence on strain-rate, maximum strain, stretching direction and deformation state.

Some models exist trying for predict the mechanical behaviour of elastomers and due to the complexity of the problem these require elaborate models to fit experimental behaviour accurately. These models are mainly developed for rubbers, thus it is investigated whether they can be used to predict the mechanical behaviour of extruded TPU in Chapter 5. To implement in finite element calculation tool the hyperelastic and viscoelastic behaviour, the strain-stress data of cyclic tests are analyzed to fit a hyperelastic model of extruded TPU and the strain data of relaxation tests are used to obtain a viscoelastic model. Assuming separation of time dependence from nonlinear stress-strain behaviour (Simo 1987), the predictions of the overlay visco-hyperelastic model are discussed. Moreover, it is studied the strong dependence on maximum strain previously achieved, i.e. on strain history, of hyperelastic behaviour and how to implement such dependence into finite element calculation tool.

The normal and sliding contact between extruded TPU and gray iron are investigated in Chapter 6 and 7, respectively. The normal contact behaviour is analyzed using experimental techniques and these results are used to discuss the reliability of model and FEA-based technique proposed. To study the sliding contact behaviour, it is obtained an experimental friction model between extruded TPU and gray iron over different ranges of contact pressure and sliding velocities. The accuracy of friction model is examined comparing experimental and finite element results.

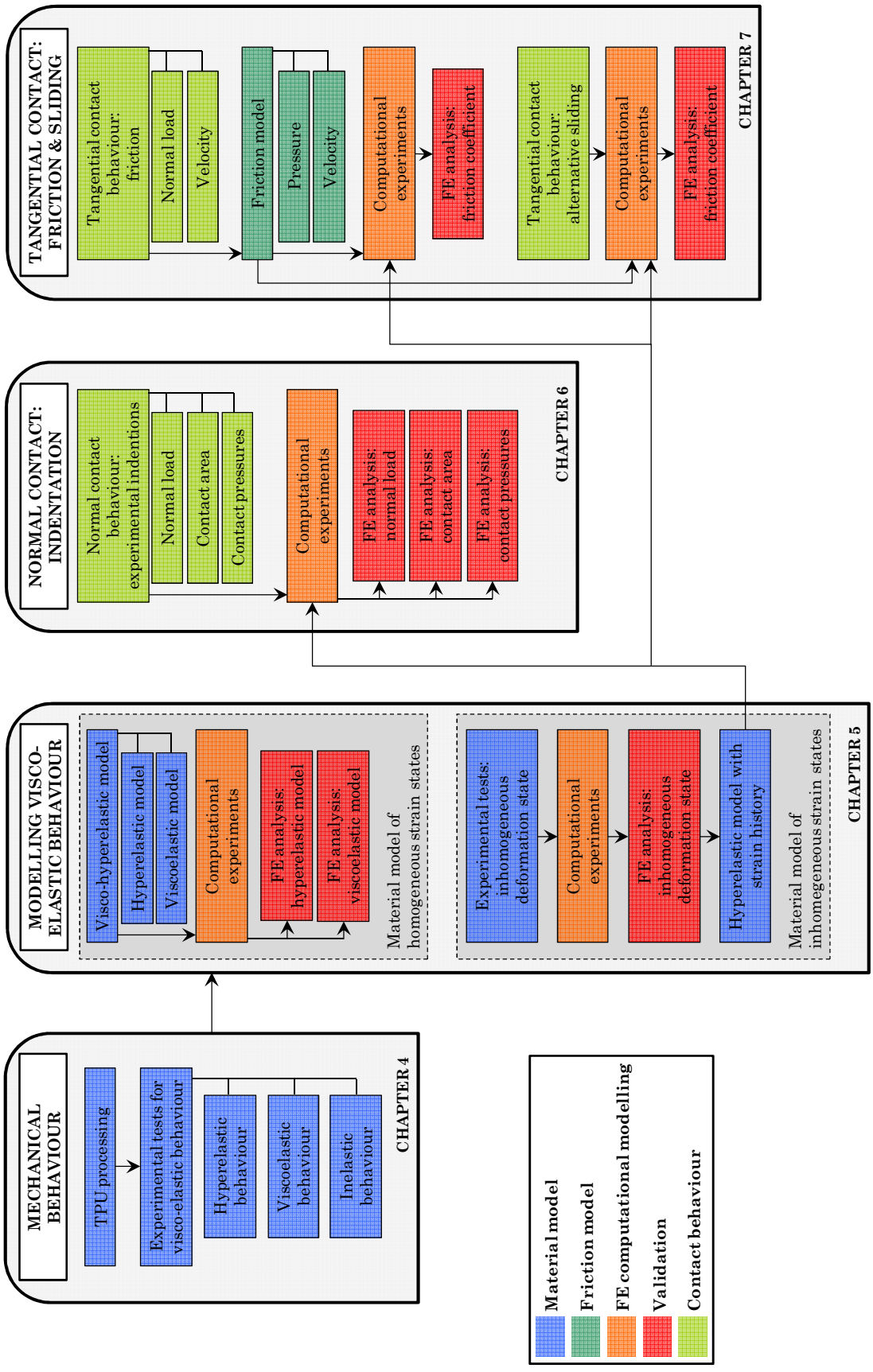

Figure 3.2: Working methodology and structure of the thesis coded by colour according to the initial strategy of work.

4 MECHANICAL BEHAVIOUR OF THERMOPLASTIC POLYURETHANE ELASTOMER

"An expert is a person who has made all the mistakes

that can be made in a very narrow field"

Niels Bohr

In this chapter, the mechanical behaviour of the thermoplastic polyurethane elastomer is characterized, starting with a description of the thermoplastic polyurethane elastomer processing (Section 4.1) and compounding (Section 4.2), followed by the measurements of density and hardness (Section 4.3). The complex behaviour of elastomers, i.e. large strains with nonlinear stress-strain relationship (hyperelasticity), viscoelasticity and effects that departure from perfect elasticity (inelasticity), is analyzed using different experimental tests (Brown 2006). These experimental methodologies used for the mechanical characterisation are described in the Section 4.4. The hyperelastic (Section 4.6) and viscoelastic (Section 4.7) behaviours are characterized using cyclic loading-unloading tests and relaxation tests, respectively. Moreover, using the data from cyclic tests, the behaviour of inelastic effects (stress softening, hysteresis loss and residual strain) are analyzed (Section 4.8). The results of cyclic and relaxation tests are also used to fit the constitutive models required (BS 2004) for thermoplastic polyurethane elastomer to be modelled using finite element analysis, which is discussed later in Chapter 5.

4.1 Processing of extruded TPU

In order to correlate the findings of this work to the coating of steel wire rope, the material used is an ether-based thermoplastic polyurethane elastomer with the trade name Elastollan[1], which is nowadays used in the lift industry. The thermoplastic polyurethane elastomer was supplied in lentil shaped pellets by Elastogran[2].

The pellets of the thermoplastic polyurethane elastomer must be dried before processing. The drying step is required to maintain a low moisture content until the product enters the processing equipment. Thus, prior to extrusion, the pellets were dried at 80 ºC for 4 hours.

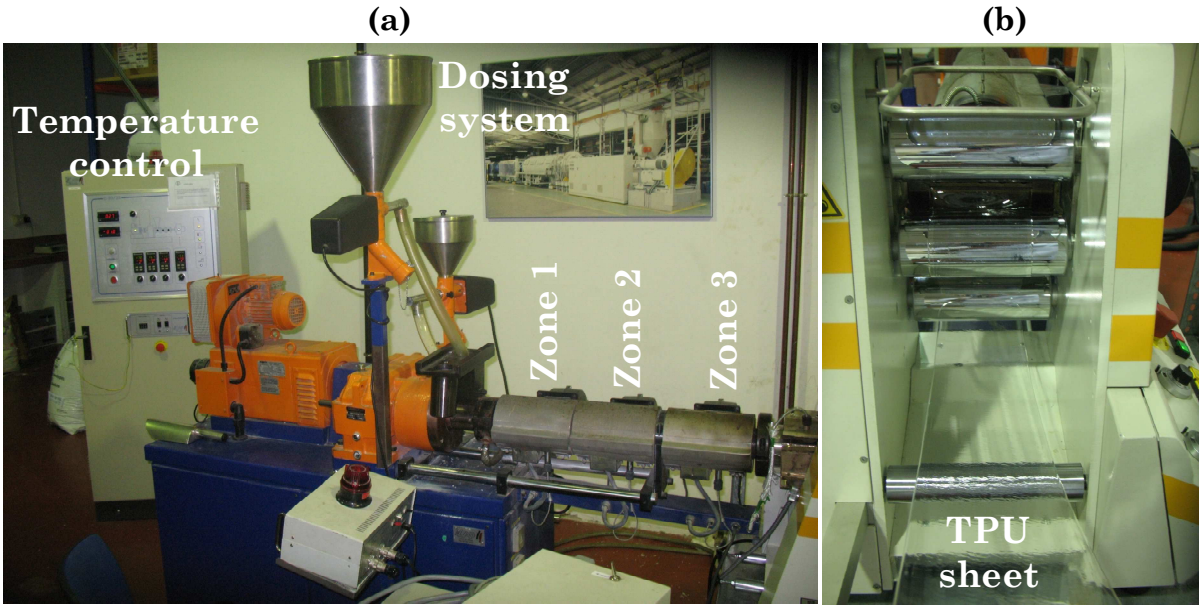

Figure 4.1: Processing set up; (a) single-screw extruder of three temperature-controlled zones and (b) calender with heated rolls.

[1]Elastollan 1190-A10

[2]BASF Poliuretanos Iberia S.A., Rubí, Spain

The thermoplastic polyurethane elastomer was processed in a single-screw extruder[3] of the *Centre Català del Plàstic*[4]. The processing thermal profile was set constant at 170 ºC in all zones (Figure 4.1a). The samples of TPU were obtained using a calender[5] with heated rolls at 28.5 ºC (Figure 4.1b) and they were conditioned in thin rectangular sheets of 0.6 mm and 2 mm thickness (reference values) and approximately 100 mm width (useful width of 80 mm). The screw speed was 27 rpm for sheets of 0.6 mm and 40 rpm for sheets of 2mm.

The sheets (0.6 mm thickness) of thermoplastic polyurethane elastomer were cut into dumbbell (Figure 4.2), type 1 of ISO 37 (ISO 2005), and rectangular (80x40 mm) specimens using two different die cutters. The specimens were cut following the extrusion direction, i.e. on melt flow direction (MD). To analyze the influence of the extrusion direction also rectangular specimens were cut in transverse melt flow direction (TD) and dumbbells at 45º to the extrusion direction, since the 100 mm width of the extruded sheets did not allow cutting dumbbell specimens at 90º.

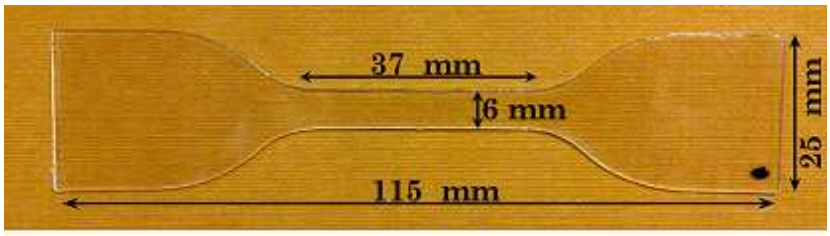

Figure 4.2: The dimensions of the type 1 dumbbell specimen (ISO 2005).

4.2 Extruded TPU compounding

As stated above (Section 2.1.2), thermoplastic polyurethane elastomers are compounded by three chemical components: a di-isocyanate (DI), a macrodiol (MDL) and a chain extender (CE) diol (Wang and Cooper 1983). The chemical analysis of the extruded TPU was carried out in the *Instituto de Ciencia y Tecnología de Polímeros*[6] using Nuclear Magnetic Resonance (NMR). The extruded TPU consists of 4,4'-methylene bis(phenyl di-isocyanate) (MDI), 1,4-butandiol (BDO) and polytetramethylene ether glycol (PTMEG) (Figure 4.3), whose mass fractions are 0.35, 0.11 and 0.54, respectively. As the hard segment is formed by the addition of chain extender to the di-isocyanate (Figure 2.4), then the hard segment mass fraction is 0.46.

[3]IQAP LAP model E30/25D

[4]Universitat Politècnica de Catalunya, Terrassa, Spain

[5]COLLIN model TEACH-LINE CR 72T

[6]Centro Superior de Investigaciones Científicas, Madrid, Spain

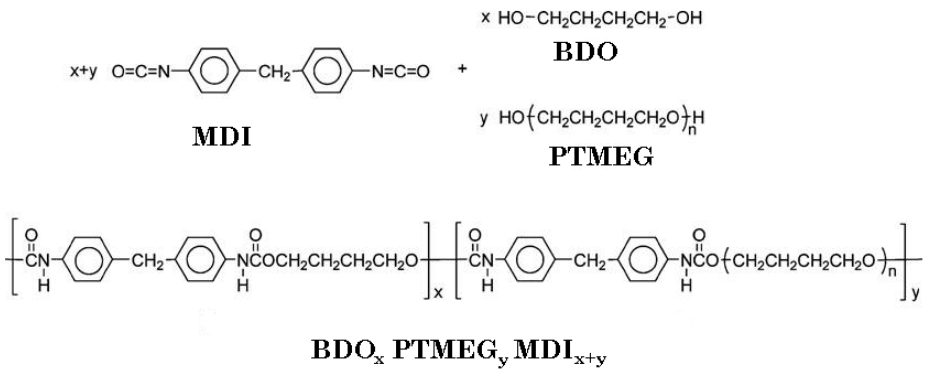

Figure 4.3: Chemical components and stoichiometry of extruded thermoplastic polyurethane elastomer.

4.3 Density and hardness

4.3.1 Density measurement

Density is defined as mass per unit volume, whereas relative density is the mass of the substance compared to the mass of an equal volume of a reference substance, usually water. The commonest method of density determination is by weighing the substance in air and in water. Therefore, using a device[7] that enables such method (Figure 4.4), the density of thermoplastic polyurethane elastomer was measured, resulting 1122±2 $kg \cdot m^{-3}$.

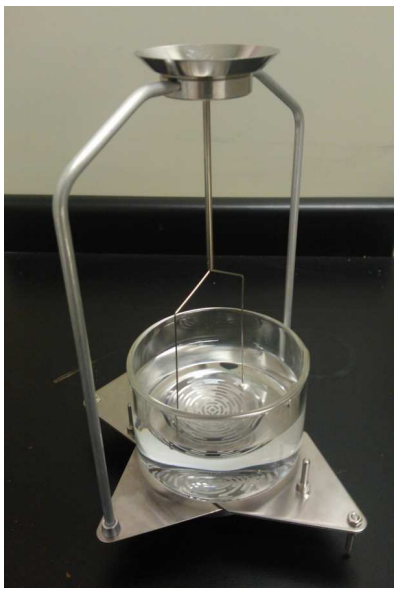

Figure 4.4: Device to measure of density using the method of weighing in air and in water.

[7]Sartorius YDK01

4.3.2 Hardness testing

A hardness measurement is a simple method of obtaining a measure of the elastic modulus of an elastomer by determining its resistance to a rigid indenter under an applied force (Brown 2006).

A Shore D scale durometer[8] was used to characterise the hardness of the thermoplastic polyurethane elastomer (Figure 4.5). The minimum dimensions for a sample are 35 mm in width and a minimum of 6 mm in thickness, as given by ASTM D 2240 (ASTM 2005). If the sample has an inadequate thickness, the standard (ASTM 2005) allows that several sheets of the same sample can be stacked together to achieve the thickness. Thus, three sheets of TPU were required, with a total thickness of 6.07±0.01 mm. To ensure reliable results the points of indentation have to be at least 12 mm distance to the sample edge. Six different points of measurement were taken, resulting 35±1 of Shore D hardness.

Figure 4.5: Shore D scale durometer.

[8]Baxlo 53505/D-U

4.4 Experimental tests for large-strain visco-elastic behaviour

The mechanical behaviour of elastomers is basically visco-elastic. Therefore, this behaviour is characterized using specific experimental methodologies (Brown 2006), which depends on the work conditions of elastomer.

4.4.1 Experimental tests for hyperelastic behaviour

The hyperelastic behaviour is analyzed using tests that determine the relationship between an applied force and the resulting deformation. The quantities measured may be expressed as stress (force per unit cross sectional area) and strain (deformation as a fraction of initial dimension) or given directly as force and deformation. As the physics of elastomer hyperelasticity is even now not fully understood, accurate stress-strain behaviour of elastomer in service should be obtained using the most suitable deformation states (see Section 2.2.3), carrying out under the most relevant test conditions and following the most appropriate methodology. But it is important bear in mind that the results are not necessarily valid when applied to very different requirements in service.

Deformation states

Useful tests to characterize the nonlinear stress-strain behaviour of elastomers are uniaxial tension, uniaxial compression, equibiaxial tension, pure (planar) shear and simple shear (Brown 2006). Assuming incompressibility, equibiaxial tension and uniaxial compression are equivalent deformation states (see Figure 2.6). Moreover, pure and simple shear are also equivalent so that no additional information may be gained by carrying out both tests. Therefore, to characterize behaviour of elastomers should be used three different deformation states, uniaxial tension, pure shear and equibiaxial tension. But another consideration when choosing tests methods is their experimental simplicity. Uniaxial tension and pure shear are straightforward to measure, requiring no sophisticated equipment. Nevertheless, equibiaxial tension requires either a special straining jig to stretch the test specimen in two perpendicular directions or an apparatus to inflate a sheet and make precise strain measurements on a curved surface. Therefore, only uniaxial tension and pure shear are recommended for providing accurate results with the minimum effort or expense (BS 2004). Thus in this work, the thermoplastic polyurethane elastomer was tested in uniaxial tension and in pure shear using the dumbbell and rectangular specimens, respectively.

Tests conditions

Test conditions should be chosen to reflect as far as possible the conditions that are experienced in service by the elastomer. Moreover, when data are obtained using more than one deformation state, the tests conditions should be consistent between them. The influence of three test conditions (level of strain or maximum strain, strain-rate and stretching direction from extrusion direction) on the stress-strain behaviour of the TPU were chosen to study.

The influence of the maximum strain was analyzed taking into account the fact that some parts of the TPU in service (specially when the TPU coating of steel wire rope is contacting on drive sheave, see Figure 1.1) might experience local strains that are rather larger than the overall strain. Thus, as the maximum strains in the characterization tests should reflect this, the samples of thermoplastic polyurethane elastomer were loaded to maximum engineering strains $e_{\max}=0.15$, $e_{\max}=0.25$, $e_{\max}=0.5$ and $e_{\max}=1$ in uniaxial tension (UT) and in pure shear (PS). The specimens in melt flow direction were used and the test rate of transverse was 10 mm/min, corresponding to strain-rates of $\dot{e}=5\times10^{-3}$ s^{-1} in UT and $\dot{e}=7\times10^{-3}$ s^{-1} in PS. The strain-rates are low to approach at quasi-static conditions; thereby the viscoelastic effects are greatly reduced.

The effect of strain-rate on stress is normally quite small (BS 2004), i.e. the stress is relatively insensitive for a change in strain-rate, up to two orders of magnitude. This fact is commonly known with rubbers, however slightly larger stress differences are found with thermoplastic polyurethane elastomers in uniaxial compressions by Qi and Boyce (2005). Therefore, the effect of strain-rate has been studied to understand whether that behaviour is exhibited by an extruded TPU. Thus, the tests were carried out to the maximum strain $e_{\max}=1$ at higher strain-rates, $\dot{e}=2.5\times10^{-2}$ s^{-1} and $\dot{e}=5\times10^{-2}$ s^{-1} in UT and $\dot{e}=3.5\times10^{-2}$ s^{-1} and $\dot{e}=7\times10^{-2}$ s^{-1} in PS.

The processing of TPU can lead to anisotropic behaviour due to the predominant direction of extrusion. Therefore, the influence of the stretching direction with respect to the extrusion one has been investigated. Thus, the samples cut at 45º (dumbbell) and in TD (rectangular) were loaded only to the maximum strain $e_{\max}=1$ at strain-rate $\dot{e}=5\times10^{-3}$ s^{-1} in UT and $\dot{e}=7\times10^{-3}$ s^{-1} in PS, respectively.

The test conditions are summarized in Table 4.1. All the tests were repeated three times and they were conducted at 23±2 ºC.

Table 4.1: Conditions for uniaxial tension (UT) and pure shear (PS) tests.

		Maximum strain e_{max}	Strain-rate $\dot{e}$ [s^{-1}]	Stretching direction
Maximum strain effect	UT	0.15 - 0.25 - 0.5 - 1	0.005	MD
	PS	0.15 - 0.25 - 0.5 - 1	0.007	MD
Strain-rate effect	UT	1	0.005 - 0.025 - 0.05	MD
	PS	1	0.007 - 0.035 - 0.07	MD
Stretching direction effect	UT	1	0.005	MD - 45º
	PS	1	0.007	MD - TD

Methodology of experimental tests

There are different recommended methods to carrying out characterization tests of elastomers (BS 2004). The method depends on the service situation, e.g. for an elastomer that is only strained occasionally, taking data from results for a unstrained test specimen at low strain-rate would be reasonable, whereas for regular cyclic stress-strain conditions in service, taking data after several conditioning cycles would prevent an inaccurate material behaviour that overestimate the stiffness.

If an elastomer in service is subjected to regular cyclic deformations, then, the recommended method of characterization is carried out by means of the preconditioned elastomer (BS 2004). An elastomer is said to be preconditioned once it approaches a steady state with constant stress-strain behaviour, i.e. when the loading-unloading loops converge. Usually, the convergence is reached after 3 to 20 cycles depending on the elastomer (Duncan et al. 1999). This method of characterization presents a further complication. After each stretch, the test specimens will not return to its original length. Thus, the strains and stresses in subsequent stretches may be determined either using the original dimensions of specimens or using the new unstrained length. Latter option makes the data handling more cumbersome due to the fact that it must be redefined the length and the cross-sectional area.

As the TPU coating in service is subjected to regular cyclic deformations, then the TPU samples were preconditioned, which consisted of twelve continuous loading-unloading cycles in both deformations states.

Displacement-controlled uniaxial tension cyclic loading-unloading tests were carried out on TPU dumbbell specimens using a universal testing machine[9] equipped with a 1 kN load cell and a freestanding extensometer[10] with a gauge length of 20 mm (Figure 4.6).

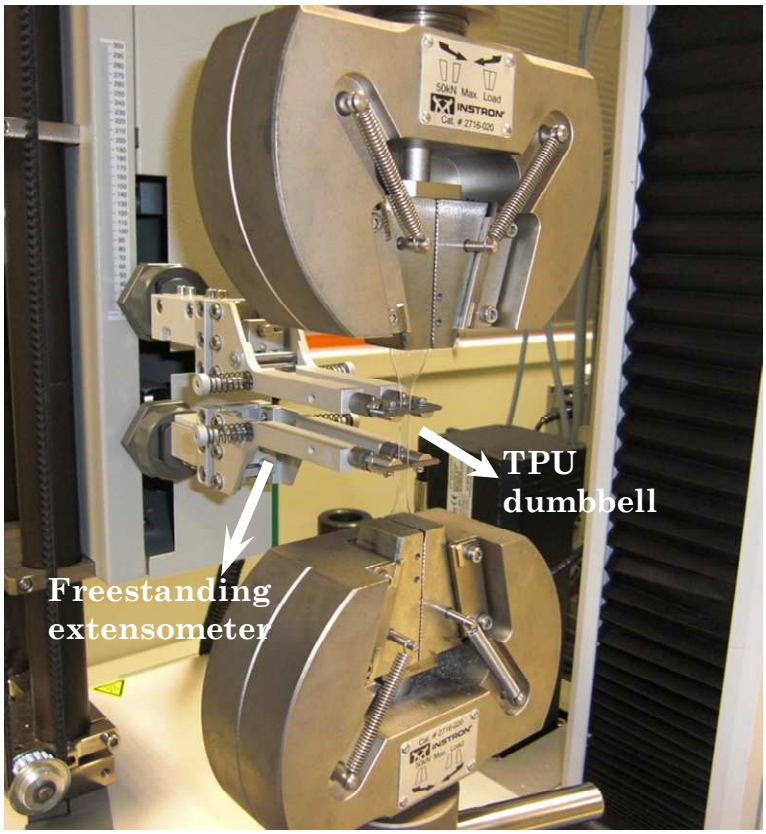

Figure 4.6: Experimental set-up of tests in uniaxial tension.

The TPU rectangular samples were stretched in displacement-controlled pure shear cyclic loading-unloading conditions using a universal testing machine[11] equipped with a 5 kN load cell with 16 mm between the grips. Deformations were followed with video extensometer, which consists of a video camera[12] in conjunction with a software[13], on a drawn square (6 mm side) on the middle of the TPU specimen (Figure 4.7). This marker square for the following unit was applied by using black ink on TPU samples.

[9]Instron EME09
[10]Zwick/Roel BTC-EXMACRO.011
[11]Galdabini Sun 2500
[12]Mitron OS-65D CCD
[13]Messphysik Windows-based

This configuration in pure shear tests was chosen to obtain a 5:1 ratio of height in the straining direction (16 mm) to the longest dimension (80 mm) of TPU samples. This is the minimum ratio to ensure pure shear state at a 45º to the stretching direction in the middle of the samples, according to BS (2004). The height of 16 mm is obtained by a measuring zone of 6 mm to follow accurately the deformations with the video extensometer and two lengths between the grids and the measuring zone of 5 mm to avoid effects of grids on measurements.

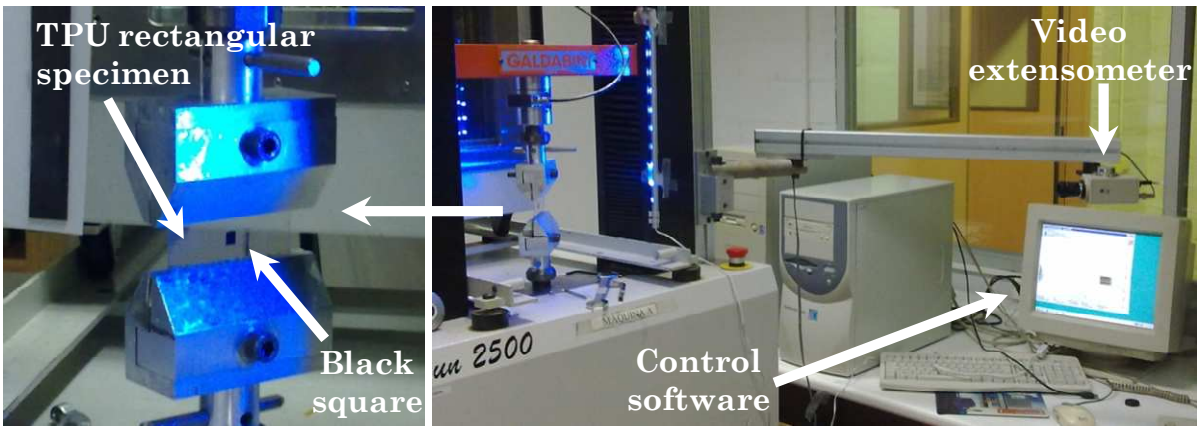

Figure 4.7: Experimental sep-up of tests in pure shear.

Processing of the test data

The experimental load-deflection data was processed to obtain stress-strain data using Matlab. The cross sectional area of each dumbbell specimen was calculated by means of the average of three measurements of the thickness at both ends of the gauge length and in the centre of specimen before each test. For rectangular specimens, the average of five measurements over the width of the sample was used in the calculation of cross sectional area. The stress-strain curve was documented for each test (Figure 4.8). If otherwise is not specified, all the stresses and strains presented in the plots throughout this work refer to the engineering stress σ and engineering strain e, respectively, which are related to the undeformed state.

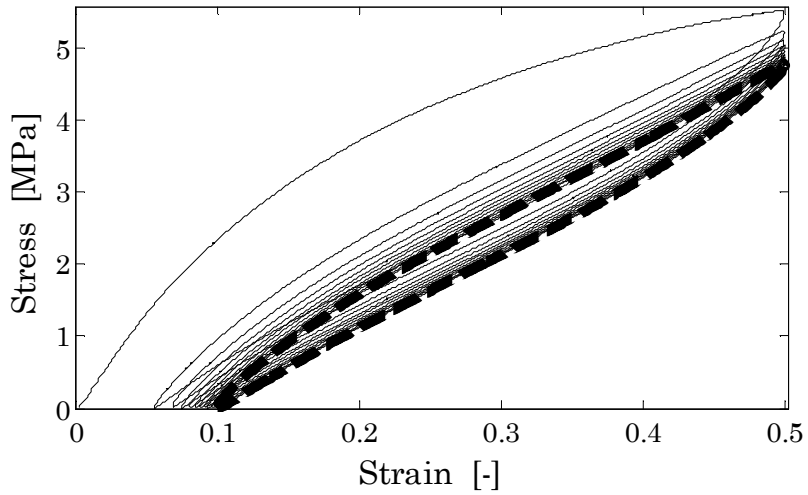

Figure 4.8: Experimental data during preconditioning method in uniaxial tension ($e_{max} = 0.5$ and $\dot{e} = 7\times10^{-3}$ s^{-1}), the last cycle is highlighted (dashed line).

4.4.2 Experimental tests for viscoelastic behaviour

Experimental data over a wide range of frequency (or time) are required for a satisfactory understanding of the viscoelastic behaviour of elastomers. The choice of experimental method depends mainly on the application, e.g. relaxation tests cover longer time-scales than dynamic tests (Figure 4.9). Hence, relaxation or creep data are appropriate for modelling events which take place over long times, whereas dynamic tests are more appropriate for modelling products subjected to vibrations.

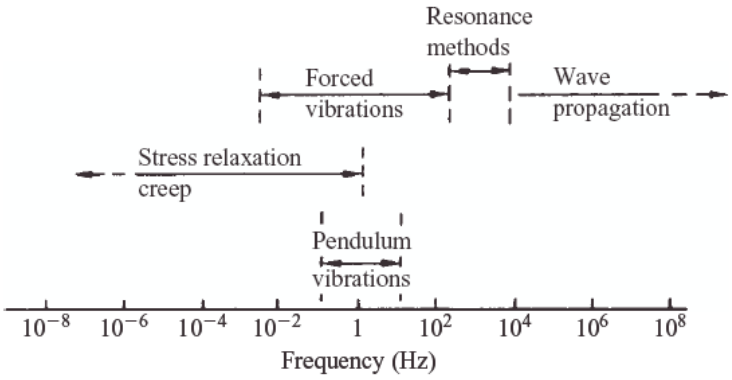

Figure 4.9: Approximate frequency scales for different experimental techniques (Ward and Sweeney 2004).

Relaxation and creep tests are methods of investigating the result of an applied strain or stress as a function of time. Relaxation test is the measurement of change of stress with time under constant strain and creep test is the measurement of the increase of strain with time under constant load. If a material exhibits linear viscoelasticity, i.e. the deformation can

be considered as the sum of independent elastic and viscous components (see Section 2.3), then the information of relaxation and creep tests is equivalent (Ward and Sweeney 2004).

To generalize the viscoelastic behaviour from a one-dimension situation (a single deformation state) to multiaxial states, it is best to work with shear (deviatoric or change in shape) and volumetric (ditational or change in volume) behaviour. But assuming incompressibility (or nearly incompressibility), the viscoelastic behaviour is entirely a shearing action, i.e. no appreciable viscoelastic behaviour in the volumetric deformation. Therefore, the data normalized to initial stress of uniaxial relaxation test can be provide as data of shear relaxation test (Brown 2006).

Relaxation tests were performed by holding a dumbbell TPU specimen in uniaxial tension at a constant tensile strain and measuring the resulting stress as a function of time. Relaxation tests were carried out using a universal testing machine[14] equipped with a 1 kN load cell and a freestanding extensometer[15]. The TPU samples were stretched to strains e = 0.5 and e = 1 at a rate of transverse of 500 mm/min. Three samples were tested to each strain magnitude at 23±2 ºC. The relaxation stresses of TPU were followed during 2500 s in each test because of an effective stabilization is observed at such time, the difference in stress at 2000 s and at 2500 s is less than 3%.

4.5 Tensile modulus

From the first loading stress-strain data obtained in uniaxial tension at $\dot{e} = 5\times10^{-3}$ s^{-1}, the tensile modulus is calculated as the gradient $\mathrm{d}\sigma/\mathrm{d}e$ at $e = 10^{-2}$, according to Buckley et al. (2010). Actually, it is determined by fitting a quadratic function to the stress-strain curve over the strain range 0.005-0.015 and differentiating analytically at $e = 10^{-2}$.

The calculated value of tensile modulus is 31±1 MPa. This calculated value of tensile modulus E can be transferred into the Shore D hardness Sh_D, using an equation given by Qi et al. (2003) as

$$Sh_D = 100 - \frac{20\left(-78.188 + \sqrt{6113.36 + 781.88E}\right)}{E}. \qquad \textbf{(4.1)}$$

[14]Instron EME09

[15]Zwick/Roel BTC-EXMACRO.011

The Shore D hardness obtained from the value of tensile modulus is 38±1 Shore D. The derivation of the experimentally measured value 35±1 MPa (Section 4.3.2) of Shore D hardness and the value obtained from tensile modulus using Equation (4.1) may result from the fact that this expression was developed using the neo-Hookean constitutive model, which presents a reduce prediction capability to segmented thermoplastic elastomers, as TPUs. However, the difference (8%) may be considered experimentally admissible.

4.6 Hyperelastic behaviour

The hyperelastic behaviour of the TPU was characterized by means of the average curves of loading-unloading stress-strain data of the last cycle (see Figure 4.8) in both deformation states. Moreover, these average curves were shifted to zero strain considering perfect elasticity (or hyperelasticity), i.e. zero stress must be zero strain (Brown 2006).

4.6.1 Influence of strain-rate

The average stress-strain curves are not dependent on strain-rate in uniaxial tension (Figure 4.10a), at least in the studied range, but they present a slightly stiffening, which should not be considered significant experimentally, with increasing the strain-rate in planar tension (Figure 4.10b). Therefore, the hyperelastic behaviour of the extruded TPU is not influenced by strain-rate between $\dot{e}=5\times10^{-3}$ s^{-1} and $\dot{e}=5\times10^{-2}$ s^{-1} in uniaxial tension and between $\dot{e}=7\times10^{-3}$ s^{-1} and $\dot{e}=7\times10^{-2}$ s^{-1} in pure shear.

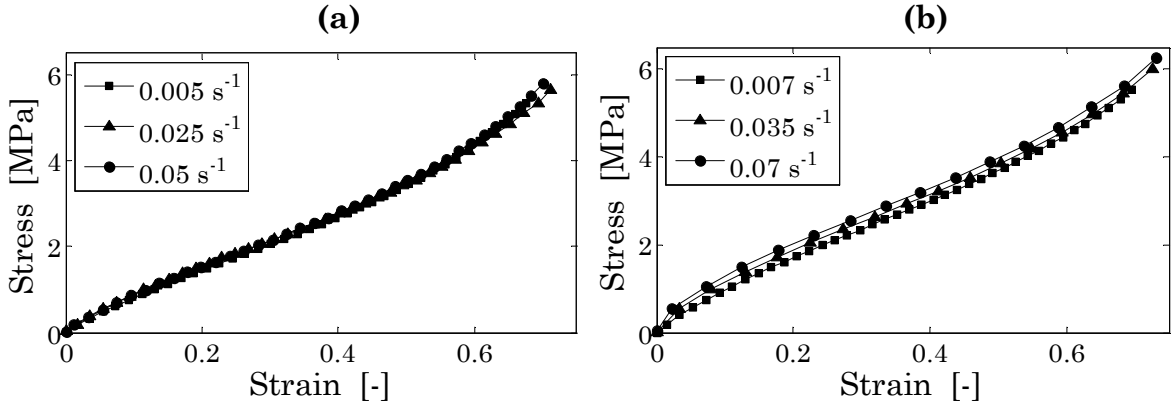

Figure 4.10: Hyperelastic stress-strain curves at different strain-rates in (a) uniaxial tension and in (b) pure shear ($e_{max}=1$).

4.6.2 Influence of maximum strain

The TPU clearly exhibits different stress-strain behaviour depending on maximum strain (Figure 4.11) in both deformation states. The TPU is less stiffness with increasing maximum strain. This behaviour should be taken into account when the TPU will be modelled, which is discussed later in Chapter 5. Furthermore, it comes out from Figure 4.11 that the stress at given strain is higher in pure shear than in uniaxial tension, which agrees with the reported in literature (Davies et al. 1994, Laraba-Abbes et al. 2003 and Kanyanta and Ivankovic 2010).

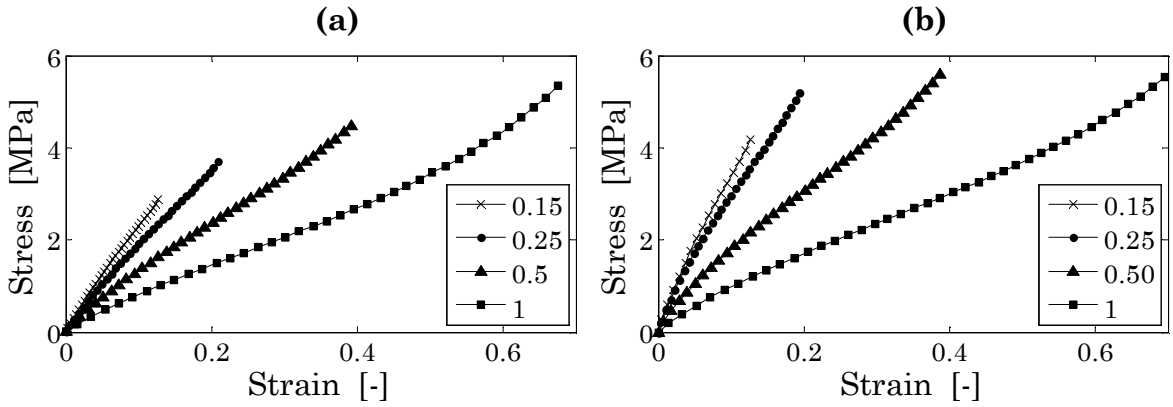

Figure 4.11: Hyperelastic stress-strain curves to different maximum strains in (a) uniaxial tension and in (b) pure shear ($\dot{e} = 5\times10^{-3}$ s^{-1} in UT and $\dot{e} = 7\times10^{-3}$ s^{-1} in PS).

4.6.3 Influence of stretching direction

The stress-strain behaviour of the TPU exhibits slight differences when the stretching direction does not coincide with the extrusion direction (Figure 4.12). The difference is more evident in pure shear than uniaxial tension. In pure shear, the behaviour of the TPU samples in TD shows a higher stiffness, which may be due to a higher density of hard segments in transverse direction (TD) than parallel (MD) direction. In uniaxial tension, samples at 45º show a slight softening compared with MD samples. The reason of this softening is not clear, but the difference can be considered no significant experimentally. Regarding the results obtained, the TPU exhibits slight anisotropic behaviour in pure shear that is no observes in uniaxial tension. But it bears in mind that these results are not comparable due to the cut directions from extrusion direction are different, at 45º in UT and on transverse (at 90º) melt flow direction in PS. Therefore, as an initial approach, isotropic behaviour will be assumed for modelling the hyperelastic behaviour of TPU (Section 5.1).

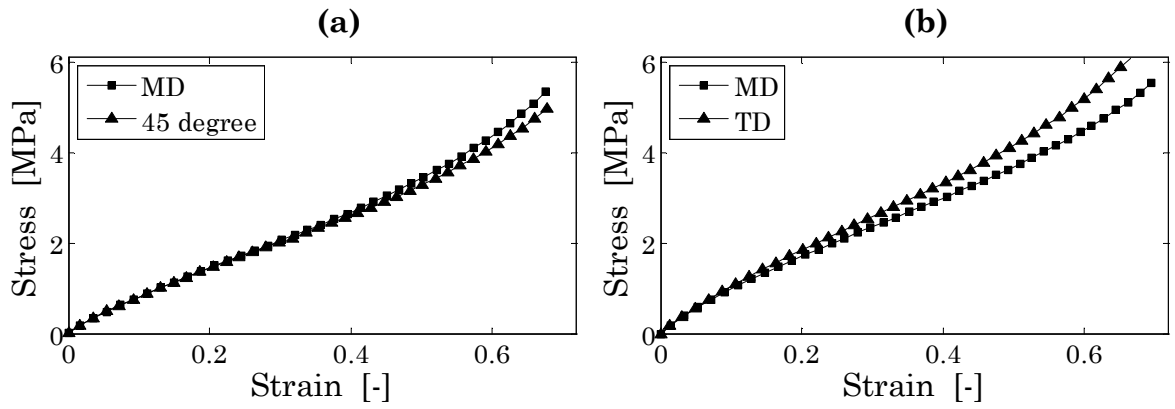

Figure 4.12: Hyperelastic stress-strain curves in different stretching directions in (a) uniaxial tension ($\dot{e} = 5\times10^{-3}$ s^{-1}) and in (b) pure shear ($\dot{e} = 7\times10^{-3}$ s^{-1}), to maximum strain $e_{max} = 1$.

4.7 Viscoelastic behaviour

The viscoelastic behaviour of the TPU was characterized using the experimental results of the stress depending on time of the relaxation tests (Figure 4.13). According to Figure 4.13, the TPU shows a marked relaxation, particularly at little time since the time needed for the stresses to drop approximately 50% is less than 100 seconds. At 2500 seconds, the stresses drop approximately 66%. These behaviours may be easily observes in Figure 4.14, where is plotted the normalized relaxation response with the initial stress σ_0 at different load levels.

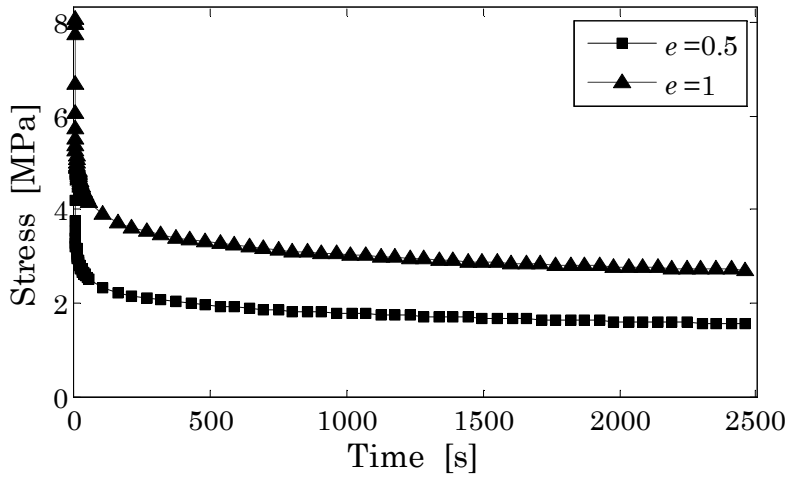

Figure 4.13: Viscoelastic behaviour: relaxation data at different strain magnitudes.

Moreover, the Figure 4.14 shows the linear viscoelastic behaviour of the TPU because of the relaxation behaviour is independent of the constant tensile strain. This fact will take into account for modelling the viscoelastic behaviour of TPU (Section 5.1).

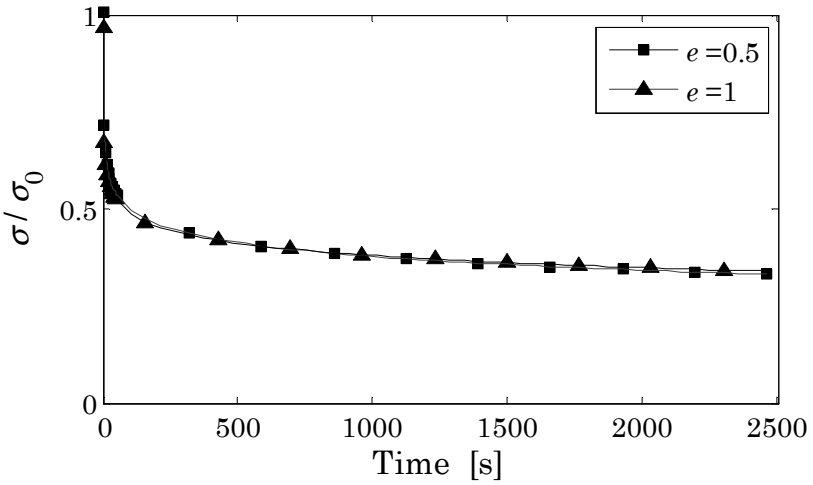

Figure 4.14: Linear viscoelastic behaviour: normalized relaxation data at different strain magnitudes.

4.8 Inelastic behaviour

As it is pointed out in Section 2.4, under cyclic loading-unloading conditions, the principal inelastic effects are stress-softening, hysteresis loss and residual strain (Figure 2.9). Therefore, from the results of cyclic tests (Section 4.4.1), the behaviour of these inelastic effects depending on maximum strain, strain-rate and stretching direction is discussed below.

4.8.1 Stress softening

The stress softening is determined from the stress to the maximum strain of each cycle and it is expressed as relative stress softening $\sigma^* = \sigma_i / \sigma_{\max}$, where $\sigma_{\max}$ is the stress at the maximum strain of first cycle and σ_i are the stresses at the maximum strain of *i*th cycle (Figure 4.15a).

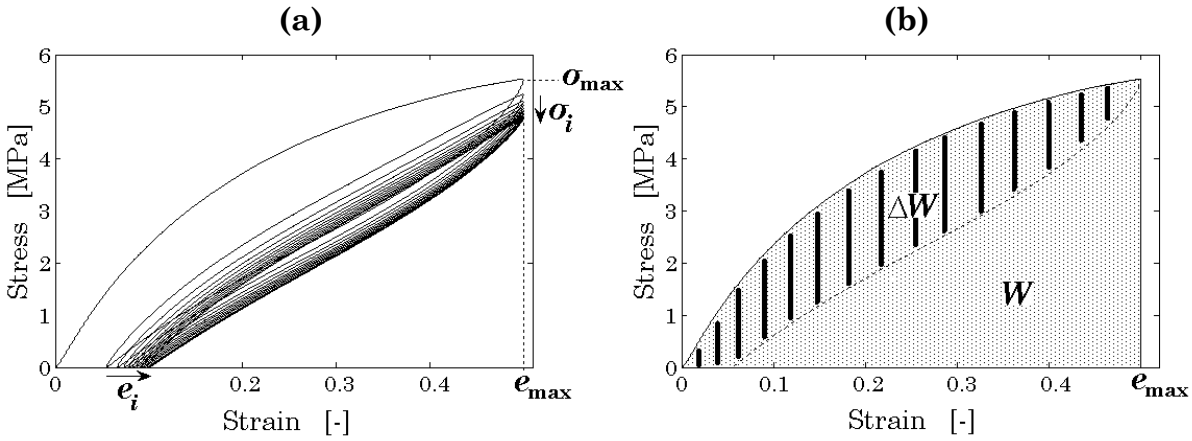

Figure 4.15: Parameters to calculate the relative inelastic effects. (a) Loading-unloading cycles with the highlighted parameters of the relative stress softening and the relative residual strain. (b) The area under loading curve (thick line) is the work input and the area between loading and unloading (dashed line) curves is the hysteresis loss.

The behaviour of relative stress softening σ^* depending on maximum strain is shown in the Figure 4.16. A remarkable feature from the results obtained is that the relative stress softening in uniaxial tension is approximately similar to that in pure shear, except to the maximum strain $e_{max}=1$. Moreover, it comes out from Figure 4.16 that the relative stress softening is more marked with increasing of the maximum strain in both deformation states.

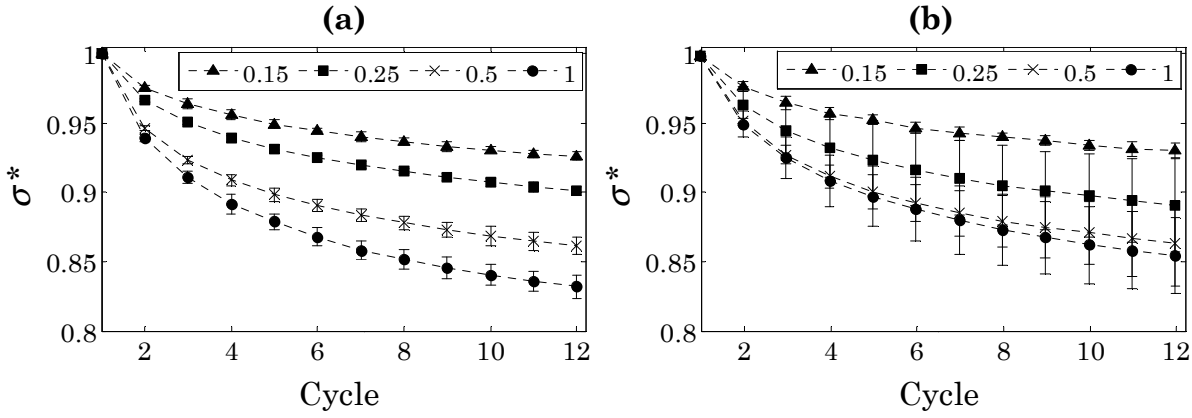

Figure 4.16: Relative stress softening in (a) UT and in (b) PS to different maximum strains.

It can be also noted that, to a given strain level ($e_{max}=1$), the behaviour of the relative stress softening appears not to be greatly influenced by strain-rate in uniaxial tension (Figure 4.17a). But it appears to be slightly influenced in pure shear (Figure 4.17b), the relative stress softening is more marked with increasing strain-rate.

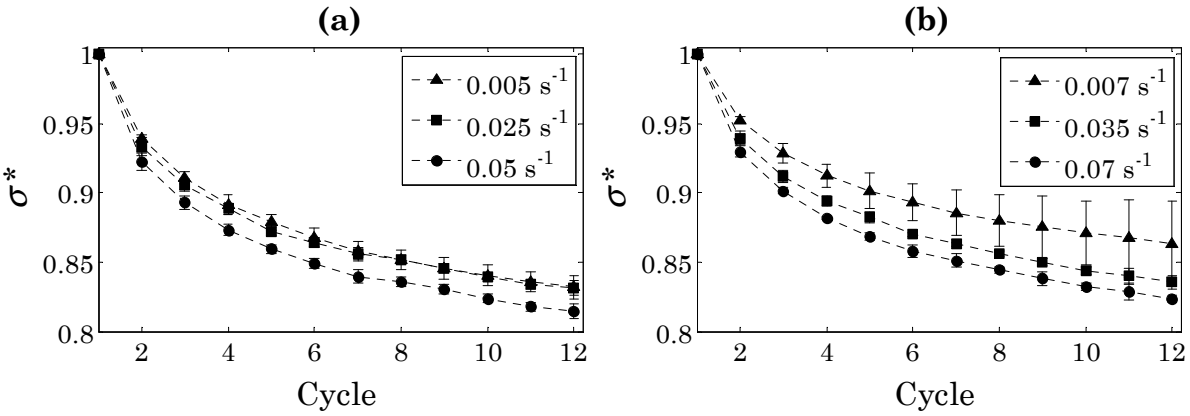

Figure 4.17: Relative stress softening in (a) UT and in (b) PS at different strain-rates.

On the contrary, the relative stress softening is not affected significantly by stretching direction in pure shear (Figure 4.18b). However it is very slightly affected in uniaxial tension (Figure 4.18a), the relative stress softening is less marked at 45º than in MD. But it bears in mind that the results are not comparable due to the stretching directions are different, at 45º from the extrusion direction in UT and at 90º, or on transverse melt flow direction (TD), in PS.

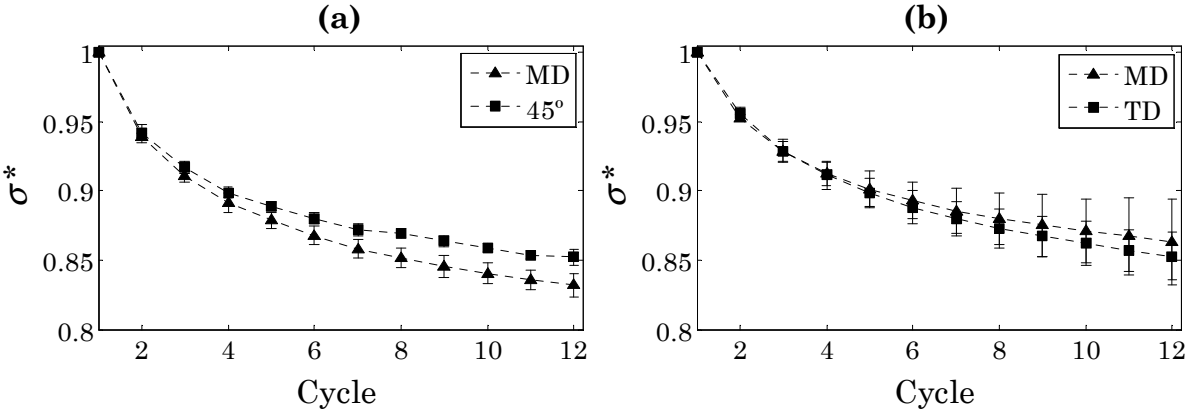

Figure 4.18: Relative stress softening in (a) UT and in (b) PS in different stretching directions.

4.8.2 Hysteresis loss

The data of cyclic tests are used to compute two different works of each cycle by the integration $W = \int \sigma de$. The work input W is obtained by integration over the loading up to the maximum strain e_{max} of each cycle and the hysteresis loss ΔW by integration over the whole loading-unloading sequence of each cycle (Figure 4.15b). In comparing the different test

conditions and deformation states, the relative hysteresis loss is expressed as the rate between hysteresis loss and work input, $W^* = \Delta W / W$.

To different maximum strains, Figure 4.19 reveals the fact that the relative hysteresis loss clearly converges to a value in PS, but this convergence is unclear or not reached after twelve cycles in UT. Moreover, the convergence approximately occurs at slight greater value of relative hysteresis loss in pure shear than in uniaxial tension.

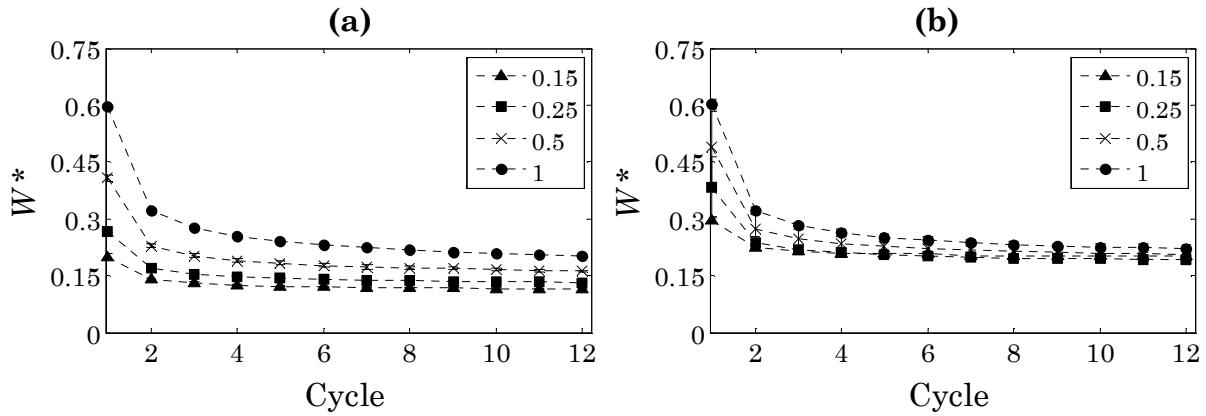

Figure 4.19: Relative hysteresis loss in (a) UT and in (b) PS to different maximum strains.

At different strain-rates, it follows from Figure 4.20 that the relative hysteresis loss increases with increasing strain-rate only in PS. However, the behaviour of hysteresis is not influenced by strain-rate in UT. Furthermore, it can be noted that the relative hysteresis loss exhibits a marked decrease between the first and second cycles in both deformation states.

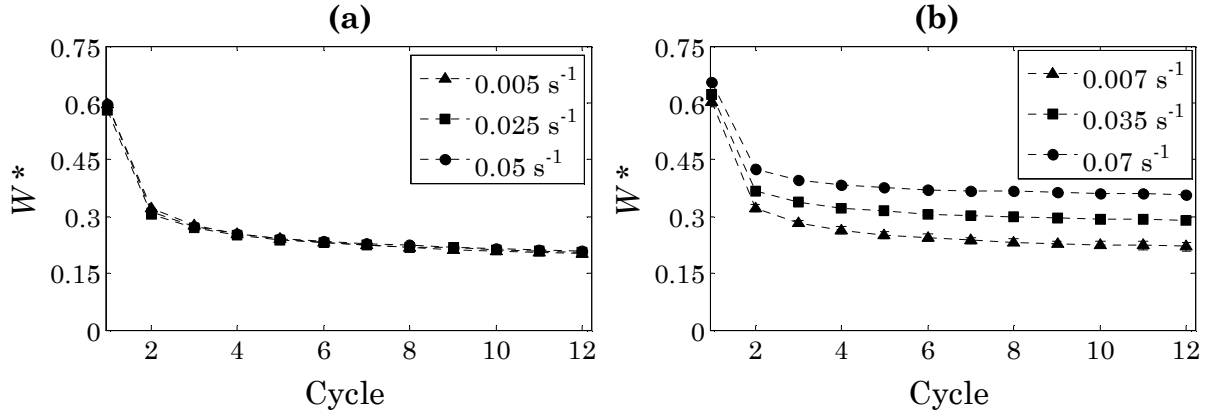

Figure 4.20: Relative hysteresis loss in (a) UT and in (b) PS at different strain-rates.

Finally, from Figure 4.21 it should be noted that the relative hysteresis loss is not affected by the stretching direction in both deformation states. Therefore, it may be assumed that the behaviour of hysteresis loss is isotropic.

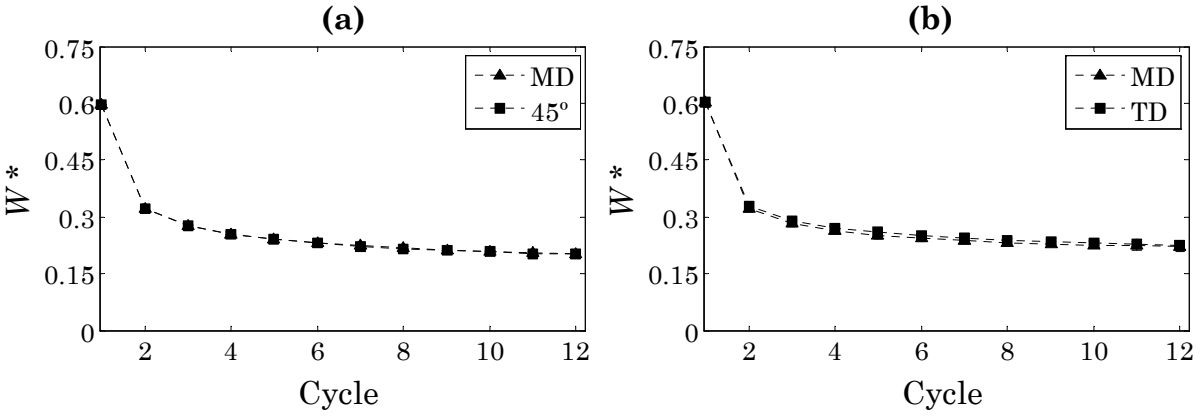

Figure 4.21: Relative hysteresis loss in (a) UT and in (b) PS in different stretching directions.

4.8.3 Residual strain

The residual strain effect has been determined from the residual strain e_i at each unloading (Figure 4.15a), expressed as relative residual strain $e_r^* = e_i / e_{max}$.

Relative residual strains obtained to different maximum strains are shown in Figure 4.22, which illustrates that the relative residual strains increase with increasing maximum strain in both deformation states. The values of relative residual strains to each maximum strain are equals up to $e_{max} = 0.5$. However, to $e_{max} = 1$, the relative residual strain is higher in uniaxial tension than in pure shear.

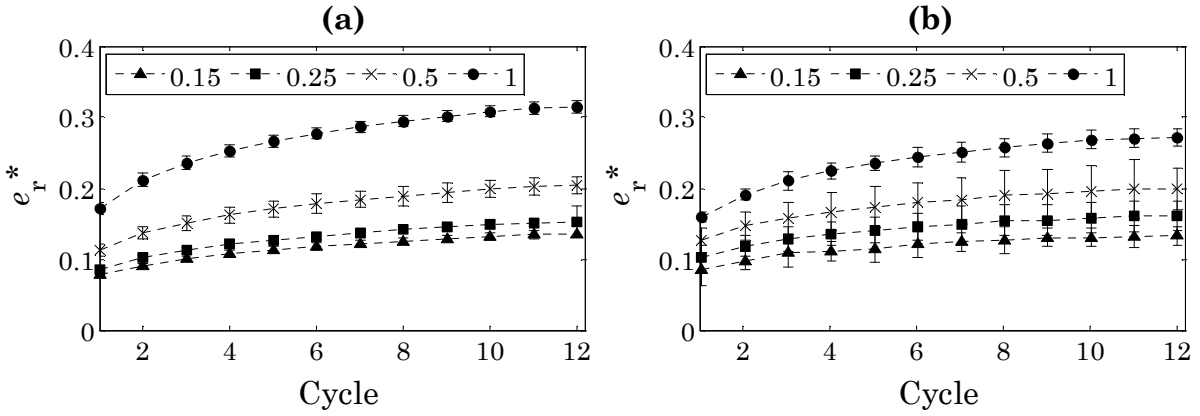

Figure 4.22: Relative residual strain in (a) UT and in (b) PS to different maximum strains.

From the Figure 4.23, it should be pointed out that the relative residual strains at lowest strain-rate appear to be slightly greater than in the case of both the other two strain-rates. Moreover, since e_{max} =1, the values of relative residual strain are greater in uniaxial tension than in pure shear, as it is noted above.

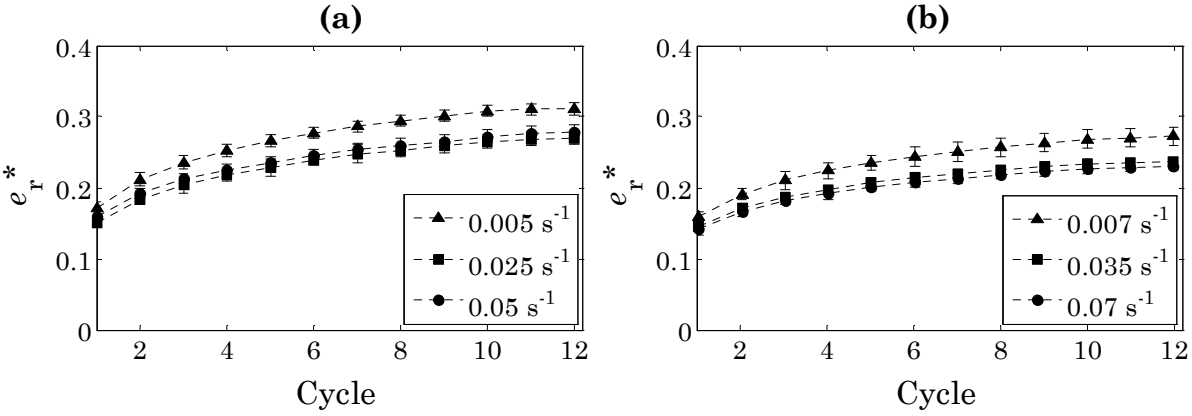

Figure 4.23: Relative residual strain in (a) UT and in (b) PS at different strain-rates.

The relative residual strains are not affected by the stretching direction as it is followed from Figure 4.24. Therefore, the residual strain exhibits an isotropic behaviour, as well as the relative hysteresis loss.

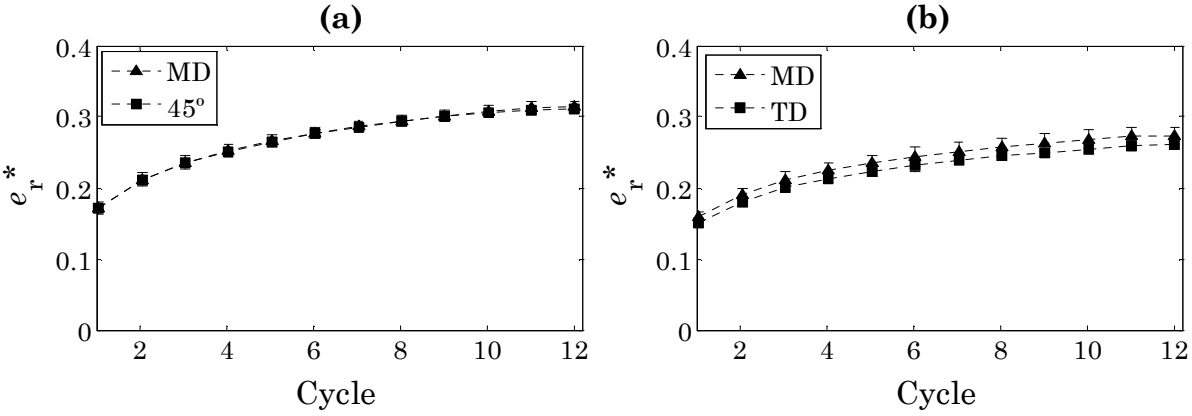

Figure 4.24: Relative residual strain in (a) UT and in (b) PS in different stretching directions.

Furthermore, to identify the degree of strain recovery or permanent set, the gauge length of deformed dumbbells and rectangular specimens were re-measured after 24 hours of testing. Figure 4.25 compares the residual strains immediately after testing and the permanent set after 24 hours in UT and in PS. It should be noted that the residual strains

are recovered, likely by long-term effects, up to the maximum strain $e_{max} = 0.5$ and the permanent set is only significant to the maximum strain $e_{max} = 1$, which agree with the observations of Desper et al. (1985) and Blundell et al. (2002) with several TPUs.

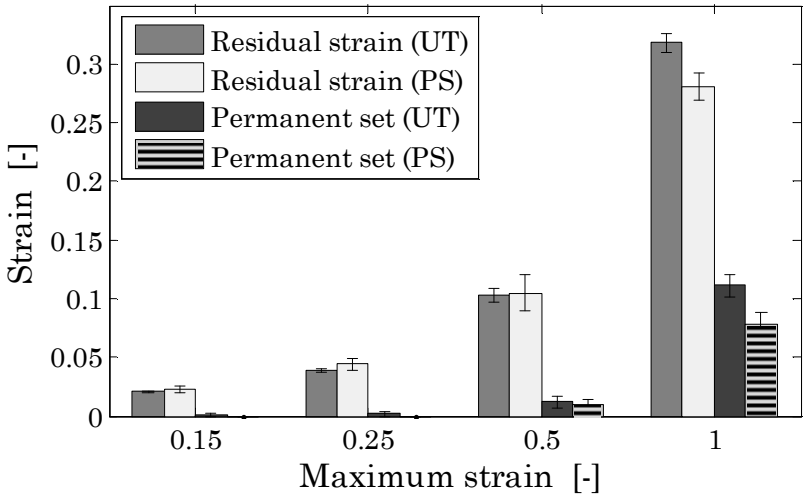

Figure 4.25: Comparison between residual strain and permanent set to different maximum strains in both deformation states, uniaxial tension (UT) and pure shear (PS).

4.8.4 Discussion of inelastic behaviour

Some features, which seem to be common to thermoplastic polyurethane elastomers (TPUs) of different chemical composition, are considered to understand the results obtained. Firstly, the dramatic difference in strain-stress response between first loading and subsequent loadings. Therefore, the second and subsequent loadings correspond to deformation of a new structure. Accordingly with Buckley et al. (2010), the mechanical response of this new structure is independent of the chemical composition of the TPU if the hard segment fraction and soft segment chain length are held constant. Moreover, this response is also independent of the maximum strain reached.

Secondly, at strains below the yield stress, TPUs present a response as two-phase composite material (Blundell et al. 2002). However, beyond the yield stress, the two-phase structure of TPUs begins to disrupt (this may occur at different strains, e.g. Blundell et al. (2002) at $e \approx 1.25$ and Yeh et al. (2003) at $e \approx$ 2-2.5). Then, two likely consequences occur. On the one hand, it could lead to the break-up of hard domains in the original structure and to the re-formation of new stress-free domains in the deformed structure (Desper et al. 1985). The original hard domains become smaller units and irreversible breakages lead to permanent set. On the other hand, it could lead to hard segments being stripped from hard

domains and they being coupled in series with the soft matrix, thus a new soft phase is produced (Enderle et al. 1986). The new soft matrix is characterized by much lower stiffness and lower hysteresis loss than the original phase. However, Qi and Boyce (2005) proposed a model which invokes parallel coupling between the stripping hard domains and soft phase, where second and subsequent cycles of loading-unloading would involve deformation of the hard phase in addition to the soft phase. But this model appears not to be consistent with the results of Buckley et al. (2010), which show a remarkable commonality of the new soft phase response between different TPUs.

Another interesting observation, when the two-phase structure of TPU begins to disrupt, is an increase in internal energy due to the less efficient ordering of hard segments (Godovsky et al. 1986). This observation might suggest a reduction in H-bonding during straining, but IR spectroscopy measurements show a density of H-bonds independent of deformation (Seymour et al. 1970). Therefore, H-bonds are broken and re-formed at the same time.

Finally, hard and soft segments are oriented along predominant directions during stretching (Estes et al. 1971). Initially hard and soft segments are predominantly oriented perpendicular and parallel, respectively, to the stretching direction. However when the strain beyond $e \approx 1$, the predominant direction of hard segments is rotated parallel to the direction of extension as the soft segments (Yeh et al. 2003 and Unsal et al 2009).

In this context, an interpretation of the results obtained for the extruded TPU is proposed taking into account these common features of TPUs.

Strain state

The results presented above reveal that the relative stress softening (Figure 4.16) and the relative residual strain (Figure 4.22) are not affected by the deformation state at strains below the yield stress, i.e. up to the maximum strain $e_{max} = 0.5$. Therefore, the structure is expected to remain undisturbed and reversible deformation to occur (see Figure 4.25). However, the results show that the behaviour at the maximum strain $e_{max} = 1$ of both inelastic effects (stress softening and residual strain) varies from experimental tests in uniaxial tension and to in pure shear. The difference might be due to the straining in UT occurs in all directions, but not in PS, since the deformation in the transverse direction to the stretching is restricted. Therefore, the effects of relative stress softening and of relative residual strain are higher in uniaxial tension than in pure shear. This behaviour of the relative stress softening and the relative residual strain is also shown by the results at different strain-

rates (Figure 4.17 and Figure 4.23, respectively) and in different stretching directions (Figure 4.18 and Figure 4.24, respectively). On the contrary, the relative hysteresis loss is slightly lower in UT than in PS (Figure 4.19), due to the restriction of strains in PS reduces the input work.

Maximum strain

The behaviour of relative stress softening (Figure 4.16) and the relative residual strain (Figure 4.22) shows a expected behaviour when the maximum strain varies, i.e. both inelastic effects are more marked with increasing of the maximum strain.

Nevertheless, the relative hysteresis loss approximately shows an independent behaviour of the maximum strain (Figure 4.19), which is consistent with the results of Buckley et al (2010). Therefore, according to Enderle et al. (1986), it may be suggest that the stripping hard segments are coupled in series with the soft matrix, but not in parallel, as it is pointed out by Qi and Boyce (2005).

Strain-rate

The influence of strain-rate is different depending on the inelastic effect. Relative stress softening (Figure 4.17) is slightly more marked with increasing of strain-rate, but relative residual strain (Figure 4.23) appears to decrease. Taking into account that permanent set is higher at low strain-rate than at higher strain-rates (Figure 4.26) in both deformation states, the damage, i.e. breakage of bonds, decreases with increasing strain-rate. Therefore, the relative stress softening appears to be more influenced by the reformation and reorientation of bonds than by the structural break-up.

Otherwise, the behaviour of relative hysteresis loss at different strain-rates is entirely different depending on deformation state. Relative hysteresis loss is independent of strain-rate in uniaxial tension (Figure 4.20a), but it increases with increasing strain-rate in pure shear (Figure 4.20b). This difference can not be explained easily, likely the stripping and coupling modes of hard segments are not equivalent in both deformation states and, in view of the results, they are influenced by strain-rate in pure shear. But, this difference of relative hysteresis loss behaviour will require a more detailed study to understand.

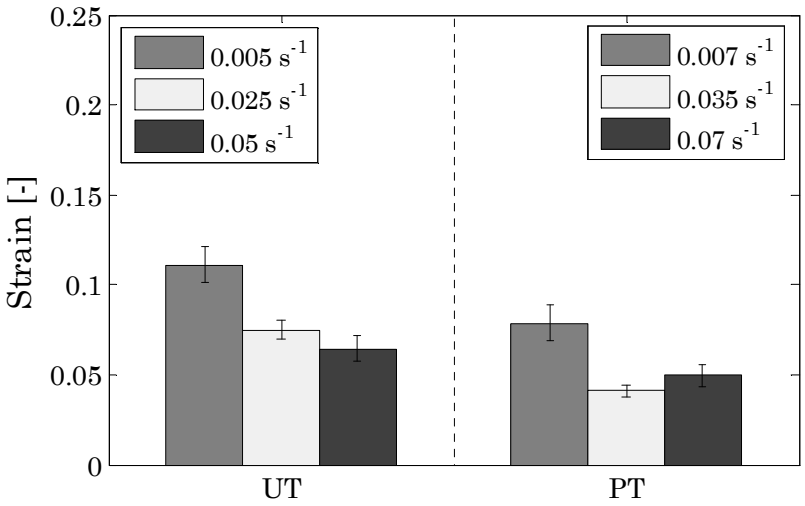

Figure 4.26: Permanent set at different strain-rates and stretching directions, in uniaxial tension (UT) and in pure shear (PS).

Stretching direction

Finally, relative hysteresis loss (Figure 4.21) and relative residual strain (Figure 4.24) appear to show an isotropic behaviour in both deformation states, i.e. their behaviour is independent of stretching direction. Nevertheless, the behaviour of relative stress softening (Figure 4.18) appears to be isotropic only during the first cycles. In fact, the results show a slight anisotropic behaviour during the last cycles, particularly in UT. Consequently, extrusion process of TPU does not lead to different behaviour regarding hysteresis loss and residual strain. But, regarding the stress softening, the behaviour obtained suggests that the stress softening could be related with the re-orientation (according to Unsal et al. 2009) and re-formation of hard segments (according to Qi and Boyce 2005).

4.9 Conclusions

The structural study and the mechanical characterisation of the extruded TPU were carried out. The chemical structure and the physical properties obtained are summed up in Table 5.1.

From the Nuclear Magnetic Resonance, it was identified the chemical components of hard segments (MDI and BDO) and of soft segments (PTMG), as well as their mass fraction, 0.46 of hard segments and 0.54 of soft segments.

Table 4.2: Chemical structure and physical properties of extruded TPU.

Material	MDL	DI	CE	Hard segment Mass fraction	Density ρ [kg·m^{-3}]	Hardness H [Shore D]	Tensile modulus E [MPa]
TPU (ether-based)	PTMG	MDI	BDO	0.46	1122±2	35±1	31±1

The tensile modulus and the hardness of the extruded TPU was measured and it was proved that these magnitudes can be related using Equation (4.1) (Qi et al. 2003) with an experimental adequate accuracy, less than 8%.

As elastomers, the extruded TPU exhibits a complex mechanical behaviour, i.e. it exhibits a non-linear stress-strain (hyperelastic) behaviour and viscoelasticity. Moreover, although the TPU is an unfilled elastomer, its behaviour closely resembles to filled elastomers, since the behaviour presents clear stress softening, hysteresis loss and residual strain (Figure 4.8).

From the experimental data obtained from cyclic loading-unloading tests, it was determined that the hyperelastic behaviour of the extruded TPU depends strongly on the undergone maximum strain (Figure 4.11), i.e. the stress-strain behaviour is sensitive to the maximum strain ever experienced. However, the strain-rate does not significantly affect the hyperelastic behaviour of the TPU (Figure 4.10). Finally, the hyperelastic behaviour appears to be slightly affected by the stretching direction from the extrusion direction in pure shear conditions (Figure 4.12b), but this fact is not clear in uniaxial tension (Figure 4.12a). Therefore, in first approach, the hyperelastic behaviour of the extruded TPU is assumed as isotropic.

From the relaxation data (Figure 4.13), it was laid down that the viscoelastic behaviour of the TPU is clearly linear, i.e. its behaviour is independent of the constant tensile strain. Moreover, from the Figure 4.25 it should be noted that the stress softening and the reduction in hysteresis with increasing number of cycles is due to meanly to a purely time dependent (visco) effect, since the permanent set, which is due to a mechanism damage, is less than 10%. Therefore, it is assumed that stress softening and reduction in hysteresis are time dependent effects and they may be modelled using the viscoelastic behaviour of the TPU (Muhr 2005).

The inelastic behaviour of the extruded TPU, specifically according to the inelastic effects of stress softening, hysteresis loss and residual strain, was discussed using the data from cyclic loading-unloading tests. The remarkable feature is that, at strains below the yield stress (up to the maximum strain $e_{\max} = 0.5$), the inelastic effects studied not depend on the deformation state under which the material is stretched. However, beyond the yield stress, residual strain and stress softening are affected by the deformation state (Figure 4.16 and Figure 4.22). Moreover, stress softening and residual strain at different strain-rates (Figure 4.17 and Figure 4.23) exhibit a contrasting behaviour. This contrast may be due to that the stress softening is more affected by the process of re-formation and re-orientation of bonds than the residual strain, which is clearly influenced by the breaking of hard segments. In view of the results, beyond the yield stress, the stress softening and the residual strain should be characterized in more than one strain state to be accurately considered by the constitutive models of the extruded thermoplastic polyurethane elastomers.

Another aspect of inelasticity of the extruded TPU is the independent behaviour of hysteresis loss with the maximum strain. This aspect suggests that the hysteresis loss of the new soft matrix is independent of the deformation level at which is formed, which aggress with Buckley et al. (2010). Furthermore, this behaviour also may suggest that the stripping hard segments, which are stripped from hard domains to soft domains, are coupled in series with the soft matrix, as it is suggested by Enderle et al. (1986).

Finally, the behaviour of hysteresis loss and residual strain not depends on stretching directions, i.e. an isotropic behaviour of these inelastic effects is exhibited by the extruded TPU. However, particularly in uniaxial tension conditions, stress softening shows a slight anisotropic behaviour, which suggests that the re-formation of bonds (Unsal et al. 2009) and the re-orientation of segments (Qi and Boyce 2005) can be affected by the stretching direction at strains beyond $e \approx 1$, as it is pointed out by Yeh et al. (2003).

5 MODELLING OF LARGE-STRAIN VISCO-ELASTIC BEHAVIOUR

"Knowing is not enough; we must apply.

Willing is not enough; we must do"

Johann Wolfgang von Goethe

In Chapter 4 it has been discussed the mechanical response of the extruded TPU up to strain $e = 1$ and it has been shown that the hyperelastic behaviour depends on the maximum strain (i.e. on the strain history). Also it has been observed that the viscoelastic behaviour of TPU is linear. Finally, it has been pointed out that the permanent set of TPU is significant only at $e = 1$, but with values less than 10%. Therefore, if the permanent set is considered to be negligible, the time dependent (viscoelastic) behaviour can explained the stress softening and the reduction in hysteresis, which are exhibited by the mechanical response of TPU in cyclic conditions. This chapter extends the previous experimental work to describe the complex mechanical behaviour of the TPU using an overlay visco-hyperelastic model.

On the one hand, fittings of the stress-strain data of preconditioned TPU are carried out (Section 5.1.1) depending on the maximum strain in both deformation states (uniaxial tension and pure shear) at the same time. The strain energy density functions (or hyperelastic models) obtained is validated to predict the stress-strain response of preconditioned TPU (Section 5.2) in both homogeneous deformation states. Moreover, the hyperelastic models depending on maximum strain are used to predict the response of the TPU in inhomogeneous deformation state (Section 5.4).

On the other hand, a viscoelastic model (Section 5.1.2) is developed from the relaxation tests in Chapter 4. As TPU exhibits a linear viscoelasticity, then its behaviour can be describe in terms of a Prony series, i.e. as a set of linear Maxwell (or viscous) elements in parallel with a spring (elastic element), see Section 2.3. To validate the overlay visco-hyperelastic model, all the cycles of experimental tests are simulated in both deformation states at different strain-rates (Section 5.3) using finite element analysis (FEA).

Finally, material model of the TPU in inhomogeneous deformation states is proposed considering the dependence on the maximum strain ever experienced (history load) of the hyperelastic behaviour (Section 5.5). This model is implemented into numerical calculus using a FEA-based technique which is developed to update the deformation history and it is validated using the experimental results of tests in inhomogeneous deformation states.

5.1 Visco-hyperelastic model

As stated in Chapter 4, the stress-strain response of elastomers at large deformations is nonlinear (hyperelastic) and time dependent (visco). Thus, the overlay visco-hyperelastic model of the extruded TPU is developed assuming separation of the non-linear stress-strain behaviour from time dependence. This assumption was used to generalize the theory of linear viscoelasticity for application to finite strains (or large-strains) by Simo (1987). Moreover, the TPU is considered incompressible as the elastomers when they are not subjected to high hydrostatic loadings (Brown 2006).

5.1.1 Hyperelastic model

The constitutive model of hyperelastic behaviour exhibited by elastomers is based on a strain energy density function (SEDF). The SEDFs may be implemented in finite element analysis by means of the relation

$$\sigma = \frac{\partial W}{\partial \lambda}. \tag{5.1}$$

The coefficients of the different SEDFs can be either determined by a least-squares fit procedure of experimental data in homogeneous deformation states. Actually, the reduced stress depending on the deformation state, Equations (2.25), (2.26) and (2.27), are fitted to obtain the hyperelastic model. Thus, the relative error

$$E_{fit} = \sum_{i=1}^{n_p} \left(1 - \frac{\left(\sigma_{\text{red}}^{i}\right)^{\text{th}}}{\left(\sigma_{\text{red}}^{i}\right)^{\text{exp}}} \right)^2, \tag{5.2}$$

is minimized, where n_p is the number of experimental data, $\left(\sigma_{\text{red}}^{i}\right)^{\text{exp}}$ are the reduced stresses from the experimental data and $\left(\sigma_{\text{red}}^{i}\right)^{\text{th}}$ are the reduced stresses from the SEDF.

The curve fitting process does not guarantee a stable hyperelastic model, i.e. a SEDF that obeys the thermodynamic laws to increases its internal energy of material when it does work on it. Therefore, the stability of model must be checked at least in the range of strains tested. The Drucker's stability postulate

$$\sum_i \mathrm{d}e_i \cdot \mathrm{d}\sigma_i \geq 0, \tag{5.3}$$

should be satisfied.

The fitting of hyperelastic model was carried out using the experimental data of preconditioned TPU (i.e. the average stress-strain data of the last cycle shifted to strain zero, see Section 4.6) in both deformation states at the same time. Moreover, equal numbers of experimental data points from each deformation state were used to ensure that there was not prevalence of the results of one deformation state over those of another deformation state. This fitting at same time is possible due to the reduced stresses from experimental data lie approximately on the same curve independent of the deformation state (as it is shown by Figure 5.1 for extruded TPU at different maximum strains), i.e. there is a simple relationship between the different deformation states, which was reported by Gregory (1979) and Davies et al. (1994) for rubbers (see Figure 2.7). Thus, the extruded TPU also exhibits this simple relationship as rubbers. Moreover, the experimental data at lowest strain-rate are used to ensure quasi-static conditions, but it bears in mind that the strain-rate does not significantly influence the experimental data (see Section 4.6).

The hyperelastic models (e. g. neo-Hookean SEDF, Rivlin SEDFs, Arruda-Boyce SEDF…) that did not fit accurately the experimental data were discarded. Thus, only three hyperelastic models, Yeoh model or 3-term reduced polynomial model, 5-term reduced polynomial model and 4-term Ogden model, were considered. The two latter models were discarded due to stability problems.

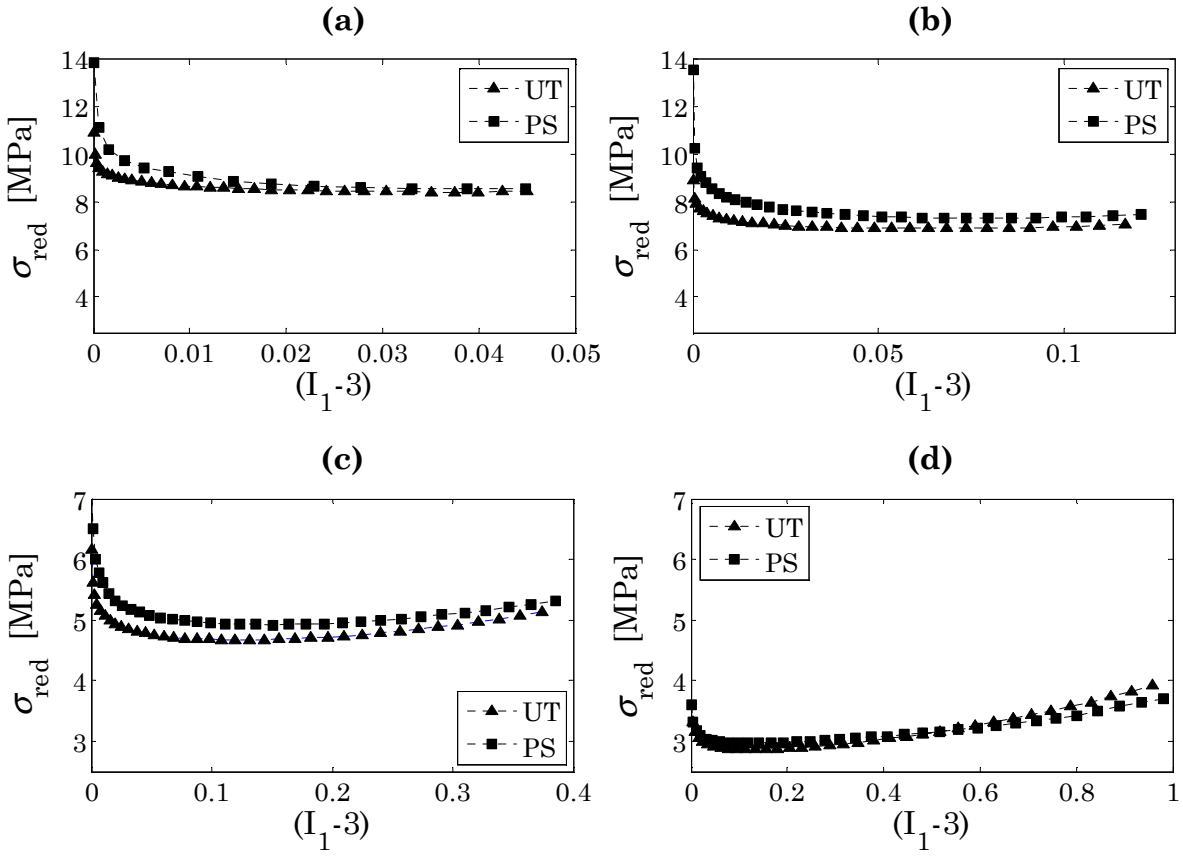

Figure 5.1: Stress-strain data of extruded TPU in UT and PS, measurements plotted as reduced stress vs. $I_1 - 3$ at (a) $e_{max} = 0.15$, (b) $e_{max} = 0.25$, (c) $e_{max} = 0.5$ and (d) $e_{max} = 1$.

On the one hand, the Ogden models present stability problems when they are considered experimental data in more than one deformation state at the same time due to they must be fitted using a nonlinear regression. On the other hand, the N-term reduced polynomial models can present stability problems when the N-terms increase. Therefore, the Yeoh model, Equation (5.4), or 3-term reduce polynomial SEDF was chosen due to fit accurately the behaviour of TPU in the both deformation states at the same time (Figure 5.2 and Figure 5.3) with fewer terms.

$$W = C_{10}(I_1 - 3) + C_{20}(I_1 - 3)^2 + C_{30}(I_1 - 3)^3, \quad \textbf{(5.4)}$$

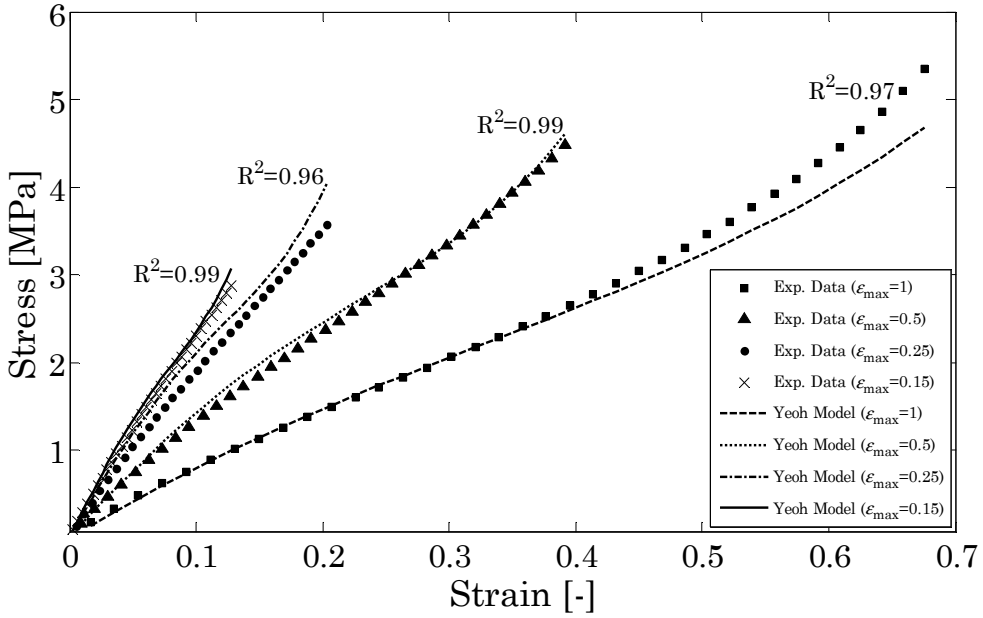

Figure 5.2: Fittings with Yeoh model of experimental data in uniaxial tension.

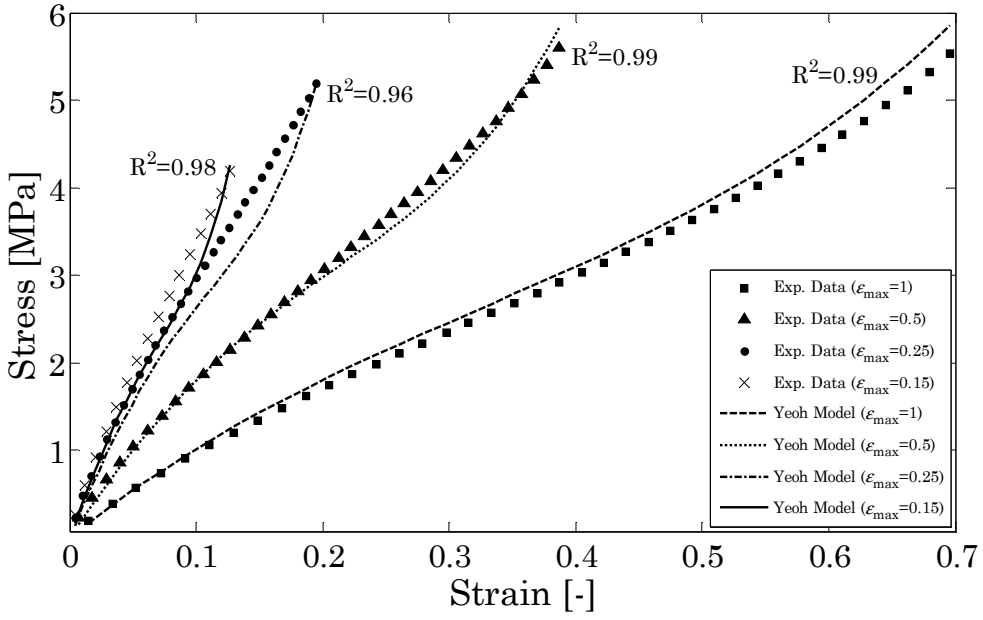

Figure 5.3: Fittings with Yeoh model of experimental data in pure shear.

As the TPU behaviour shows greatly dependence of maximum strain (Figure 4.11), then different coefficients of Yeoh SEDF were obtained depending on the maximum strain. The values of Yeoh SEDF coefficients depending on maximum strain are listed in Table 5.1.

Table 5.1: Values of the fitting constants for Yeoh model depending on the maximum strain.

	$e_{max} = 0.15$	$e_{max} = 0.25$	$e_{max} = 0.5$	$e_{max} = 1$
C_{10}	5.0±0.4	4.3±0.3	2.7±0.1	1.46±0.07
C_{20}	-24±2	-10.4±0.8	-1.68±0.07	-0.071±0.004
C_{30}	280±20	53±4	2.9±0.1	0.151±0.008

5.1.2 Viscoelastic model

The large-strain viscoelasticity theory may be implemented in finite element method using a time domain generalization of the hyperelastic constitutive model. Assuming incompressibility the stress in function of time *t* can be written as

$$\sigma(t) = \sigma_0(t) - \int_{-\infty}^{t} E(t-\tau)\frac{\mathrm{d}e(\tau)}{\mathrm{d}\tau}\mathrm{d}t, \tag{5.5}$$

where τ is the relaxation time, $E(t-\tau)$ is the stress relaxation modulus or function and $\sigma_0(t)$ is the instantaneous stress at time *t* (Ward and Sweeney 2004), which can be replaced by nonlinear elasticity relationship $\sigma_0 = \sigma_0(e)$ to allow the generalization of nonlinear elastic deformations. If the material exhibits a linear viscoelasticity (Figure 4.14), i.e. the dimensionless stress relaxation function is independent of the magnitude of the deformation, the hereditary integral of Equation (5.5) may be replaced by incremental relations (Muhr 2005), which is an advantage from numerical viewpoint. Usually, the replacement is carried out by Prony series expansion of the dimensionless relaxation modulus

$$E(t) = E_0\left(1 - \sum_{i=1}^{N_p} g_i\left(1 - e^{-t/\tau_i}\right)\right), \tag{5.6}$$

where the material coefficients are up to N_p pairs of g_i and τ_i and E_0 is the instantaneous elastic modulus. The number of Prony series terms, i.e. the value of *N*, must be chosen depending on the logarithmic decades of relaxation time, as a rule one term per decade.

Therefore, as the relaxation time was 2500 s., the viscoelastic model

$$E(t) = 2.64 \cdot \left(1 + 0.942e^{-t/1.41} + 0.625e^{-t/33.63} + 0.482e^{-t/779}\right)\ \text{MPa}, \tag{5.7}$$

was obtained by fitting a 3-term Prony series to the relaxation experimental data.

5.2 Finite element analysis of hyperelastic model

In order to validate the proposed hyperelastic models at each maximum strain, firstly it was verified that the TPU behaviour in both deformation states can be simultaneously predicted. Therefore, the experimental tests in uniaxial and in pure shear were simulated by means of the finite element method using the package ABAQUS/Standard 6.8 (Simulia 2009). Implicit finite element method was used because of the hybrid (mixed formulation) elements only can be used with this method. The hybrid elements are recommended for use with hyperelastic materials (Simulia 2009), as they are almost incompressible. The incompressibility constrain is imposed by means of the penalty method when displacement formulation element are used. But the penalty method can sometimes lead to numerical difficulties. Therefore, the hybrid elements allow the imposition of the incompressibility constrain without using the penalty method.

The TPU was characterized using the Yeoh model, Equation (5.4), depending on the maximum strain, i.e. using the different coefficient values of the Table 5.1. In all computational experiments, 8-node hybrid linear brick elements with hourglass control (C3D8RH) were used to model the TPU specimen. The computational experiments were displacement-controlled.

In uniaxial tension, the model consisted of 9640 elements and a fixed displacement along experimental stretching direction was applied to the nodes belonging to one of the widest part of dumbbell specimen. The edge of the other widest part was fixed fully. The areas of these widest parts which were clamped by grips in the experimental test were restricted to permit only displacement in the stretching direction using a boundary condition (Figure 5.4).

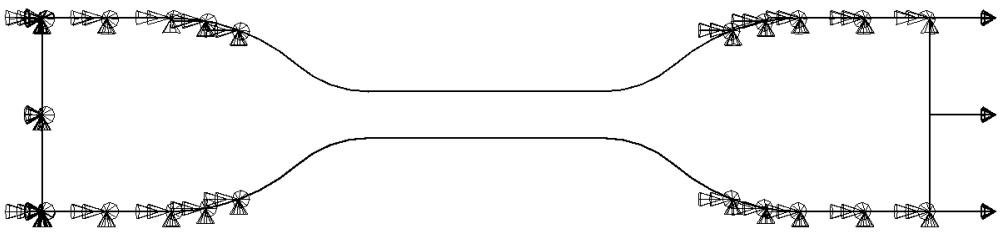

Figure 5.4: FEA model of computational experiments in uniaxial tension.

In pure shear, the model consisted of 12800 elements and a displacement along experimental stretching direction was applied to the nodes belonging to the upper area clamped by grips the movements in others directions were restricted. The nodes of the lower area were fixed fully (Figure 5.5).

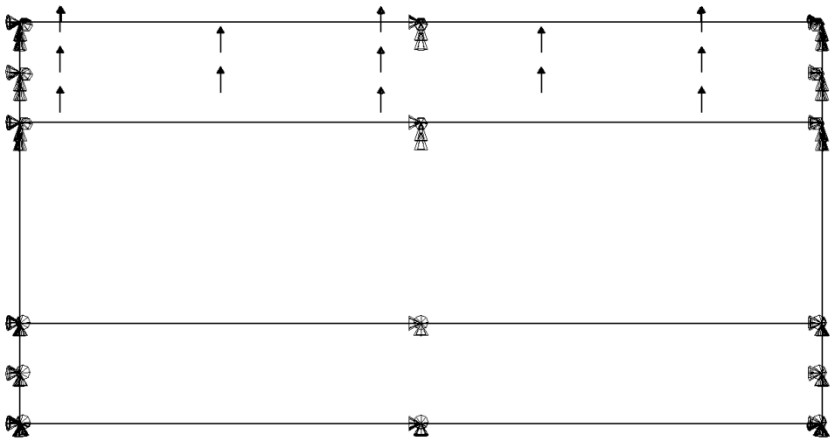

Figure 5.5: FEA model of computational experiments in pure shear.

The nominal stress and strains along the stretching direction of an element in the central section of the specimens were recorded and these values are compared with the experimental data depending on the maximum strain (Figure 5.6). In both deformation states, the numerical results are in good agreement with the experimental data, particularly at the large maximum strains ($e_{\max} = 0.5$ and $e_{\max} = 1$).

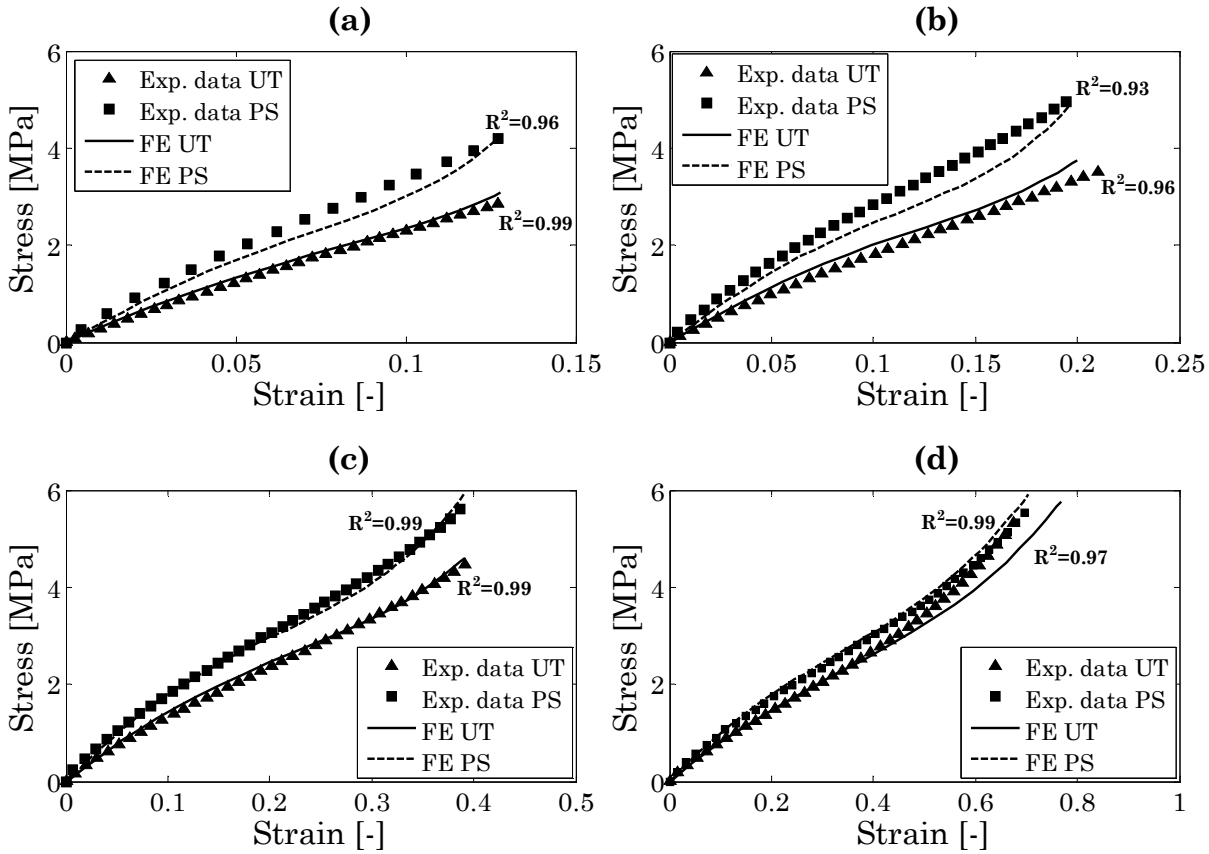

Figure 5.6: Validation of the Yeoh model for hyperelastic behaviour of the TPU in uniaxial tension (UT) and in pure shear (PS): comparisons between experimental data and results of computational experiments at different maximum strains (a) $e_{max} = 0.15$, (b) $e_{max} = 0.25$, (c) $e_{max} = 0.5$ and (d) $e_{max} = 1$.

5.3 Finite element analysis of visco-hyperelastic model

To validate the overlay visco-hyperelastic model, the cycles of experimental tests in uniaxial tension and in pure shear were simulated. The computational experiments were displacement-controlled and time-controlled using 8-node hybrid linear brick elements with hourglass control (C3D8RH), the models (Figure 5.4 and Figure 5.5) were identical that for hyperelastic validation.

Hyperelastic behaviour of TPU was characterized with Yeoh model, Equation (5.4), using different constant values depending on the maximum strain and viscoelastic behaviour using the 3-term Prony series, Equation (5.7). The values of load and displacement along the stretching direction were compared with the experimental data of cycles (Figure 5.7).

At maximum strain below the yield stress, i.e. up to $e_{\max} = 0.5,$ the stress softening and the reduction in hysteresis with the increasing number of cycles is due to a purely time dependent (visco) effect because of the permanent set is neglected (Figure 4.25). Therefore, as expected, the results of calculation experiments are in good agreement with the experimental data for the different cycles, except for the loading of first cycle, in both deformations strains (Figure 5.7 and Figure 5.8).

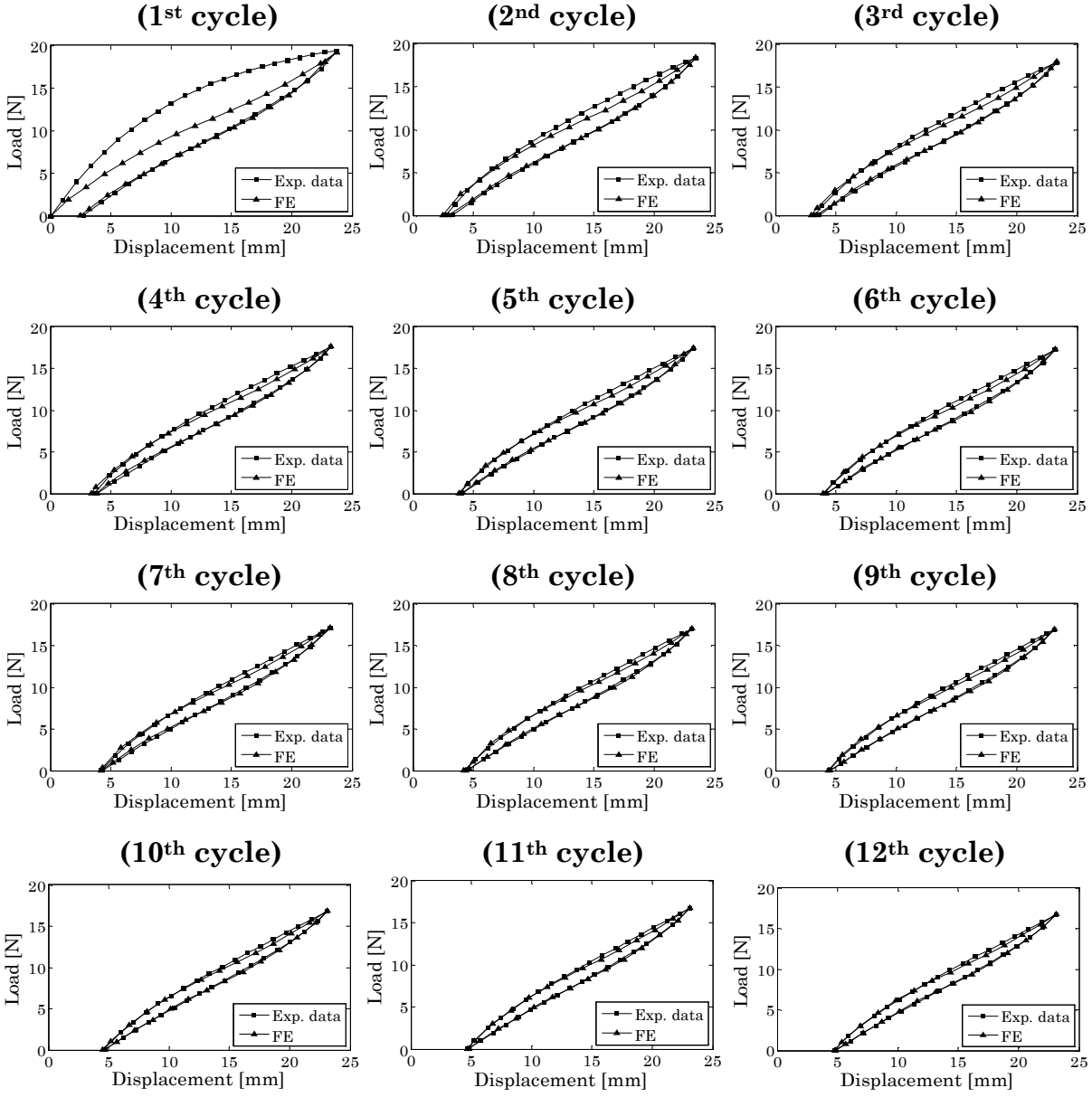

Figure 5.7: Comparison between experimental data and computational results in uniaxial tension from the first to 12th cycle. The maximum strain is $e_{\max} = 0.5$ and the strain-rate is $\dot{e} = 5\times10^{-3}$ s^{-1}.

The loading of first cycle is the virgin or non-preconditioned behaviour of an elastomer and this behaviour is totally different to the subsequent cycles (see Section 4.8.4). Therefore, in view of the computational results, it should be pointed out that this virgin behaviour of the TPU can not be predicted by the proposed visco-hyperelastic model. Moreover, it bears in mind that the hyperelastic model of the TPU was developed without considering this virgin behaviour (see Section 4.4.1).

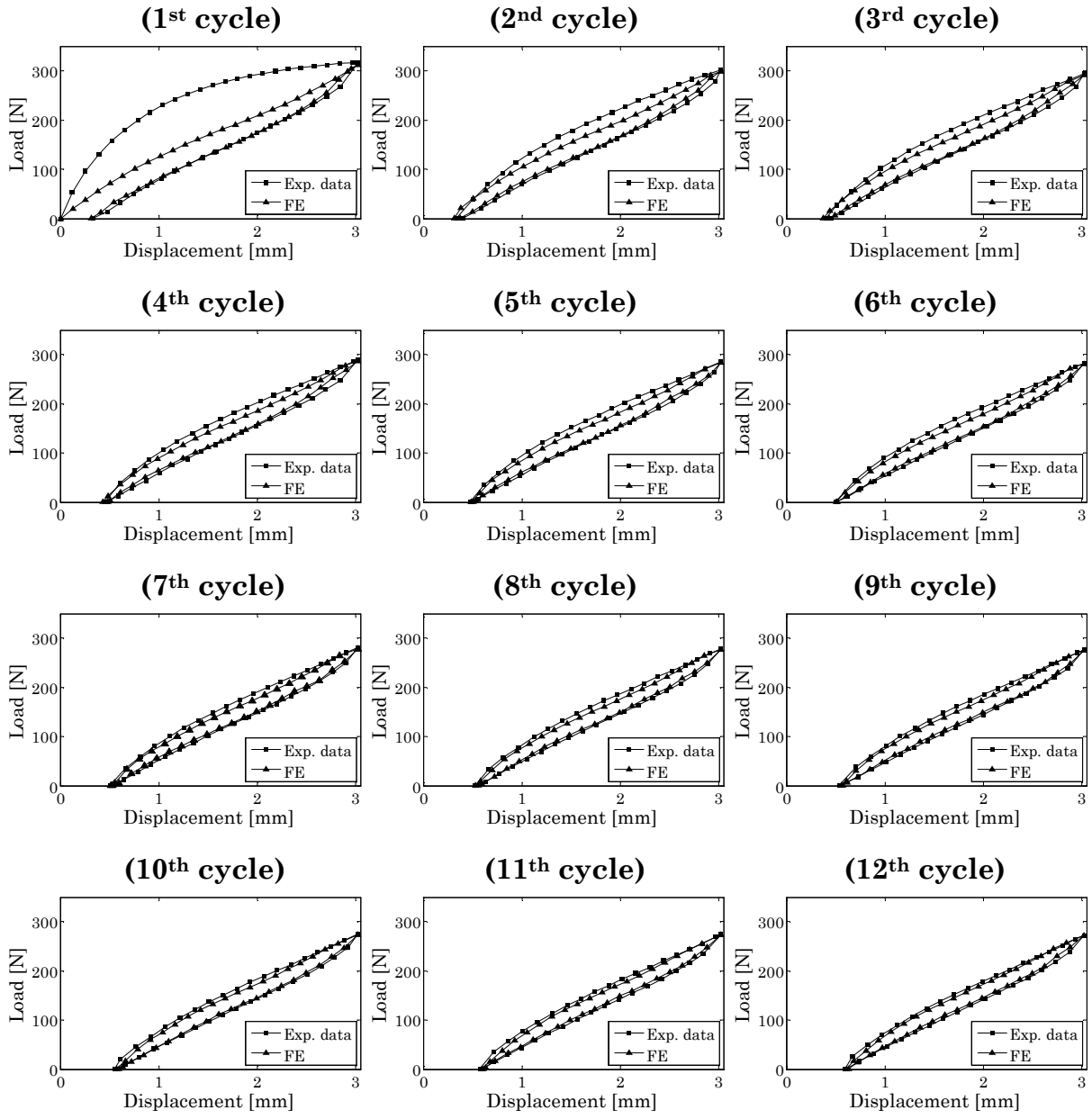

Figure 5.8: Comparison between experimental data and computational results in pure shear from the first to 12th cycle. The maximum strain is $e_{max} = 0.5$ and the strain-rate is $\dot{e} = 7\times10^{-3}$ s^{-1}.

It should also be pointed out that the accuracy in predicting the experimental response is better in the unloading stage, which agrees with the results of Marvalova (2007) using carbon-black filled rubbers.

Beyond the yield stress (at maximum strain $e_{max}=1$), the computational results agree with the experimental data for the different cycles (Figure 5.9 and Figure 5.10), except also for the loading of first cycle. But it can be noted that the computational results agree better in uniaxial tension (Figure 5.9) than in pure shear (Figure 5.10). Consequently, the visco-hyperelastic model proposed can be predicted accurately the behaviour of the TPU at maximum strain $e_{max}=1$, in spite of being beyond the yield stress. It may be due to the permanent set at maximum strain $e_{max}=1$ is still small, around 10%.

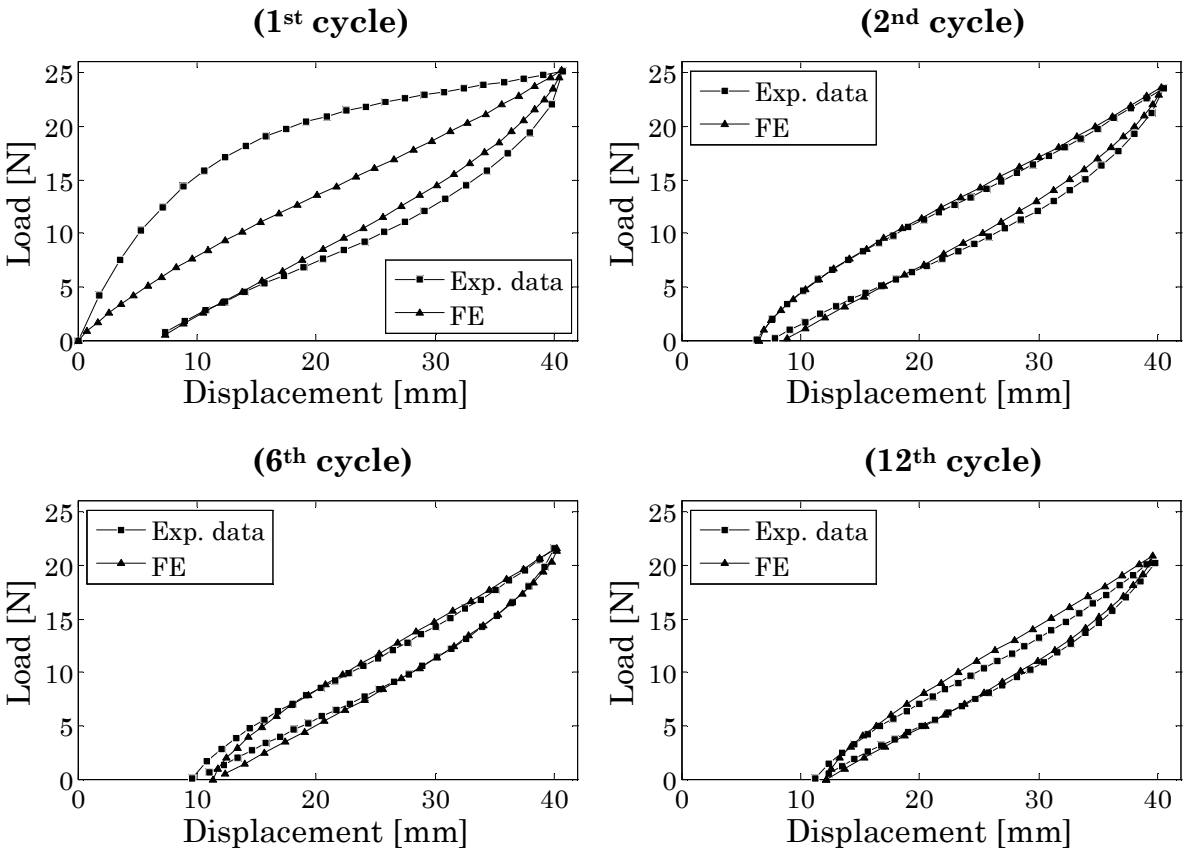

Figure 5.9: Comparison between experimental data and computational results in uniaxial tension of 1st cycle, 2nd cycle, 6th cycle and 12th cycle. The maximum strain is $e_{max}=1$ and the strain-rate is $\dot{e}=5\times10^{-3}$ s^{-1}.

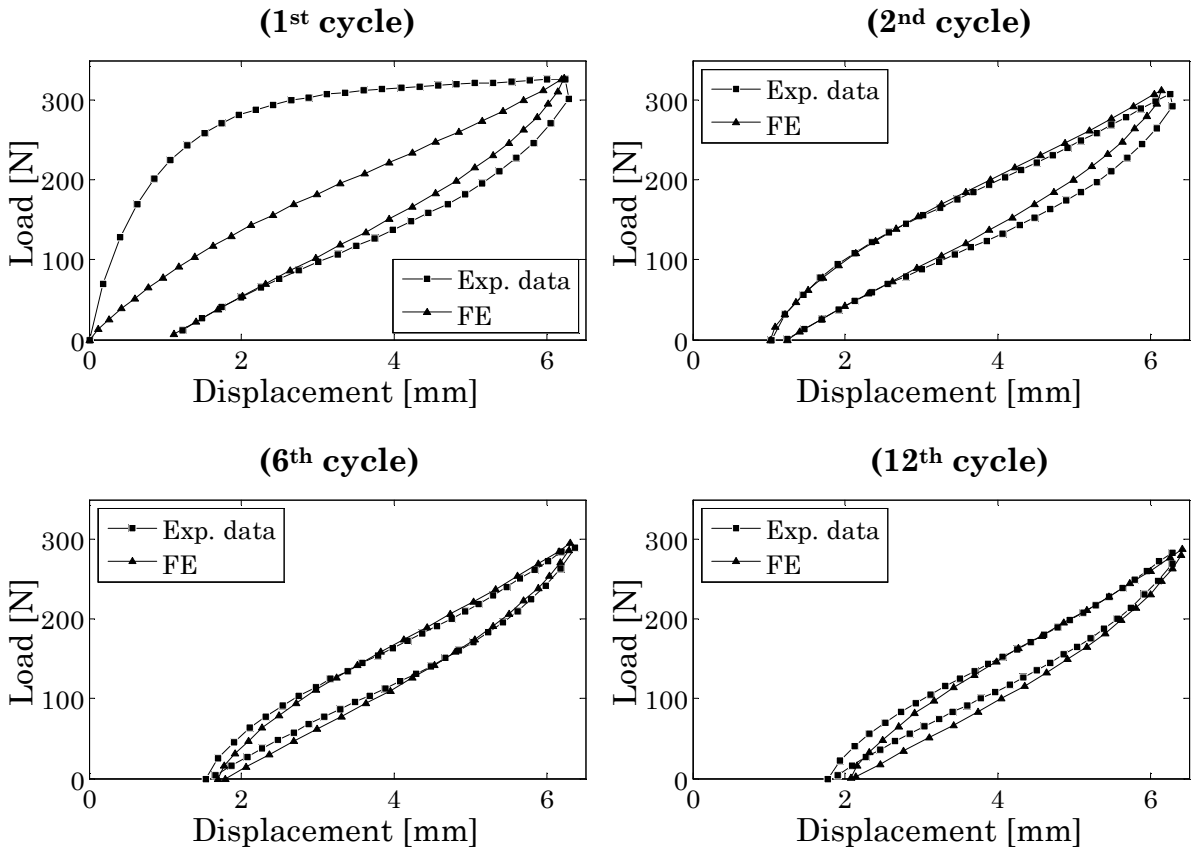

Figure 5.10: Comparison between experimental data and computational results in pure shear of 1st cycle, 2nd cycle, 6th cycle and 12th cycle. The maximum strain is $e_{max} = 1$ and strain-rate is $\dot{e} = 7 \times 10^{-3}$ s^{-1}.

Furthermore, the agreement between experimental data and computational results is slightly worse in predicting the TPU behaviour with increasing strain-rate (Figure 5.11), which was also observed by Marvalova (2007) with carbon-black filled rubbers. This fact is more evident in pure shear (Figure 5.11c and Figure 5.11d) than in uniaxial tension (Figure 5.11a and Figure 5.11b). The reasons for this worsening in pure shear are unclear, especially considering that the permanent set is smaller at higher strain-rates than at lowest strain-rate (Figure 4.26).

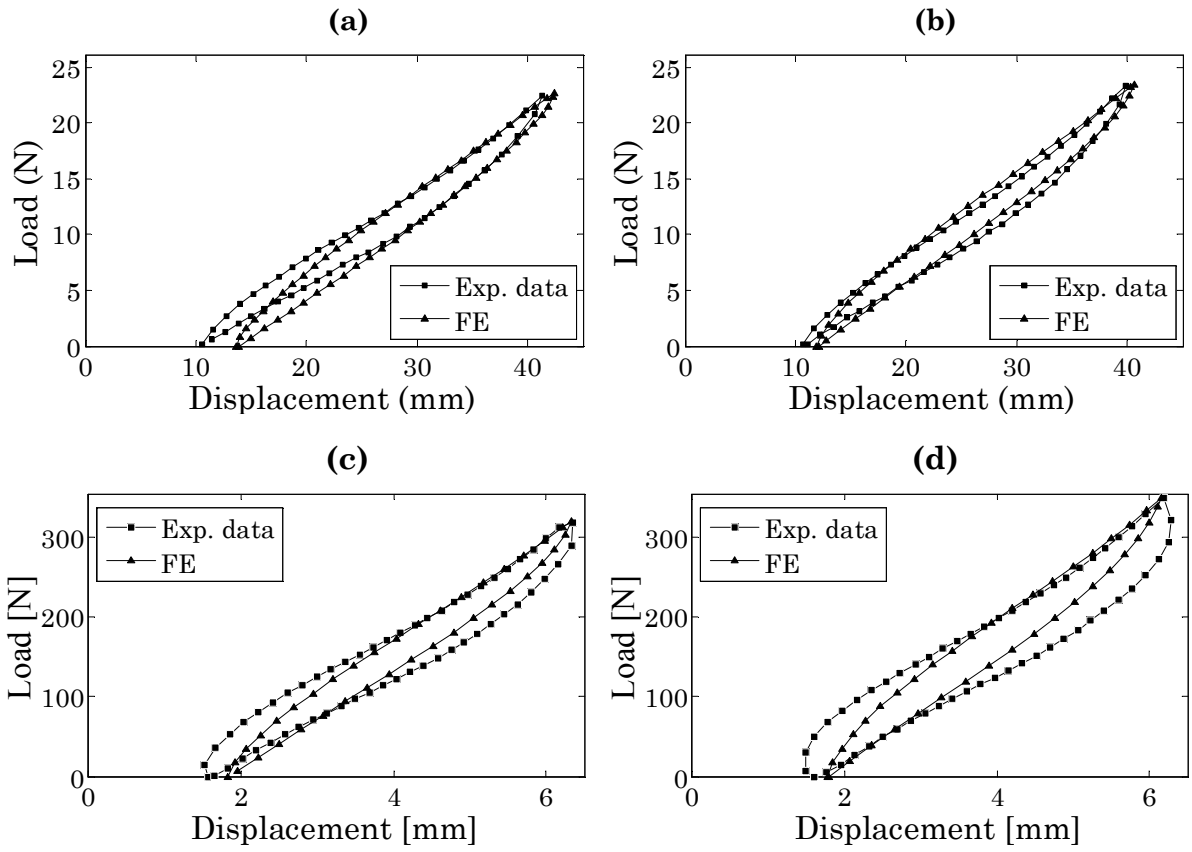

Figure 5.11: Comparison between experimental data and computational results of 12th cycle. The maximum strain is $e_{max} = 1$ and the strain-rates are (a) $\dot{e} = 2.5 \times 10^{-2}$ s^{-1} and (b) $\dot{e} = 5 \times 10^{-2}$ s^{-1} in uniaxial tension and (c) $\dot{e} = 3.5 \times 10^{-2}$ s^{-1} and (d) $\dot{e} = 7 \times 10^{-2}$ s^{-1} in pure shear

5.4 Hyperelastic model in inhomogeneous deformation state

In view of the results, the hyperelastic model proposed predicts accurately the behaviour of the TPU in homogeneous deformation states (uniaxial tension and pure shear). However, in work conditions the TPU usually is in inhomogeneous deformation states.

Therefore, in order to validate the hyperelastic model in inhomogeneous deformation state, the experimental data that uses digital image correlation to determine strains in inhomogeneous conditions are compared with results of computational experiments.

5.4.1 Experimental tests in inhomogeneous deformation state

The TPU was tested using rectangular samples (80x70 mm) with a hole (Ø=16 mm) in the middle to provide an inhomogeneous deformation state. The distance between grips was 40 mm. For preconditioning the material, the samples were subjected to cyclic displacements

of 20 and 40 mm, thus reference nominal strains $e_{\text{ref}} = 0.5$ and $e_{\text{ref}} = 1$ respectively were considered. The tests were carried out at strain-rate $\dot{e} = 6.5 \times 10^{-3}$ s^{-1} and the specimens were stretched in the direction of extrusion, i.e. on melt flow direction (MD).

A commercially available optical strain measurement system[16], that utilizes two digital cameras and the digital image correlation (DIC) methodology (Figure 5.12), was used to assess the distribution of strains. The effective strain variations according to von Mises

$$e_{vm} = \sqrt{\frac{2}{3}\left(e_1^2 + e_2^2 + e_3^2\right)}, \tag{5.8}$$

of the last cycle were recorded during testing. The e_i are the principal strains.

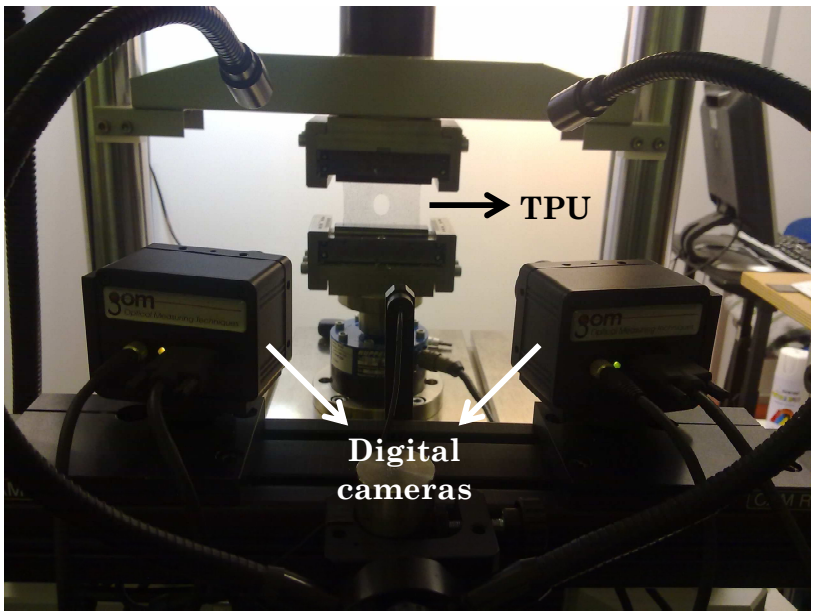

Figure 5.12: Experimental set-up of inhomogeneous tests.

5.4.2 Finite element analysis

The computational experiments in inhomogeneous deformation state were carried out at two different reference strains, $e_{\text{ref}} = 0.5$ corresponding to a displacement of 20 mm and $e_{\text{ref}} = 1$ to a one of 40 mm. The models consisted of 35190 and 42669 elements, respectively. The hyperelastic behaviour of TPU was characterized with the constants of Yeoh model (see Table 5.1) at maximum strains of 0.5 and 1 depending on the reference strain. The hyperelastic model was used because of the distributions of strains were recorded for preconditioned material.

[16]ARAMIS of GOM GmbH, Braunschweig (Germany)

The comparisons between the experimental data recorded with the DIC method and the computational results are shown in Figure 5.13 and in Figure 5.14, at $e_{\text{ref}} = 0.5$ and at $e_{\text{ref}} = 1$, respectively. Geometrically, the deformed shape of experimental samples agrees with the finite element shape at both reference strains. Furthermore, on an overall view, the optical distribution of von Mises strains shows a reasonable correlation with the finite element distribution.

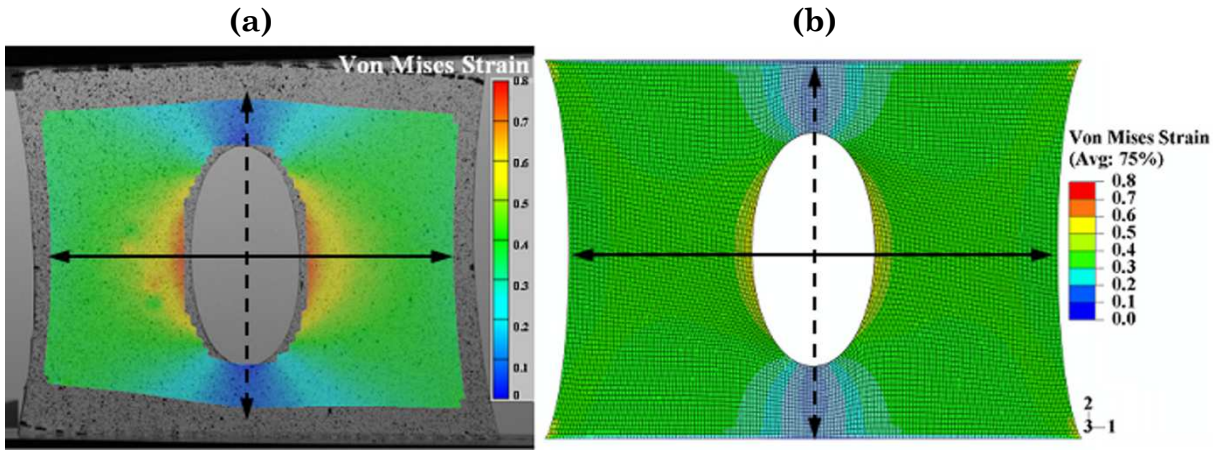

Figure 5.13: Comparison of the von Mises strains between (a) experimental measurements and (b) computational results, at reference strain $e_{\text{ref}} = 0.5$.

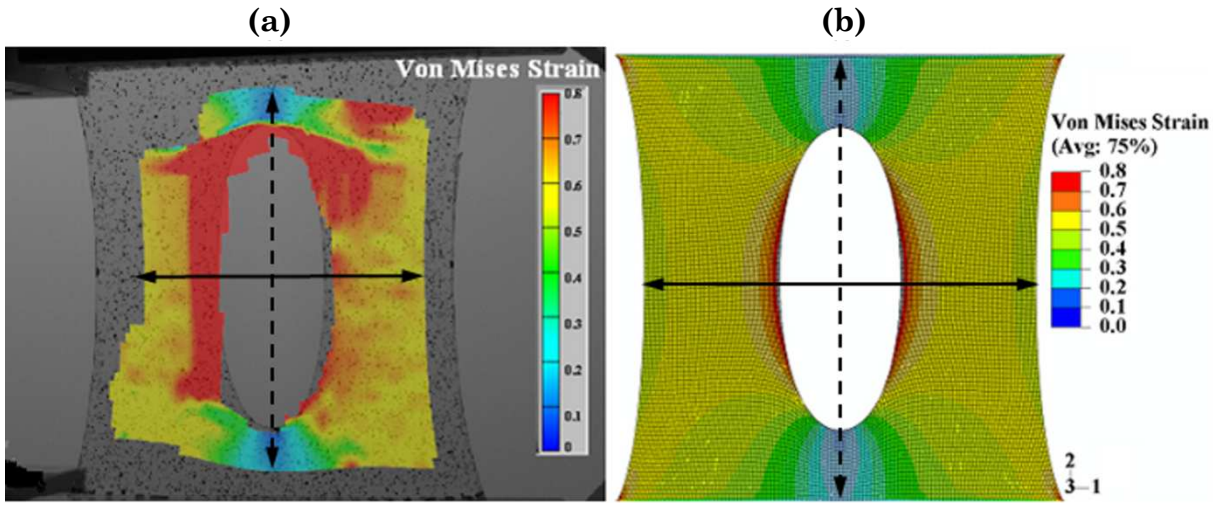

Figure 5.14: Comparison of the von Mises strains between (a) experimental measurements and (b) computational results, at reference strain $e_{\text{ref}} = 1$.

In order to compare locally optical and finite element distributions of strains, longitudinal and vertical sections, continuum and dashed line respectively (see Figure 5.13 and Figure 5.14) were chosen.

The point to point values of von Mises strains across the longitudinal section show an acceptable agreement between computational results using model in homogeneous strain states (for graphical representation this model is labelled as Homog.-model) and experimental data (Figure 5.15), especially at reference strain $e_{\text{ref}} = 0.5$.

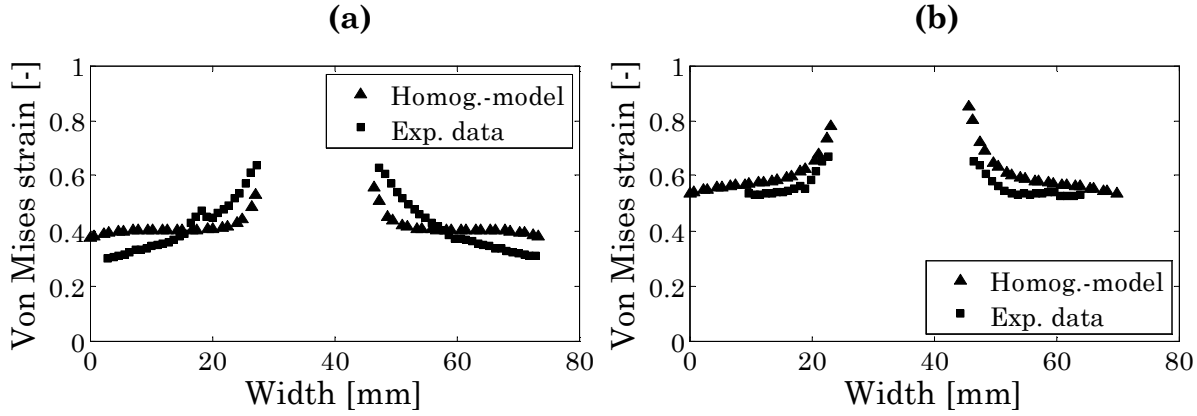

Figure 5.15: Comparison between point to point DIC measurements and computational results across longitudinal section. The reference strains are (a) $e_{\text{ref}} = 0.5$ and (b) $e_{\text{ref}} = 1$.

However, the experimental point to point values of von Mises strains across the vertical section are significantly disagreed with computational results (Figure 5.16). This disagreement can be produced due to the material points of vertical section are subjected to strains below from the maximum strains that were taken into account to carry out the computational experiments in inhomogeneous strain states.

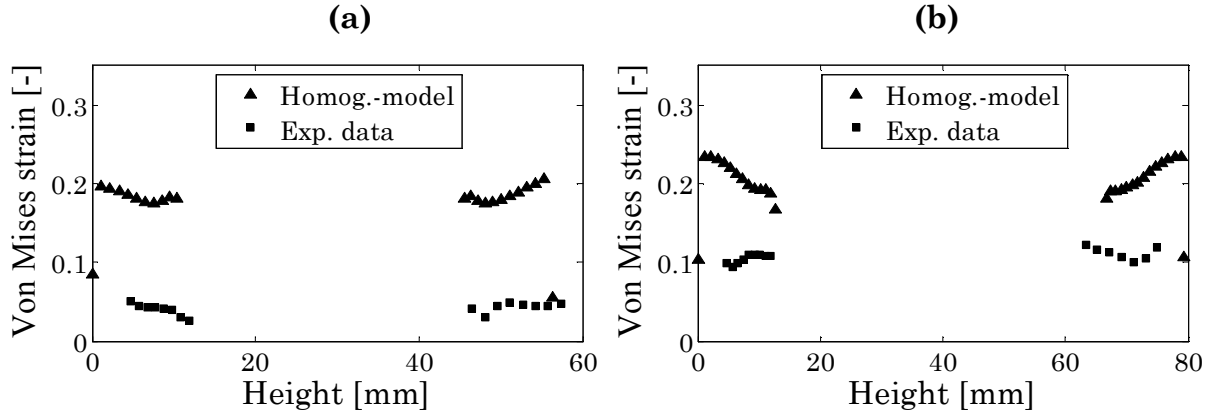

Figure 5.16: Comparison between point to point DIC measurements and computational results across vertical section. The reference strains are (a) $e_{\text{ref}} = 0.5$ and (b) $e_{\text{ref}} = 1$.

This effect is also shown when comparing the experimental data of load-deflection with the computational results (Figure 5.17). When the reference strain $e_{\text{ref}} = 0.5$, the numerical results are acceptably agreed with experimental data because most of material points are subjected to a maximum principal strain interval between 0.35 and 0.45 (values from DIC strain measurements) whose strains are comparable to the maximum strain $e_{\max} = 0.5$ of the TPU model used in the computational experiment. However, when the reference strain $e_{\text{ref}} = 1$, most of material points are subjected to maximum principal strains between 0.55 and 0.7 (values from DIC strain measurements) clearly below maximum strain $e_{\max} = 1$ of the TPU model. Therefore the numerical results are considerably disagreed with the experimental data. However the numerical results show a decrease of TPU stiffness with increasing maximum strain which is consistent with the behaviour shown in Figure 5.2 and Figure 5.3.

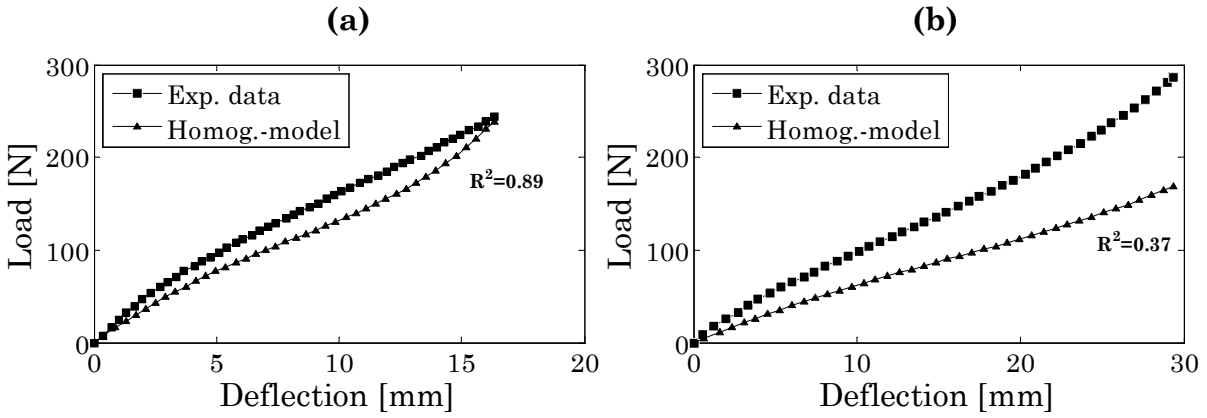

Figure 5.17: Comparison between experimental data and computational results in inhomogeneous deformation state. The reference strains are (a) $e_{\text{ref}} = 0.5$ and (b) $e_{\text{ref}} = 1$.

It can be noted from the above results that the phenomenological behaviour of the TPU depends on the maximum strain, especially on the maximum strain ever experienced. Therefore, the hyperelastic models of Yeoh proposed can be used only at specific maximum strains. In the following section, this aspect is analyzed for improving the hyperelastic model of preconditioned TPU considering the deformation history.

5.5 Hyperelastic model with deformation history

As discussed above, the hyperelastic model depends on the deformation history, i.e. on the maximum strain ever experienced. In this section, this aspect is incorporated into the hyperelastic model.

Firstly, it is discussed how to incorporate mathematically this dependence with the maximum strain ever experienced into the hyperelastic model by means of fitting functions for the model constants. Secondly, a FEA-based technique is proposed to update the behaviour of the TPU depending on the maximum strain. Finally, is analyzed the ability of the material model with deformation history proposed to predict the behaviour of the TPU in inhomogeneous deformation states using computational experiments.

5.5.1 Dependence with maximum strain ever experienced

As shown in Section 5.1.1, the constants of the Yeoh model present different values depending on the maximum strain of experimental test (see Table 5.1). Therefore, whether the coefficients are introduce into the hyperelastic model as a function depending on the maximum strain, then the model at different maximum strains can be obtained.

Parameter of fitting functions

Actually, the constants of hyperelastic model depend on the major strain, i.e. the largest value of the principal strains. This scalar parameter of strain is useful in homogeneous deformation states, but it does not represent the deformation accurately when the material is subjected to complex loads. Therefore, different scalar parameters of strains were considered to fit the strain history.

Besdo and Ihlemann (2003) proposed an invariant

$$e_{\text{fit}} = \max\left\{\left|e_1 - e_2\right|, \left|e_2 - e_3\right|, \left|e_3 - e_1\right|\right\}, \tag{5.9}$$

which represents the maximum difference of the principal strains, to define the scalar parameter. But, either this invariant or the first invariant of the right Cauchy-Green tensor, Equation (2.11), were unsuccessful results to fit the strain history of the TPU.

Murh (2005) said that the "norm" defined as

$$\|\mathbf{T}\| \equiv \sqrt{\mathrm{tr}\left(\mathbf{T}^2\right)}, \tag{5.10}$$

is quite often used as a scalar "magnitude" of a tensor $\mathbf{T}$, where $\mathrm{tr}\left(\mathbf{T}\right) = t_{ii} \equiv t_{11} + t_{22} + t_{33}$ Therefore the "norm" of the deformation strain measures tensor

$$e_{\mathrm{fit}} = \sqrt{e_1^2 + e_2^2 + e_3^2}, \tag{5.11}$$

was probed as scalar parameter to fit the strain history of the TPU. Using this parameter, the results and fitting functions obtained were more successful.

Fitting functions for constants of hyperelastic model

The values of coefficients covers the range of maximum strains between $e_{\max} = 0.15$ and $e_{\max} = 1$. But the range of small strains ($e_{\max} < 0.15$) is not cover, therefore experimental tests in uniaxial tension were carried out at maximum strain $e_{\max} = 2\times10^{-2}$, $e_{\max} = 5\times10^{-2}$ and $e_{\max} = 0.1$. These experimental tests gave information about the possible values of the coefficients in the range of small strains. But it bears in mind that the model at small strains is more close to neo-Hookean, Equation (2.15), then the first coefficient C_{10} control the hyperelastic model.

The fitting functions (Figure 5.18) were obtained using the values of coefficients in Table 5.1 and the values obtained at small strains ($e_{\max} < 0.15$) in function of the strain parameter e_{fit}, Equation (5.11). The coefficient C_{10} was fitted by an exponential function in all the ranges of the strain parameter. The others coefficients, C_{20} and C_{30}, were fitted by parts taking into account that their values are not significant in the range of small strains. Beyond $e_{\mathrm{fit}} = 0.15$, they were fitted by means of an exponential function and a potential function, respectively. Below $e_{\mathrm{fit}} = 0.15$, were use to fit them a polynomial and an exponential function. For better graphical representation, the later functions, as well as the points at small strains in the case of C_{30}, are not included in Figure 5.18.

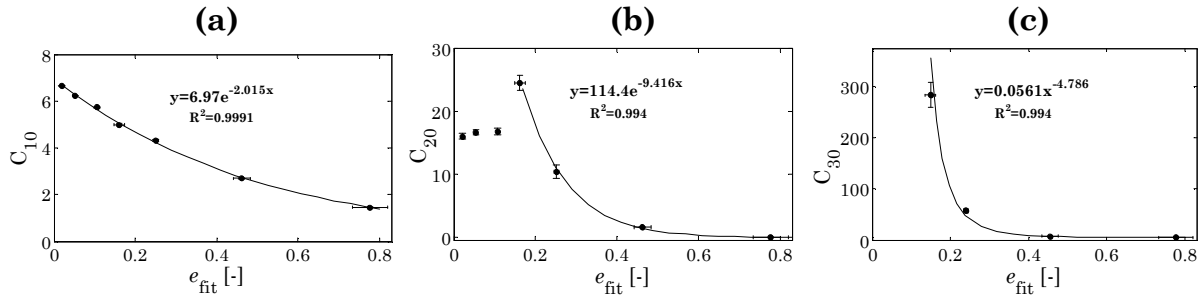

Figure 5.18: Fitting functions for the constants, (a) C_{10} (b) C_{20} and (c) C_{30} of the Yeoh model.

Using the fitting functions of the Yeoh SEDF's coefficients, the hyperelastic SEDF of the TPU can be written as

$$W(I_1, e_{\text{fit}}) = \sum_{i=1}^{3} f_i(e_{\text{fit}})(I_1 - 3)^i, \tag{5.12}$$

where f_i are the fitting functions.

5.5.2 FEA-based technique: methodology to implement the strain history

The fitting functions of the coefficients enable that the Yeoh model can be updated using the strain history of the TPU. To update the Yeoh model in FE code, actually the coefficients of the hyperelastic model, it is used an iterative method that allows updating the maximum strains ever experienced of each element. This iterative method is sketched in Figure 5.19.

To begin the iterative process, the initial values of the coefficients are taken from the hyperelastic model obtained (Table 5.1) to a given maximum strain. Therefore, all the elements are modelled using equal values of the coefficients. These values of coefficients are introduced in FE calculus by means of the UHYPER subroutine (Simulia 2009). This subroutine is used to define the SEDF for hyperelastic materials. After FE calculus, the strains of the elements are obtained, and then the scalar strain parameter e_{fit} is calculated for each element. Using these values of the scalar strain parameter, the values of the coefficients are updated. The new values are introduced again in FE calculus using the UHYPER subroutine. This iterative process is controlled by means of a convergence criteria, which consist of the maximum difference between the strains of the current iteration and the previous is less than a value. The iterative method was programmed using Matlab.

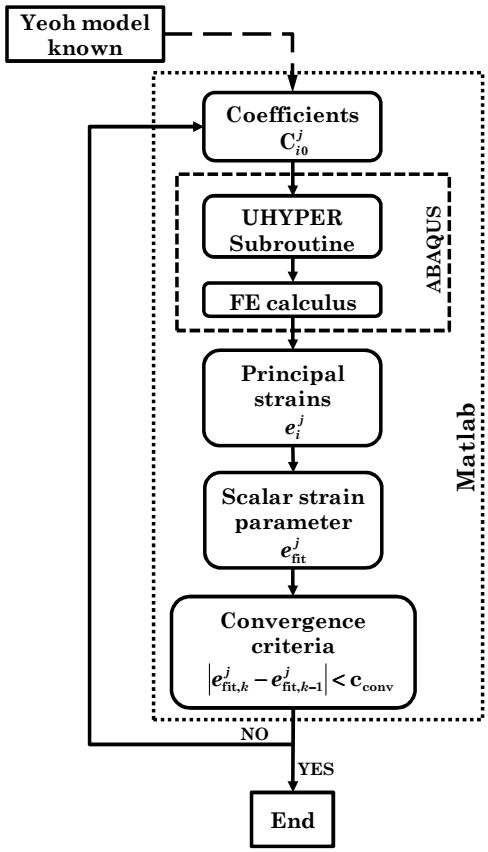

Figure 5.19: Methodology to implement the strain history for element *j* in iteration *k*.

5.5.3 Validation of material model with deformation history

Using the FEA based technique described above to implement the hyperelastic model considering deformation history (for graphical representations this model is labelled as DH-model), the computational experiments in inhomogeneous deformation state (Section 5.4.2) were carried out again.

From Figure 5.20, it should be noted that the experimental measurements of the point to point values of von Mises strains across the longitudinal section agree better with the computational results using the material model to take into account the history strain than not use it. This fact is more evident for the data across the vertical section (Figure 5.21). The improvement in agreement is more clear at reference strain $e_{ref} = 1$ than at $e_{ref} = 0.5$ for both sections.

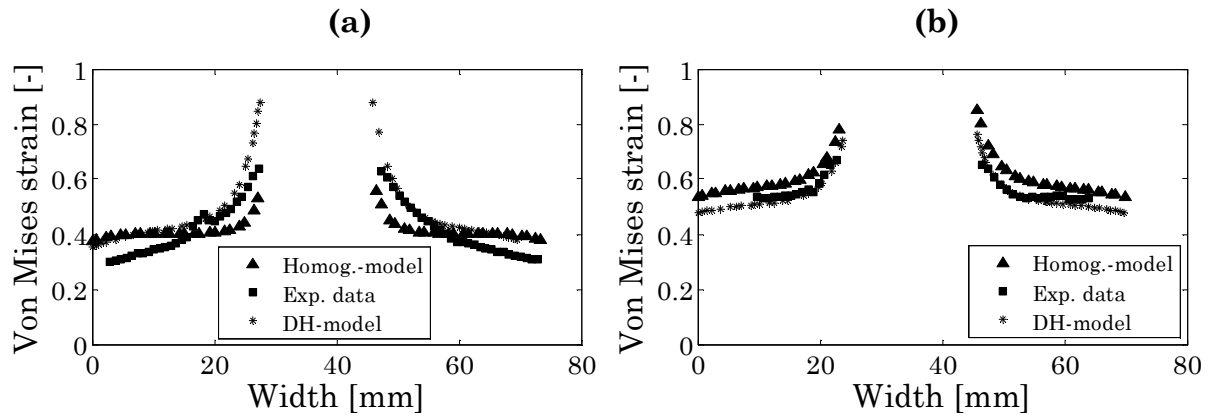

Figure 5.20: Comparison between point to point DIC measurements and computational results considering and not considering the strain history across longitudinal section. The reference strains are (a) $e_{ref} = 0.5$ and (b) $e_{ref} = 1$.

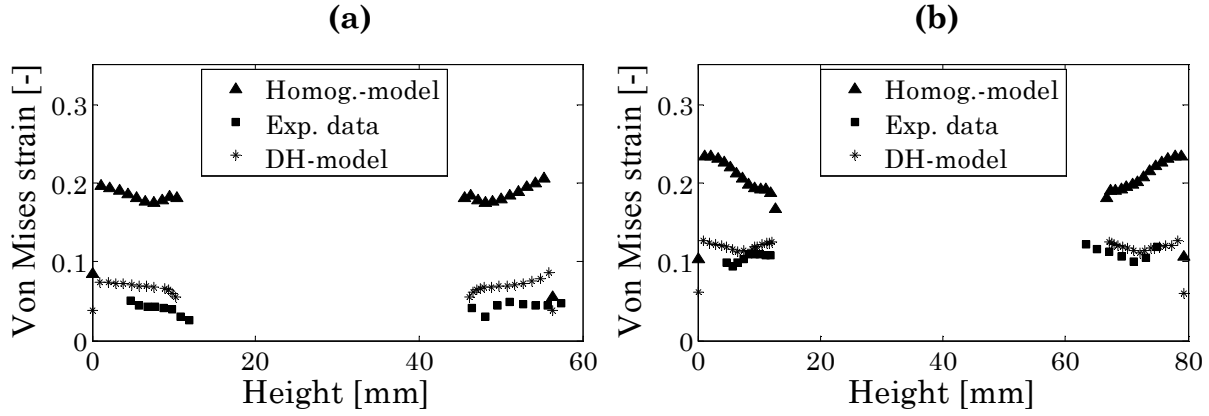

Figure 5.21: Comparison between point to point DIC measurements and computational results considering and not considering the strain history across longitudinal section. The reference strains are (a) $e_{ref} = 0.5$ and (b) $e_{ref} = 1$.

Comparing the Figure 5.17 and Figure 5.22, the hyperelastic model with strain history show clearly the improvement in predicting the response of the TPU in inhomogeneous deformation states, specially at reference strain $e_{ref} = 1$.

Therefore, in view of the results, it may be pointed out that the material model considering strain history predicts better the behaviour of the preconditioned TPU than the individual models of Yeoh which do not take into account that the mechanical behaviour of the TPU is modified by the previous deformations undergone by the material.

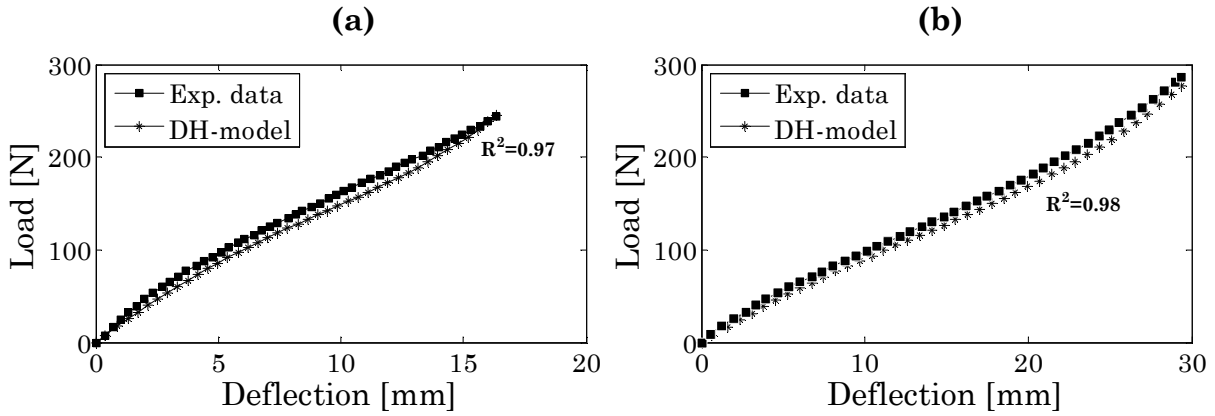

Figure 5.22: Comparison between experimental data and computational results considering the strain history in inhomogeneous deformation state. The reference strains are (a) $e_{ref} = 0.5$ and (b) $e_{ref} = 1$.

5.6 Conclusions

The behaviour of the TPU was modelled using an overlay visco-hyperelastic model. The nonlinear strain-stress response (hyperelastic behaviour) of the TPU was modelled using Yeoh SEDF, Equation (5.4). The linear viscoelastic behaviour of the TPU was modelled by means of the Prony series, Equation (5.7).

The overlay visco-hyperelastic model predicts accurately the visco-hyperelastic behaviour of the TPU in homogeneous deformation states, as uniaxial tension and pure shear. As this model depends on the maximum strain ever experienced by the TPU, the capacity of prediction of the model is greatly reduced in inhomogeneous deformation states due to the maximum deformation ever experienced is different locally, i.e. by each material point.

The maximum strain ever experienced by each material point was considered by the proposed material model with deformation history, Equation (5.12). This model exhibits parameters that are interpolation functions of the parameters of models in homogeneous strain states. These functions were obtained using a scalar that can be defined as the "norm" of the deformation strain measures tensor, see Equation (5.11).

The material model with strain history is implemented into numerical calculus using a FEA based technique that was developed for this purpose. This technique basically consists of an iterative process to update the strain ever experienced by the material. Using this material model with deformation history, the response of the TPU in inhomogeneous strain states was modelled by finite element method obtaining successful results, even at locally level.

6 NORMAL CONTACT: INDENTATION

"No problem is too small or too trivial

if we can really do something about it"

Richard Feynman

In order to study the contact behaviour of extruded TPU, it is divided in two problems, normal contact (or indentation) and tangential contact with friction. The normal contact on elastomers is investigated in this chapter and the tangential contact in the Chapter 7.

Firstly, the normal contact is analyzed experimentally using indentation tests (Section 6.2). The experimental contact behaviour is discussed regarding compressive force (Section 6.3), contact area (Section 6.4) and contact pressures (Section 6.5).

Secondly, the previously proposed material model with deformation history is used to predict the normal contact behaviour of the TPU (Section 6.6) and the results of computational experiments are validated using the experimental results.

6.1 Introduction of normal contact on elastomers

The normal contact on elastomers may involve different configurations, e.g. a rigid body (metal or plastic) contacting elastomers, elastomer against elastomer self-contact, etc. With the purpose of adjusting the test rig to the conditioned shape of the TPU by extrusion, the case of a rigid body coming into normal contact with an elastomer surface is considered in this study. Specifically, the geometry of the test rig is that of a spherical indenter (rigid body) with a TPU sheet.

The analytical solution for the normal contact of two spheres problem at small strains was proposed firstly by Hertz (1882). From this general solution, it is possible to derive the solution to the normal contact (or indentation) of a rigid ball into a semi-infinite elastic body. This simplification is derived assuming that the indenter is infinitely stiff, i.e. a rigid body,

and that the flat surface is equivalent to a sphere with an infinite radius. Therefore, assuming an incompressible elastomer, i.e. Poisson's ratio $\nu = 0.5$, the relationship between the depth of indentation x and the compressive normal load F_N is

$$x = \left(\frac{9}{256}\right)^{1/3} \frac{F_N^{2/3}}{R^{1/3} G^{2/3}}, \tag{6.1}$$

where R is the radius of indenter and G is the shear modulus of elastomer (Bhushan 2001). From Equation (2.2), it is derived for incompressible materials that the shear and tensile moduli are related by $E = 3G$ (Ward and Sweeney 2004). Thus, the Equation (6.1) may be rewritten as

$$F_N = \left(\frac{16}{9}\right) x^{1.5} R^{0.5} E. \tag{6.2}$$

If the indentation was small, Gent (1958) showed that Equation (6.2) was appropriate to predict the normal contact behaviour when he was discussing the relationship between the measure of hardness and the tensile modulus for elastomers. However, previously Scott (1948) had derived the relationship

$$F_N = 1.91 x^{1.35} R^{0.65} E, \tag{6.3}$$

from the investigation of normal contact (or indentation) behaviour of vulcanized rubbers using two different indenters.

Yeoh (1984) suggested that the disagreement between the Equations (6.2) and (6.3) comes from the difficulty in measuring experimentally the tensile modulus, which is increased by the non-linear behaviour of elastomers. Moreover, it can be also noted that the tensile modulus is measured in compression by Gent whereas it was determined in tension by Scott.

Using the Hertz theory, it can be predicted, at small depths of indentation x, the radius of contact area a between the indenter of radius R and the flat sheet of elastomer, as

$$a = (Rx)^{1/2}. \tag{6.4}$$

This Equation (6.4) lays down that the contact area A_c varies nonlinear with the normal force $A_c \propto F_N^{2/3}$, which disagrees with the contact area exactly proportional to the normal load proposed for elastomers by Persson (2001) that considers surface roughness at any length scale.

The Hertz theory, that is described above, should be considered for semi-infinite sheet of elastomers, i.e. the thickness of the sheets should be large enough compared with the radius of the contact area to avoid complications arising due to the rigid support underneath the elastomer sheet being felt. Busfield and Thomas (1999) showed for rubbers that the ratio

of thickness to the radius of circular contact must be at least 20:1. With a ratio being less than this, a greater compressive normal force at a given depth of indentation is experienced than that calculated using Hertz theory (Waters 1965).

The problem about the enough thickness was tackled by Tangorra (1966) using expressions to represent the effect of the elastomer thickness δ on the load-depth of indentation relationship. The solution consisted of a factor that multiplies the compressive normal load F_N^{Hz} predicted by the Hertz theory, thus

$$F_N = F_N^{Hz} e^{(c_1/x-\delta)}, \tag{6.5}$$

where c_1 is an empirical constant dependent on the indenter radius. On the other hand, Waters (1965) pointed out that the linear dimensions of the stress field scales with the radius of the contact area a and proposed the relationship

$$F_N = F_N^{Hz}\left(1 - e^{-c_2\delta/a_\delta}\right), \tag{6.6}$$

where c_2 is an empirical constant deduced and a_δ is the radius of contact area when the normal contact involves a rubber sheet of thickness δ. Busfield and Thomas (1999) proposed a modification of the Equation (6.6)

$$F_N = F_N^{Hz}\left(1 - \frac{c_3\delta}{a_\delta}\right), \tag{6.7}$$

that led a better fit to the finite element results for small depths of indentation.

Finally, when the contact test rig consist of a rigid sphere on a flat incompressible material (elastomer) with a tensile modulus E, it may be deduced from the Hertz theory that the pressure distribution at a distance r onto the radius of contact area is

$$p(r) = \frac{8}{3\pi R} E\left(a^2 - r^2\right)^{1/2}. \tag{6.8}$$

6.2 Experimental tests for normal contact behaviour

The behaviour of the TPU on normal contact was analyzed using indentation tests. The geometry of the contact test rig was a spherical indenter into a sheet of the TPU. The spherical indenter consisted of a chrome steel ball[17] of radius R = 3.000±0.001 mm and of a holder with a conical hollow to set the ball (Figure 6.1). The holder tries to ensure that the indentation force is applied in the normal direction to the surface of the TPU sheet.

[17]AISI 52100

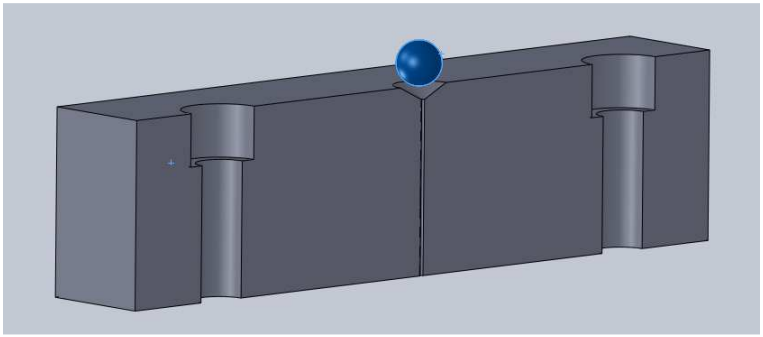

Figure 6.1: Holder to set the steel balls used for experimental tests of indentation.

The TPU sheets of 2 mm thickness (reference value) processed by extrusion (Section 4.1) were chosen to study the normal contact behaviour of the TPU because of the sheets of 0.6 mm thickness were very thin. Therefore, the TPU sheets of thickness 2 mm were cut into rectangular specimens (46x30 mm).

The indention tests of the TPU were carried out using a universal testing machine[18] equipped with a 1 kN load cell. The test was displacement-controlled at low rate of transverse, 1 mm/min, to be at quasi-static conditions. The TPU specimens were fixed at the bottom of the testing machine using double side tape to avoid the movement during the measurements. The friction between steel ball and the TPU was decreased by coating the TPU surface with a thin layer of talcum powder.

To discuss the effect of TPU thickness on normal contact, one, two and three TPU specimens were stacked together. Thus, three different reference thicknesses $\delta_{ref} = 2$ mm, $\delta_{ref} = 4$ mm and $\delta_{ref} = 6$ mm were tested. Moreover, the influence of the depth of indentation was also analyzed. Therefore, the indention tests were carried out to 0.5, 1.1 and 1.7 mm depths of indentation; in addition 0.8 and 1.4 mm depths were also tested only with reference thickness $\delta_{ref} = 2$ mm, i.e. one specimen stacked.

In order to preconditioned the TPU (see Section 4.4.1), the TPU specimens were subjected to continuous cyclic loading-unloading indention tests. In this case, the behaviour of the TPU was steady at only eight cycles. The compressive load-deflection curves were recorded for each indention test (Figure 6.2). All the indentation test were repeated three times and they were conducted at 23±2 ºC.

[18]Instron 4206

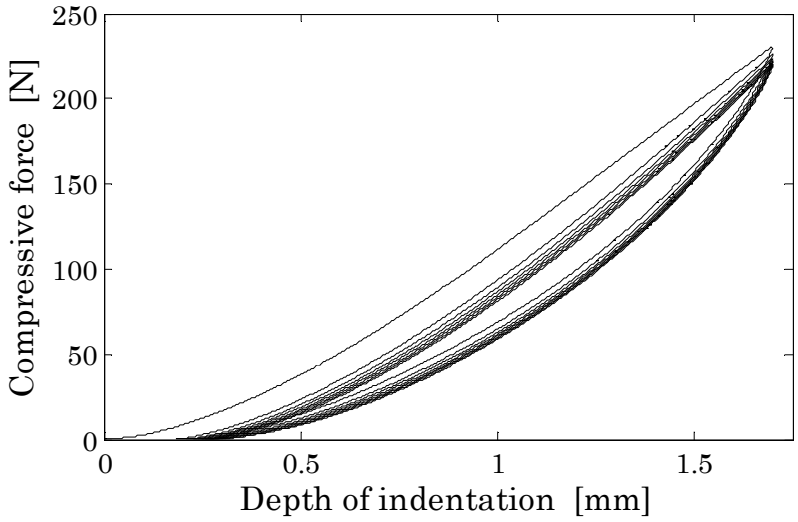

Figure 6.2: Experimental data during test of indentation (x = 1.7 mm and δ_{ref} = 4 mm).

A pressure measuring film[19] was used to measure the contact area. Therefore, for each test, the film was laid upon the TPU surface and an indentation was carried out. On the other hand, the contact pressures were measured only with the reference thickness $\delta_{ref} = 6$ mm (three specimens stacked together) to depths of indention $x = 0.5$ mm, $x = 1.1$ mm and $x = 1.7$ mm. The contact pressures were measured using pressure measuring films of six different ranges[20] (0.2-0.5 MPa, 0.5-2.5 MPa, 2.5-10 MPa, 10-50 MPa, 50-130 MPa and 130-300 MPa). The measurements were carried out similarly that in the case of the contact area but using six different pressure measuring films.

6.3 Normal contact behaviour of the TPU

The normal contact behaviour of the TPU depending on the thickness is discussed based on the compressive force, the contact area and the contact pressures.

6.3.1 Experimental results of compressive normal load

The behaviour of the compressive normal force is using the experimental data of the loading of the first cycle because of the theory (Section 6.1) was developed for rubbers un-preconditioned. It comes out from Figure 6.3 that the maximum compressive normal force decreases with increasing the thickness of the TPU. This behaviour is consistent with the fact that the effect of the support underneath the TPU specimen being felt decreases with increasing the thickness

[19]Fuji prescale film LW (2.5-10 MPa)

[20]Fuji prescale film: LLLW, LLW, LW, MS, HS and HHS, respectively

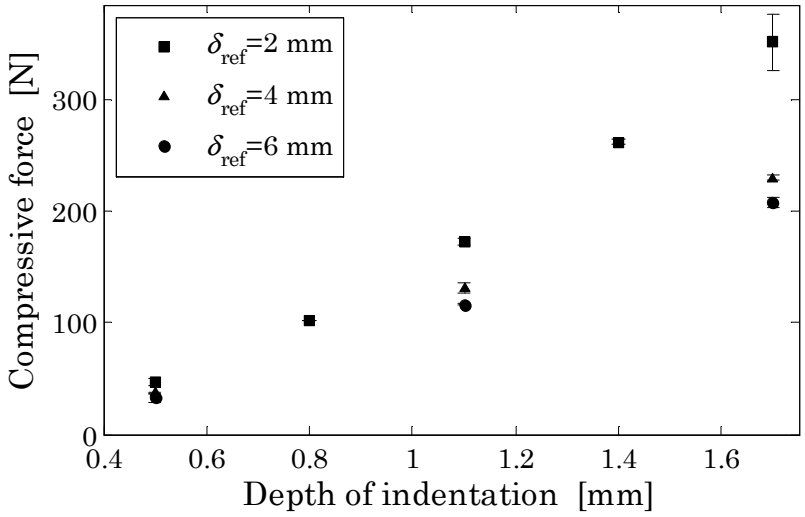

Figure 6.3: Maximum compressive force of indention depending on thickness of the TPU.

In view of these behaviour, the experimental results of reference thickness $\delta_{ref} = 6$ mm were fitted (Figure 6.4) using a model

$$F_N = k_1 x^n R^m E, \tag{6.9}$$

of compressive force behaviour without considering the effect of the support, as Equations (6.2) and (6.3). Using the radius R = 3 mm of the chrome steel ball and the tensile modulus E = 31 MPa of the TPU, the values of the constant are $k_1 = 1.82 \pm 0.03$, $m = 0.504 \pm 0.001$ and $n = 1.496 \pm 0.001$, (for graphical representation this model is labelled as Model-wS). Therefore, the model of the normal force behaviour for the TPU is approximately as Equation (6.2) in spite of the tensile modulus E was determined in tension (Section 4.5).

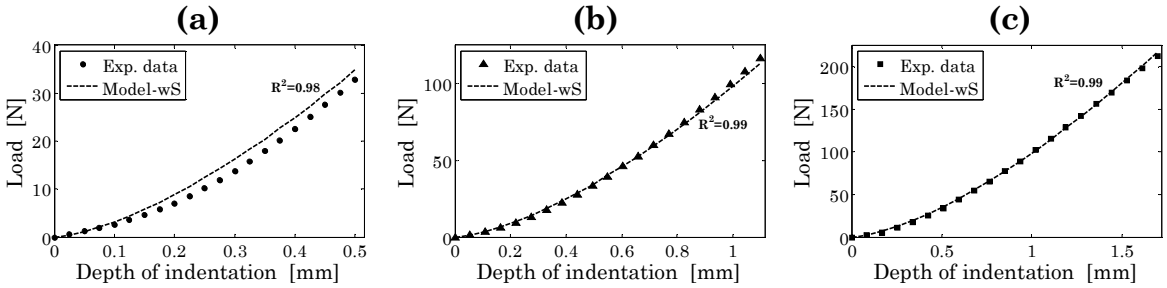

Figure 6.4: Fittings of experimental data using the model without considering the support effect with δ_{ref} = 6 mm at (a) x = 0.5 mm, (b) x = 1.1 mm and (c) x = 1.7 mm.

However, when the Equation (6.9), i.e. the model without considering the effect of the support, is used to fit the experimental results of reference thickness $\delta_{ref} = 4$ mm, the fittings (Figure 6.5) are not as good as the results of reference thickness $\delta_{ref} = 6$ mm.

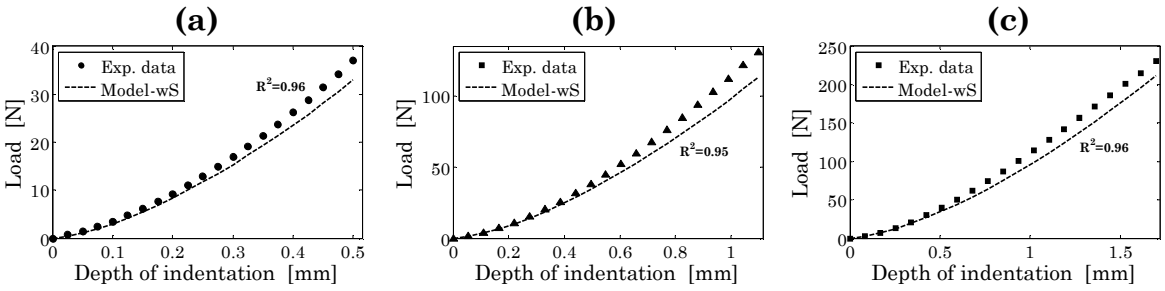

Figure 6.5: Fittings of experimental data using the model without considering the support effect with δ_{ref} = 4 mm at (a) x = 0.5 mm, (b) x = 1.1 mm and (c) x = 1.7 mm.

Therefore, the experimental results of reference thickness $\delta_{\mathrm{ref}} = 2$ mm and $\delta_{\mathrm{ref}} = 4$ mm were fitted using models that consider the effect of the support, Equations (6.5), (6.6) and (6.7). The value of the normal load predicted by Hertz theory F_N^{Hz} was obtained from the above results. The best fittings (Figure 6.6 and Figure 6.7) were obtained using a model

$$F_N = F_N^{\mathrm{Hz}} e^{(\mathrm{k}_2 R/x-\delta)}, \tag{6.10}$$

as Tangorra (1966) proposed with a constant that depends on radius of indenter linearly, where $\mathrm{k}_2 = (7.6 \pm 0.2)\times 10^{-2}$ (for graphical representation this model is labelled as Model-S). From Equation (6.10), it should be noted that this model is actually a correction of the Hertz theory using an exponential parameter.

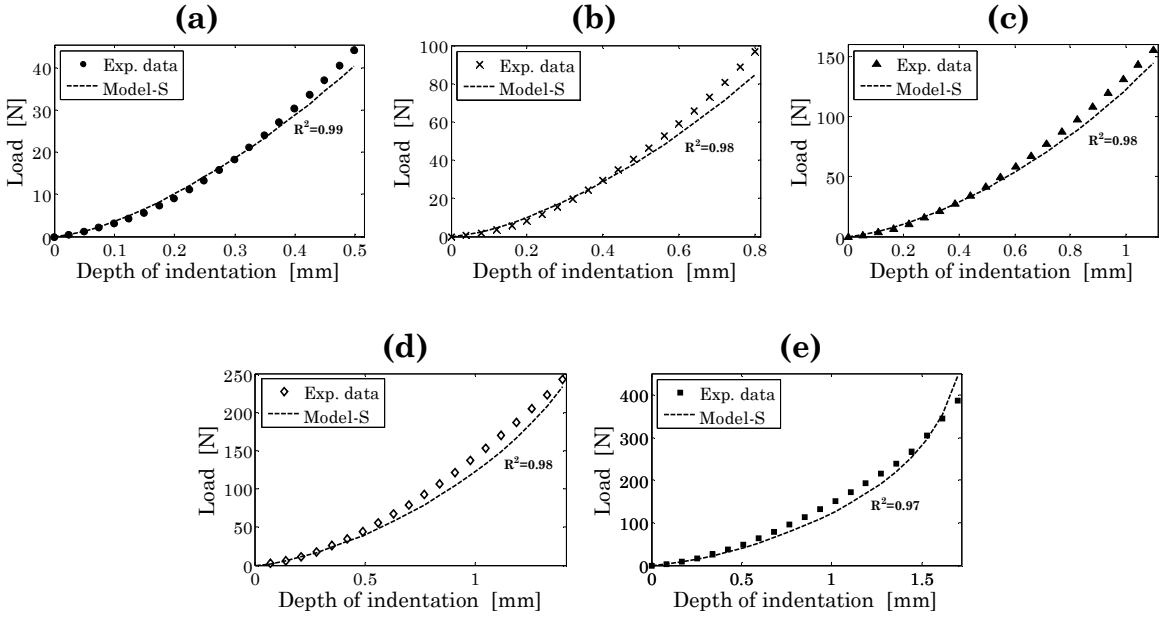

Figure 6.6: Fittings of experimental data using correction of Hertz theory to consider the support effect with δ_{ref} = 2 mm at (a) x = 0.5 mm, (b) x = 0.8 mm, (c) x = 1.1 mm, (d) x = 1.4 mm and (e) x = 1.7 mm.

Regarding the curve fittings (Figure 6.4), it can be stated that effect of the support underneath the TPU being felt is insignificant using the reference thicknesses $\delta_{ref} = 6$ mm. Therefore, the ratio (1:20) of radius of circular contact to the thickness proposed by Busfield and Thomas (1999) is strongly overrated in the case of this extruded TPU, as the ratio is approximately 1:3 at $x = 1.7$ mm.

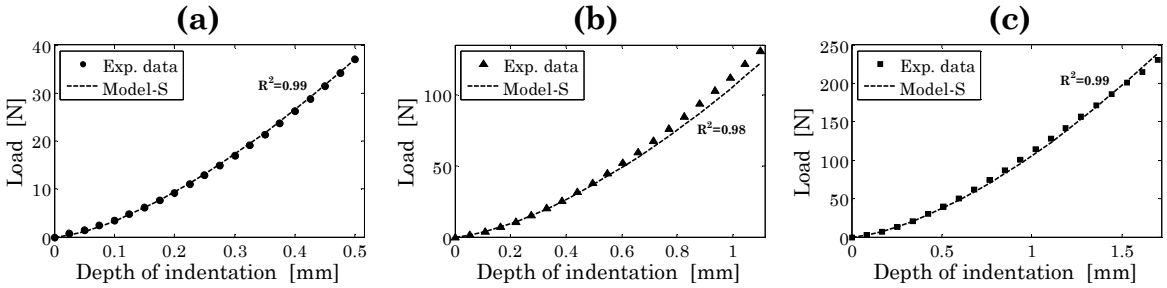

Figure 6.7: Fittings of experimental data using correction of Hertz theory to consider the support effect with δ_{ref} = 4 mm at (a) x = 0.5 mm, (b) x = 1.1 mm and (c) x = 1.7 mm.

The ratio of radius of circular contact to the thickness a/δ presents values between a range that depends on the thickness δ, as follows

$$\frac{a}{\delta} = \frac{(Rx)^{1/2}}{\delta} = \begin{cases} 0 & \text{if } x = 0 \\ \left(\frac{R}{\delta}\right)^{1/2} & \text{if } x = \delta \end{cases} . \qquad \textbf{(6.11)}$$

Then, this ratio can not be used as global value to divide when the behaviour of the compressive force may be modelled using Hertz theory or not. For a same value of this ratio, the model of the compressive force may be obtained using Hertz theory or not (Figure 6.8). Using the experimental results of the TPU, the Hertz theory should be used for $a/\delta \leq 0.31$ (with $\delta_{ref} = 6$ mm and $x = 1.7$ mm). But the ratio is $a/\delta = 0.31$ when $\delta_{ref} = 4$ mm and $x = 0.5$ mm, which is modelled using the correction to Hertz theory, i.e. Equation (6.10).

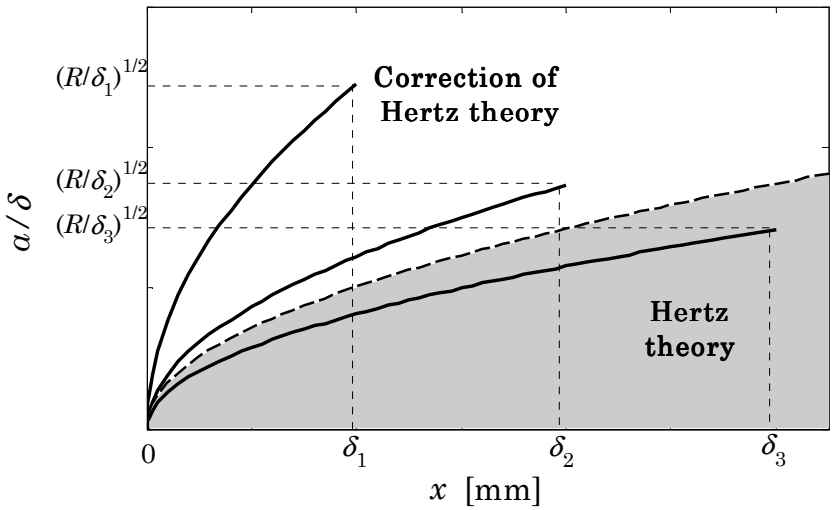

Figure 6.8: Ratio of contact radius to thickness vs. depth of indentation for different thicknesses separated depending on whether the compressive load is modelled using Hertz theory or using a correction of such theory.

Therefore, taking into account the correction proposed by Tangorra (1966), the ratio of radius of indenter R to the thickness of elastomer that is not deformed $(\delta - x)$, i.e.

$$\frac{R}{x'} = \frac{R}{\delta - x}, \tag{6.12}$$

is proposed to analyze the indentation behaviour of elastomers. This ratio allows dividing whether the compressive force is affected by the support underneath the elastomer being felt or it is not affected, because of its range of values is

$$\frac{R}{x'} = \frac{R}{\delta - x} = \begin{cases} \dfrac{R}{\delta} & \text{if } x = 0 \\ \infty & \text{if } x = \delta \end{cases}. \tag{6.13}$$

Moreover, this ratio gives some better insight of the indentation deformation, which can be considered as the sum of contact and compression deformations (Figure 6.9).

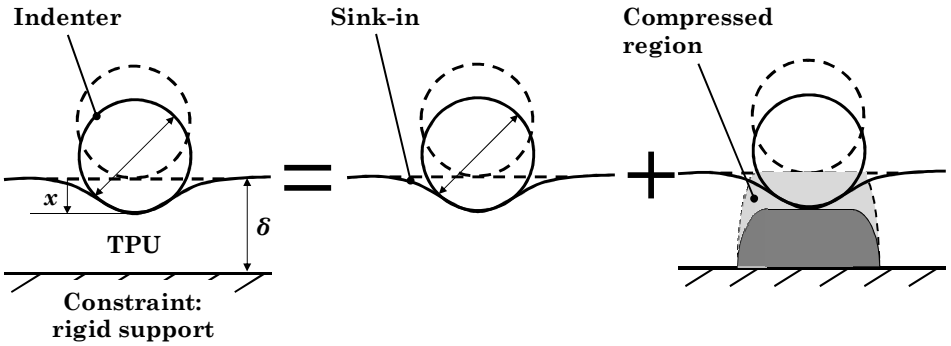

Figure 6.9: Indentation deformation as the sum of contact and compression deformations.

From the experimental results obtained with the TPU and using the ratio of radius of indenter to the thickness of elastomer that is not deformed $R/(\delta - x)$, it should be pointed out that the Hertz theory is valid up to values of 0.7 and the correction of Hertz theory, Equation (6.10), should be used for values of the ratio over 0.85 (see Figure 6.10).

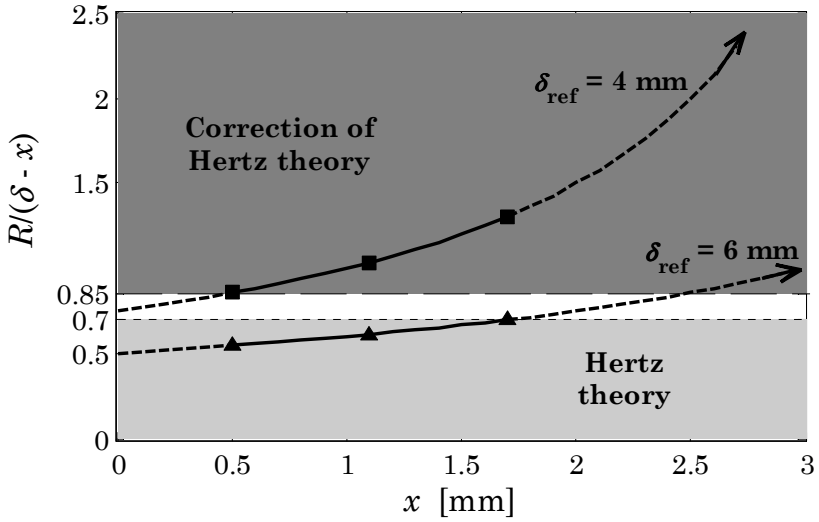

Figure 6.10: Ratio of radius of indenter to the undeformed thickness vs. depth of indentation for the reference thicknesses δ_{ref} = 4 mm and δ_{ref} = 6 mm.

In order to prove that the application ranges of each theory are valid with others conditions, a indentation at depth $x = 2.7$ mm with reference thickness $\delta_{ref} = 6$ mm, thus the ratio of radius of indenter to the undeformed thickness is 0.9, was carried out. From Figure 6.11, it is pointed out that the model based on Hertz theory, Equation (6.9), gives worse fitting than the model that considers the support effect, Equation (6.10), even though the reference thickness $\delta_{ref} = 6$ mm.

Indentation tests with different radius of indenter

In addition to this indentation at depth δ_{ref}=6 mm, indentation tests for different radius of indenter, R = 6.0000±0.0005 mm and R = 9.000±0.001 mm, were carried out to prove the application ranges of the compressive load models on normal contact for the TPU. Two values of the ratio $R/(\delta - x)$, one into the application range of Hertz theory and the other into the application range of the correction of Hertz theory (see Figure 6.10), were used for both radius of indenter. As the indentation depth $x = 1.7$ mm was constant for these indentation tests then the thickness of the TPU was chosen to lie on the different application ranges. But bearing in mind that the thickness is obtained stacking together specimens,

therefore only thicknesses multiples of δ_{ref}=2 mm could be obtained. Table 6.1 sums up the conditions of the indentation tests and the values of the ratio.

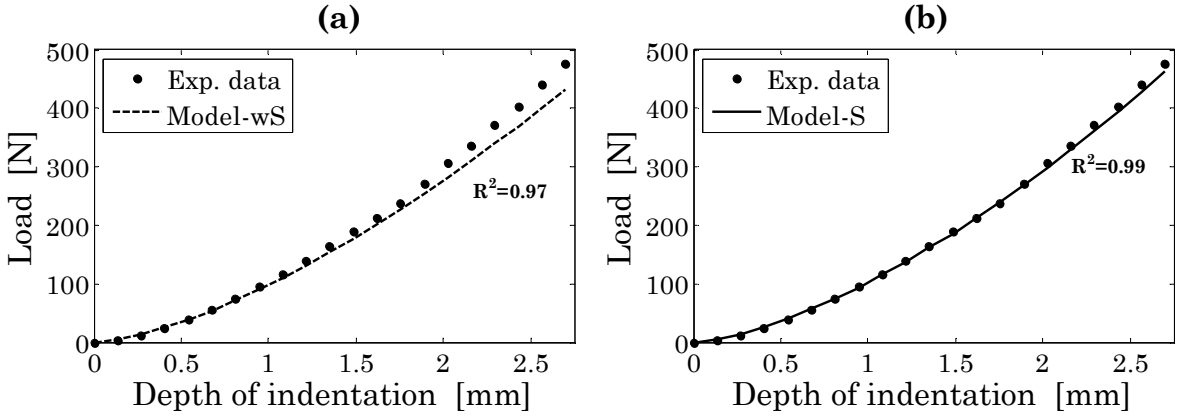

Figure 6.11: Comparison between the fittings of experimental data using (a) the model of Hertz theory and (b) the model of correction of Hertz theory with δ_{ref} = 6 mm at x = 2.7 mm.

Table 6.1: Experimental conditions for indentation tests with different radius of indenter.

Depth of indentation [mm]	Radius of indenter [mm]	Reference thickness [mm]	$R/(\delta - x)$
x =1.7	R = 6	δ_{ref}=6	1.39
		δ_{ref}=10	0.72
	R = 9	δ_{ref}=6	2.09
		δ_{ref}=14	0.73

The values of ratio of the indention tests with δ_{ref} = 6 mm are clearly grater than 0.85, i.e. these values lie on the application range of correction of Hertz theory. Therefore, Equation (6.10) was used to model the behaviour of the compressive force (Figure 6.12).

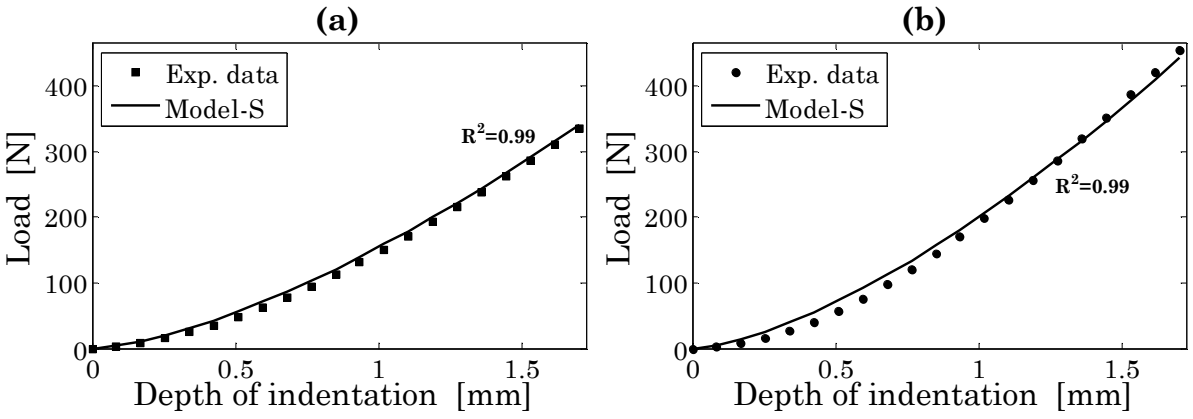

Figure 6.12: Fittings of the experimental data of indentation tests with δ_{ref} = 6 mm using the correction of Hertz theory for (a) R = 6 mm and (b) R = 9 mm.

However, the values of ratio with $\delta_{ref} = 10$ mm and with $\delta_{ref} = 14$ mm lie on the undefined gap, i.e. between 0.7 and 0.85 (see Figure 6.10). Therefore, the experimental data were fitted using both models, i.e. Hertz theory and its exponential correction (Figure 6.13 and Figure 6.14). Regarding these fittings, it is shown that the model of Hertz theory predicts better the response of the TPU than the exponential correction. Therefore, bearing in mind that the limit of the ratio of radius of indenter to the undeformed thickness at $x = 0$ mm with $\delta_{ref} = 4$ mm is 0.75 (see Figure 6.10), the undefined gap can be vanished considering 0.75 as the value of ratio that divides both ranges of application. Moreover, the differences of compressive load between both models are approximately only 6% for this value of ratio. Thus, summarizing the results obtained for indentation tests, the model proposed to predict the behaviour of compressive force using the TPU is as follows

$$F_N = \begin{cases} \mathrm{k}_1 E x^{\mathrm{n}} R^{\mathrm{m}} & \text{if} \quad R/(\delta - x) < 0.75 \\ \mathrm{k}_1 E x^{\mathrm{n}} R^{\mathrm{m}} e^{\mathrm{k}_2 R/\delta - x} & \text{if} \quad R/(\delta - x) \geq 0.75 \end{cases}, \tag{6.14}$$

where E is the tensile modulus of the TPU, R is the radius of indenter, x is the depth of indentation, δ is the thickness of the TPU and the values of constants are summed up in Table 6.2.

Table 6.2: Values of constants for the model of compressive force in indentations of spherical rigid body (steel ball) over TPU.

$\mathbf{k_1}$	$\mathbf{k_2}$	**M**	**n**
1.82± 0.03	$(7.6\pm0.2)\times10^{-2}$	0.504±0.001	1.496±0.001

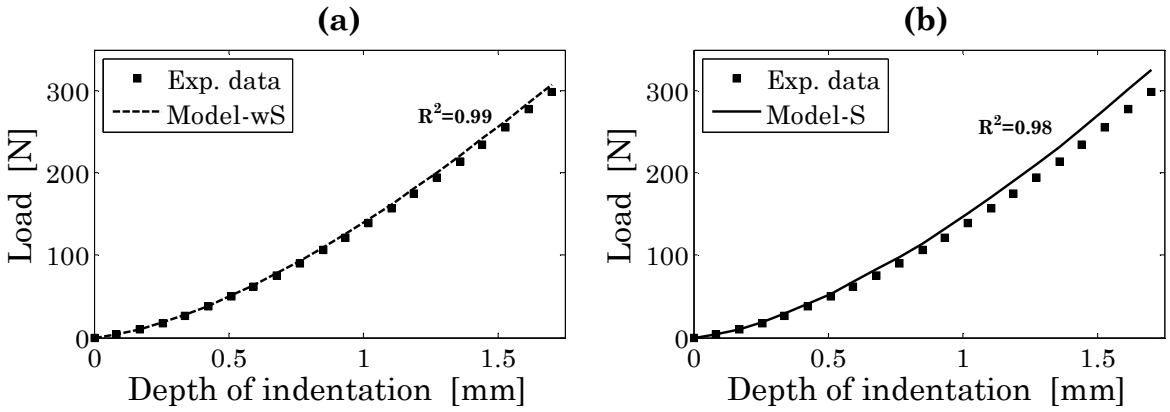

Figure 6.13: Comparison between the fittings of the experimental data of indentation tests for R = 6 mm using (a) the Hertz theory and (b) the correction of Hertz theory with $\delta_{ref} = 10$ mm.

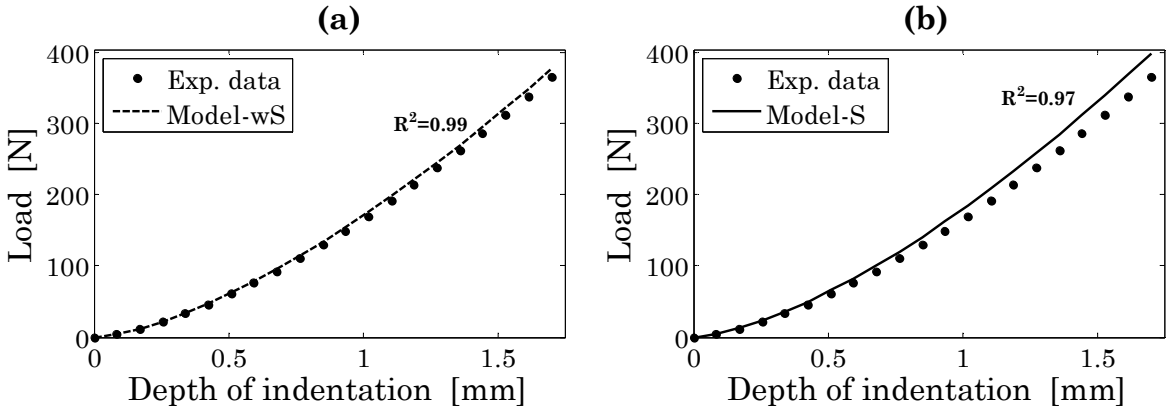

Figure 6.14: Comparison between the fittings of the experimental data of indentation tests for R = 6 mm using (a) the Hertz theory and (b) the correction of Hertz theory with $\delta_{ref} = 14$ mm.

6.3.2 Experimental results of contact area

As stated above (Section 6.2), the measurements of the contact area were carried out using a pressure measuring film[21] that covers the pressure range from 2.5 MPa to 10 MPa. This pressure measuring film was chosen because of it covers the pressure range of interest without being extremely sensible at low pressures. Sensitivity at low pressures hinders accurate measurements of contact area due to unclear patches.

Therefore, it bears in mind that the measurements of contact area using this pressure measuring film introduce a error because of the zone of the contact area with pressures below of 2.5 MPa are not capture.

[21]Fuji prescale film LW (2.5-10 MPa)

In order to process the patches of pressure measuring films, they were scanned[22] with 1200 dpi resolution and 12 bpp colour depth together a scale in millimetres (Figure 6.15) to known the length of each pixel. Then the scanned images were processed digitally using Matlab. The measurement of contact area was obtained by means of two different ways or techniques, counting pixels and measuring diameter.

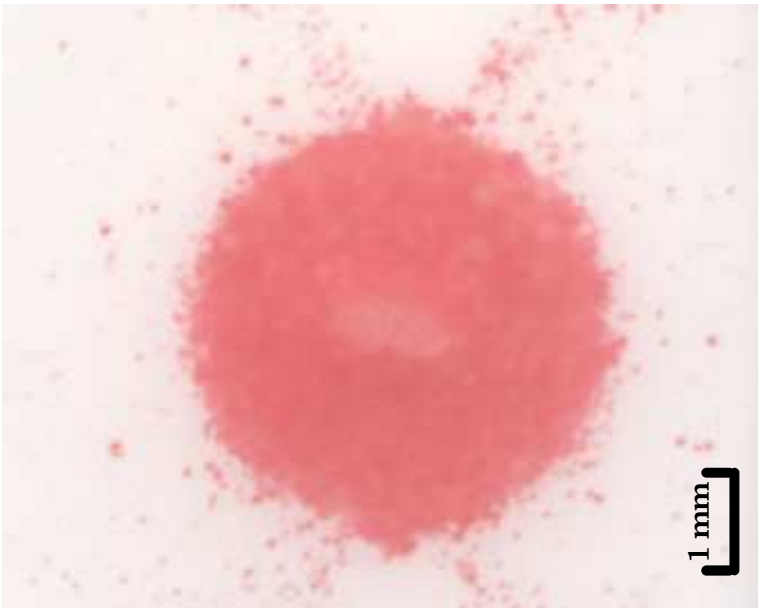

Figure 6.15: Patch of pressure measuring film scanned (δ_{ref} = 6 mm and x = 1.1 mm).

Counting pixels technique

The counting pixels technique consisted in processing the different colours of the scanned patch and then reducing these colours from the RGB colour model into fractions or ranges of colours. The scanned patches were processed using the image toolbox of Matlab and the programs performed to carry out the following tasks. Firstly the colours were divided into three fractions or ranges: black, white and other colour; and then the pixels of this other colour were counted. Secondly the colours were divided into ten fractions: black, white and other eight colours; and then the pixels of these other eight colours were counted. Finally, the contact area in pixel units was obtained using the average of the two countings of pixels. The contact area in pixels units were converted into square millimetres taking into account the area of a pixel in the scanned image.

[22]Epson Perfection 1200 U

Measuring diameter technique

This technique consisted of measuring manually in pixel units the diameter of the scanned patch by means of the *imtool* function of Matlab. The measurement in pixel units of the diameter was carried out in three different points (Figure 6.16). The average of the three measurements in pixel units was calculated and then it was converted to millimetres taking into account the length of a pixel in the scanned image. Finally the contact area was obtained assuming circular area.

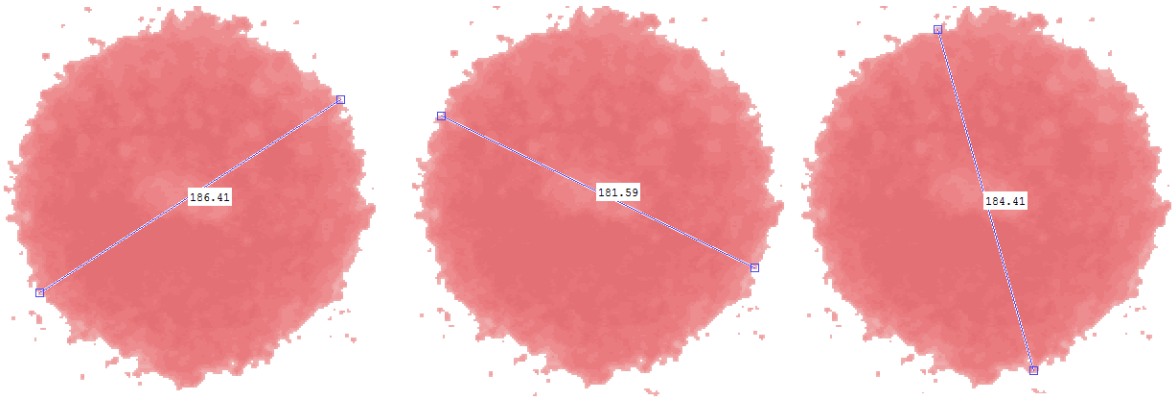

Figure 6.16: Measurements of the diameter in pixel units using *imtool* function in three different points for the same patch.

Experimental results

The experimental contact areas are summed up in Table 6.3. From the results obtained, it can be noted that there are not significant differences between both proposed techniques of measurement, except at high depth of indentation with $\delta_{ref} = 2$ mm. This difference could be due to the edge of the patches becomes more irregular with increasing depth of indentation. And thus, the approximation to circular area gives lower values of the contact area than counting pixels. Moreover, this fact also is the reason that the obtained errors of the measuring diameter technique are slightly greater than those of the counting pixels technique.

As expected from the discussion in the later section (Section 6.3.1), the contact areas with $\delta_{ref} = 6$ mm present closer values to the contact area obtained using the Hertz theory than with other reference thicknesses (Figure 6.17). Furthermore it bears in mind that the experimental contact areas are smaller due to the pressure measuring film did not record values less than 2.5 MPa.

Table 6.3: Experimental measurements of contact areas.

Reference thickness [mm]	Depth of indentation [mm]	Contact area [mm²]	
		Counting pixels	Measuring diameter
$\delta_{ref} = 2$	$x = 0.5$	4.1±0.2	4.2±0.3
	$x = 0.8$	7.3±0.1	7.3±0.1
	$x = 1.1$	11.2±0.4	11.0±0.4
	$x = 1.4$	16.2±0.2	15.4±0.4
	$x = 1.7$	20.4±0.1	19.3±0.4
$\delta_{ref} = 4$	$x = 0.5$	3.9±0.1	4.0±0.1
	$x = 1.1$	10.7±0.2	10.5±0.4
	$x = 1.7$	16.8±0.6	16.7±0.9
$\delta_{ref} = 6$	$x = 0.5$	3.7±0.1	3.8±0.2
	$x = 1.1$	9.9±0.3	9.8±0.3
	$x = 1.7$	15.2±0.7	14.9±0.9

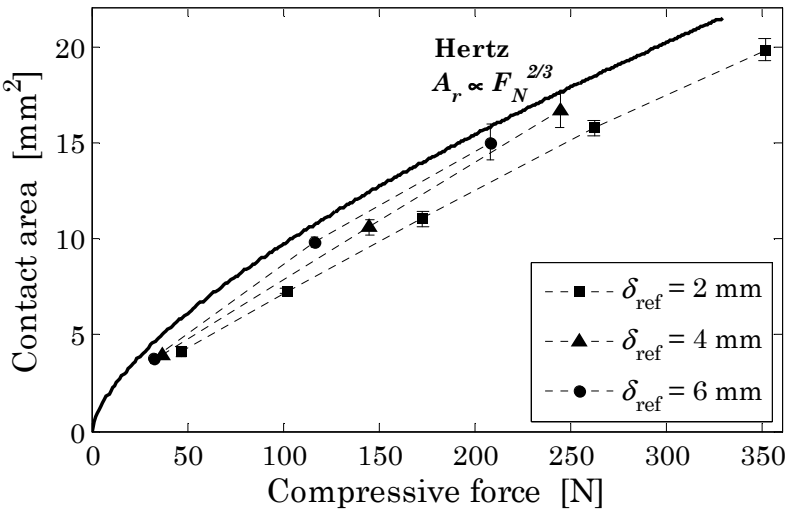

Figure 6.17: Experimental contact areas (average of both techniques of measurement) with different reference thicknesses comparing to the values obtained using the Hertz theory.

On the other hand, according to Persson (2001), the contact area is proportional to the normal force F_N. Using this model, the linear fittings of experimental contact areas (Figure 6.18) have an independent term. The independent term can be considered as the contact area

due to the adhesion, i.e. the contact area whether no load is applied (Johnson et al. 1971). This area of adhesion is related to the force which is necessary to separate the two surfaces of bodies. Moreover it can be noted from Figure 6.18 that the value of independent terms appear to no depend on reference thickness, which is consistent with the fact that adhesion is a surface effect. Therefore, further experiments would be needed to study the adhesion effect. In that regard, experimental tests of pull-off force (Kröger et al. 2004), i.e. a steel ball was squeezed against the TPU applying a preload and then they are rapidly separated while the contact force was measured by a load cell of a universal testing machine[23], were carried out. But the experimental results were inconclusive due to the very low forces obtained. Then, for an initial investigation into the normal contact of the TPU, adhesion effects were not included.

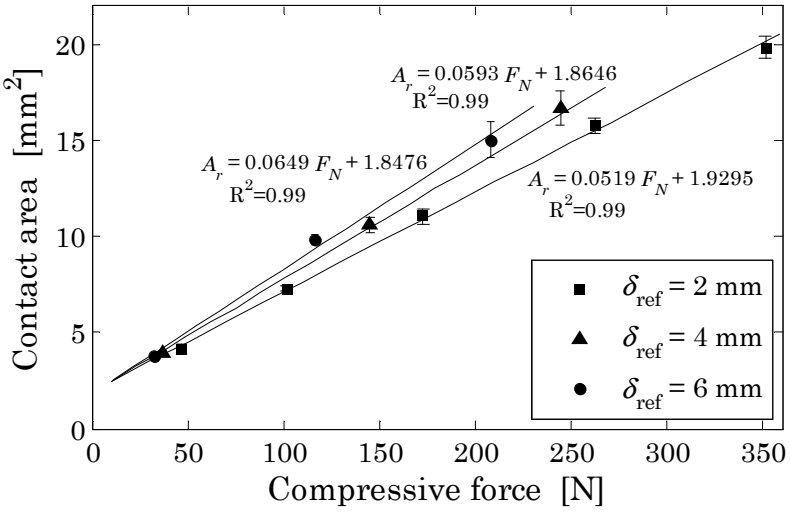

Figure 6.18: Linear fittings of the experimental contact areas (average of both techniques of measurement) as function of load.

6.3.3 Experimental results of contact pressures

The contact pressures to different depths of indentation ($x = 0.5$ mm, $x = 1.1$ mm and $x = 1.7$ mm) were studied using the reference thickness $\delta_{ref} = 6$ mm. As quantitative values of contact pressure from the pressure measuring films were unobtainable, then a pressure map (or pressure distribution) on contact area was sought overlaying concentrically (see Figure 6.19) the patches obtained using pressure measuring films of different ranges[24] (0.2-0.5 MPa, 0.5-2.5 MPa, 2.5-10 MPa, 10-50 MPa, 50-130 MPa and 130-300 MPa).

[23]Instron 4206

[24]Fuji prescale film: LLLW, LLW, LW, MS, HS and HHS, respectively

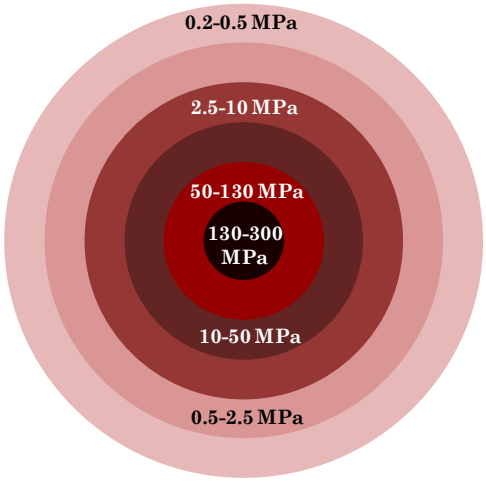

Figure 6.19: Schematic figure of pressure map overlaying concentrically the contact areas obtained at different ranges of pressure.

The patches at the two lowest ranges (0.2-0.5 MPa, 0.5-2.5 MPa) were unprocessed due to the high sensitivity of the films results in an unclear contact area (Figure 6.20). Moreover, patches were not obtained at the two highest ranges (50-130 MPa and 130-300 MPa), i.e. there were no contact pressures higher than 50 MPa to any depth of indentation. Therefore, only patches at middle ranges (2.5-10 MPa, 10-50 MPa) were used to create the pressure map.

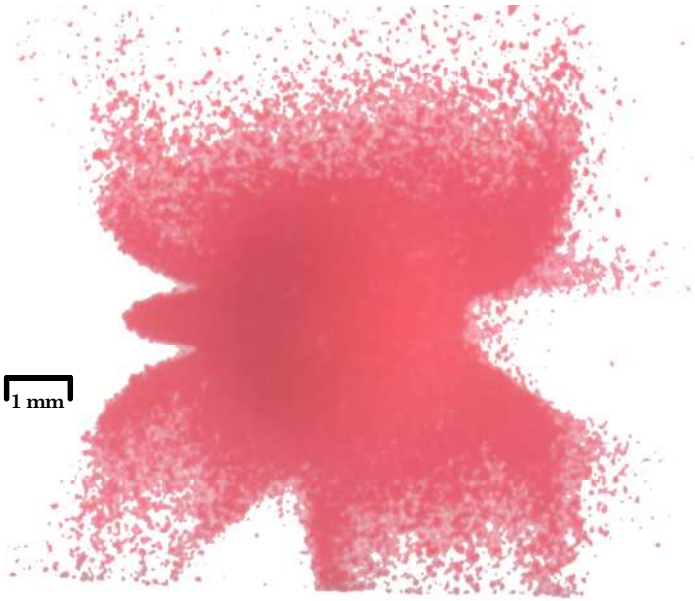

Figure 6.20: Patch of pressure measuring film of range 0.5-2.5 MPa (δ_{ref} = 6 mm and x = 1.7 mm).

The patches of pressure measuring films were scanned[25] as pointed out above, but only the measuring diameter technique was used to measure the contact area. The counting pixels technique was not used due to there were patches with uncoloured spaces (Figure 6.21). Actually this fact is not a problem because there are not significant differences between both techniques of measurement.

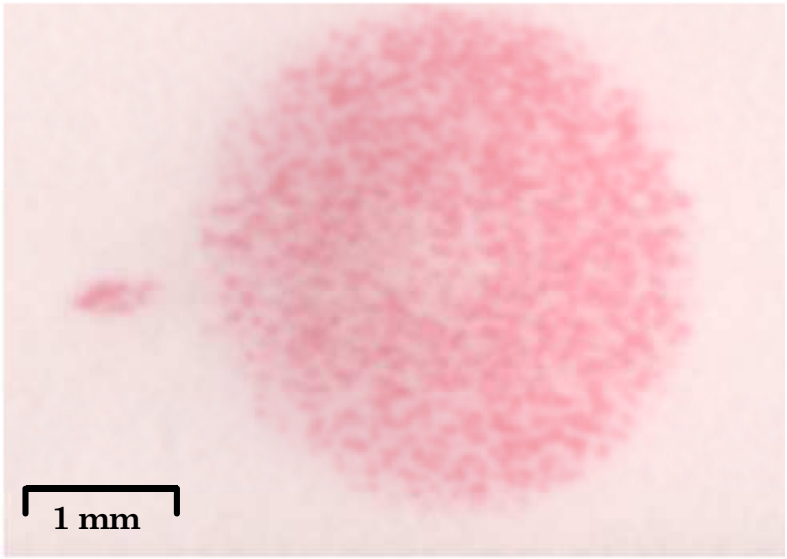

Figure 6.21: Patch of pressure measuring film of range 10-50 MPa (δ_{ref} = 6 mm and x = 1.1 mm).

The experimental contact areas using pressure measuring films of different ranges are summed up in Table 6.4. As expected, the contact areas obtained using the film of range 10-50 MPa are smaller than using the film of 2.5-10 Mpa. Therefore, as only two different pressure measuring films were used, the percentage reduction,

$$\frac{A_c^{\text{film 2.5-10 MPa}} - A_c^{\text{film 10-50 MPa}}}{A_c^{\text{film 2.5-10 MPa}}} \times 100, \qquad \textbf{(6.15)}$$

in contact area between the both films is the percentage of contact area with contact pressures between 2.5 and 10 MPa (see Figure 6.22).

[25]Epson Perfection 1200 U

Table 6.4: Experimental measurements of contact areas using pressure measuring films of different pressure ranges.

Reference thickness [mm]	Depth of indentation [mm]	Contact area [mm²]	
		Film of 2.5-10 MPa	Film of 10-50 MPa
$\delta_{ref} = 6$	$x = 0.5$	3.8±0.2	3.39±0.09
	$x = 1.1$	9.8±0.2	9.2±0.1
	$x = 1.7$	14.9±0.3	14.6±0.2

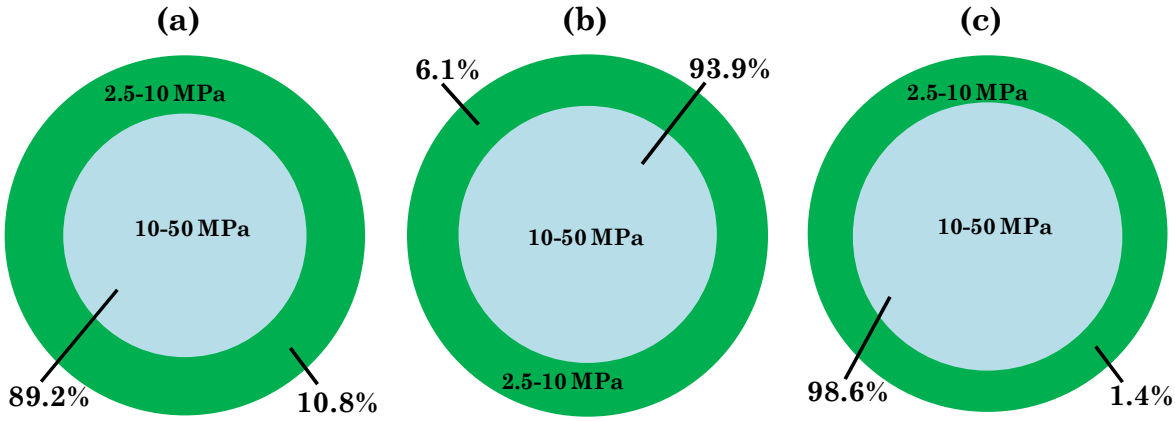

Figure 6.22: Schematic figures of pressure map overlaying concentrically the contact areas obtained at different ranges of pressure with $\delta_{ref} = 6$ mm to different depths of indentation, (a) $x = 0.5$ mm, (b) $x = 1.1$ mm and (c) $x = 1.7$ mm.

6.4 Numerical analysis of the normal contact behaviour

The computational experiments of indentations were carried out using the package ABAQUS/Standard 6.8 (Simulia 2009) which works well for modellings subjected to large deformations and where complex contact is encountered (Sun et al. 2000).

6.4.1 Mesh convergence

The accuracy of finite element models improves as the number of elements is increased because of the nature of the finite element method. Nevertheless, there is a convergence point at which a further increase of mesh density no longer results in a change in the calculated output.

The compressive load (Figure 6.23a) and the contact area (Figure 6.23b) of a spherical rigid pin indenting into a TPU sheet is shown for different element sizes. More accurate results are gained with a decrease in element size and below an element size of 0.05 mm the calculated results converge without an excessive increase in computational time (Figure 6.23c). Consequently, this element size was chosen for the modellings of indentations.

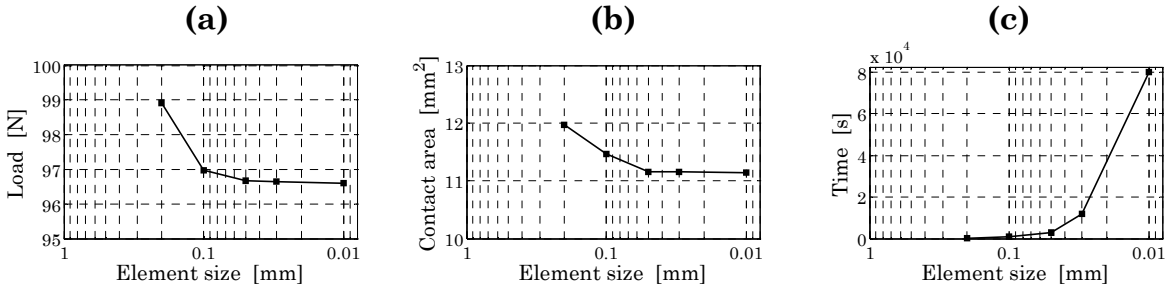

Figure 6.23: Examples for the mesh convergence of a finite element model is shown as the calculated (a) load and (b) contact area which are predicted more accurately as the element size is reduced. Further reduction of the element size does not alter the result significantly, but increases (c) computational time (δ_{ref} = 2 mm at x = 0.8 mm).

Similar procedures were conducted for each of the different modellings used through this thesis in order to decide on an appropriate mesh size to represent the modelling without increasing greatly the computational time.

6.4.2 Modelling of indentations

Due to the experimental indentations have geometry and loading conditions which do not vary in its longitudinal direction, then they can be modelled as a two dimensional problem using the plane strain condition. Moreover, the indentations present a middle symmetric axis, i.e. the 3D model can be created by revolving the 2D model about such axis. Therefore, the computational experiments were solved as axisymmetric 2D displacement-controlled models.

The steel ball, used in the experimental indentations, is modelled as rigid body due to the large difference in modulus compared to the TPU. Therefore, no deformation of the rigid body was assumed which saved computational costs. The TPU was characterized using the hyperelastic model with deformation history proposed in the previous chapter with 4-node hybrid bilinear quadrilateral elements (CAX4H). This constitutive model was implemented into calculus by means of the FEA based technique described in Section 5.5.2

Depending on the reference thickness, $\delta_{ref} = 2\,\text{mm}$, $\delta_{ref} = 4\,\text{mm}$ and $\delta_{ref} = 6\,\text{mm}$, the model consisted of 8000, 16000 and 24000 elements respectively. The bottom of TPU sheet was fixed fully and a fixed displacement, depending on the depth of indentation, in the normal direction was enforced at the reference point which controlled boundary conditions of rigid body (Figure 6.24).

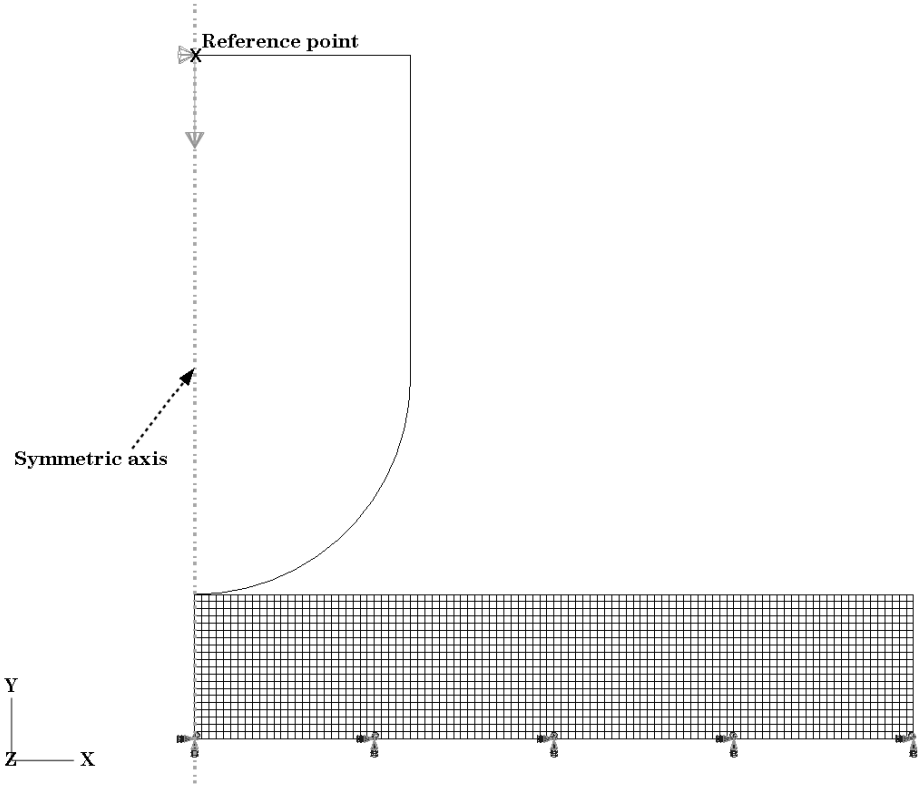

Figure 6.24: FEA model of computational experiments of indentations.

6.4.3 Computational results of compressive normal load

The compressive normal load, which is calculated as the total reaction force at the reference point of the rigid body (indenter), is compared with the experimental compressive load, which is the average value of loading and unloading loads in the last cycle of the indentation test (see Figure 6.2). The computational results agree with the experimental data when there is effect of support (Figure 6.25) as well as when no there is (Figure 6.26).

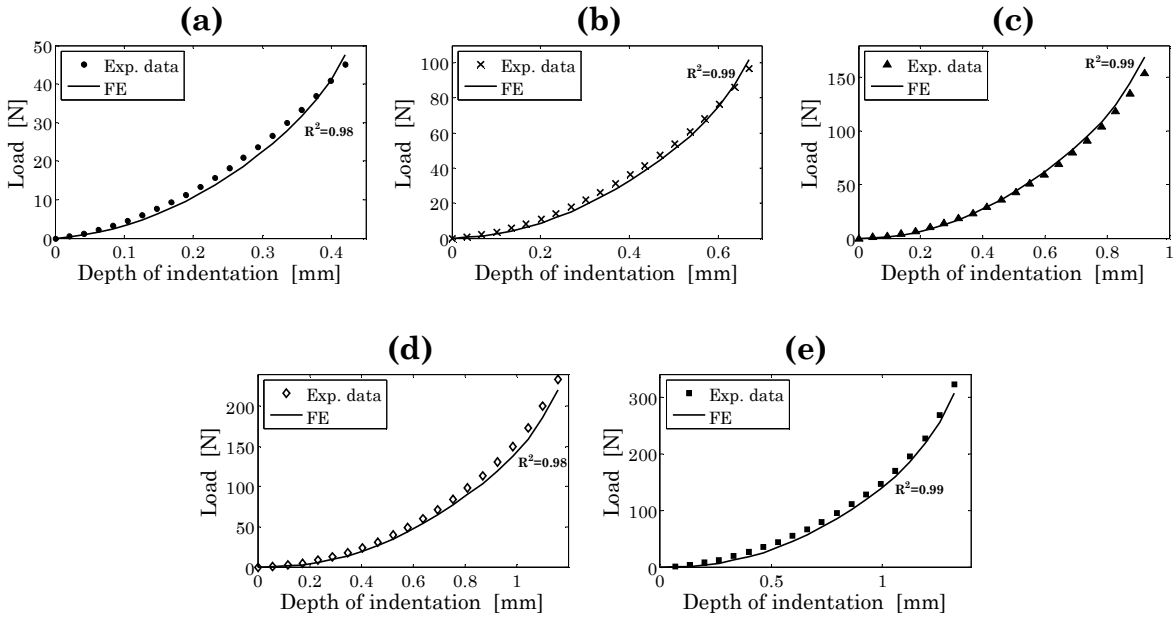

Figure 6.25: Comparison between experimental data and computational results for the last cycle of indentations with δ_{ref} = 2 mm and R = 3 mm at (a) x = 0.5 mm, (b) x = 0.8 mm, (c) x = 1.1 mm, (d) x = 1.4 mm and (e) x = 1.7 mm.

Therefore, in view of the agreement between computational results and experimental data, the material model with deformation history to predict the behaviour of the preconditioned TPU is validated in compressive problems despite it has been developed using experimental data from tension tests.

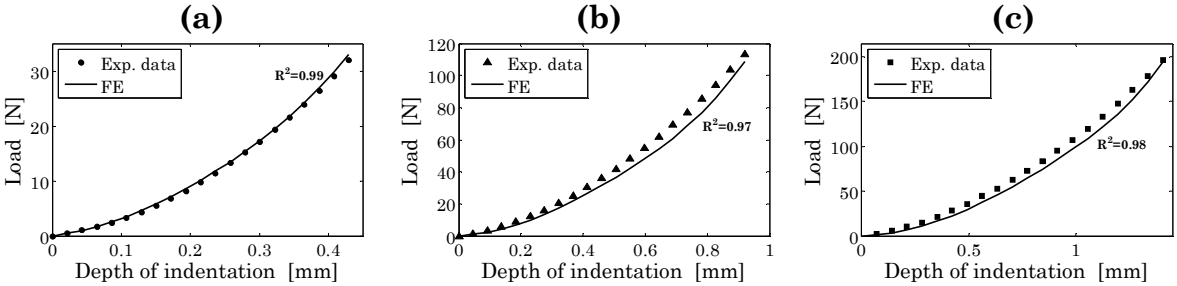

Figure 6.26: Comparison between experimental data and computational results for the last cycle of indentations with δ_{ref} = 6 mm and R = 3 mm at (a) x = 0.5 mm, (b) x = 1.1 mm and (c) x = 1.7 mm.

Moreover, the results of the computational experiments are also more accurate (Figure 6.27) using FEA based technique to implement the constitutive model with strain history of the preconditioned TPU than using the Yeoh models with constant coefficient (see Table 5.1).

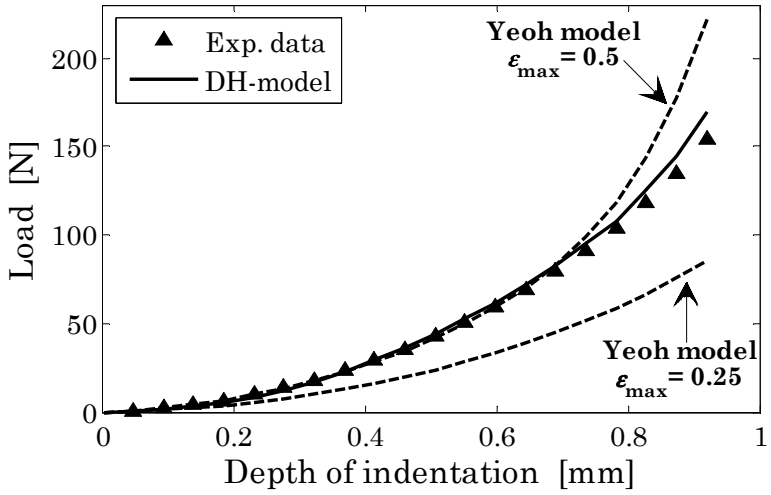

Figure 6.27: Comparison between experimental data and the computational results using different behaviour models for the TPU (δ_{ref} = 2 mm, R = 3 mm and x = 1.1 mm).

6.4.4 Computational results of contact area

To be compared with the experimental contact area (Section 6.3.2), the contact area from the computational experiments is obtained as the projection on the contact plane of the area with contact pressures above 2.5 MPa. These contact areas calculated from FE results are compared (Figure 6.28) with the average value of the contact areas which were measured using both techniques (counting pixels and measuring diameter).

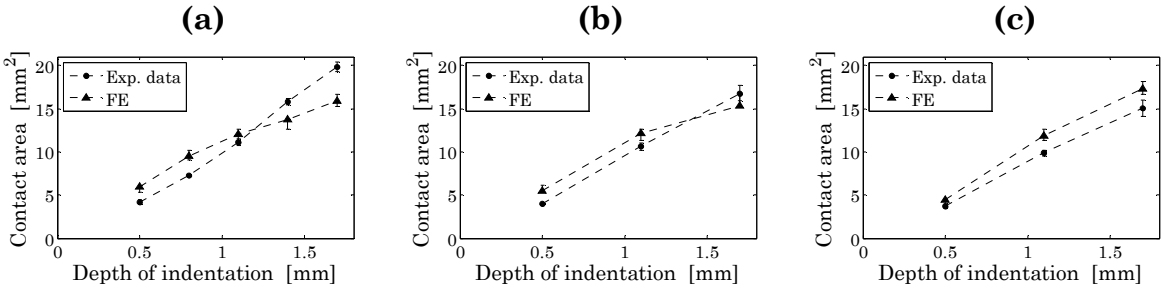

Figure 6.28: Comparison of contact areas (with contact pressures above 2.5 MPa between experimental data and computational results of indentations with (a) δ_{ref} = 2 mm, (b) δ_{ref} = 4 mm and (c) δ_{ref} = 6 mm using an indenter of R = 3 mm.

From the Figure 6.28, it is shown that the computational results of contact areas whose pressures are higher than 2.5 MPa present a good agreement with the experimental results, the relative errors are below 20%, except for $\delta_{ref} = 2$ mm at $x = 0.5$ mm and at $x = 1.7$ mm and for $\delta_{ref} = 4$ mm at $x = 0.5$ mm.

Furthermore it also should be pointed out that the calculated contact areas from computational experiments are greater than the experimental contact areas, probably due to the enforcement time on the films is not enough to break all ink-filled spheres. Nevertheless, this behaviour is not satisfied at the highest depths of indentation with the lowest thicknesses. This fact can be due to the irregular edges of the patches that increase the experimental contact areas at high depths of indentation.

On the other hand, the total contact area can be calculated from the computational experiments. It follows from Figure 6.29 that, independently of the TPU thickness, the total contact area is proportional to the normal load, except at $x = 1.7$ mm with $\delta_{\text{ref}} = 2$ mm due to the support effect is very high for this case. Therefore, regarding the curve fitting (Figure 6.29), the contact area exhibits a linear behaviour with the load according to Persson contact theory (Persson 2001) and the independent term may be related to the adhesion effects. This same linear behaviour is exhibited by the experimental contact areas measured using pressure measuring films (see Figure 6.29, these experimental data are the same as those in Figure 6.18 but the linear fitting is carry out using all points together, except the value at $x = 1.7$ mm with $\delta_{\text{ref}} = 2$ mm). The experimental slope of linear fitting is smaller than the computational due to the experimental data are limited by the sensitivity of the pressure measuring film used, i.e. only contact area with pressures above 2.5 MPa were measured. But the independent term of both linear fittings appears to be similar and this value can be related to the adhesion effects.

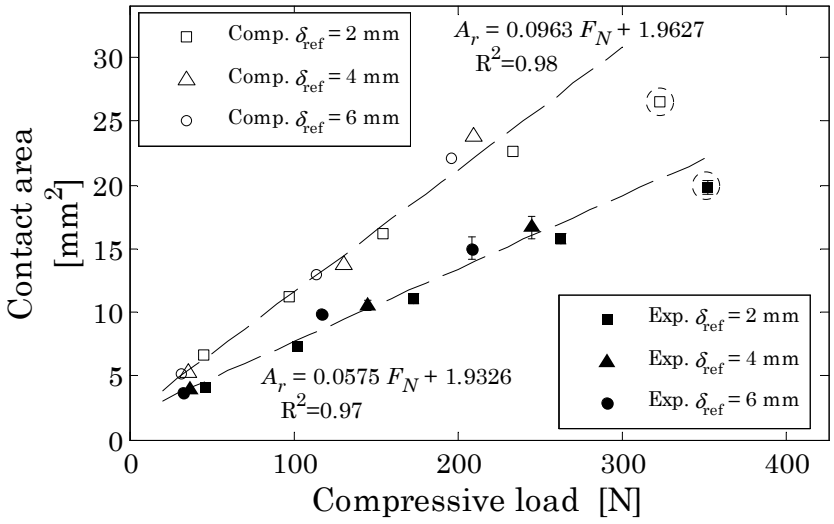

Figure 6.29: Linear behaviour of total contact area from computational experiments as function of load.

6.4.5 Computational results of contact pressures

The contact pressure from computational experiments is obtained by means of the output variable CPRESS, which may be defined as the ratio of the contact force at a node between the contact nodal area that is assigned to such node.

To compare with the experimental pressure maps that were obtained overlaying patch of films with different sensitivity ranges (see Figure 6.22), only pressures above 2,5 MPa (Figure 6.30) were considered to calculated the percentages of contact area that are covered by each range (2.5-10 MPa and >10 MPa).

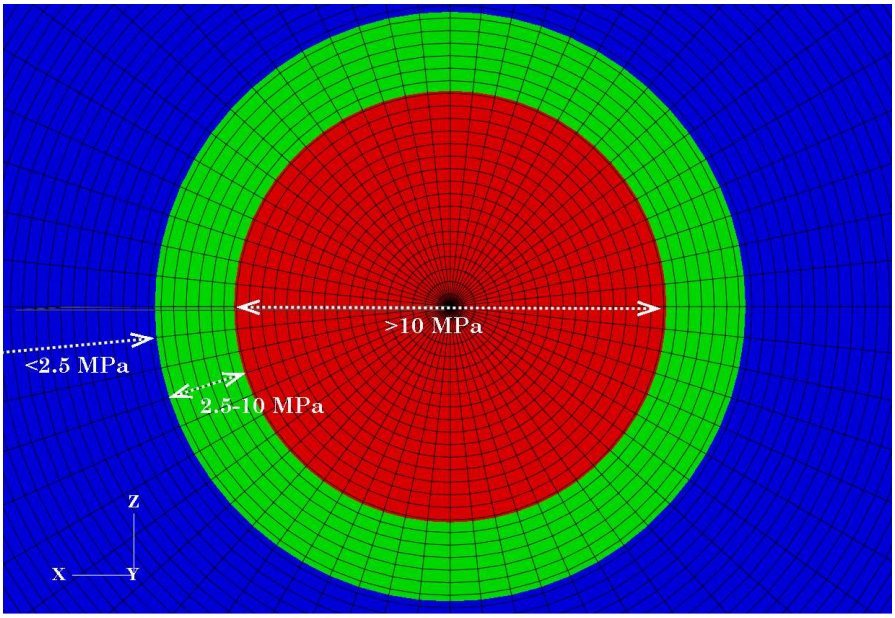

Figure 6.30: Pressure map with three different ranges corresponding to the pressure ranges of the films used experimentally (δ_{ref} = 6 mm, R = 3 mm and x = 1.7 mm).

Although the experimental and computational contact areas (Table 6.5) present values with relative error below 20%, the computational results of the distributions of contact pressures completely disagree with the experimental results, see Table 6.6.

Table 6.5: Experimental and computational results of contact areas with contact pressures above 2.5 MPa.

Reference thickness [mm]	Depth of indentation [mm]	Contact area (>2.5 MPa) [mm²]	
		Experimental	Computational
$\delta_{ref} = 6$	$x = 0.5$	3.8±0.2	4.42
	$x = 1.1$	9.8±0.2	11.71
	$x = 1.7$	14.9±0.3	17.33

It should also be noted that the zone with pressures above 10 MPa is clearly oversized comparing with the computational results, e.g. at $x = 0.5$ mm. all the computational contact pressures are below 10 MPa but experimentally the contact area with pressures above 10 MPa is approximately 90%. Therefore, the pressure measuring films only gives quantitative values of contact pressures which are very distant from the expected ones.

Table 6.6: Experimental and computational percentages of contact area that are covered by the different pressure ranges.

Reference thickness [mm]	Depth of indentation [mm]	Contact area [%]			
		2.5-10 MPa		>10 MPa	
		Exp.	Comp.	Exp.	Comp.
$\delta_{ref} = 6$	$x = 0.5$	10.8	100	89.2	–
	$x = 1.1$	6.1	64.3	93.9	35.7
	$x = 1.7$	1.4	44.5	98.6	55.5

On the other hand, the contact pressures from numerical simulations are compared with the contact pressures that are calculated using the analytical solution (Johnson 1985), which is deduced from the Hertz theory, for the pressure distribution

$$p(r) = \frac{8}{3\pi}\frac{E}{R}\left(a^2 - r^2\right)^{1/2}, \tag{6.8}$$

over the contact area of radius a when a rigid sphere of radius R is pressed into contact with an incompressible material with a tensile modulus E (Figure 6.31). But this analytical solution is inadequate to predict the contact pressures of indentations involving TPU, as it predicts higher pressures than those are calculated using finite element method.

Moreover, from the computational results obtained, it should be noted that the distribution of pressures presents a trend to spread uniformly on the contact area, i.e. the maximum pressures are smoothed over the contact area. This behaviour is more clear when the thickness of TPU is reduces (Figure 6.32).

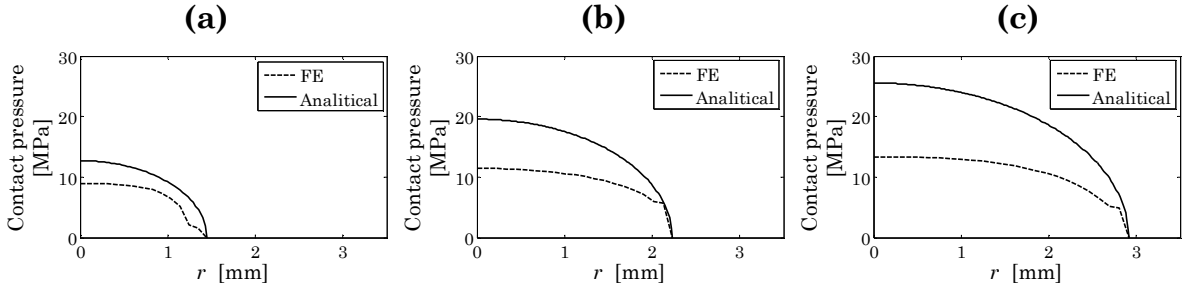

Figure 6.31: Comparison of analytical and computational contact pressures of indentations with δ_{ref} = 6 mm at (a) x = 0.5 mm, (b) x = 1.1 mm and (c) x = 1.7 mm using an indenter of R = 3 mm.

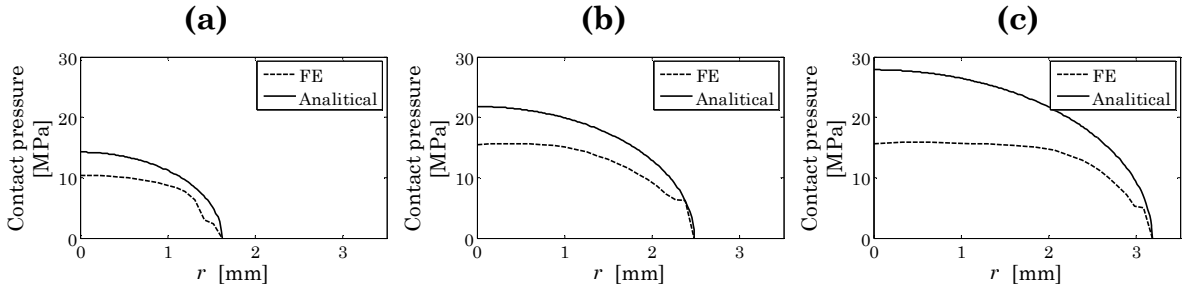

Figure 6.32: Comparison of analytical and computational contact pressures of indentations with δ_{ref} = 2 mm at (a) x = 0.5 mm, (b) x = 1.1 mm and (c) x = 1.7 mm using an indenter of R = 3 mm.

6.5 Conclusions

The behaviour of the TPU on normal contact (indentations) is discussed regarding three different variables; compressive load, contact area and distribution of contact pressures.

The behaviour of the compressive load in function of the indentation depth is predicted using a proposed model, Equation (6.14). Actually, this model is the coupling of Hertz theory and a correction of it depending on the ratio of the radius of indenter and the thickness of TPU that is not deformed $R/(\delta - x)$. Moreover, using the constitutive model of the TPU with deformation history, Equation (5.12), which is implemented using the FEA based technique proposed in the Chapter 5, the behaviour of the compressive load in the indentations is accurately predicted independently of the TPU thickness. Therefore the proposed constitutive model with strain history of the TPU is validated under compression conditions although the model was developed using experimental tensile conditions.

The contact area was measured using pressure measuring films and two different techniques were developed to process the patch obtained with such films. There are not significant differences in the results between both proposed techniques. The values of experimental contact area are limited by the film range of sensitivity, in this case between 2.5 and 10 MPa, i.e. only the contact area with pressures higher than 2.5 MPa were considered. Despite this restriction, the behaviour of the experimental contact areas depending on compressive load and TPU thickness is as expected from the contact theories (Hertz and Persson). Nevertheless, the computational contact areas using numerical analysis (finite element) and considering the restriction of sensitivity are slightly higher than the experimental, except at high depths of indentation with low thickness. On the other hand, the total computational contact area, i.e. without restriction, was considered. These values of total contact area present a linear dependency on compressive load independently of the TPU thickness.

Finally, the pressure distribution was measured overlaying the patch obtained using films of different sensitivity ranges. But the experimental results fully disagree when they are compared with the computational results of contact pressures. In view of the computational results for compressive load and contact area, the technique of measurement using pressure measuring films appears to be inappropriate for contact pressure distributions. Moreover, the computational contact pressures on the contact area with different TPU thicknesses exhibit more uniform distribution than the analytical solution from Hertz theory.

7 TANGENTIAL CONTACT: FRICTION & SLIDING

"I have not failed. I've just found

10,000 ways that won't work"

Thomas A. Edison

In this chapter is discussed the behaviour of the TPU in tangential contact or sliding, i.e. when there is relative displacement between the contacting bodies. Thus, friction is shown up in these contact problems with relative movement. Therefore, firstly, friction behaviour between the TPU and a gray iron is analyzed experimentally (Section 7.2). Using these experimental results, a friction model is developed (Section 7.3) and it is implemented into finite element analysis. Using the constitutive model with deformation history of the TPU to predict the mechanical behaviour of the TPU, the computational experiments of friction (Section 7.4) are carried out to validate the friction model proposed. Moreover, finally, the capacity of prediction of the friction model is proved using the experimental results in reciprocating contact configuration (Section 7.5).

7.1 Introduction

The contact is present in all mechanical systems. The contact transmits forces through the surfaces of bodies and it originates forces at the interface between the bodies. The global contact may be divided into normal and tangential contacts. The normal contact (discussed in Chapter 6) mainly deals to the contact of bodies without relative movement between them at macroscopic scale. It is bears in mind that there are relative displacement at microscopic scale, which are caused by the differences between the deformations of the contacting bodies. Meanwhile, the tangential contact deals to the contact when the bodies are in relative movement at macroscopic scale. In these contacts, the friction phenomenon, which is resulted from the action of tangential restraint, namely friction force, occurring at the interface between the contacting bodies, appears.

Friction is usually defined as the resisting tangential force to the common boundary between bodies when, under the action of external force, one body moves or tends to move relative to the surface of the other (Bhushan 2001). Others authors, as Tabor (1965), consider that friction depends on complex processes which occur in the real contact areas and in the surface layers when the bodies in contact are in relative tangential movement. Nevertheless, considering the essence through the processes of friction, then friction is an energy transforming effect, not force. Therefore, the friction may be defined as an energy transforming effect generated in the interface between contacting bodies in relative motion when an external force is applied. Thus friction should not be confused with friction force, due to friction is a different concept from frictional force, although they have close relation.

When one of the bodies in contact is an elastomer, the frictional force can be described as is given in section 2.6.2:

$$F_f = F_{adhesion} + F_{hysteresis} + F_{viscous} + F_{cohesion}. \quad \textbf{(7.1)}$$

Thus the complexity of elastomer friction can not be described by only a single term. Nevertheless, depending on the contact conditions, some contributions may be neglected, as the lubricated contribution $F_{viscous}$ when is considered a dry contact. Moreover, with a certain experimental configurations it is possible to enforce or suppress some contributions. In dry and smooth contacts, the configuration contact between a rigid cylinder and a rubber surface can be dominated by different contributions, in these cases the adhesion $F_{adhesion}$ and the deformation $F_{hysteresis}$. When the experimental configuration consists of cylinder roles over the rubber, then it is assumed a dominating hysteresis contribution (Tabor 1960). But when the cylinder is rotated in a fixed position relative to the fixed rubber surface, i.e. the rubber after an initial deformation does not change its geometry, then the adhesion contribution is dominant (Roberts and Thomas 1975).

Moreover the elastomer friction presents a run-in state in which the friction coefficient varies as the sliding time, or sliding distance, during the beginnings of relative motion. In this period the friction coefficient gradually increases with the sliding time until an approximately constant limiting value is reached (Zhang 2004). As it is pointed out above, the friction is an energy transforming effect, thus the energy of interface is constantly changing in the run-in state although the operating and environmental conditions are kept constant. The reasons of why and how this energy changes are not fully understood.

Elastomer friction depends on the different variables (see Table 2.3), which has been well discussed for rubbers (Blau 2001), but it is not extensively studied for thermoplastic elastomers. This dependence leads to a coefficient of friction, which is defined as the ratio between normal and friction forces normal force, that depends on the different variables

(applied normal force, sliding velocity between bodies, temperature, roughness of counterpart (rigid body), hardness of elastomer, etc). Regarding a macroscopic scale, it is known that the coefficient of friction decreases with the increase in normal load and it presents a maximum value with sliding velocity (Figure 7.1) when the elastomer is a rubber (Persson 1998 and Brown 2006).

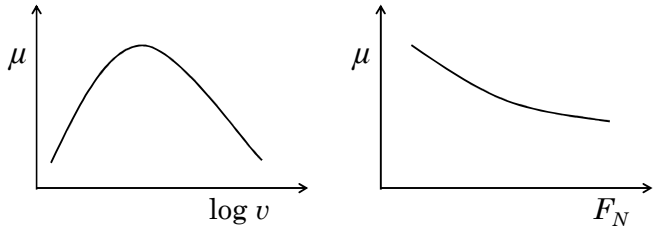

Figure 7.1: Schematic behaviour of coefficient of friction in function of sliding velocity and normal force.

Elastomer friction is determined as a result of an analytical, numerical or experimental approach. The experimental data points are included within the simulations as an approximation function of them or directly. But this later option is not reasonable from a physical point of view due to the points are not continuous which leads to equivocal dynamics effects (Moldenhauer and Kröger 2010).

The variable coefficient of friction for elastomers is characterizes using friction models (see Section 2.6.3), i.e. the coefficient of friction is a function of different variables and of their interactions. These models are developed mainly for rubbers (filled and unfilled) and its application to thermoplastic elastomers can be limited.

7.2 Experimental tests for TPU friction

The frictional behaviour of the TPU is analyzed using experimental tests which determine the relationship between an applied normal force F_N and the resulting force (friction force) F_r in opposite direction of the moving velocity. Therefore, the so-called coefficient of friction, i.e. the ratio between normal and friction forces, is usually used to compare the different experimental conditions.

The contact partners whose friction is characterized are the extruded TPU and a gray iron[26] (E=190 GPa) which is chosen because the traction sheaves of the lifts are of this material.

[26]GG-25

7.2.1 Tribometer test rig

The experimental configuration of friction tests was pin-on-disc (Figure 7.2), with the hemispherical pin (or slider) of gray iron and the flat surface of TPU. The circular path diameter of the pin over the TPU was 30 mm. The pin-on-disc configuration is chosen due to the adhesion contribution of elastomer friction should be dominating when the steady state of experimental test is reached. After the run-in state, the wear of the TPU causes that the deformation in the front of the contact is negligible. Therefore, the deformation and wear contributions of elastomer friction are much reduced in the steady state of experimental tests and then the adhesion contribution must be dominating.

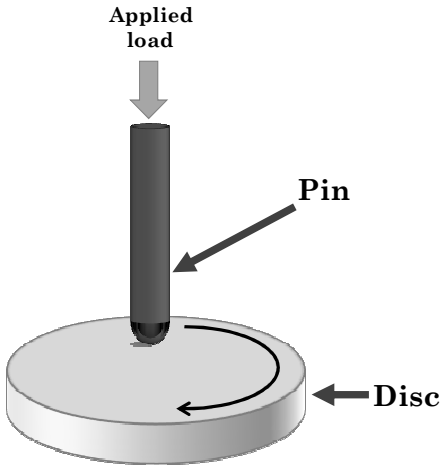

Figure 7.2: Pin- on-disc configuration of experimental friction tests between the TPU/gray iron contact partners.

The experimental tests were carried on a test rig that is a rotational tribometer[27] (Figure 7.3). The relative velocity between the contact bodies is provided by a rotating disc. The disc which is mounted with the TPU sample is driven by a servo motor. The gray iron specimen is fixed onto a holder, which has one translational degree of freedom normal to the TPU surface in order to apply the normal force by dead weights. The holder is placed in one end of a horizontal arm that is balanced using counterweights that are placed in the other end. The friction force, i.e. the tangential force to the contact surface that is directed against the sliding direction, is measured from the deflection of the horizontal arm using strain gages.

[27]MicroTest MT/60/NI/1000rpm

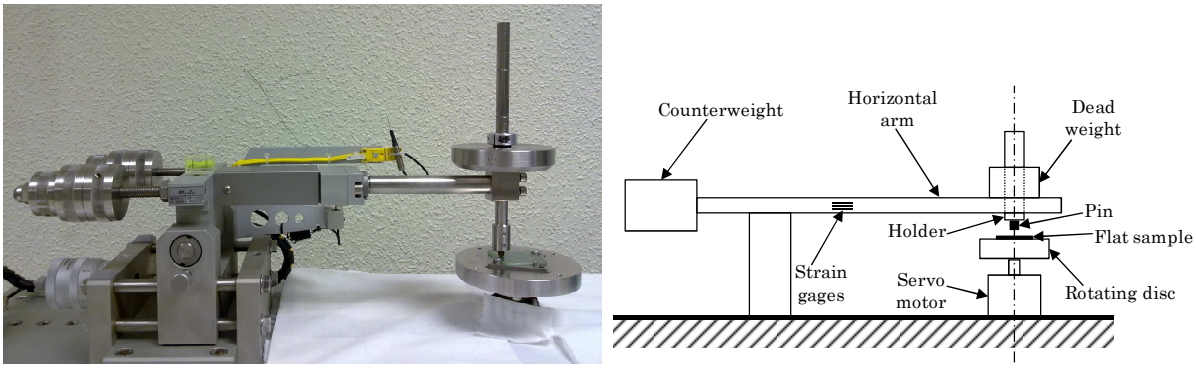

Figure 7.3: Tribometer test rig.

7.2.2 Specimens of friction tests

As in experimental tests of normal contact, the TPU sheets of reference thickness $\delta_{ref} = 2$ mm that had been processed by extrusion (Section 4.1) were cut into square specimens with the dimensions 40x40 mm, (Figure 7.4).

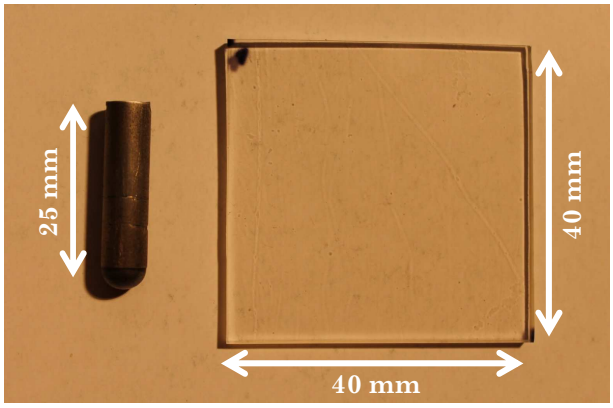

Figure 7.4: TPU specimen and gray iron pin of the experimental tests of friction.

In order to characterize experimentally a realistic contact between the TPU coated steel wire rope and the drive sheave, the hemispherical pins of gray iron were machined from a whole drive sheave which is used in the lift industry. Firstly, a ring was cut of the outside of the sheave by electric discharge machining (EDM). Secondly, this ring was cut by EDM in prismatic sections that were machined into cylinders with diameter of 6 mm. Finally, these cylinders were also cut longitudinally to the length of 26 mm by EDM and one end of them was machined into hemispherical shape. Thus ten different pins of gray iron (Figure 7.4) were obtained with length of 25 mm and radius of 3 mm.

Prior to testing the TPU specimens were cleaned with water and neutral soap to remove any possible surface contaminations. This cleaning procedure was chosen due to the TPU surface was very modified (Figure 7.5) with others products, as ethanol, acetone, etc.

The gray iron pins were also cleaned prior each trial. In this case, the cleaning procedure consists of three ultrasonic baths of 5 minutes with distilled water, acetone and ethanol in this order.

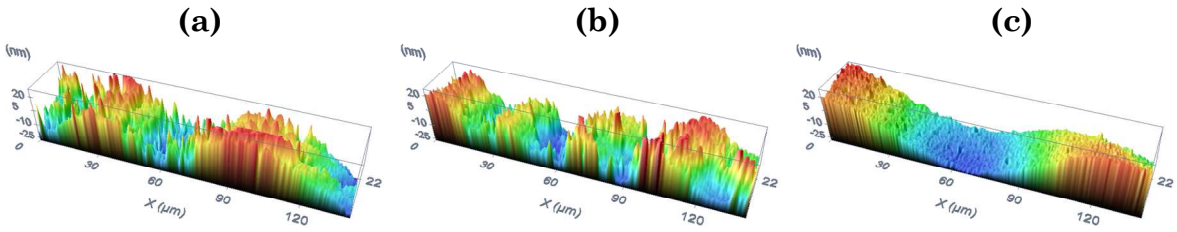

Figure 7.5: 3D topography scans of TPU surface that is (a) unclean, (b) cleaned with water and neutral soap and (c) cleaned with ethanol. The 3D topography scans (140x22x0.045 µm^3) were obtained using a confocal profilometer[28].

The TPU square specimens were fixed using double sided tape to avoid the movement during the experimental friction tests at metal sheets which were screwed on the rotating disc. The pins were placed into the holder of tribometer securing them by means of screws (Figure 7.6).

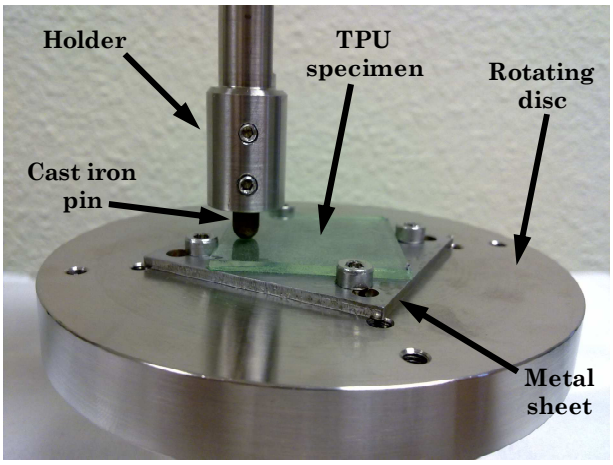

Figure 7.6: Set up of the experimental friction tests with the TPU specimen and gray iron pin.

[28]Sensofar Plµ

7.2.3 Methodology of friction tests

The contact partners (TPU and gray iron) were tested at a broad range of test conditions (Table 7.1) in order to investigate the frictional behaviour, but taking into account the work conditions of the contact partners and the limits of the tribometer. Therefore the normal forces ranged from 5 N to 40 N due to the contact pressures are low (<10 MPa) between the TPU cover and the drive sheave of gray iron in lift industry. The range of sliding velocities included values from 0.5 $\text{mm}\cdot\text{s}^{-1}$, because of lower velocities than this value are not controlled accurately by the tribometer, to 1100 $\text{mm}\cdot\text{s}^{-1}$. This wide rage of velocities was chosen due to the known logarithmic dependence of friction coefficient with the sliding velocity (Figure 7.1).

All the tests were repeated three times and they are conducted at 23±2 ºC. Moreover, in order to avoid effects of the pins in the friction measurements, each test under the same conditions of sliding velocity and normal force was carried out using a different pin from the available ones.

The sliding time was chosen to reach a stationary friction force, which was reached when the friction force did not varied in at least one third of the total test time. Therefore, the total sliding time, whose values are pointed in Table 7.1, of each friction test depended on the sliding velocity. $\delta_{\text{ref}} = 2$

Table 7.1: Conditions and contact partners of experimental friction tests.

Test conditions		
	Sliding velocity v [$\text{mm}\cdot\text{s}^{-1}$]	0.5 – 5 – 50 – 500 - 1100
	Normal load F_N [N]	5 – 10 – 20 – 30 – 40
	Sliding time t [s]	4×10^4 – 6×10^3 – 8×10^3 – 2.7×10^2 – 10^2
Contact partners		
	Hemispherical pin	Gray iron R = 6 mm
	Flat surface	TPU 40x40 mm $\delta_{\text{ref}} = 2$ mm

7.2.4 Processing of friction data

After each test, different friction coefficients were derived from the recorded values using Matlab. Figure 7.7 shows the different friction coefficient and the states of the experimental tests. The friction coefficient μ was calculated dividing the measured data of friction forces by the applied normal load. The initial friction coefficient μ_{in} represents the average value calculated from the first ten data of the test. Meanwhile the stationary friction coefficient μ_{st} represents the average value calculated from the data of the last third of the test.

Moreover the experimental data of each test were smoothed using *smooth* function of Matlab. In this case, the *smooth* function uses Savitzky-Golay filter which is a generalized moving average with filter coefficients determined by an unweighted linear least-squares regression and a polynomial model of specified degree. This filter was chosen because it tends to preserve better features of the initial points such relative maxima and minima and their widths than other smooth techniques or filters. Therefore, using the smooth data, the peak friction coefficient μ_{pk} was determined of each test. This peak friction coefficient represents the maximum value of the friction coefficient that is unaffected by the dispersion of the experimental data.

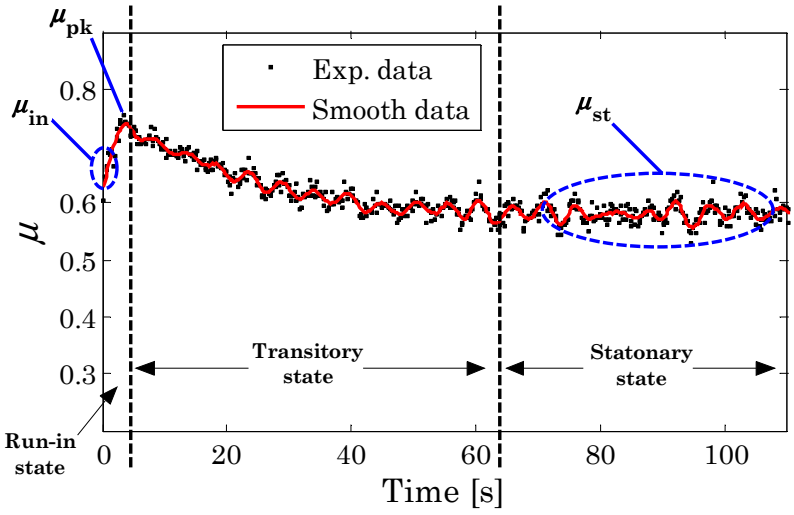

Figure 7.7: States of experimental test and friction coefficients from the experimental data ($F_N = 20$ N and $v = 500$ mm $\cdot$ s^{-1}).

7.3 Results of friction tests

From the experimental data of friction coefficient is shown that the friction of the TPU exhibits clearly two different behaviours, unsteady and steady. Therefore these friction behaviours are discussed separately.

7.3.1 Unsteady friction behaviour

During the beginnings of relative movement, the friction behaviour varies as the sliding time until a steady coefficient of friction is reached. But this friction behaviour presents an evolution of friction coefficient depending on sliding velocity.

At high sliding velocities ($\geq 50\ \mathrm{mm \cdot s^{-1}}$), the friction coefficient increases with the sliding time (run-in state) until a limiting value and then the friction coefficient decreases (transitory state) until a constant value (stationary state), see Figure 7.7. At given sliding velocity, the values of friction coefficient are smaller with increasing normal load (Figure 7.8), which is as expected (Figure 7.1). Moreover it should be pointed out that the maximum value (peak friction coefficient) is reached before with the increase in normal load, i.e. the run-in state lasts less time. But the constant friction coefficient appears to be reached at the same sliding time.

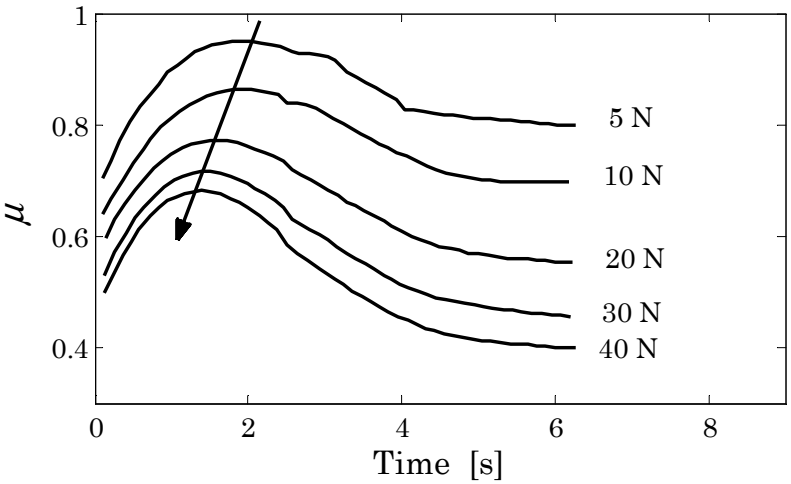

Figure 7.8: The evolution of friction coefficient smoothed using Savitzky-Golay filter during unsteady friction behaviour ($v = 1100\ \mathrm{mm \cdot s^{-1}}$).

At low sliding velocities ($\leq 5\ \mathrm{mm \cdot s^{-1}}$), the friction coefficient gradually increases with the sliding time (run-in state) until a constant value (Figure 7.9), i.e. there is not transitory state. At a given sliding velocity, the constant value is reached at the same sliding time.

Therefore the run-in state occurs at about the same time irrespective of normal load. But the values of friction coefficient are smaller with increasing normal load.

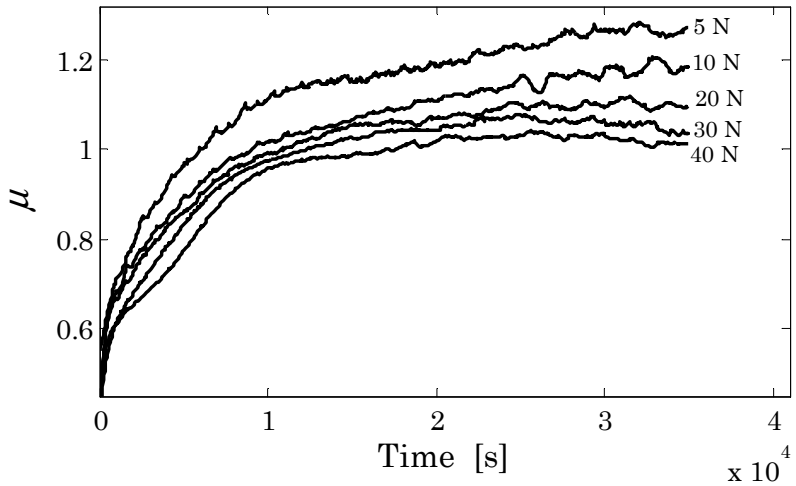

Figure 7.9: The evolution of friction coefficient smoothed using Savitzky-Golay filter during unsteady friction behaviour ($v = 0.5$ mm $\cdot$ s^{-1}).

Initial friction coefficient

It follows from Figure 7.10 that the initial coefficient of friction μ_{in} appears to be more or less stable in all the experimental tests of friction, i.e. the initial coefficient of friction does not depend on sliding velocity or normal load.

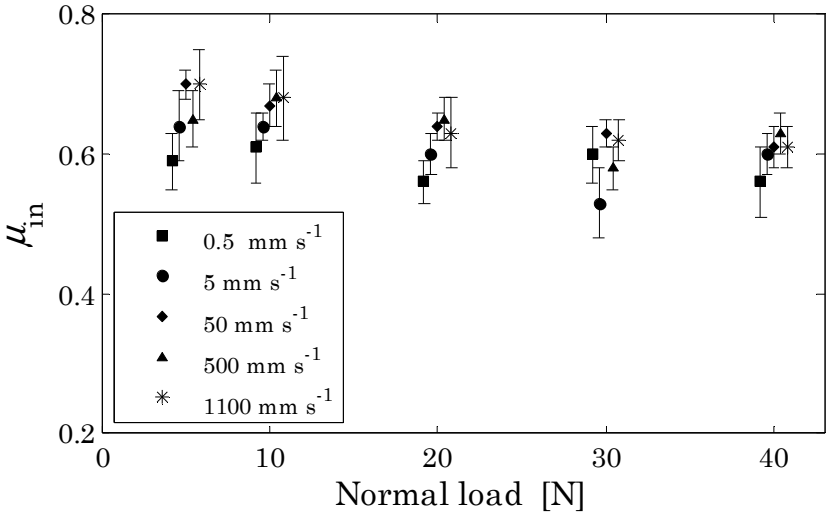

Figure 7.10: Initial coefficient of friction calculated from the experimental friction data of the TPU during unsteady friction behaviour.

Peak friction coefficient

Meanwhile, from Figure 7.11 it should be noted that the peak coefficient of friction decreases with increasing normal load as well as sliding velocity. Moreover, as the peak friction coefficient is not exhibited at low sliding velocities then it should present a maximum depending on sliding velocity between 5 $mm \cdot s^{-1}$ and 50 $mm \cdot s^{-1}$.

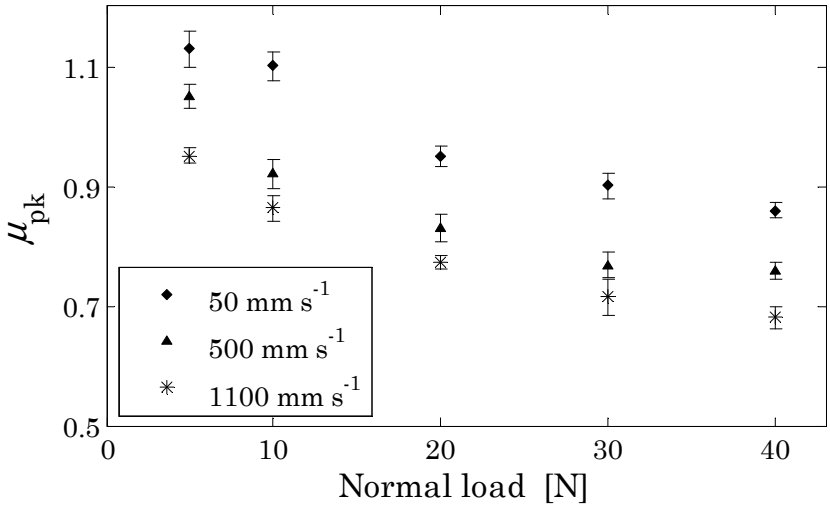

Figure 7.11: Peak coefficient of friction calculated from the smoothed friction data of the TPU during unsteady friction behaviour.

7.3.2 Steady friction behaviour

After of unsteady friction behaviour, all the experimental tests becomes at steady friction behaviour, i.e. the stationary state is reached. In this state it is calculated the stationary friction coefficient μ_{st}, see Section 7.2.4. The values of such friction coefficients are summed up in Table 7.2.

It comes out from the results obtained that the stationary coefficient of friction is decreased with an increase in normal load as well as in sliding velocity. Therefore the behaviour of stationary friction coefficient depending on normal force is as expected (Figure 7.1) from literature. But the behaviour of stationary friction coefficient depending on sliding velocity does not present the expected maximum.

Table 7.2: Values of the stationary friction coefficients calculated from the experimental friction data of the TPU depending on sliding velocity and normal load.

	5 N	**10 N**	**20 N**	**30 N**	**40 N**
0.5 mm · s^{-1}	1.24±0.09	1.16±0.04	1.06±0.03	0.97±0.02	0.95±0.02
5 mm · s^{-1}	1.13±0.02	1.03±0.03	1.0±0.1	0.96±0.02	0.92±0.06
50 mm · s^{-1}	1.06±0.04	0.94±0.01	0.82±0.01	0.76±0.04	0.69±0.01
500 mm · s^{-1}	0.80±0.01	0.67±0.05	0.58±0.01	0.54±0.02	0.54±0.02
1100 mm · s^{-1}	0.78±0.03	0.60±0.01	0.52±0.01	0.44±0.01	0.40±0.01

7.3.3 Discussion of friction behaviour

In unsteady friction behaviour, all the TPU friction tests starts with more or less the same (initial) friction coefficient (see Figure 7.10), this fact can be due to wear is not yet occurred. Then the friction coefficient gradually increases with sliding time until a constant value (stationary coefficient of friction) at low sliding velocities (≤ 5 mm · s^{-1}) or until a limiting value (peak coefficient of friction) at high sliding velocities (≥ 50 mm · s^{-1}). This increment of friction coefficient should be due to the contact area is increased in size by the deformation and wear. The different behaviour depending on the sliding velocity can be due to the effect of local temperature, according to Persson (2006) who found that the rubber friction is altered by local heating of the rubber block sliding on an asphalt surface at velocities higher than 10 mm · s^{-1}.

Finally the friction behaviour of the TPU experimental tests becomes steady. The (stationary) coefficient of friction (Table 7.2) exhibits the expected behaviour depending on normal load, i.e. it decreases with increasing normal load. But the friction coefficient does not present the characteristic maximum depending on sliding velocity. This fact may be explained by two different reasons. First, the maximum is not yet reached due to the sliding velocity is not sufficiently low. But, taking into account the values of sliding velocities at which the maximum friction coefficients are found in the literature for rubbers, this reason appears to be the most unlikely. Second, the TPU friction does not present a maximum depending on sliding velocity. In order to decide what is the appropriate, then experimental friction tests at lower sliding velocities than the tested ones would be required, but they can not be carry out accurately due to the limits of the used tribometer.

7.4 Friction model

An analytical friction model to be implemented in numerical calculus by means of finite element method was developed using the experimental stationary coefficients of friction. In order to accomplish this friction model, firstly the equivalences between the tested normal loads and the mean contact pressure in the pin-on-disc configuration of experimental friction tests were determined. Then the experimental data were fitted using a non-linear regression with known models for rubbers of the literature and new proposed models.

7.4.1 Equivalences between normal force and contact pressure

In order to remove any effect of contact area, the normal load of experimental friction tests should be related to the corresponding mean contact pressure. Therefore, using the finite element model of indentations (see Section 6.4.2.), new computational force-controlled frictionless indentations were carried out. The mean contact pressure was calculated dividing the normal load applied by the contact area from the finite element model. The results to 5, 10, 20, 30 and 40 N were 4, 5.12, 5.73, 6.88 and 7.5 MPa, respectively.

7.4.2 Friction models considered

Firstly friction models for rubbers of the literature, as Rieger (1968), Gutzeit et al. (2004), Wriggers and Reinelt (2009), Moldenhauer and Kröger (2010), etc. (see Section 2.6.3), were probed, but the fittings were unsatisfactory.

Therefore, taking into account the different friction models of rubbers that were found in the literature, it was proposed a general mathematical expression

$$\mu(p,v) = f(p) + f(v) + f(p,v), \tag{7.2}$$

between the output variable, i.e. coefficient of friction μ, and the predictive variables, i.e. sliding velocity v and contact pressure p. This general expression consists of three terms; a function of contact pressure, a function of sliding velocity and another one of the interaction between both variables. Thus, considering different classes of functions (potential, exponential, logarithmic…), the friction model of the TPU was fitted using non-linear regressions.

7.4.3 Friction model of the TPU

The best fitting, i.e. whose sum of squared residuals was minimum with less coefficients (Figure 7.12), of the experimental friction data consists of a potential function of contact pressure, a logarithmic function of sliding velocity and an exponential function of the interaction between them,

$$\mu(p,v) = c_1 p^{c_2} + c_3 \ln v + c_4 e^{c_5 pv}. \quad \textbf{(7.3)}$$

This friction model has five coefficients c_i to be determined. The values are indicated in Table 7.3.

Table 7.3: Coefficients of friction model of the TPU.

Coefficient	Value
$\mathbf{c_1}$	2.52±0.09
$\mathbf{c_2}$	-0.40±0.02
$\mathbf{c_3}$	-0.101±0.005
$\mathbf{c_4}$	-0.28±0.04
$\mathbf{c_5}$	-0.05±0.01

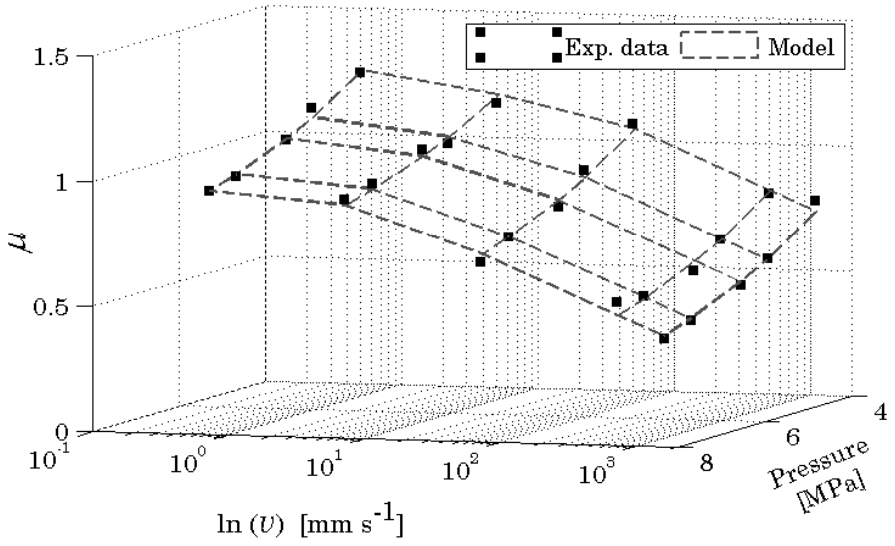

Figure 7.12: Fitting model of experimental friction data of the TPU.

7.5 Computational experiments of TPU friction

The computational experiments of friction tests were carried out using the package ABAQUS/Standard 6.8 (Simulia 2009) which works well for modellings subjected to large deformations and where complex contact and friction is encountered (Sun et al. 2006).

7.5.1 Modelling of friction tests

The computational experiments of friction tests were solved as 3D force-displacement-controlled models (Figure 7.13). The pin of gray iron, used in the experimental tests, is modelled as rigid body due to the large difference in tensile modulus compared to the TPU. Therefore, assuming no deformations of the rigid body, the computational costs are reduced. The TPU was characterized using the hyperelastic model with deformation history, Equation (5.12), with 8-node hybrid linear brick elements with hourglass control (C3D8RH). Friction between rigid body and TPU was characterized using the friction model proposed.

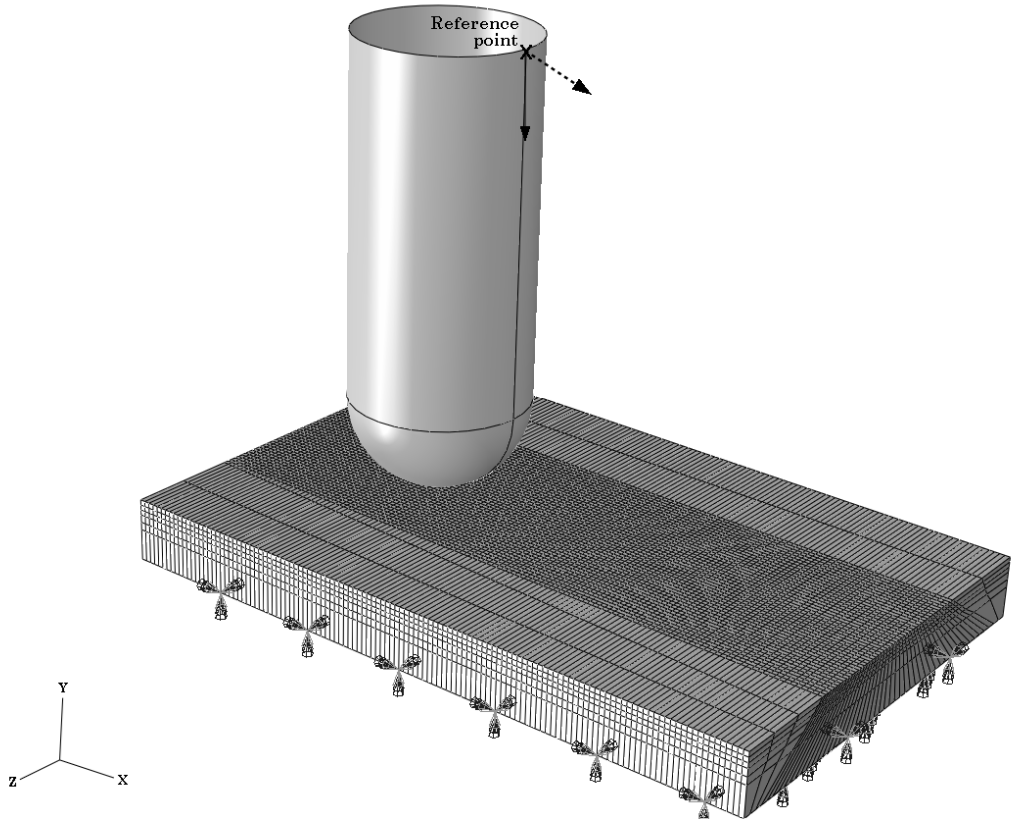

Figure 7.13: FEA model of computational experiments of friction tests.

The finite element model consisted of 37800 elements. The mesh density is greater on the top of TPU sheet, i.e. where the contact is occurred. The bottom of TPU sheet was fixed fully. In the first step, a normal force was applied on the reference point which controlled boundary conditions of rigid body. In the second step, a sliding displacement is enforced at the reference point of rigid body.

7.5.2 Results of computational experiments

The coefficient of friction, which is calculated dividing the total reaction force at the reference point of the rigid body by the normal force applied, is compared with the stationary coefficient of friction that are measured experimentally (Figure 7.14). Taking into account the approximations and assumptions that were considered to develop the friction model of the TPU, it should be pointed out that the proposed friction model works properly when it is implemented into the finite element. Moreover it bears in mind that the friction model is developed using coefficients of friction at macroscale level but it is applied locally into the numerical calculus of finite elements, i.e. it is applied at each point contact element. But the computational results appear to be no influenced by this scale problem due to the distribution of the contact pressures in pin-on-disc configuration may be considered rather uniform to the applied normal loads (see Figure 6.32).

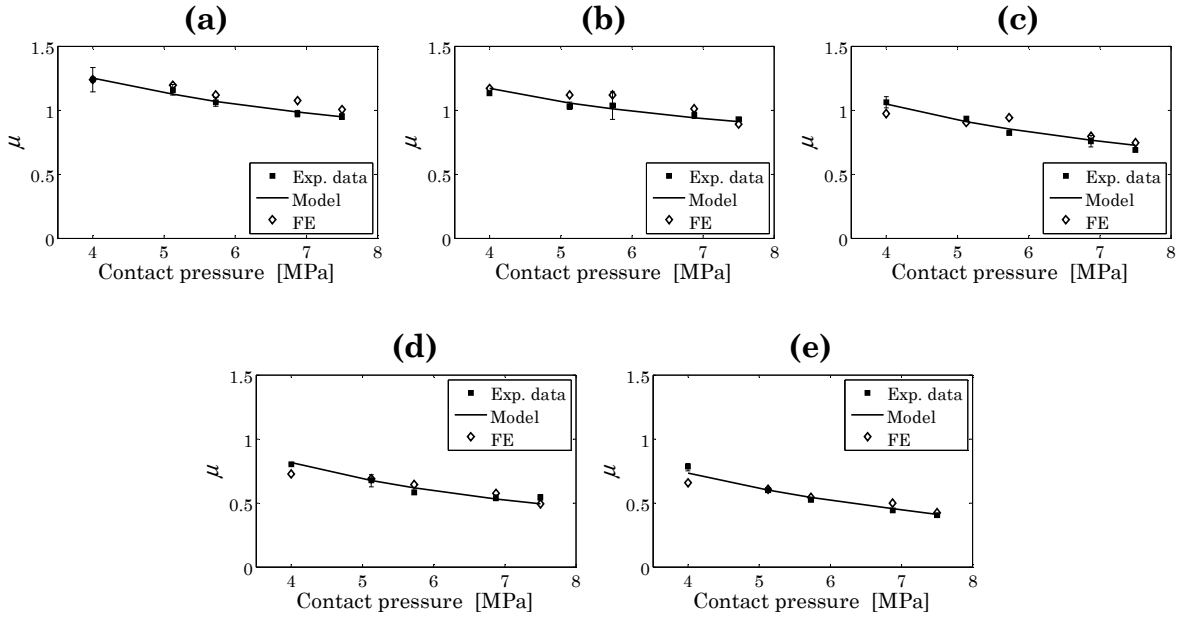

Figure 7.14: Comparison between the coefficients of friction that are measured experimentally determined using analytic model and calculated computationally at (a) $v = 0.5$ mm·s^{-1}, (b) $v = 5$ mm·s^{-1}, (c) $v = 50$ mm·s^{-1}, (d) $v = 500$ mm·s^{-1} and (e) v=1100 mm·s^{-1}.

The largest relative error between computational results and its corresponding value, that is calculated with the friction model proposed, is about ~15% (only for two cases, for the rest of them the relative errors are <10%). But it bears in mind that the friction model was developed using these same experimental data of fiction tests which are calculated computationally. Therefore the friction model of the TPU is validated under different experimental conditions in the following section.

Friction model at locally level

When it is checked the applied friction model at locally level, i.e. node to node, the finite element code smoothes the implemented friction coefficient in some cases (Figure 7.15). This smoothing appears to be applied to avoid problems of continuity, which may be due to the friction coefficient can reaches very different values at neighbouring nodes. Therefore, the mistakable dynamic effects due to very different friction forces at neighbouring nodes are minimized using smooth values. This fact should be considered whether the friction model is used with others finite element models.

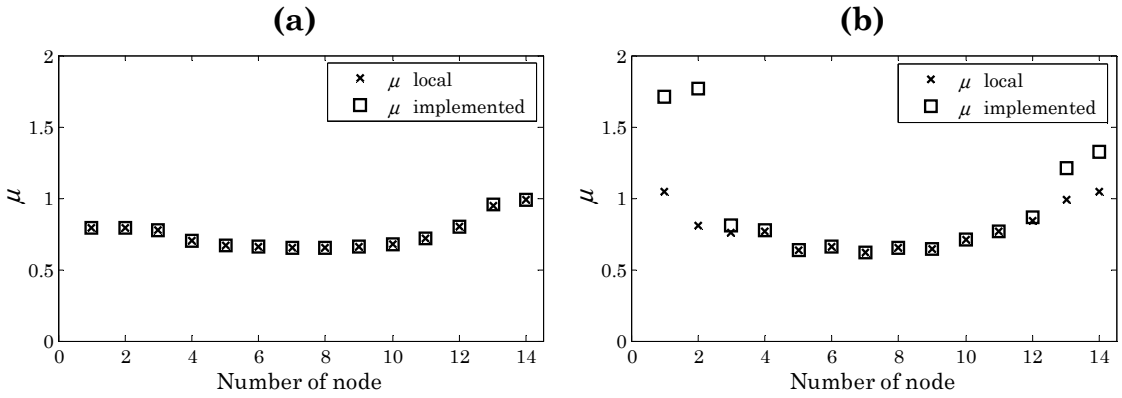

Figure 7.15: Comparison between the coefficient of friction implemented and the actually used locally by finite element code in (a) longitudinal and (b) transversal paths over the contact area (20 N and 50 mm s^{-1}).

7.6 Validation: reciprocating friction

This section describes the friction tests and their conditions that were carried out to validate the friction model proposed for the TPU. The objective of this validation is to discuss the capacity of prediction of the friction model, which was characterised under specific conditions (see Sections 7.3 and 7.4), under different conditions in normal load as well as in sliding velocity with a reciprocating movement.

7.6.1 Friction tests under reciprocating relative movement

Originally the reciprocating movement of the tribometer[29] was obtained transmitting the rotary movement of the servo motor to a device (a guided car) by means of a crank. Thus the evolution of sliding velocity was sinusoidal (Figure 7.16, dotted line), which is inadequate whether the friction tests should be controlled by velocity.

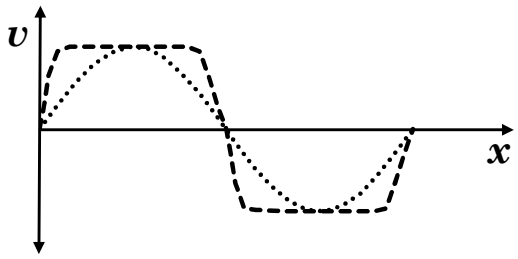

Figure 7.16: Schematic sinusoidal (dotted line) evolution of sliding velocity and quasi-constant evolution (dashed line).

Device to reciprocating friction at constant sliding velocity

Therefore, in order to carry out the friction tests under reciprocating movement at constant sliding velocity, a new device was designed, built and proved. This device consists basically of two gears and a chain which is fixed to the guided car of the tribometer (see Figure 7.17). In this way the new device allows to converse the rotary movement of the motor to a movement with a constant sliding velocity during most of the stroke (Figure 7.16, dashed line).

[29]MicroTest MT/60/NI/1000rpm

Experimental conditions of reciprocating friction

As initial, the geometry of contact was kept, thus hemispherical pins of radius $R = 3$ mm and TPU sheets of reference thickness $\delta_{ref} = 2$ mm were used to carry out the friction tests with reciprocating movement of sliding stroke $\Delta x = 105$ mm.

Prior each test, the TPU specimens were cleaned with water and neutral soap to remove surface contaminations and the gray iron pins were cleaned by means of three ultrasonic baths of 5 minutes with distilled water, acetone and ethanol in this order, as it is noted in Section 7.2.2.

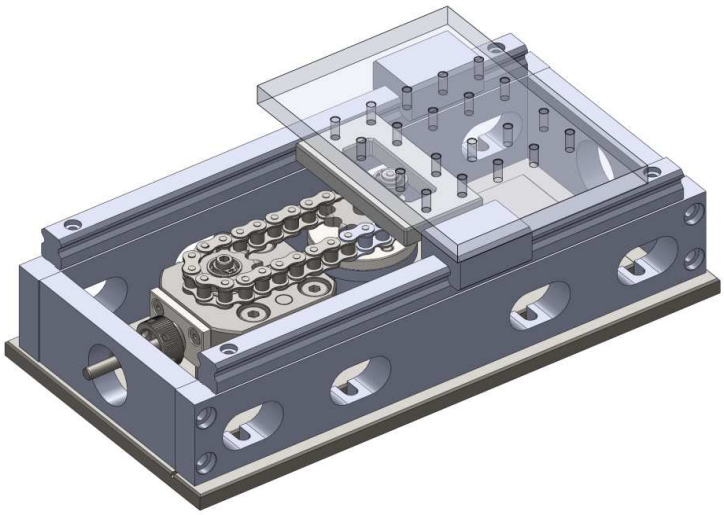

Figure 7.17: Device developed to get reciprocating friction tests at constant sliding velocity.

Two different sliding velocities and normal loads, whose values had to be between the ranges tested to obtain the friction model, were chosen to be tested. The test conditions are summarized in Table 7.4. All the tests were repeated three times and they are conducted at 23±2 ºC. As it is pointed out below (Section 7.2.3), different pin was used in each test under same conditions in order to avoid effects of the pins in the friction measurements. The sliding time was chosen to reach a stationary friction force due to the stationary coefficient of friction was used to fit the model.

Table 7.4: Conditions and contact partners of friction tests with reciprocating movement.

Test conditions		
	Sliding velocity v [$\mathrm{mm \cdot s^{-1}}$]	7.5 – 75.5
	Normal load F_N [N]	7.5 – 25
	Number of cycles	200 – 400
	Sliding stroke Δx [mm]	105
Contact partners		
	Hemispherical pin	Gray iron R = 6 mm
	Flat surface	TPU 130x80 mm $\delta_{ref} = 2$ mm

Experimental results of reciprocating friction

After each test the coefficient of friction were derived from the record values. In these reciprocating tests, the coefficient of friction was calculated using two different ways. First, the recorded values of friction force during the stroke at constant sliding velocity were divided by the applied normal force. Second, the friction force is calculated from the area inside the friction loops (Figure 7.18). This area corresponds to the friction energy dissipated during one cycle. The results of two ways are similar values of friction coefficient (Figure 7.19).

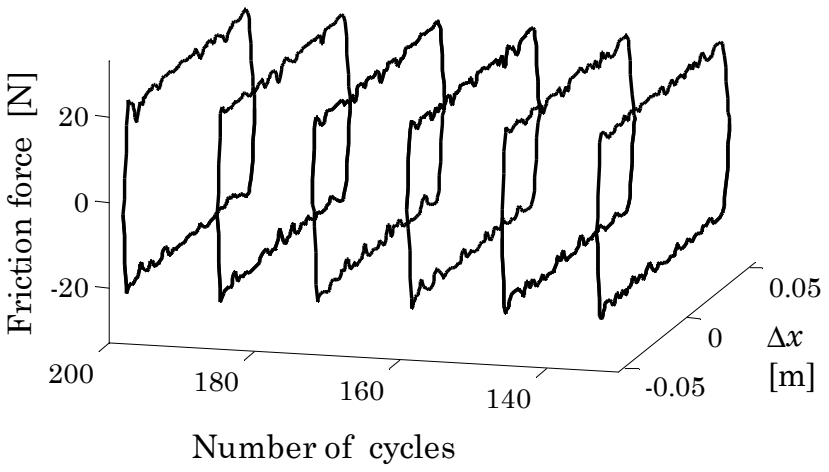

Figure 7.18: Sliding stroke loops of friction force at different cycles (v = 7.5 $\mathrm{mm \cdot s^{-1}}$ and F_N = 25 N).

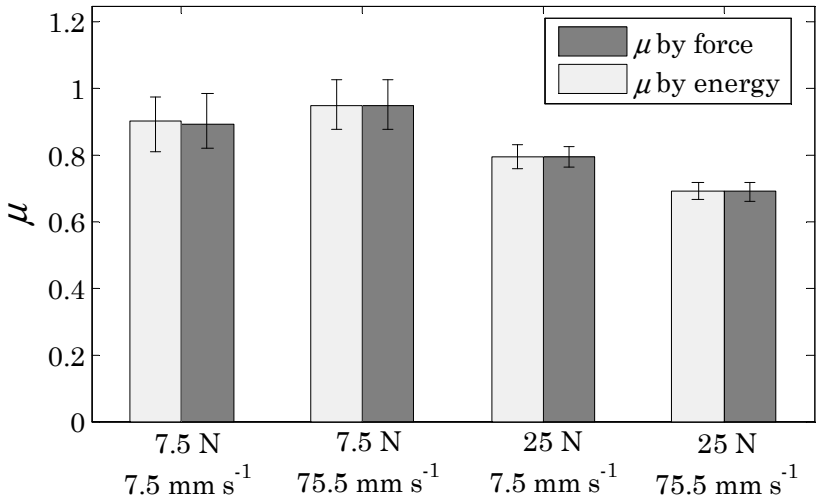

Figure 7.19: Comparison between the coefficients of friction calculated using the measured friction force and using the friction energy dissipated during one cycle.

7.6.2 Computational experiments

Using the finite element model described in Section 7.5.1, the computational experiments were carried out taking into account the conditions of friction tests under reciprocating movement. It is follow from Figure 7.20 that the computational values are slightly greater than the experimental friction coefficients, except to 7.5 N at 75.5 $mm \cdot s^{-1}$.

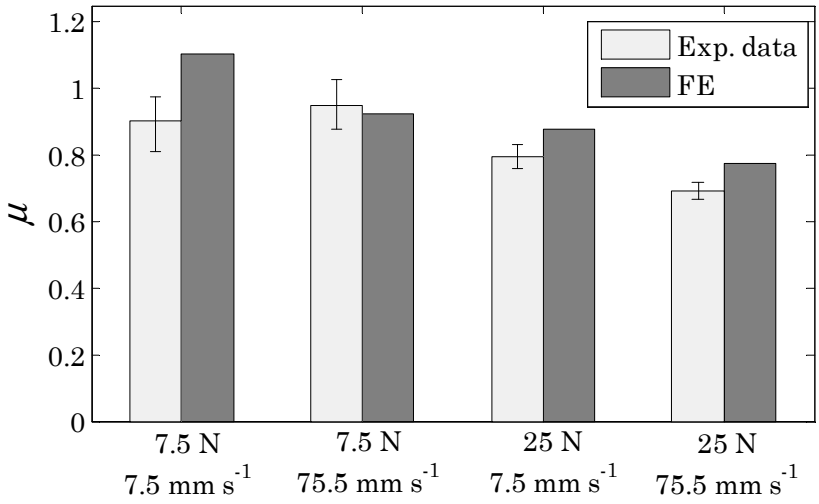

Figure 7.20: Comparison between the experimental and computational coefficients of friction under reciprocating movement.

7.6.3 Discussion of reciprocating friction tests

The value of stationary coefficient of friction under reciprocating conditions does not depend on the method to calculate it from the experimental friction forces recorded in tests (Figure 7.19). Nevertheless the experimental results present an unexpected behaviour, i.e. the friction coefficient increases with an increment in sliding velocity to 7.5 N. Moreover slight higher dispersions than rotating tests are exhibited. Therefore friction tests were carried out under reciprocating movement with some of the previously tested conditions using rotating pin-on-disc (10 N – 500 $mm \cdot s^{-1}$, 20 N – 50 $mm \cdot s^{-1}$ and 30 N – 5 $mm \cdot s^{-1}$). The results obtained in reciprocating tests were approximately 10% lower than rotating tests (Figure 7.21).

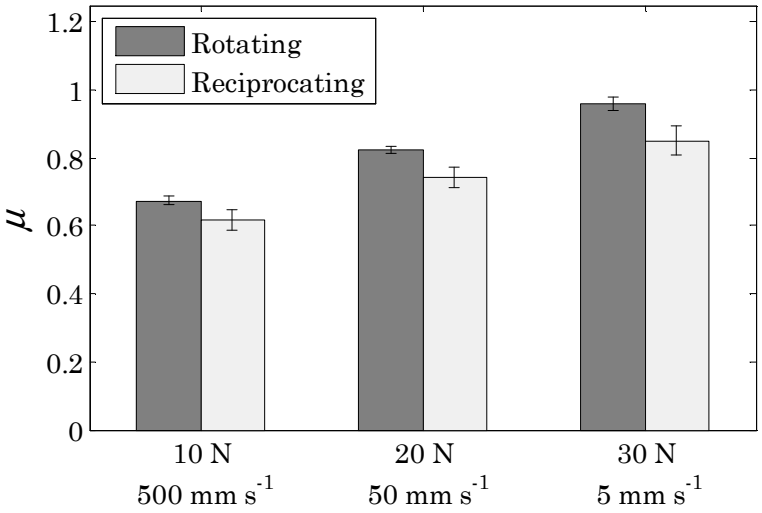

Figure 7.21: Comparison between the experimental coefficients of friction under rotating and reciprocating conditions.

Therefore it appears that the reduction in friction coefficient is facilitated by the configuration of friction tests under reciprocating movement. Taking into account that the reciprocating movement is followed in a linear path and that the elastomers tend to wear by means of frictional wear (Zhang 2004), i.e. by roll-formation, it may be concluded that the rolled wear debris (Figure 7.22) act as third-body lubricating the contact, i.e. rolled wear debris of TPU are accumulated between the pin and the TPU surface. Moreover the largest dispersions, which are presented in these tests, would be also explained by this fact.

This effect is higher in reciprocating movement due to the free debris of TPU in rotating movement are ejected by the centrifugal force.

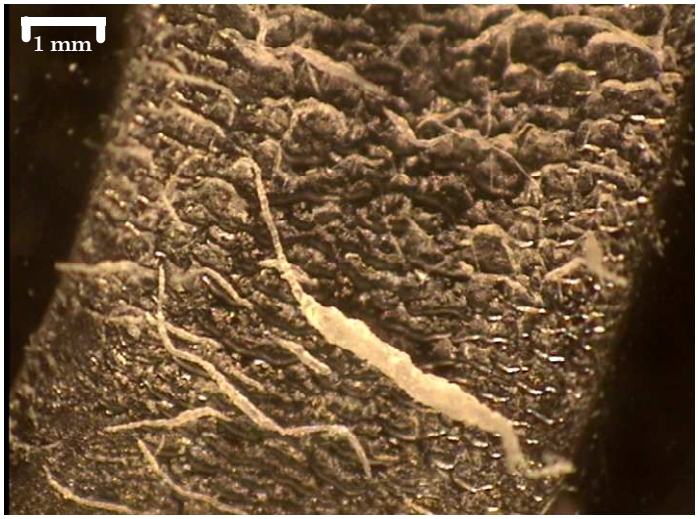

Figure 7.22: Fibril shaped debris of TPU wear generates by roll-formation or frictional wear ($v = 7.5$ mm $\cdot$ s^{-1} and $F_N = 7.5$ N).

7.7 Conclusions

The behaviour of the TPU in tangential contact or sliding is discussed. Thus, firstly, the tangential contact between the TPU and a gray iron is analyzed experimentally in terms of their frictional behaviour. The sliding velocity and normal load dependence was investigated when the gray iron slides over the TPU in a configuration of pin-on-disc. The resulting friction behaviour is characterized using the coefficient of friction. This varies as the sliding time until a steady value, therefore unsteady and steady friction behaviours were presented.

In unsteady friction behaviour, it was shown that the initial coefficient of friction is approximately constant and then it gradually increases with sliding time until a value which depends on the sliding velocity. At high sliding velocities ($\geq 50\ \text{mm} \cdot \text{s}^{-1}$) it is a limiting value, i.e. a maximum or peak value. However, at low sliding velocities ($\leq 5\ \text{mm} \cdot \text{s}^{-1}$) reaches directly the constant value of steady friction behaviour.

In steady friction behaviour, it was shown that the coefficient of friction decreases with increasing normal load as well as sliding velocity. Assuming that the friction coefficient in this steady behaviour characterizes the friction between the TPU and the gray iron, then it is proposed an analytic friction model, Equation (7.3), depending on the sliding velocity and contact pressure.

Using the constitutive model with strain history to characterize the mechanical behaviour of the TPU, the proposed friction model was also implemented in finite element to be probed. It was shown that the computational results agree with the experimental data.

Finally, it was studied the capacity of prediction of proposed friction model between the TPU and the gray iron under different conditions as well as reciprocating movement. It was shown that the computational results are poor due to the experimental data between the different sliding movements are not equivalent. Since the wear debris of TPU appears to act as lubricant during the contact in the reciprocating tests of friction.

8 CONCLUSIONS AND FUTURE WORKS

"There is as yet insufficient data

for a meaningful answer"

"The last question", Isaac Asimov

The work presented in this study investigates the contact experienced by an extruded thermoplastic polyurethane elastomer (TPU) against a rigid body (gray iron in sliding contact). The discussion of contact behaviour, which is divided between normal (indentation) and tangential (sliding) contacts, is carried out experimentally as well as computationally. For the purpose of this, the mechanical behaviour of the TPU and the friction behaviour with the gray iron are also investigated in this work.

8.1 Concluding remarks and findings of mechanical behaviour

The complex mechanical behaviour (hyperelasticity, viscoelasticity and inelastic effects) of the TPU as elastomer was investigated under cyclic loading-unloading conditions, i.e. preconditioned behaviour, at moderate strains (up to 100%) in this work. It was shown experimentally that the hyperelastic behaviour of the TPU depends strongly on the maximum strain ever experienced. But it is not affected by the strain-rate over one order of magnitude and appears to be slightly affected by the stretching direction in pure shear conditions. It was also shown experimentally that the viscoelastic behaviour of the TPU is linear, i.e. it is independent of the tensile strain.

The inelastic effects (stress softening, residual strain and hysteresis loss) were also studied under loading-unloading conditions. It was observed that the inelastic effects are unaffected by the deformation state under which the TPU is stretched at strains below the yield stress. However the behaviour of the inelastic beyond the yield stress and depending on maximum strain, strain-rate and stretching direction is not fully understood.

Future works of mechanical behaviour

In order to clarify the results for the inelastic effects, it is suggested that a study of the microstructure regarding to the hard and soft segments should be considered, e.g. swelling before and after the experimental tests of samples in solvents that do not destroy hard blocks. These results would allow knowing quantitatively what part of hard domain is destroyed during tests. Moreover, using infrared spectroscopy, the separation between hard and soft phases as well as the hydrogen bonding would be analyzed.

8.2 Concluding remarks and findings of material model

Using the experimental data in homogeneous deformation states (uniaxial tension and pure shear), an analytic material model of preconditioned mechanical behaviour of the TPU is proposed by means of an overlay visco-hyperelastic models depending on the maximum strain reached, so called material model of homogeneous deformation states. The hyperelastic (non-linear stress strain) behaviour was modelled using Yeoh SEDF. And Prony series were used to model the linear viscoelastic behaviour of TPU. It was shown that this proposed material model predicts accurately the mechanical behaviour in homogeneous deformation states at strains below 100%, but it is not enforced in inhomogeneous deformation states.

In order to predict the mechanical behaviour under inhomogeneous strain states, another analytic material model is proposed considering strain history, i.e. maximum strain ever experienced, so called material model with deformation history. The strain history was modelled by fitting functions of the Yeoh model parameters and it was implemented into numerical calculus using a FEA based technique that is developed innovatively for this purpose. It was shown and confirmed that this proposed material model of the TPU works accurately under inhomogeneous deformation states and in compression conditions, despite it had been developed using experimental data in tensile deformation states.

Future works of material model

Future investigations might wish to complete the material model with deformation history for un-preconditioned behaviour of the TPU, i.e. the virgin behaviour. This fact can be achieved characterizing and modelling the un-preconditioned behaviour and implemented into numerical calculus using a step function. Moreover it might be optimized the FEA based technique to be more robust and to reduce the computation time. Further investigations might wish to include the inelastic effect that can not be modelled using the viscoelastic model, as the stress softening beyond the yield stress. Finally it also might be considered thermal and dynamic effects.

8.3 Concluding remarks and findings of normal contact

The normal contact behaviour of the TPU was discussed regarding to compressive load, contact area and contact pressure distribution. For this purpose, experimental indentations of a hemispherical rigid body over the TPU sheets were carried out. Moreover, using the constitutive model of the TPU with deformation history, computational indentations also were performed.

Using experimental and computational experiments of indentations it was shown and confirmed that the compressive load in function of the indentation depth is affected by the support underneath the TPU felt, but it can be modelled using a correction of Hertz theory depending on the ratio of the radius of indenter and the thickness of the TPU that is not deformed. Moreover, it was also shown that the results of experimental and computational indentations agree regarding to compressive load.

Taking into account that only the contact area with pressures higher than 2.5 were considered computationally and experimentally, it was shown that the results of both agreed quite successfully. Moreover the total computational contact area, i.e. without restriction, was also considered, and it was found that they depends on compressive load linearly.

Finally the experimental results of distribution of contact pressures fully disagree with the computational results. In view of the computational results for compressive load and contact area, the technique of measurement using pressure measuring films appears to be inappropriate for distributions of contact pressure.

Future works of normal contact

As the measurement technique using pressure measuring films appears to be inappropriate for contact pressures, it is suggested that they might be experimentally investigated using other techniques, as micro-indentation, pressures sensors, etc. Moreover it might be considered the roughness of TPU and counterpart as well as the adhesion forces between them.

8.4 Concluding remarks and findings of friction and tangential contact

The friction behaviour between the TPU and a gray iron in tangential contact or sliding was discussed depending on sliding velocity and normal load using a pin-on-disc configuration. It was shown that the friction evolution depending on sliding velocity is different during the unsteady behaviour, i.e. when the coefficient of friction varies as the sliding time. At low velocities ($\leq 5\ mm \cdot s^{-1}$), the friction coefficient gradually increases until a constant value, but at high velocities ($\geq 50\ mm \cdot s^{-1}$) the friction coefficient exhibits a maximum from which decreases until a constant value. It was also shown that the coefficient of friction decreases with increasing normal load as well as sliding velocity in steady friction behaviour.

Using the friction coefficient during the steady behaviour, a friction model between the TPU and the gray iron depending on the sliding velocity and contact pressure is proposed. This friction model between the TPU and gray iron and the material model with deformation history of the TPU were implemented in finite element and the obtained results were agreed with the experimental data.

Meanwhile it was confirmed that the capacity of prediction of proposed friction model, which is characterized under specific conditions, between the TPU and the gray iron is very limited under different conditions. This fact is due to the coefficient of friction are not equivalent between different relative movements and configurations of contact.

Future works of friction model

In order to develop further the contact sliding investigations in the future, particularly the computational study, it is advised that the friction behaviour should be characterized under configurations, relative movements and operative conditions, which are very close to the real work conditions. Moreover in these cases, it must also be considered the scale problem, i.e. friction models would be developed at macroscale level but they should be locally applied when they are implemented into numerical calculus using finite element method.

On the other hand, the implementation might be required controlling precisely taking into account that the finite element code smoothes the implemented friction coefficient in some cases. Therefore it is suggested that to understand and to control using this smoothing, computational experiment series should be considered to analyze the results in detail.

CONFERENCES AND PUBLICATIONS

Withing the present thesis different contributions in national and international scientific congress and publications in international journals were presented:

Publications of international journals

Bartolomé, L., Aginagalde, A., Martínez A. B., Urchegui M. A. and Tato, W. (2011). Experimental characterization and modelling of large-strain visco-elastic behaviour of a thermoplastic polyurethane elastomer. *Rubber Chemistry and Technology* (ready for publication).

Bartolomé, L., Aurrekoetxea, J., Urchegui M. A. and Tato, W. Inelastic behaviour of an extruded thermoplastic polyurethane elastomer: Sensitivity to strain state and experimental conditions. Manuscript prepared for submission.

International conferences

Bartolomé, L., Tato, W., Urchegui M. A., Hernández, J. A. and Portolés, S. J. (2010). Initial steps in the definition of thermoplastic polyurethane elastomer/cast iron contact model by finite element method. In *Proceedings of Symposium on the Mechanics of Slender Structures (MoSS)*. San Sebastian (Spain).

National conferences

Bartolomé, L., Tato, W., Urchegui M. A., Aginagalde, A., Hernández, J. A. and Portolés, S. J. (2010). Análisis del rozamiento TPU/fundición existente en el contacto en un sistema cable-polea. In *Actas del XI Congreso Nacional de Materiales*. Zaragoza (Spain).

REFERENCES

Amontons, G. (1699). De la résistance causée dans les machines. *Histoire de l'Académie Royale des Sciences avec les Mémoires de Mathématiques et de Physique*, 257-282.

Archard, J. F. (1957). Elastic deformation and the laws of friction. *Proceedings of the Royal Society of London, Series A* **243**, 190-205.

Arruda, E. M. and Boyce, M. C. (1993). Three-dimensional constitutive model for the large stretch behavior of rubber elastic materials. *Journal of the Mechanics and Physics of Solids* **41**, 389-412.

ASM Handbook (1992). *Friction, lubrication and wear technology (vol. 18).* United States of America. ASM Internacinal.

ASTM (2005). *Test method for rubber property. Durometer hardness (ASTM D2240).* West Conshohocken (Pennsylvania, USA), ASTM International.

Barquins, M. (1993). Friction and wear of rubber-like materials. *Wear* **160**, 1-11.

Baumberger, T. and Caroli, C. (2006). Solid friction from stick-slip down pinning and aging. *Advances in Physics* **55**, 279-348.

Belytschko, T., Liu, W. K. and Moran, B. (2000). *Nonlinear finite elements for continua and structures*. Chichester (United Kingdom), John Wiley & Sons Ltd.

Besdo, D. and Ihlemann, J. (2003). A phenomenological constitutive model for rubberlike materials and its numerical applications. *International Journal of Plasticity* **19**, 1019-1036.

Bhushan, B. (2001). *Modern tribology handbook*. Boca Raton (Florida, USA). CRC Press LLC.

Blau, P.J. (2001). The significance and use of the friction coefficient. *Tribology International* **34**, 585-591.

Blundell, D. J., Eeckhaut, G., Fuller, W., Mahendrasingam, A. and Martin, C. (2002). Real time SAXS/stress–strain studies of thermoplastic polyurethanes at large strains. *Polymer* **43**, 5197-5207.

Bowden, F. P. and Tabor, D. (1964). *The friction and lubrication of solids*. Oxford (United Kingdom), Claredon Press.

Boyce, M. C. and Arruda, E. M. (2000). Constitutive models of rubber elasticity: A review. *Rubber Chemistry and Technology* **73**, 504-523.

Bradley, R. S. (1932). The cohesive force between solid surfaces and the surface energy of solids. *Philosophical Magazine* **13**, 853-862.

Brown, R. (2006). *Physical testing of rubber*. 4th Edition. New York (New York, USA), Springer Science+Business Media, Inc.

BS (2004). *Physical testing of rubber – Part 5: Guide to the application of rubber testing to finite element analysis (BS 903-5)*. London (United Kingdom), British Standards Institution.

Buckley, C. P., Prisacariu, C. and Martin, C. (2010). Elasticity and inelasticity of thermoplastic polyurethane elastomers: Sensitivity to chemical and physical structure. *Polymer* **51**, 3213-3224.

Buehler, B. (2006). *Molecular adhesion and friction at elastomer-polimer*. University of Akron. Akron (Ohio, USA).

Busfield, J. J. C. and Thomas, A. G. (1999). Indentation tests on elastomer blocks. *Rubber Chemistry and Technology* **72**, 876-894.

Bush, A. W., Gibson, R. D. and Thomas, T. R. (1975). The elastic contact of a rough surface. *Wear* **35**, 87-111.

Coulomb, C. A. (1785). Théorie des machines simples, en ayant égard au frottement de leurs parties et à la roideur des cordages. *Mémoire de Mathématique et de. Physique de l'Académie Royale* **6**, 161-332.

Davies, C., De, D. and Thomas, A. (1994). Characterization of the behavior of rubber for engineering design purposes: 1.Stress-strain relations. *Rubber Chemistry and Technology* **67**, 716-728.

Derjaguin, B. V., Muller, V. M. and Toporov, Y. P. (1975). Effect of contact deformations on the adhesion of particles. *Progress in Surface Science* **45**, 131-143.

Desaguliers, J. T. (1734). *A course of experimental philosophy*, *vol. 1.* London (United Kingdom), John Senex.

Desper, C., Schneider, N., Jasinski, J. and Lin, J. (1985). Deformation of microphase structures in segmented polyurethanes. *Macromolecules* **18**, 2755-2761.

Drobny, J. G. (2007). *Handbook of thermoplastic elastomers*. Norwich (New York, USA), William Andrew Inc.

Duncan, B. C.; Maxwell, A. S.; Crocker, L. E. and Hunt, R. A. (1999). Verification of hyperelastic tests methods. *National Physical Laboratory Report-CMMT(A)226*, 1-23.

Enderle, H. F., Kilian, H. G., Heise, B., Mayer, J. and Hespe, H. (1986) Irreversible deformation of semicrystalline PUR-elastomers — A novel concept. *Colloid and Polymer Science* **264**, 305-322.

Estes, G. M., Seymour, R. W. and Cooper, S. L. (1971). Infrared studies of segmented polyurethan elastomers: II.Infrared dichroism. *Macromolecules* **4**, 452-457.

Euler, L. (1748a) Sur le frottement des corps solides. *Historie de l'Académie Royale des Sciences et Belles-Lettres de Berlin* **4**, 122-132.

Euler, L. (1748b). Sur le diminution de la resistance du frottement. *Historie de l'Académie Royale des Sciences et Belles-Lettres de Berlin* **4**, 133-148.

Ferry, J. D. (1980). *Viscoelastic properties of polymers*. 3rd Edition. New York (New York, USA), John Wiley & Sons, Inc.

Fukahori, Y. and Yamazaki, H. (1995). Mechanism of rubber abrasion, Part 3: how is friction linked to fracture in rubber abrasion?. *Wear* **188**, 19-26.

Gäbel, G., Moldenhauer, P. and Kröger, M. (2008). Local effects between the tyre and the road. *AutoTechnology* **8**, 48-53.

Gabriel, P., Thomas, A. G. and Busfield, J. J. C. (2010). Influence of interface geometry on rubber friction. *Wear* **268**, 747-750.

Gent, A. N. (1958). On the relation between indentation hardness and Young's modulus. *Transactions of the Institution of the Rubber Industry* **34**, 46-57.

Gent, A. N. (1996). New constitutive relation for rubber. *Rubber Chemistry and Technology* **69**, 59-61.

Godovsky, Y., Bessonova, N. and Mironova, N. (1986). Thermodynamics of the deformation of segmented polyurethanes with various percentages of hard block: 1.The initial deformation. *Colloid and Polymer Science* **264**, 224-230.

Godovsky, Y., Bessonova, N. and Mironova, N. (1989). Thermodynamics of the deformation of segmented polyurethanes with various hard block contents: 2.Stress softening and mechanical hysteresis. *Colloid and Polymer Science* **267**, 414-420.

Grady, B. P. and Cooper, S. L. (2005). Thermoplastic elastomers. In Mark, J. E., Erman, B. and Eirich, F. R. *The Science and Technology of Rubber*. 3rd Edition. San Diego (California, USA), Elsevier Inc.

Gregory, M. J. (1979). The stress-strain behaviour of filled rubbers at moderate strains. *Plastic and Rubber: Materials and Applications* **4**, 184-188.

Greenwood, J. A. and Williamson, J. B. P. (1966). Contact of nominally flat surfaces. *Proceedings of the Royal Society of London, Series A* **295**, 300–319.

Grosch, K. A. (1963). The relation between the friction and viscoelastic properties of rubber. *Proceedings of the Royal Society of London, Series A* **274**, 21–39.

Gutzeit, F., Kröger, M., Lindner, M. and Popp, K. (2004). Experimental investigations on the dynamical friction behaviour of rubber. In *Proceedings 6th Fall Rubber Colloquium*. Hannover (Germany), 523-532.

Harwood, J. A. C. and Payne, A. R. (1968). Hysteresis and strength of rubbers. *Journal of Applied Polymer Science* **12**, 889-901.

Haupt, P. and Sedlan, K. (2001). Viscoplasticity of elastomeric materials: Experimental facts and constitutive modelling. *Archive of Applied Mechanics* **71**, 89-109.

Hertz, H. (1882). Über die Berührung fester elastischer Köper. *J. reine und angewandte Mathematik* **92**, 156-171.

Isihara, A., Nashitsume, N. and Tatibana, M. (1951). Statistical theory of rubber-like elasticity, IV: Two dimensional stretching. *Journal of Chemical Physics* **19**, 1508-1512.

ISO (2003). *Thermoplastic elastomers: Nomenclature and abbreviated terms (ISO 18064*). Geneva (Switzerland), International Organization for Standardization.

ISO (2005). *Rubber, vulcanized or thermoplastic. Determination of tensile stress-strain properties (ISO 37).* Geneva (Switzerland), International Organization for Standardization.

James, H. M. and Guth, E. (1943). Theory of elastic properties of rubber. *Rubber Chemistry and Technology* **11**, 455-481.

James, A. G., Green, A. and Simpson, G. M. (1975) Strain energy functions of rubber: I. Characterization of gum vulcanizates. *Journal of Applied Polymer Science* **19**, 2033–2058.

Janovský, L. (1999). *Elevator mechanical design*. 3rd Edition. Mobile (Alabama, USA), Elevator World, Inc.

JOBST (2008). *Scales & Polymers Hardness Range (company data sheet).* Prior Lake (Minnesota, USA), Jobst Inc.

Johnson, K.L., Kendall, K. and Roberts, A.D. (1971). Surface energy and the contact of elastic solids. *Proceedings of the Royal Society of London, Series A* **324**, 301-313.

Johnson, K. L. (1985). Contact mechanics. Cambridge (United Kingdom), Cambridge University Press.

Johnson, K. L. (1998). Mechanics of adhesion. *Tribology International* **31**, 413-418.

Kanyanta, V. and Ivankovic, A. (2010). Mechanical characterisation of polyurethane elastomer for biomedical applications. *Journal of the Mechanical Behavior of Biomedical Materials* **3**, 51-62.

Karger-Kocsis, J. (2006). Dry friction and sliding behavior of organoclay reinforced thermoplastic polyurethane rubbers. *Kautschuk Gummi Kunststoffe* **59**, 537-543.

Karger-Kocsis, J., Felhos, D. and Thomann, R. (2008). Tribological behavior of a carbon-nanofiber-modified santoprene thermoplastic elastomer under dry sliding and fretting conditions against steel. *Journal of Applied Polymer Science* **108**, 724-730.

Kluppel, M. and Heinrich, G. (2000). Rubber friction on self-affine road tracks. *Rubber Chemistry and Technology* **73**, 578-606.

Kröger, M., Popp, K. and Kendziorra, N. (2004). Experimental and analytical investigation of rubber adhesion. *Machine Dynamics Problems* **28**, 79-89.

Kummer, H. W. (1966). *Unified theory of rubber and tire friction*. Engineering research bulletin B-94, Pennsylvania State University.

Lambert-Diani, J. and Rey, C. (1999). New phenomenological behavior laws for rubbers and thermoplastic elastomer. *European Journal of Mechanics, A Solids* **18**, 1027-1043.

Laraba-Abbes, F., Ienny, P. and Piques, R. (2003). A new "tailor-made" methodology for the mechanical behabiour analysis of rubber-like materials: II.Application to the hyperelastic behaviour characterization of a carbon-black filled natural rubber vulcanizates. *Polymer* **44**, 821-840.

Le Gal, A. and Kluppel, M. (2006). Investigation and modelling of adhesion friction on rough surfaces. *Kautschuk Gummi Kunststoffe* **59**, 308-315.

Lion, A. (1996). A constitutive model for carbon black filled rubber: Experimental investigations and mathematical representation, *Continuum Mechanics and Thermodynamics* **8**, 153-169.

Lion, A. (1997). On the large deformation behaviour of reinforced rubber at different temperatures. *Journal of the Mechanics and Physics of Solids* **45**, 1805-1834.

Mardel, J. I., Chynoweth, K. R. and Hill, A. J. (1995). Wear of polyurethane elastomers. *Materials Forum* **19**, 117-128.

Marvalova, B. (2007). Viscoelastic properties of filled rubber. Experimental observations and material modelling. *Journal of Engineering Mechanics* **14**, 81-89.

Maugis, D. (1992). Adhesion of spheres: the JKR-DMT transition using a Dugdale model. *Journal of Colloid and Interface Science* **150**, 243-269.

Miehe, C., Göktepe, S. and Lulei, F. (2004). A micro-macro approach to rubber-like materials-Part I: the non-affine micro-sphere model of rubber elasticity. *Journal of the Mechanics and Physics of Solids* **52**, 2617-2660.

Moldenhauer, P. and Kröger, M. (2010). Simulation and experimental investigations of the dynamic interaction between tyre tread block and road. In *Elastomer friction. Lecture notes in applied and computational mechanics 51*. Besdo, D., Heimann, B., Klüppel, M., Kröger, M. Wriggers, M. and Nackenhorst, U. Heidelberg (Germany), Springer-Verlag, 165-200.

Mooney, M. (1940). A theory of large elastic deformation. *Journal of Applied Physics* **11**, 582-592.

Mullins, L. (1947). Effect of stretching on the properties of rubber. *Journal of Rubber Research* **16**, 275-289.

Muhr, A. H. (2005). Modeling the stress-strain behavior of rubber. *Rubber Chemistry and Technology* **78**, 391-425.

Nakenhorst, U. (2000). *Rollkontakdynamik-Numerische Analyse der Dynamik rollender Köper mit der Finite Element Methode*. University of the Federal Armed Forces. Hamburg (Germany).

Ogden, R. W. (1972). Large deformation isotropic elasticity – on the correlation of theory and experiment for incompressible rubber-like solids. *Proceedings of the Royal Society of London, Series A* **326**, 565-584.

Persson, B. N. J. (1998). On the theory of rubber friction. *Surface Science* **401**, 445-454.

Persson, B. N. J. (2001). Elastoplastic contact between randomly rough surfaces. *Physical Review Letters* **87**, 116-101.

Persson, B. N. J., Albohr, O., Tartaglino, U., Volokitin, A. I. and Tosatti, E. (2005). On the nature of surface roughness with application to contact mechanics, sealing, rubber friction and adhesion. *Journal of Physics Condensed Matter* **17**, 1-62.

Persson, B. N. J. (2006). Rubber friction: role of the flash temperature. *Journal of Physics Condensed Matter* **18**, 7789-7823.

Petrovic, Z. and Ferguson, J. (1991). Polyurethane elastomers. *Progress in Polymer Science* **16**, 695-836.

PTS (2007). *Thermoplastic elastomers (company data sheet).* Adelshofen/Tauberzell (Germany), Plastic Technologie Service.

Qi, H. J., Joyce, K. and Boyce, M. C. (2003). Durometer hardness and the stress-strain behavior of elastomeric materials. *Rubber Chemistry and Technology* **76**, 419-435.

Qi, H. J. and Boyce, M. C. (2003). Stress-strain behavior of thermoplastic polyurethanes. *Mechanics of Materials* **37**, 817-839.

Rieger, H. (1968). *Experimentelle und theoretische Untersuchungen zur Gummireibung in einem grossen Geschwindigkeits- und Temperaturbereich unter Berücksichtigung der Reibungswärme*. Technical report, Technische Universität Darmstadt.

Rivlin, R. S. (1948). Large elastic deformations of isotropic materials I: Fundamental concepts. *Philosophical Transactions of the Royal Society, A* **240**, 459-470.

Rivlin, R. S. and Saunders, D. W. (1951). Large elastic deformations of isotropic materials VII: Experiments on the deformation of rubber. *Philosophical Transactions of the Royal Society, A* **243**, 451-288.

Rivlin, R. S. (1956). Large elastic deformations. In Eirich, F. R. *Rheology,* Vol. 1. New York (New York, USA), Academic Press.

Roberts, A. D. and Thomas, A. G. (1975). The adhesion and friction of smooth surfaces. *Wear* **67**, 55-69.

Savkoor, A. R. (1966). Some aspects of friction and wear of tyres arising from deformations slip and stresses at ground contact. *Wear* **9**, 66-78.

Schallamach, A. (1952). The load dependence of rubber friction. *The Proceedings of the Physical Society, B* **65**, 657-661.

Schallamach, A. (1971) How does rubber slide?. *Wear* **17**, 301-312.

Scott, J. R. (1948). Improved method of expressing hardness of vulcanised rubber. *Journal of Rubber Research* **17**, 145-152.

Seymour, R., Estes, G. and Cooper, S. (1970). Infrared studies of segmented polyurethan elastomers: I.Hydrogen bonding. *Macromolecules* **3**, 579-583.

Simo, J.C. (1987). On a fully three-dimensional finite-strain viscoelastic damage model: formulation and computational aspects. *Computer Methods in Applied Mechanics and Engineering* **60**, 153-73

Simulia (2009). *Abaqus user's manual, v. 6.8.3*, Providence (Rhode Island, USA), Simulia.

Sun, J. L., Lee, K. H. Lee H. P. (2000). Comparison of implicit and explicit finite element methods for dynamic problems. *Journal of Materials Processing Technology* **105**, 110-118.

Tabaddor, F. (1989). Finite element analysis of a rubber block in frictional contact. *Computers and Structures* **32**, 549-62.

Tabor, D. (1960). Hysteresis losses in the friction of the lubricated rubber. *Rubber Chemistry and Technology* **33**, 142-150.

Tabor, D. (1976). Surfaces forces and surface interactions. *Journal of Colloid and Interface Science* **58**, 1-13.

Tangorra, G. (1966). Hardness, modulus and thickness. *Rubber Chemistry and Technology* **36**, 1520-1525.

Thirion, P. (1946). The coefficient of adhesion of rubber. *Rubber Chemistry and Technology* **21**, 505-515.

Tomlinson, G. A. (1929). A molecular theory of friction. *Philosophical Magazine* **7**, 905–939.

Treloar, L. R. G. (1944). Stress-strain data for vulcanised rubber under various types of deformations. *Transactions of Faraday Society* **40**, 59-70.

Treloar, L. R. G. (1946). The elasticity of a network of long-chain molecules. *Transactions of Faraday Society* **42**, 83-94.

Treloar, L. R. G. (1975). *The physics of rubber elasticity*. Oxford (United Kingdom), Clarendon Press.

Tschoegl, N. W. (1971). Constitutive equation for elastomers. *Journal of Polymer Science, Part A-1* **9** 1959-1970.

Unsal, E., Yalcin, B., Yilgor, I., Yilgor, E. and Cakmak, M. (2009). Real time mechano-optical study on deformation behavior of PTMO/CHDI-based polyetherurethanes under uniaxial extension. *Polymer* **50**, 4644-4655.

Varga, O. H. (1966). *Stress - Strain behavior of elastic materials: selected problems of large deformations*. New York (New York, USA), Interscience Publishers.

Verheyde, B., Rombouts, M., Vanhulsel, A., Havermans, D., Meneve, J. and Wangenheim, M. (2009). Influence of surface treatment of elastomers on their frictional behaviour in sliding contact. *Wear* **266**, 468-475.

Wang, C. B. and Cooper, S. L. (1983). Morphology and properties of segmented polyether polyurethaneureas. *Macromolecules* **16**, 775-786.

Ward, I. M. and Sweeney, J. (2004) *An introduction to the mechanical properties of solid polymers*. 2nd Edition. Chichester (United Kingdom), John Wiley & Sons Ltd.

Waters, N. E. (1965). The indentation of thin rubber sheets by spherical indenters. *British Journal of Applied Physics* **16**, 557-563.

White, J. R. and De, S. K. (2001). *Rubber technologist's handbook*. Shawbury (United Kingdom), Rapra Technology Ltd.

Wriggers, P. (2006). *Computational contact mechanics*. 2nd Edition. Heidelberg (Germany), Springer-Verlag.

Wriggers, P. and Reinelt, J. (2009). Multi-scale approach for frictional contact of elastomers on rough rigid surfaces. *Computer Methods in Applied Mechanics and Engineering* **198**, 2996-2008.

Yeh, F., Hsiao, B., Sauer, B., Michel, S. and Siesler, H. (2003). In-situ studies of structure development during deformation of a segmented poly(urethane-urea) elastomer. *Macromolecules* **36**, 1940-1954.

Yeoh, O. H. (1984). On hardness and Young's modulus of rubber. *Plastics and Rubber Processing and Applications* **4**, 141-144.

Yeoh, O. H. (1993). Some forms of the strain energy function for rubber. *Rubber Chemistry and Technology* **66**, 754-771.

Zhang, S.-W. (2004). *Tribology of elastomers*. Amsterdam (The Netherlands), Elsevier B. V.

“Non ignoravi me mortalem genuisse”

Marcus Tullius Cicero